UNCERTAINTY QUANTIFICATION FOR ELECTROMAGNETIC ANALYSIS VIA EFFICIENT COLLOCATION METHODS

by

Abdulkadir C. Yucel

A dissertation submitted in partial fulfillment
of the requirements for the degree of
Doctor of Philosophy
(Electrical Engineering)
in The University of Michigan
2013

Doctoral Committee:

Professor Eric Michielssen, Chair
Assistant Professor Hakan Bağcı, King Abdullah University of Science and Technology
Associate Professor Anthony Grbic
Professor Kenneth G. Powell
Professor Fawwaz T. Ulaby

To my mother and father

ACKNOWLEDGEMENTS

I would like to express my gratitude to my advisor, Professor Eric Michielssen, for his encouragement, support, and guidance throughout the course of this work. The work presented in this thesis would not be possible without his profound knowledge and intuition. His sincerity, enthusiasm, and dedication have set an excellent example for this student. I would like to thank to Professors Fawwaz T. Ulaby, Kenneth G. Powell, and Anthony Grbic for serving on my committee, as well as providing valuable constructive criticism on this thesis. My special thanks go to Professor Hakan Bağcı for his support and contributions to the preparation of this thesis during his post-doctoral stay in University of Michigan and for his friendship.

My gratitude is extended to my extraordinary colleagues in current/former Professor Michielssen's research group. I feel lucky to work with Professor Francesco P. Andriulli, Felipe Valdes, Luis Gomez, Pelumi Osoba, Yang Liu, and Han Guo. I also would like to thank to all of my friends in the Radiation Laboratory. I owe a particular thanks to Seyit A. Sis, Gurkan Gok, Mohammadreza F. Imani, Meysam Moallem, Amit Patel, Farhad Bayatpur, Carl Pfeiffer, Michael Benson, Hatim Bukhari, Waleed Alomar, Fikadu Dagefu, Victor Lee, Sangjo Choi, Jungsuek Oh, Young Jun Song, Seungku Lee, Armin Jam, Ning Wang, Emre Alan, Tolga Yardimci, Sebahattin Eker, Amr A. Ibrahim, Jackie Vitaz…

I would like to thank to Professor A. Arif Ergin of Gebze Institute of Technology for his mentorship, support, and friendship during my undergrad and grad years. He believed in me and guided me in research in computational electromagnetics when I was a junior undergrad. And this journey started… I would like to express my gratitude to Professor Ahmet Rumeli of Middle East Technical University for his support, guidance, and mentorship throughout my undergrad years.

I would like to give my greatest gratitude to my mother Sevtap Yücel, my father Dr. T. Savaş Yücel, and my brothers Dr. Ali B. Yücel and Abdullah Yücel. All this work wouldn't have been possible without their support and encouragement. Last but not least, I would like to thank to my wife Sevinç. Her presence, love, and endurance have supported me through the hardest trials and pulled me back to life whenever I've stepped closer to the edge.

TABLE OF CONTENTS

LIST OF FIGURES

LIST OF TABLES

LIST OF APPENDICES

CHAPTER 1
INTRODUCTION

1.1 Background

Today, computational electromagnetic (EM) tools are widely used for analyzing EM phenomena in electronic systems installed on complex and multiscale platforms as well as for synthesizing a plethora of electronic devices ranging from absorbers to microwave filters, waveguide devices, and antennas. In practice, the analyses and syntheses conducted by these tools are often fraught by the uncertainties in electronic systems' geometry, configuration, and excitation. Examples of such uncertainties include the positions of cables, scatterers, and electronic units; the values of lumped electronic components and material constitutive parameters; the locations of transmitters, receivers, and internal noise sources; and the polarization and direction of arrival of impinging EM waves. Oftentimes, these uncertain quantities – henceforth termed "random variables" – strongly and nonlinearly impact voltages and currents on mission-critical circuits or receivers – further called "observables". To enhance the credibility of analyses and to ensure the functionality and performance of synthesized electronic devices, this dependency must be accurately quantified [1].

The need to quantify uncertainties in EM analysis is most frequently met by Monte Carlo (MC) methods [2-4]. Classical MC methods call for the evaluation of

observables using deterministic EM simulators for many realizations of the system and its excitation, selected according to the known/assumed probability density function (pdf) of the random variables [5]. MC methods are straightforward to implement and readily provide the statistical moments and pdfs of the observables. That said, they often converge slowly and require a large number of deterministic EM simulations to yield sufficiently accurate statistical data. This limits their applicability to the statistical characterization of EM phenomena on complex and large-scale platforms, for which each deterministic simulation requires significant CPU resources.

Difficulties in the use of classical MC methods to extract statistics from large-scale simulations are not unique to EM analysis and have been encountered in many branches of computational science and engineering. Not surprisingly, a host of MC alternatives for statistically characterizing outputs of large-scale simulations given randomness in their inputs have been developed. Oftentimes, these methods construct surrogate models for the observable, which can be efficiently integrated to obtain observable averages and standard deviations, or probed via MC to extract their pdfs. Within the uncertainty quantification community, techniques for generating surrogate models using generalized polynomial chaos (gPC) and stochastic collocation expansions [refs], which approximate observables using entire-domain orthogonal polynomials and Lagrange polynomials, respectively, have gained significant traction. The determination of gPC expansion coefficients may proceed via Galerkin [6-9] or collocation [10-12] methods. While gPC Galerkin methods are *slightly* more accurate than their collocation counterparts [10], they call for the solution of large systems of coupled equations in gPC expansion coefficients, as well as rather intrusive modifications to deterministic solvers

[11]. See [12-14] for applications of gPC Galerkin methods in EM analysis. gPC collocation methods are computationally more efficient as they compute gPC expansion coefficients via multi-dimensional integration; moreover, their implementation is non-intrusive as they can use available deterministic simulators to compute observables on integration/collocation points [10], i.e. combinations of random variables. See [15-17] for applications of gPC collocation methods in EM analysis. The stochastic collocation (SC) methods show striking resemblance to gPC collocation methods; their implementation is non-intrusive and they are computationally as efficient as gPC collocation methods. Their distinction is that the SC expansion coefficients are solely the observable values on the integration/collocation points. See [18-24] for applications of stochastic collocation methods in EM analysis. In some sense, SC and gPC collocation methods combine the strengths of MC and gPC Galerkin methods. Just like MC methods, they only require the repeated execution of an existing deterministic simulator for a select number of inputs. And very much like gPC Galerkin methods, they tend to be highly accurate and rapidly convergent, at least for observables that vary smoothly throughout the domain of random variables, i.e. random domain.

As well as gPC and SC methods, the perturbation methods have received significant attention for statistical EM analysis [25-27]. These methods require intrusive changes to the existing deterministic solvers; the governing equations of such solvers are modified due to multivariate Taylor series expansions of observables. Typically, the statistical moments and pdfs of observables are estimated using approximate expressions derived from modified governing equations. Oftentimes, the second-order Taylor series expansion makes the resulting governing equations extremely complicated; truncating the

expansion at such order limits the applicability of perturbation methods to the observables that vary almost linearly throughout the random domain. Another class of intrusive techniques relies on Nuemann expansions which were applied to the inverses of random matrices, entries of which are functions of random variables [28]. Just like perturbation methods, their applicability is limited to almost linearly varying observables [10]. For this reason, both perturbation and Neumann methods are out of the scope of this thesis.

The classical gPC and SC methods can seldom be applied directly to statistical EM analysis as they become inefficient and inaccurate for observables that vary non-smoothly in the random variables, as do voltages in resonant circuits subject to minor perturbations in the values of lumped elements, or fields in over-moded or quasi-resonant cavities. This deficiency stems from the fact that accurate representations of such observables only can be achieved using very high-order polynomials. Recently, several adaptive methods have been proposed to address this limitation. The multi-element gPC (ME-gPC) [29, 30], probabilistic collocation (ME-PC) [31], and hierarchical sparse grid (SG) collocation methods [34-36] are *h*-adaptive refinement schemes for use in conjunction with gPC Galerkin, gPC collocation, and SC methods, respectively. ME-gPC and ME-PC methods achieve their efficiency and accuracy by recursively and adaptively dividing the random domain into subdomains guided by the decay rates of the observables' local variances and by constructing separate local and low-order gPC expansions for each subdomain. Initial versions of these methods assumed uniformly distributed random variables [29], but recent adaptations allow for arbitrary distributions [30, 31]. The hierarchical SG collocation methods [34-36] derive their efficiency and

accuracy from a similar strategy; they adaptively and recursively divide the random domain into subdomains guided by the approximation errors obtained at two successive levels of local SG constructions and approximate the local variations of observables in subdomains via either low-order piecewise multilinear or Lagrange polynomial basis functions. These methods were proposed initially for uniformly distributed random variables [32, 33] and then extended for the arbitrary distributions [34].

Efficient as they may be for moderate-dimensional random domains, the classical gPC and SC methods and their *h*-adaptive extensions lose their accuracy and efficiency while constructing surrogate models in high-dimensional random domains. This deficiency, so called *curse of dimensionality*, stems from the fact that the number of collocation points in gPC collocation and SC methods and linear equations in gPC Galerkin methods scale exponentially with the number of random variables. To weaken or even break the curse of dimensionality, the high dimensional model representation (HDMR) technique was developed in [35]. The technique relies on decomposing the observables in high-dimensional random domains into their contributions in lower-dimensional random domains (i.e., representing the high-dimensional problems in terms of lower-dimensional subproblems). Specifically, it expresses the observable as superposition of "component functions" that represent independent and combined contributions of random variables to the observable. The lowest-order component functions reveal the "independent" contributions of the random variables while higher-order ones reveal combined contributions of random variable groups; the number of random variables participating to the groups increases as the order of component function increases. The HDMR expansion is constructed using only low-order (often up to third

order) component functions for observables that weakly depend on high-order correlations of the random variables. Such observables are frequently encountered in realistic stochastic problems and ideal candidates for being efficiently approximated by the HDMR technique.

The component functions that feature in HDMR expansion are defined as the observable values on cuts (i.e., lines, planes, and hyperplanes) passing through a reference point in random domain, which is often selected as the centroid of the random domain. To this end, the HDMR technique is also referred as CUT-HDMR to make it distinct from the analysis of variance (ANOVA) decomposition in statistics [36-38], which was proposed to measure the contributions of random variables groups' variances to the overall variance of the observable. The component functions in ANOVA decomposition are defined via high-dimensional integrals and thereby expensive to compute for large-scale stochastic problems. On the other hand, the component functions in CUT-HDMR method involve the observable values on cuts defined in lower dimensional random domains and are approximated via ME-PC method [39], hierarchical SG collocation method [40], and classical tensor-product based collocation methods [41, 42].

Despite to be truncated at very low orders, the HDMR expansions may have very large number of component functions while generating surrogate models in very high dimensional random domains. As an example, 166751 component functions are needed for a third-order HDMR expansion constructed in a 100-dimensional random domain. This high cost can be reduced considerably by integrating an iterative scheme to the HDMR technique, which automatically selects the random variables that significantly

contribute to the observable and iteratively includes these variables' higher-order component functions in the HDMR expansion. Such iterative scheme was proposed in [43, 44] and applied to the statistical framework combining CUT-HDMR with the hierarchical SG collocation method in [40]. This scheme, also referred as iterative HDMR in this work, to our knowledge has never been applied to a statistical framework combining CUT-HDMR with the ME-PC method as done in this thesis.

1.2 Statement of Purpose

The purposes of this thesis are to propose accurate and efficient collocation methods for the uncertainty quantification of EM observables, to develop extensions for finely tuning them for EM applications, and to demonstrate their applicability to the real-world stochastic EM scenarios.

For these purposes, first, a Stroud-based SC method is introduced for statistically characterizing electromagnetic compatibility and interference (EMC/EMI) phenomena on electrically large and complex platforms. The accuracy and efficiency of Stroud-based SC method are demonstrated via its application to the several real-world stochastic EMC/EMI scenarios including characterizations of coupled voltages at the terminals of RG-58 coaxial cables suspended at several nodes, at the feed pins of cable-interconnected and shielded computer cards, and at the terminals of cables situated inside the bay of an airplane cockpit.

Although the Stroud-based SC method yields sufficient accuracy for many realistic EMC/EMI scenarios, it become highly inaccurate for observables that vary non-smoothly in the random variables, as do voltages in resonant circuits, or electric fields in

chaotic environments such as mine tunnels. To this end, second, a computational framework that builds upon the adaptive ME-PC method is developed for statistically characterizing EMC/EMI observables that potentially vary rapidly/nonsmoothly across the random domain and for statistically characterizing transverse magnetic (TM) and EM wave propagation through mine tunnels. The computational framework is finely tuned to specific EM applications by hybridizing the ME-PC method with Dirichlet kernel. The accuracy and efficiency of the proposed computational framework are demonstrated via its applications to the several real-world stochastic EMC/EMI scenarios including statistical characterization of voltages in resonant circuits connected to the transmission lines, voltages in shielded/unshielded microwave amplifiers, and magnetic fields induced on car tire pressure sensors. Moreover, the proposed framework is also applied to the statistical characterization of TM and EM wave propagation in various mine tunnel configurations. To apply the adaptive ME-PC method to EM wave propagation in mine tunnels, a novel three-dimensional full-wave EM simulator is proposed for computing the observables on integration/collocation points. This EM simulator is the first-ever integral equation based full-wave solver capable of characterizing EM wave propagation in hundreds of wavelengths long mine tunnels.

Motivated from the abovementioned limitations of the ME-PC method, third, a computational framework combining iterative HDMR technique with the ME-PC method is proposed for statistical characterization of EMC/EMI observables that involve a large number of random variables. The proposed framework is unique among the UQ methods used in computational sciences and engineering as a similar framework in [39] doesn’t employ an iterative scheme. Furthermore, the computational framework is finely tuned to

broadband EM applications by hybridizing the iterative HDMR method with the expansion of partial fractions, coefficients of which are obtained by well-known vector fitting algorithm. The proposed framework is applied to the several real-world EMC/EMI scenarios including statistical characterization of coupled voltages at the terminals of parallel wires, parallel interconnects, and a cascaded multiconductor transmission line network. Moreover, the proposed framework is applied to surrogate-model based EM optimization problems. Specifically, the surrogate models of EM observables/objective functions generated using the proposed scheme are used by a classical genetic algorithm (GA) that searches the high-dimensional domain for optimal designs. The efficiency and accuracy of the proposed framework are demonstrated via its application to the several real-world EM optimization problems including selection of locations of stacked-patch microstrip antennas in a linear array and the placement of monopole antennas on a naval ship.

1.3 Organization of Chapters

The remainder of this thesis is organized as follows: Chapter 2 reviews the classical SC methods and presents the proposed Stroud-based SC method and its application to the statistical characterization of EMC/EMI phenomena on electrically large, loaded, and complex platforms. In addition, it gives detailed information about the deterministic EM solver used to compute observables on collocation points. Chapter 3 describes gPC collocation method and presents the ME-PC method and its hybrization with Dirichlet kernel. It also verifies the accuracy and efficiency of the ME-PC method via various realistic stochastic EMC/EMI scenarios. Chapter 4 discusses the possible

uncertain parameters in a mine geometry, configuration, and excitation and presents the application of the ME-PC method to the statistical characterization of TM wave propagation in various mine tunnel configurations. Chapter 5 expounds the novel three-dimensional full-wave EM solver for characterization of EM wave propagation in mine tunnels and presents the application of the ME-PC method to the statistical characterization of EM wave propagation in rectangular mine tunnel configurations. Chapter 6 presents the HDMR technique, its integration with the ME-PC method, and the iterative HDMR technique. Furthermore, it details the hybridization of HDMR technique with the expansion of partial fractions for broadband EM applications. It illustrates the accuracy and efficiency of iterative HDMR method via its application to the several EMC/EMI scenarios that involve large numbers of random variables. Chapter 7 discusses the possible design parameters in an EM optimization problem and explains the utilization of HDMR-generated surrogate models in an EM optimization problem. In addition, it presents the application of the iterative HDMR method to the GA-based optimization of EM devices. Finally, Chapter 8 summarizes the conclusions of this thesis, discusses the ongoing studies, and presents the list of journal/conference papers and conference abstracts being prepared or published during the course of this thesis.

CHAPTER 2
STOCHASTIC COLLOCATION METHOD

2.1 Introduction

To quantify the uncertainties in large-scale simulations, the stochastic collocation (SC) methods have received significant attention in recent years. These methods have been applied in many branches of computational sciences ranging from finance, fluid dynamics to biophysics [45]. They owe their popularity to the facts that they are non-intrusive (i.e. they use existing deterministic simulator without intrusive modifications) and exhibit fast convergence. In some sense, they combine the strengths of MC methods and stochastic Galerkin methods: just like MC methods, they only require repetitive execution of existing deterministic simulator. And very much like stochastic Galerkin methods, they are rapidly convergent and yield accurate statistical information (i.e. mean, standard deviation, probability density function (pdf), cumulative density function (cdf)) of observables that vary smoothly throughout the domain of random variables, i.e. random domain.

The SC methods use multivariate Lagrange polynomials to generate surrogate models of observables (i.e., compact polynomial representations of observables), which can be probed via MC methods to generate pdfs/cdfs of observables. While generating surrogate models, they allow computing the statistical moments (i.e. mean and standard

deviation) of observables as well using the multivariate integration rules. The earlier works on SC methods [46, 47] leveraged the multivariate integration rules based on tensor product (TP) grids for low-dimensional random domains. Later on, the SC methods were applied using Stroud-2 (S-2)/Stroud-3 (S-3) and sparse grid (SG) integration rules to decrease the computational cost of surrogate model generation and statistical moment computation for moderate and high dimensional random domains [4, 5]. Not surprisingly, the earlier works on application of SC methods to EM analysis evolved in a similar way: the SC methods employing TP integration rules were introduced first with the name "unscented transform" [22, 25, 26] and the ones based on the Stroud and SG integration rules were used later on for statistical characterizations of EM observables on complex platforms [15, 18-20].

In this chapter, a Stroud integration rules based SC method [19] suitable for statistical characterization of EMC/EMI phenomena on electrically large and complex platforms is expounded. To compute the multidimensional integrals pertinent to the statistical moments of observables, the method calls for the evaluation of observables (using a deterministic EMC/EMI simulator) at collocation (integration) points dictated by Stroud rules. Assuming the dimension of the random domain is N_{dof}, S-2 and S-3 integration rules require only $N_{\text{dof}}+1$ and $2N_{\text{dof}}$ collocation points to evaluate the N_{dof}-dimensional integrals defining the statistical moments of the observable, respectively; for S-2/S-3 rules to deliver accurate results, the observable and its square should be adequately described by a second/third order polynomial in the N_{dof}-dimensional random domain. The selection of the collocation points is influenced by the random variables' (assumed) pdfs, which may be normal or beta.

The Stroud-based SC method used here are far more efficient than the traditional MC method or TP based SC methods. Indeed, the traditional MC method call for the evaluation of the observable at randomly selected points in the N_{dof}-dimensional random domain; the accuracy of the traditional MC method is proportional to the one over square root of the number of random points [5]. Even though their implementation is straightforward, the traditional MC method often requires too many deterministic simulations to yield reasonably accurate data. In fact, much more accurate statistical moments can be obtained using the SC methods based on TP integration rules. Unfortunately, if an n point one-dimensional (1D) integration rule is used along each dimension of an N_{dof}- dimensional integral, the TP integration rule requires $n^{N_{\text{dof}}}$ deterministic simulations. The computational cost associated with these evaluations often is prohibitive even for moderate n and N_{dof}, and stands in stark contrast with that incurred when using S-2 and S-3 rules, which call for $N_{\text{dof}}+1$ and $2N_{\text{dof}}$ number of deterministic simulations, respectively. In addition, the SG integration rule based SC methods strike an interesting compromise between the efficiency of Stroud based ones and the accuracy of the TP based ones. However, it was proven that the SG based SC methods are not as efficient and accurate as the Stroud based ones for the observables that can be adequately described by second or third order polynomials [48].

2.2 Formulation

This section details the MC method, the SC method, used for statistically characterizing EMC/EMI phenomena on electrically large, multiscale, and loaded

platforms, and the deterministic simulator used in this work. The definitions required for stochastic analysis are given first. Then the traditional MC method is explained. The SC method based on TP, SG, and S-2/S-3 integration rules are detailed next. Finally, a TDIE-based deterministic simulator that is used to compute observable values on collocation points is described.

2.2.1 The Stochastic Model

Let $\mathbf{x} = \left[x^1, x^2, ..., x^{N_{\text{dof}}-1}, x^{N_{\text{dof}}} \right]$ denote a vector in the N_{dof}-dimensional random domain $D = \prod_{i=1}^{N_{\text{dof}}} D^i$ that parameterizes N_{dof} random variables/uncertainties/degrees of freedom in a system's geometry, configuration, or excitation. The elements x^i of $\mathbf{x}$ are assumed mutually independent and distributed with known pdfs $w^i(\cdot)$. Furthermore, let $W(\mathbf{x})$ denote the assumed multivariate pdf of $\mathbf{x}$. Here, $W(\mathbf{x})$ is expressed as the tensor product of pdfs, $w^i(\cdot), i = 1, \ldots, N_{\text{dof}}$, i.e.

$$W(\mathbf{x}) = \prod_{i=1}^{N_{\text{dof}}} w^i\left(x^i\right). \tag{2.1}$$

Throughout this work, the random variables x^i, $i = 1, ..., N_{\text{dof}}$, are assumed to be either normally distributed with mean μ^i and standard deviation σ^i in the unbounded 1D domains $D^i = (\infty, \infty)$, or beta (or uniform) distributed in the bounded 1D domains $D^i = \left[a^i, b^i \right]$ with exponential parameters c^i and d^i. Table 2–1 presents explicit expressions for normal and beta pdfs; note that the uniform pdf is a special case of the beta distribution with $c^i = d^i = 0$. Even though integration rules for both normal and beta

pdfs are implemented in this work, modeling uncertainties with normal distributions is typically not recommended because of inefficiencies incurred with the modeling of the distribution's infinite tail [21]. In practical applications, normal distributions are often well-approximated by beta distributions [21].

	$w^i\left(x^i\right),\ i=1,...,N_{\text{dof}}$
Normal	$\frac{1}{\sigma^i\sqrt{2\pi}}e^{-\left(\frac{x^i-\mu^i}{\sqrt{2}\sigma^i}\right)^2},\ x^i\in\left(-\infty,+\infty\right)$
Beta	$\frac{\left(x^i-a^i\right)^{d^i}\left(b^i-x^i\right)^{c^i}}{B\left(c^i+1,d^i+1\right)\left(b^i-a^i\right)^{c^i+d^i+1}},\ x^i\in\left[a^i,b^i\right]$

Table 2–1 Definitions of normal and beta pdfs

Let $V\left(\mathbf{x}\right)$ represent an observable (e.g., a voltage or current on a mission-critical circuit or component). The main purpose of the statistical frameworks explained in this work is to obtain the statistical information (average, standard deviation, pdf, cdf, etc.) of $V\left(\mathbf{x}\right)$. The mean and standard deviation of $V\left(\mathbf{x}\right)$ are computed using

$$E\left[V\left(\mathbf{x}\right)\right]=\int_D V\left(\mathbf{x}\right)W\left(\mathbf{x}\right)d\mathbf{x}, \tag{2.2}$$

$$\text{std}\left[V\left(\mathbf{x}\right)\right]=\sqrt{\int_D\left(V\left(\mathbf{x}\right)-E\left[V\left(\mathbf{x}\right)\right]\right)^2W\left(\mathbf{x}\right)d\mathbf{x}}. \tag{2.3}$$

The pdfs/cdfs of $V\left(\mathbf{x}\right)$ can be approximated by maximum entropy principle that uses the higher order statistical moments of $V\left(\mathbf{x}\right)$ [28]. Although this method allows obtaining well-shaped (smooth) pdf of $V\left(\mathbf{x}\right)$, it may lead to erroneous pdfs in some cases since the unknown pdf of $V\left(\mathbf{x}\right)$ is approximated via an assumed pdf [28, 49]. The most popular method to obtain pdf/cdf of $V\left(\mathbf{x}\right)$ is the traditional MC method explained next.

2.2.2 The MC Method

The implementation of the traditional MC method is straight forward: it can be achieved by (i) selecting N_{MC} number of random points, $\mathbf{x}_i$, $i=1,\ldots,N_{\mathrm{MC}}$, in accordance with $W(\mathbf{x})$, (ii) performing deterministic simulations to obtain observable values corresponding to random points, $V(\mathbf{x}_i)$, $i=1,\ldots,N_{\mathrm{MC}}$, and (iii) computing the mean and standard deviation of $V(\mathbf{x})$ by

$$E\left[V(\mathbf{x})\right] \approx \frac{1}{N_{\mathrm{MC}}} \sum_{i=1}^{N_{\mathrm{MC}}} V(\mathbf{x}_i), \tag{2.4}$$

$$\mathrm{std}\left[V(\mathbf{x})\right] \approx \sqrt{\frac{1}{N_{\mathrm{MC}}} \sum_{i=1}^{N_{\mathrm{MC}}} \left(V(\mathbf{x}_i)\right)^2 - \left(E\left[V(\mathbf{x})\right]\right)^2}\,. \tag{2.5}$$

To compute $V(\mathbf{x})$'s pdf, $\mathrm{p}^{\mathrm{V}}(z)$, one needs to divide the range between the minimum and maximum values of $V(\mathbf{x}_i)$, $[z_{\min}\ z_{\max}]$, into N_{bin} equally spaced intervals, (i.e. bins), $[z_k\ z_{k+1}]$, $z_k = z_{\min} + (k-1)(z_{\max} - z_{\min})/N_{\mathrm{bin}}$, $k=1,\ldots,N_{\mathrm{bin}}$. The number of $V(\mathbf{x}_i)$ satisfying $V(\mathbf{x}_i) \in [z_k\ z_{k+1}]$, $k=1,\ldots,N_{\mathrm{bin}}$, is counted; let this number be represented by N_k^{V}; finally, $\mathrm{p}^{\mathrm{V}}(z) \propto N_k^{\mathrm{V}}$ for $z \in [z_k\ z_{k+1}]$. To obtain $V(\mathbf{x})$'s cdf, $C^{\mathrm{V}}(z) = \int_{z_{\min}}^{z} \mathrm{p}^{\mathrm{V}}(z')\,dz'$, the number of $V(\mathbf{x}_i)$ falling into the k^{th} bin and the bins preceding it are summed, i.e. $C^{\mathrm{V}}(z) \propto \sum_{j=1}^{k} N_j^{\mathrm{V}}$, for $z \in [z_k\ z_{k+1}]$. Note that $\mathrm{p}^{\mathrm{V}}(z)$ and $C^{\mathrm{V}}(z)$ can be normalized with N_{MC} and scaled with the bin size, $(z_{\max} - z_{\min})/N_{\mathrm{bin}}$, in order to be compared with traditional pdfs/cdfs. Obviously, $\mathrm{p}^{\mathrm{V}}(z)$ and $C^{\mathrm{V}}(z)$ can be estimated more accurately by increasing N_{bin} and N_{MC}.

In addition to traditional MC method, (quasi-) MC methods based on stratified sampling, Latin hypercube sampling, importance sampling, low-discrepancy sequences (such as Sobol, Halton, Faure sequences) can be used to obtain statistical information of $V(\mathbf{x})$ [5, 50]. In general, the quasi-MC methods converge to exact statistical moments (specifically average) at a rate of $O(N_{\mathrm{MC}}^{-1}(\log N_{\mathrm{MC}})^{N_{\mathrm{dof}}})$, substantially better than that of traditional MC method, $O(N_{\mathrm{MC}}^{-1/2})$, for low dimensional random domains. However, for moderate and high-dimensional random domains, such as $N_{\mathrm{dof}} > 12$, the quasi-MC methods are not as efficient as the traditional MC [51]. It should be noted here that the convergence rate of the traditional MC is independent of N_{dof}. To this end, the results obtained via traditional MC method using large number of random points are often used as "benchmark" results while assessing the efficiency and accuracy of statistical methods used for obtaining the statistical information of $V(\mathbf{x})$ in high-dimensional random domains.

To estimate $V(\mathbf{x})$'s pdf/cdf via traditional MC method, using approximate values probed from a surrogate model of $V(\mathbf{x})$ instead of exact $V(\mathbf{x})$ values drastically reduce the computational cost of the method. Furthermore, using an efficient multivariate integration rule to evaluate N_{dof}-variate integrals pertinent to $V(\mathbf{x})$'s statistical moments (in (2.2) and (2.3)) yields more accurate results compared to those obtained using randomly selected points (via (2.4) and (2.5)). The SC method that constructs accurate surrogate model of $V(\mathbf{x})$ for pdf estimation and computes $V(\mathbf{x})$'s statistical moments via an efficient multivariate integration rule is explained next.

2.2.3 The SC Method

The SC method approximates $V(\mathbf{x})$ in terms of N_{dof}-variate Lagrange interpolation functions $\mathbf{L}(\cdot)$ as [52]

$$V(\mathbf{x}) \cong \sum_{m=1}^{N_{\text{SC}}} V(\mathbf{x}_m)\mathbf{L}_m(\mathbf{x}), \tag{2.6}$$

where N_{SC} is the total number of collocation points selected on a structured grid in D, $V(\mathbf{x}_j)$ is the coefficient of SC expansion, which is nothing more than the observable value on m^{th} collocation point. In (2.6), $\mathbf{L}_m(\cdot)$ is constructed as the tensor product of 1D Lagrange functions $L_{m^i}(\cdot)$, each of which is defined for each dimension as

$$L_{m^i}(x^i) = \prod_{\substack{k=1 \\ k \neq m^i}}^{N^i} \frac{x^i - x_k^i}{x_{m^i}^i - x_k^i}, \quad m^i = 1, \ldots, N^i, \tag{2.7}$$

where, apparently $L_{m^i}(x^i) = 1$ when $x^i = x_{m^i}^i$, N^i is the number of collocation points selected along i^{th} dimension. Using 1D Lagrange functions in (2.6) yields

$$V(\mathbf{x}) \cong \sum_{m^1=1}^{N^1} \cdots \sum_{m^{N_{\text{dof}}}=1}^{N^{N_{\text{dof}}}} V\left(x_{m^1}^1, \ldots, x_{m^{N_{\text{dof}}}}^{N_{\text{dof}}}\right)\left(L_{m^1}(x^1) \cdots L_{m^{N_{\text{dof}}}}\left(x^{N_{\text{dof}}}\right)\right). \tag{2.8}$$

Here, $x_{m^i}^i$ is the $(m^i)^{\text{th}}$ collocation point selected along i^{th} dimension. It's now clear that the N_{SC} in (2.6) is the sum of $N^i, i = 1, \ldots, N_{\text{dof}}$.

During the estimation of pdf/cdf via the traditional MC method explained in Section 2.2.2, the surrogate model (formulated in (2.8)) for $V(\mathbf{x})$ is used instead of the $V(\mathbf{x})$ produced by the deterministic simulator. Let C_{exc} and C_{sur}, represent the

computational costs of evaluating $V(\mathbf{x})$ and its surrogate model at a single point, respectively. Assuming that the cost of binning $V(\mathbf{x}_i)$, $i=1,\ldots,N_{\mathrm{MC}}$, and its surrogates are negligible, the computational costs of extracting $V(\mathbf{x})$'s and its surrogate model's pdfs are $N_{\mathrm{MC}}C_{\mathrm{exc}}$ and $N_{\mathrm{SC}}C_{\mathrm{exc}}+N_{\mathrm{MC}}C_{\mathrm{sur}}$, respectively. Since, $N_{\mathrm{MC}} \gg N_{\mathrm{SC}}$ and $C_{\mathrm{exc}} \gg C_{\mathrm{sur}}$, the cost of estimating the surrogate model's pdf is much smaller than that of extracting $V(\mathbf{x})$'s pdf. Of course, the surrogate model's pdf/cdf is only an approximation to $V(\mathbf{x})$'s pdf/cdf; the accuracy of this approximation depends on the accuracy of N_{dof}-variate Lagrange interpolation. In principle, the number of collocation points used by Lagrange interpolation can be increased to make the difference between the surrogate model and $V(\mathbf{x})$ arbitrarily small.

It goes without saying that the statistical moments of the surrogate model can be obtained from its MC samples and are approximations to those of $V(\mathbf{x})$. Moreover, the statistical moments of $V(\mathbf{x})$ can also be directly computed using N_{dof}-variate integration rules defined on the structured grid by which N_{dof}-variate Lagrange interpolation is performed. By substituting (2.6) into (2.2), the mean of $V(\mathbf{x})$ over D can be obtained as

$$\begin{aligned} E\left[V(\mathbf{x})\right] &\cong \int_D \sum_{m=1}^{N_{\mathrm{SC}}} V(\mathbf{x}_m)\mathbf{L}_m(\mathbf{x})W(\mathbf{x})d\mathbf{x} \\ &\cong \sum_{m=1}^{N_{\mathrm{SC}}} V(\mathbf{x}_m)\int_D \mathbf{L}_m(\mathbf{x})W(\mathbf{x})\,d\mathbf{x} \end{aligned}. \tag{2.9}$$

Since the evaluation of the integral in (2.9) via a multivariate integration rule yields the weights of such integration rule, α_m, one can obtain [52]

$$E\left[V\left(\mathbf{x}\right)\right] \cong \sum_{m=1}^{N_{\mathrm{SC}}} V\left(\mathbf{x}_m\right)\alpha_m \,. \tag{2.10}$$

In a similar way, the standard deviation of $V\left(\mathbf{x}\right)$ over D can be approximated as

$$\mathrm{std}\left[V\left(\mathbf{x}\right)\right] \cong \sqrt{\sum_{m=1}^{N_{\mathrm{SC}}} \left(V\left(\mathbf{x}_m\right) - E\left[V\left(\mathbf{x}\right)\right]\right)^2 \alpha_m} \,. \tag{2.11}$$

The multivariate integration rule can be selected as either TP [53], SG [54], or S-2/S-3 [55, 56] integration rules. As the TP rules suffer from the "curse of dimensionality" (i.e., an exponential growth of the number of collocation points with the number of random variables), they are prohibitively expensive in high-dimensional random domains [13]. However, they're highly accurate and efficient for low-dimensional random domains, e.g. $N_{\mathrm{dof}} < 3$. The SG rules restrict the polynomials used in the approximation of the observable to a subset that can be handled by TP methods; for many practical scenarios they yield accuracies on par with TP methods while requiring far fewer collocation points (i.e., executions of the deterministic solver). The S-2/S-3 integration rules are even more efficient than the SG ones but assume at most third-order polynomials. In this chapter, we heavily rely on S-2/S-3 integration rules because of their efficiency in computing moderate to high-dimensional integrals.

2.2.3.1 The TP Integration Rule

Let $\alpha^i_{m^i}$ and $x^i_{m^i}$, $m^i = 1,...,N^i$, and N^i represent the weights, quadrature points, and number of points of a 1D integration rule, respectively. Here i represents a given dimension and m^i denotes the index pertinent to the i^{th} dimension. Using this rule for computing the integral of the function $f\left(x^i\right)$ over the domain D^i yields

$$\int_{D^i} f\left(x^i\right) dx^i \cong \sum_{m^i=1}^{N^i} f\left(x_{m^i}^i\right) \alpha_{m^i}^i \,. \tag{2.12}$$

The TP rule [53] uses the above 1D integration rule to approximate the N_{dof}-dimensional integrals in (2.2) and (2.3) as

$$I(\mathbf{x}) = \int_D f(\mathbf{x})\, d\mathbf{x} \cong \sum_{m^1=1}^{N^1} \cdots \sum_{m^{N_{\text{dof}}}=1}^{N^{N_{\text{dof}}}} f\left(x_{m^1}^1, \ldots, x_{m^{N_{\text{dof}}}}^{N_{\text{dof}}}\right) \left(\alpha_{m^1}^1 \cdots \alpha_{m^{N_{\text{dof}}}}^{N_{\text{dof}}}\right). \tag{2.13}$$

Here, $f(\mathbf{x}) = V(\mathbf{x}) W(\mathbf{x})$ or $f(\mathbf{x}) = \left(V(\mathbf{x}) - E\left[V(\mathbf{x})\right]\right)^2 W(\mathbf{x})$ depending on whether (2.2) or (2.3) is approximated. The 1D integration rule in (2.12) is typically chosen with respect to $w^i(\cdot)$ among Gaussian integration rules: Gauss-Hermite for normal pdf, Gauss-Jacobi for beta pdf, and Gauss-Legendre for uniform pdf [57, 58]. It is clear from (2.13) that the TP rule generates $\prod_{i=1}^{N_{\text{dof}}} N^i$ number of collocation points. By employing N number in each dimension, i.e. $N^i = N$, $i = 1, \ldots, N_{\text{dof}}$, the TP rule based on a Gaussian rule can evaluate accurately polynomials of order $2N-1$ or less. Then, the total number of collocation points becomes $N^{N_{\text{dof}}}$. This exponential growth in the number of collocation points, so called "curse of dimensionality", renders the TP integration rules inefficient for evaluating moderate and high dimensional integrals [10].

2.2.3.2 The SG Integration Rule

The SG integration rules are highly preferable over the TP ones especially for evaluating moderate dimensional integrals as they require considerably less number of collocation points while preserving the accuracy of the latter. The SG rule uses the

abovementioned TP rule and constructs the linear combinations of the TP grids [55, 60-64]:

$$I(\mathbf{x}) \cong \sum_{l-N_{\text{dof}}+1 \le |k| \le l} \sum_{m^1=1}^{N^1(k^1)} \cdots \sum_{m^{N_{\text{dof}}}=1}^{N^{N_{\text{dof}}}(k^{N_{\text{dof}}})} f\left(x_{m^1}^1, \ldots, x_{m^{N_{\text{dof}}}}^{N_{\text{dof}}}\right)(-1)^{l-|k|}\binom{N_{\text{dof}}-1}{l-|k|}\left(\alpha_{m^1}^1 \cdots \alpha_{m^{N_{\text{dof}}}}^{N_{\text{dof}}}\right), \quad (2.14)$$

where $k = k^1 k^2 \ldots k^{N_{\text{dof}}}$ represents a multi-index and $|k| = k^1 + \ldots + k^{N_{\text{dof}}}$ for $k^i \ge 0$, $i = 1, \ldots, N_{\text{dof}}$ and $l \ge 0$ is the provided maximum "level" of SG construction. The number of points used in 1D Gaussian integration rule N^i, $i = 1, \ldots, N_{\text{dof}}$, is a function of each component of multi-index k^i: $N^i\left(k^i\right) = 2^{k^i+1} - 1$, $i = 1, \ldots, N_{\text{dof}}$. The total number of collocation points used in SG is less than $\sum_{l-N_{\text{dof}}+1 \le |k|}^{l} \prod_{i=1}^{N_{\text{dof}}} N^i(k^i)$ since some collocation points are commonly used by the different TP grids used during the construction of SG and should be considered only once. The SG construction and its distinction from TP construction can be best explained by an example. Suppose $N_{\text{dof}} = 2$ and $l = 4$. For such case, the SG rule in (2.14) can be re-written as

$$I(\mathbf{x}) \cong \sum_{3 \le |k| \le 4} \sum_{m^1=1}^{N^1(k^1)} \sum_{m^2=1}^{N^2(k^2)} f\left(x_{m^1}^1, x_{m^2}^2\right)(-1)^{4-|k|}\binom{1}{4-|k|}\left(\alpha_{m^1}^1 \alpha_{m^2}^2\right). \quad (2.15)$$

The multi-indices $k = k^1 k^2$ and the number of collocation points selected along each dimension on third and fourth level (i.e. $|k| = 3$ and $|k| = 4$) of SG construction, $N^i\left(k^i\right)$, $i = 1, 2$, are given in Table 2–2. The collocation points on SG are obtained by just combining the collocation points on TP grids formed using $N^i\left(k^i\right)$, $i = 1, 2$, in Table 2–2.

$\lvert k \rvert$	$k = k^1 k^2$	$N^1\left(k^1\right)$	$N^2\left(k^2\right)$
3	3 0	15	1
3	2 1	7	3
3	1 2	3	7
3	0 3	1	15
4	4 0	31	1
4	3 1	15	3
4	2 2	7	7
4	1 3	3	15
4	0 4	1	31

Table 2–2 For the example case $N_{\text{dof}} = 2$ and $l = 4$, the multi-indices and the number of collocation points selected along each dimension during SG construction.

Note that the total number of collocation points obtained via linear combinations of the TP grids is 273. However, since some of Gaussian collocation points are commonly used by the TP grids at consecutive levels, the total number of collocation points obtained via SG construction is 225. It should be noted here that in case the same maximum number of collocation points is selected along each dimension during the TP construction in (2.13), the resulting number of collocation points is 961. The reduction in number collocation points in SG construction (in (2.15)) with respect to TP construction (in (2.13)) is shown in Figure 2–1.

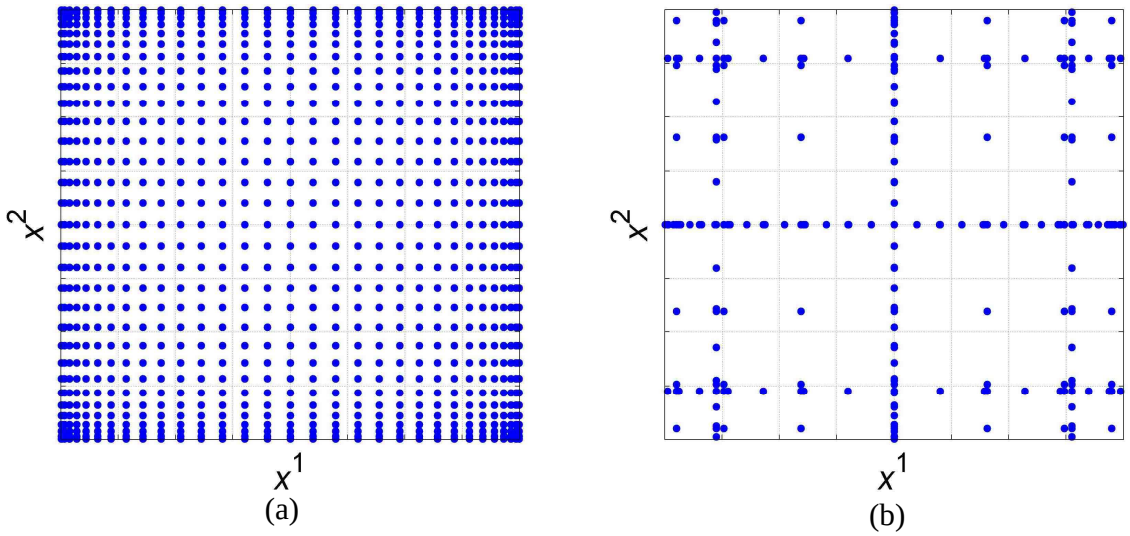

Figure 2–1 For $N_{\text{dof}} = 2$ and $l = 4$, the collocation points on random domain D obtained via (a) TP construction and (b) SG construction.

The accuracy of integration rules obtained by TP and SG constructions can be examined by evaluating integrands that compose of multinomials. Let p^i and p define the order of monomials selected for each dimension, and the total order of multinomials formed by multiplying monomials, i.e. $p = \sum_{i=1}^{N_{\text{dof}}=2} p^i$ for this example. The (Gaussian based-) integration rule constructed by the TP rule is capable of evaluating multinomials that compose of $(x^1)^{p^1}(x^2)^{p^2}$, $p^1 = 0,\ldots,61$, $p^2 = 0,\ldots,61$. On the other hand, the integration rule constructed by the SG rule can evaluate the multinomials that can be covered by the TP grids formed using $N^i\left(k^i\right)$, $i = 1,2$, in Table 2–2. All possible orders of multinomials that can be integrated via the integration rules obtained by the TP and the SG constructions are given in Figure 2–2.

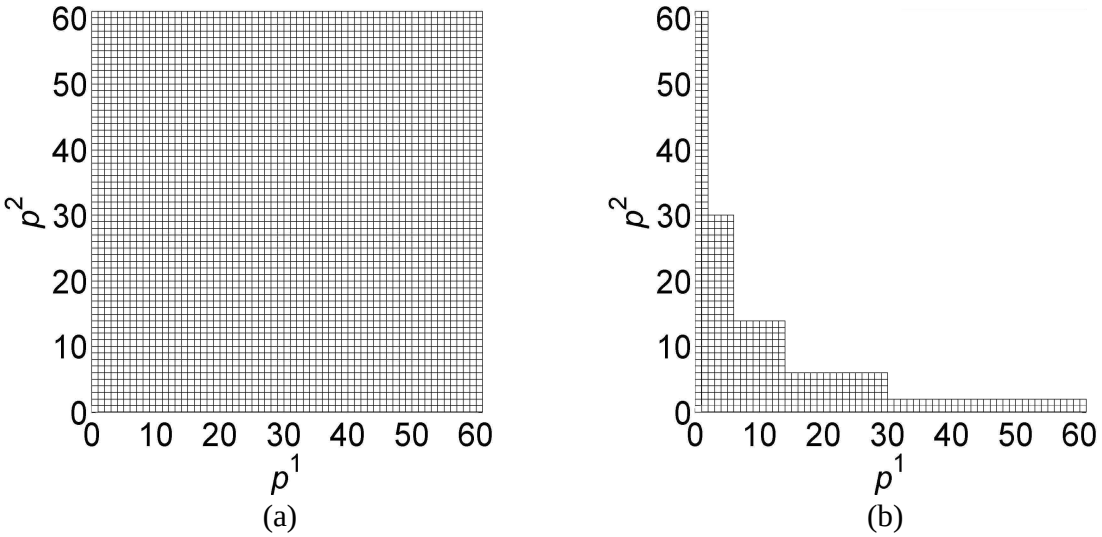

Figure 2–2 For $N_{\text{dof}} = 2$ and $l = 4$, all possible orders of multinomials that can be integrated via Gaussian based integration rules obtained by (a) the TP and (b) the SG constructions

A note regarding the accuracy and efficiency of SG construction is in order. As seen from Figure 2–1, the number of collocation points in the SG construction is far less than that in the TP construction. This reduction becomes substantial in moderate and high dimensional random domains and mitigates the "curse of dimensionality". As seen from Figure 2–2, the number of multinomials is excessive in the TP construction while that's limited in the SG construction. In fact, the maximum total order p of multinomials that can be evaluated by the SG construction is limited to a given number especially when the number of collocation points in each level is linearly increased, i.e. $N^i\left(k^i\right)=2k^i+1$. This limitation makes the integration rules constructed by the SG rule more suitable for the chaos expansions, which limits the total order of orthogonal polynomial bases in approximation to the observables explained in next chapter. More details on properties of the SG construction can be found in [55, 60-64].

2.2.3.3 The S-2/S-3 Integration Rules

The S-2 and S-3 integration rules originally proposed by Stroud [55] and recently extended to allow for the approximation of multidimensional integrals with arbitrary weighting functions in [59] allow for the efficient evaluation of (2.2)-(2.3) provided $V\left(\mathbf{x}\right)$ and $\left[V\left(\mathbf{x}\right)\right]^2$ are (or can be well-approximated by) second or third order polynomials in $\mathbf{x}$. These rules approximate these integrals as in (2.13), i.e.

$$I\left(\mathbf{x}\right)\cong\sum_{m=1}^{N_{\mathrm{ST}}}V\left(\mathbf{x}_m\right)\alpha_m\,. \tag{2.16}$$

Here, N_{ST} is the number of collocation points, and $\mathbf{x}_m$ and α_m, $m=1,...,N_{\mathrm{ST}}$, are collocation points and weights. The expressions for Stroud integration rules are given in

Table 2–3 for normal and beta pdfs; the expressions provided were derived from those in [59], which assumed standard normal distributions ($\mu^i = 0$, $\sigma^i = 1$) and normalized beta distributions ($\left[a^i, b^i\right] = [-1,1]$) via a linear mapping.

	α_m	x_m^i	z_m^i
Normal	$1/N_{\mathrm{ST}}$	$x_m^i = \sigma^i z_m^i + \mu^i$, $x_m^i \in (-\infty, \infty)$, $z_m^i \in (-\infty, \infty)$	$z_m^{2r-1} = \sqrt{2}\cos\left(\frac{2\pi a}{N_{\mathrm{ST}}}\right)$ $z_m^{2r} = \sqrt{2}\sin\left(\frac{2\pi a}{N_{\mathrm{ST}}}\right)$ where $a = r(m-1)$ for S-2 and $a = m(2r-1)$ for S-3, $r = 1,\ldots,\lfloor N_{\mathrm{dof}}/2 \rfloor$, If N_{dof} is odd, then $z_m^{N_{\mathrm{dof}}} = (-1)^{(m-1)}$
Beta	$1/N_{\mathrm{ST}}$	$x_m^i = \frac{a^i + b^i + z_m^i (b^i - a^i)}{2\sqrt{2c^i + 3}}$, $c^i = d^i$, $x_m^i \in \left[a^i, b^i\right]$, $z_m^i \in [-1,1]$	

Table 2–3 The S-2/S-3 integration rules ($i = 1,\ldots,N_{\mathrm{dof}}$, $m = 1,\ldots,N_{\mathrm{ST}}$)

In practice, the approximation in (2.16) will converge to the exact integral provided that the observable exhibits smooth variations that can be modeled by second/third order polynomials. S-2 and S-3 integration rules require $N_{\mathrm{ST}} = N_{\mathrm{dof}} + 1$ and $N_{\mathrm{ST}} = 2N_{\mathrm{dof}}$ number of collocation points, respectively. This renders Stroud integration rules much more efficient when compared to the TP or SG ones.

2.2.4 The Deterministic Simulator

The deterministic hybrid integral-equation simulator described in [60, 61] is used to compute $V(\mathbf{x})$ at collocation points called for by the SC methods. This simulator permits the characterization of EMC/EMI phenomena on deterministically configured, electrically large, and multi-scale platforms loaded with electronic systems that are

interconnected by coaxial and multi-conductor cables. The simulator achieves its efficiency and accuracy by hybridizing three distinct solvers: (i) an integral equation solver that computes electromagnetic fields on electrically large platforms; (ii) a circuit solver that computes currents and voltages on lumped elements of (non-)linear circuits that terminate or interconnect cables; and (iii) an integral equation solver that computes currents and voltages along coaxial and multi-conductor cables. These three solvers are interfaced at the cable terminations and along the cable shields; the resulting coupled system of equations is solved simultaneously for all field, circuit, and cable unknowns. The bottleneck in the solution of this coupled system of equations is the computation of fields on the platforms and the voltages and current along the cables; both computations are accelerated using FFT-based algorithms. Further acceleration is achieved by parallelizing the computation of fields on the platform [62].

2.3 Application to the EMC/EMI Problems

This section presents numerical examples that demonstrate the accuracy, efficiency, and practicality of the Stroud based SC method via its application to the statistical characterization of plane wave coupling into suspended coaxial cables, onto the feed pins of shielded and cable-interconnected computer cards, and into the coaxial cables situated in the bay of an airplane cockpit. All simulations were carried out on a cluster of dual-core 2.8-GHz AMD Opteron 2220 SE processors located at the Center for Advanced Computing, University of Michigan.

2.3.1 Suspended RG-58 Coaxial Cables

The proposed approach is used to estimate the average and standard deviation of voltages coupled into the terminals of an RG-58 coaxial cable excited by a plane wave. The cable has polyethylene dielectric filling, wave speed $c_{\mathrm{CBL}} = 0.78c_0$ with c_0 the free-space speed of light, outer shield radius $a_o = 1.524\,\mathrm{mm}$, inner shield radius $a_i = 1.397\,\mathrm{mm}$, and inner conductor radius $a = 0.180\,\mathrm{mm}$. The cable shield's transfer impedance is approximated as

$$\hat{T}^{\mathrm{i}}(f) = R_0\left[(1+j)(a_{\mathrm{o}} - a_{\mathrm{i}})/\delta\right] / \sinh\left[(1+j)(a_{\mathrm{o}} - a_{\mathrm{i}})/\delta\right] + j2\pi f L_a, \qquad (2.17)$$

where $\delta = \sqrt{1/\pi f \sigma\mu}$ is the skin depth, $\sigma = 5.0\times10^7$ S/m is the conductivity, $\mu = \mu_0$ is the free-space permeability, $L_a = 1.0\,\mathrm{nH/m}$, and $R_0 = 14.3\,\mathrm{m\Omega/m}$ [63]. Due to the high optical coverage of the cable, the shield's transfer admittance is negligible [63]. The cable resides in free-space, is flexible and uniform, and is suspended at fixed nodes that lie on the x-axis; the sagging between any two nodes is characterized using the catenary curve equation [64]. The cable is terminated by two resistors and illuminated by a plane wave propagating in the $\hat{\mathbf{k}} = \hat{\mathbf{x}}\cos(\phi) + \hat{\mathbf{y}}\sin(\phi)$ direction with $E_\phi = 1\,\mathrm{V/m}$. Two different scenarios are simulated.

2.3.1.1 RG-58 Cable Suspended at Three Points

In the first scenario, an RG-58 coaxial cable of length $6\,\mathrm{m}$ is suspended at three nodes that are spaced $d = 2\,\mathrm{m}$ apart [Figure 2–3]. In this example, five parameters characterize the uncertainty ($N_{\mathrm{dof}} = 5$): the values of the terminating resistors, R_1 and

R_2, the maximum cable sag between the fixed nodes, h_1 and h_2, and the plane wave's angle of arrival, ϕ. All five variables are assumed normally distributed.

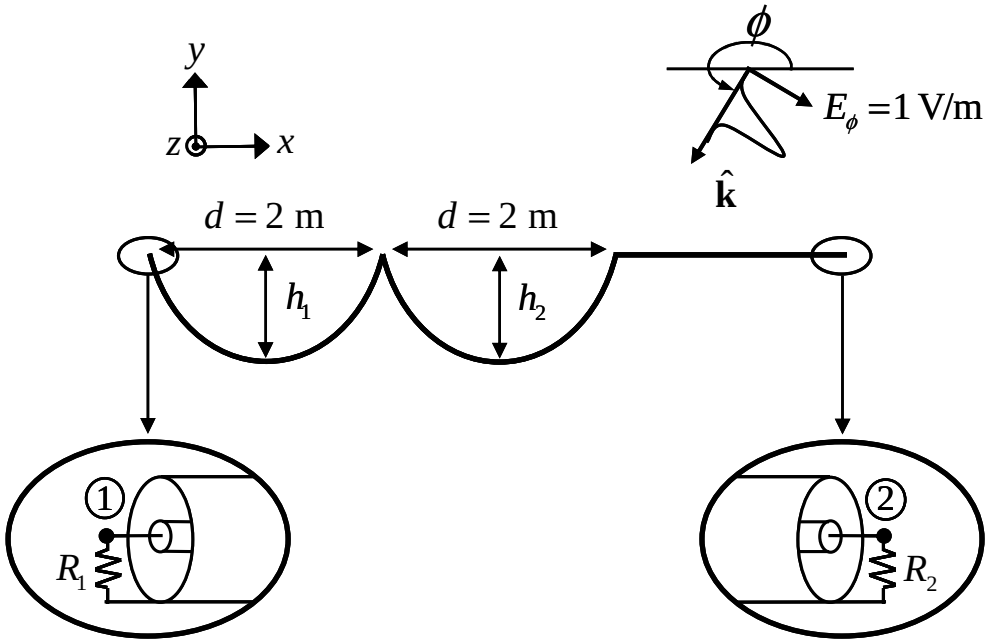

Figure 2–3 Geometry description of the RG-58 coaxial cable suspended at three nodes and the plane wave excitation.

Five sets of simulations ($i = 1,...,5$) are performed in which these variables' standard deviations are geometrically increased while their means are kept constant (Table 2–4). The average and standard deviation of the coupled voltages at node 1, $V_1(\mathbf{x})$, are computed at $f = 100$ MHz using S-2/S-3 integration rules, an 5-point Gauss-Hermite quadrature based TP integration rule, and the traditional MC method; the results obtained using the TP integration rule were verified to be accurate to 8 and 5 digits for the first and last simulations, respectively (by comparison to results obtained using even higher-order TP integration rules).

| Set 1 | Set 2 | Set 3 | Set 4 | Set 5 |

	μ^i	σ^i	μ^i	σ^i	μ^i	σ^i	μ^i	σ^i	μ^i	σ^i
$i=1,\ h_1\ (\mathrm{m})$	0.515	0.0037	0.515	0.0075	0.515	0.015	0.515	0.03	0.515	0.06
$i=2,\ h_2\ (\mathrm{m})$	0.515	0.0037	0.515	0.0075	0.515	0.015	0.515	0.03	0.515	0.06
$i=3,\ R_1\ (\Omega)$	50	0.5	50	1	50	2	50	4	50	8
$i=4,\ R_2\ (\Omega)$	50	0.5	50	1	50	2	50	4	50	8
$i=5,\ \phi\ (^\circ)$	224	0.25	224	0.5	224	1	224	2	224	4

Table 2–4 Values of μ^i and σ^i, $i=1,...,5$ for all five sets of simulations of the plane-wave coupling scenario involving the RG-58 coaxial cable suspended at three nodes

Figure 2–4 (a) shows the relative error between the averages computed using the S-2/S-3 ($k=2,3$) integration rules(S) and the TP integration rule (TP),

$$err_i^{\mathrm{E,Re},k}=\frac{E_i^{\mathrm{S},k}\left[\mathrm{Re}\left\{V_1(\mathbf{x})\right\}\right]-E_i^{\mathrm{TP}}\left[\mathrm{Re}\left\{V_1(\mathbf{x})\right\}\right]}{E_i^{\mathrm{TP}}\left[\mathrm{Re}\left\{V_1(\mathbf{x})\right\}\right]},\ i=1,...5,\ k=2,3, \tag{2.18}$$

$$err_i^{\mathrm{E,Im},k}=\frac{E_i^{\mathrm{S},k}\left[\mathrm{Im}\left\{V_1(\mathbf{x})\right\}\right]-E_i^{\mathrm{TP}}\left[\mathrm{Im}\left\{V_1(\mathbf{x})\right\}\right]}{E_i^{\mathrm{TP}}\left[\mathrm{Im}\left\{V_1(\mathbf{x})\right\}\right]},\ i=1,...,5,\ k=2,3. \tag{2.19}$$

Similarly, Figure 2–4 (b) shows the relative difference between the standard deviations computed by the S-2/S-3 ($k=2,3$) integration rules (S) and the TP integration rule (TP),

$$err_i^{\mathrm{std,Re},k}=\frac{\mathrm{std}_i^{\mathrm{S},k}\left[\mathrm{Re}\left\{V_1(\mathbf{x})\right\}\right]-\mathrm{std}_i^{\mathrm{TP}}\left[\mathrm{Re}\left\{V_1(\mathbf{x})\right\}\right]}{\mathrm{std}_i^{\mathrm{TP}}\left[\mathrm{Re}\left\{V_1(\mathbf{x})\right\}\right]},\ i=1,...5,\ k=2,3, \tag{2.20}$$

$$err_i^{\mathrm{std,Im},k}=\frac{\mathrm{std}_i^{\mathrm{S},k}\left[\mathrm{Im}\left\{V_1(\mathbf{x})\right\}\right]-\mathrm{std}_i^{\mathrm{TP}}\left[\mathrm{Im}\left\{V_1(\mathbf{x})\right\}\right]}{\mathrm{std}_i^{\mathrm{TP}}\left[\mathrm{Im}\left\{V_1(\mathbf{x})\right\}\right]},\ i=1,...,5,\ k=2,3. \tag{2.21}$$

In (2.18)-(2.21), $E_i^{\mathrm{S},2}[.]/\mathrm{std}_i^{\mathrm{S},2}[.]$, $E_i^{\mathrm{S},3}[.]/\mathrm{std}_i^{\mathrm{S},3}[.]$, and $E_i^{\mathrm{TP}}[.]/\mathrm{std}_i^{\mathrm{TP}}[.]$ represent the averages/standard deviations computed by the S-2/S-3 and the TP integration rules for the i^{th} set of simulations, respectively. As expected, relative errors plotted in Figure 2–4 (a)-

(b) increase as the standard deviations σ^i increase (because the effective domain of integration enlarges). Additionally, one can say that for a given set, the error in averages is one-two orders of magnitude smaller than the error in standard deviation; this is expected since the integral needed for average involves only the coupled voltage $V_1(\mathbf{x})$, rather than $\left[V_1(\mathbf{x})\right]^2$, which is integrated for computing the standard deviation (i.e., the function being integrated for computing the average is smoother than the one integrated for computing the standard deviation).

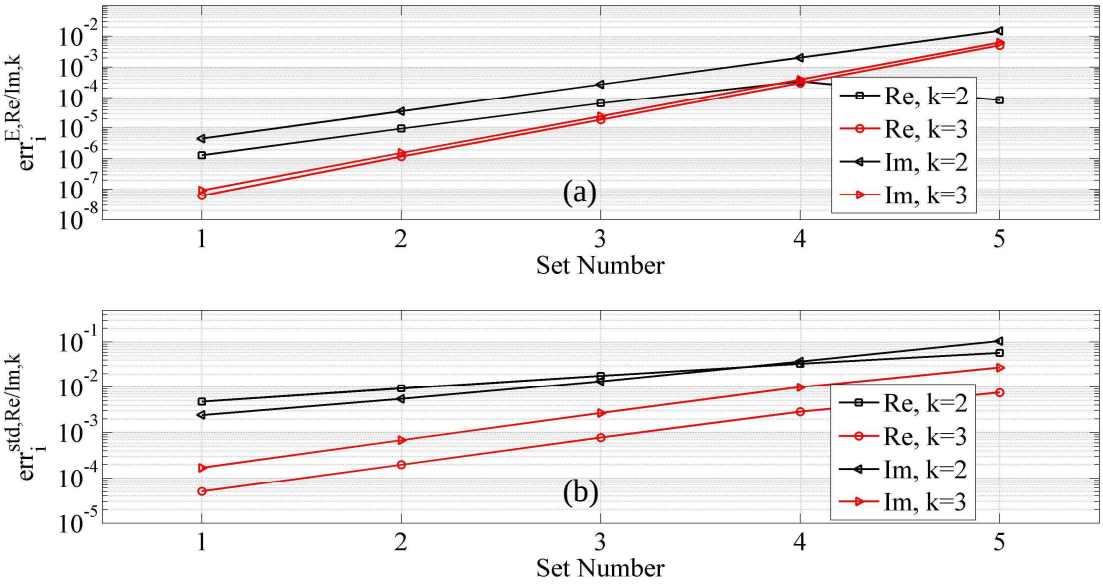

Figure 2–4 (a) $err_i^{\mathrm{E,Re},k}$ and $err_i^{\mathrm{E,Im},k}$, $k=2,3$, $i=1,...,5$, and (b) $err_i^{\mathrm{std,Re},k}$ and $err_i^{\mathrm{std,Im},k}$, $k=2,3$, $i=1,...,5$ (relative error between averages and standard deviations of the real and imaginary parts of the $V_1(\mathbf{x})$ computed by the S-2/S-3 and the TP integration rules.

For a more detailed comparison of the S-2/S-3, the TP integration rules, and the MC method, Table 2–5 presents the results computed for the third set of simulations by these methods (the third simulation is the one in the middle for plots presented in Figure 2–4 (a)-(b)). In Table 2–5 $E_3^{\mathrm{MC}}[.]/\mathrm{std}_3^{\mathrm{MC}}[.]$ represents the average/standard deviation

computed by the MC method for the third set of simulations. To obtain the results given in the Table 2–5, the S-2/S-3, the TP integration rules, and the MC method required 6, 10, 3125, and 5000 deterministic EMI/EMC simulations, respectively. As expected, for both the average and the standard deviation computations, the S-3 method gives more accurate results than the S-2 method (assuming that the most accurate results are obtained by the TP integration method). Additionally, both S-2 and S-3 methods are approximately one digit more accurate than 5000-point MC method. For the MC method to yield roughly the same accuracy as the S-2/S-3 methods, it would require approximately 100×5000 points. It is clear from the results presented in this section that, for a stochastic problem this size, the S-2/S-3 methods are the most efficient and can provide one-two digits of accuracy even for relatively large integration domains.

superscript (k)	$E_3^{\mathrm{k}}\left[\mathrm{Re}\{V_1(\mathbf{x})\}\right]$ $(\mathrm{m}V)$	$E_3^{\mathrm{k}}\left[\mathrm{Im}\{V_1(\mathbf{x})\}\right]$ $(\mathrm{m}V)$	$\mathrm{std}_3^{\mathrm{k}}\left[\mathrm{Re}\{V_1(\mathbf{x})\}\right]$ $(\mathrm{m}V)$	$\mathrm{std}_3^{\mathrm{k}}\left[\mathrm{Im}\{V_1(\mathbf{x})\}\right]$ $(\mathrm{m}V)$
k = MC	-0.16006	0.06422	0.02460	0.01468
k = TP	-0.16018	0.06407	0.02435	0.01439
k = S,2	-0.16019	0.06405	0.02479	0.01459
k = S,3	-0.16018	0.06407	0.02433	0.01443

Table 2–5 Averages and standard deviations of the $V_1(\mathbf{x})$ computed by the S-2/S-3, the TP integration rules, and the MC method for the third simulation

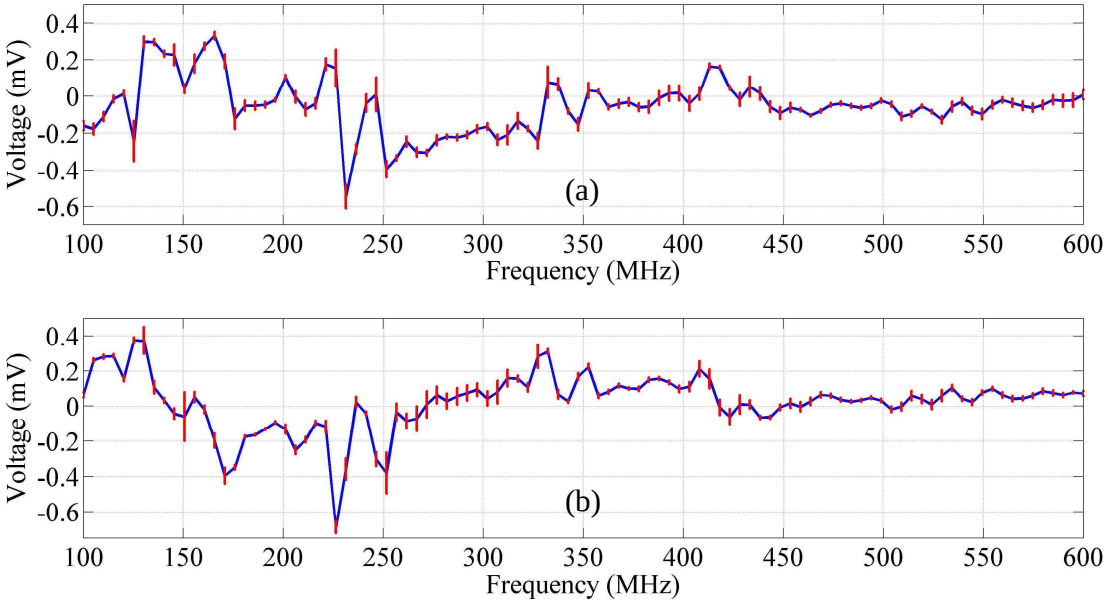

Figure 2–5 Error-bar plots for the average of (a) real part and (b) imaginary parts of $V_1(\mathbf{x})$ at 100 frequencies equally located between $f = 100$ MHz and $f = 600$ MHz (computed by the S-3 integration rule).

For the sake of completeness, Figure 2–5 (a)-(b) show $E_3^{S,3}\left[\mathrm{Re}\{V_1(\mathbf{x})\}\right]$ and $E_3^{S,3}\left[\mathrm{Im}\{V_1(\mathbf{x})\}\right]$ vs. frequency with error bars obtained from $\mathrm{std}_3^{S,3}\left[\mathrm{Re}\{V_1(\mathbf{x})\}\right]$ and $\mathrm{std}_3^{S,3}\left[\mathrm{Im}\{V_1(\mathbf{x})\}\right]$, respectively. As expected, the standard deviation of $V_1(\mathbf{x})$ increases near the cable's resonant frequencies, where the cable's response is more sensitive to perturbations in the excitation and the configuration of the cable.

2.3.1.2 RG-58 Cable Suspended at Eleven Points

In the second scenario, the RG-58 coaxial cable of length 18.63 m is suspended at 11 nodes that are spaced $d = 1$ m apart [Figure 2–6]. 13 parameters characterize the uncertainty ($N_{\mathrm{dof}} = 13$): the values of the terminating resistors R_1 and R_2, the maximum cable sag between nodes $h_i, i = 1,\ldots,10$, and the angle of arrival of excitation ϕ [Figure

2–6]. The variables R_1, R_2, h_i, $i=1,\ldots,10$, and ϕ are assumed uniformly distributed in the ranges $[45,55]\ \Omega$, $[45,55]\ \Omega$, $[0.5,0.7]$ m, and $[225,235]^\circ$, respectively.

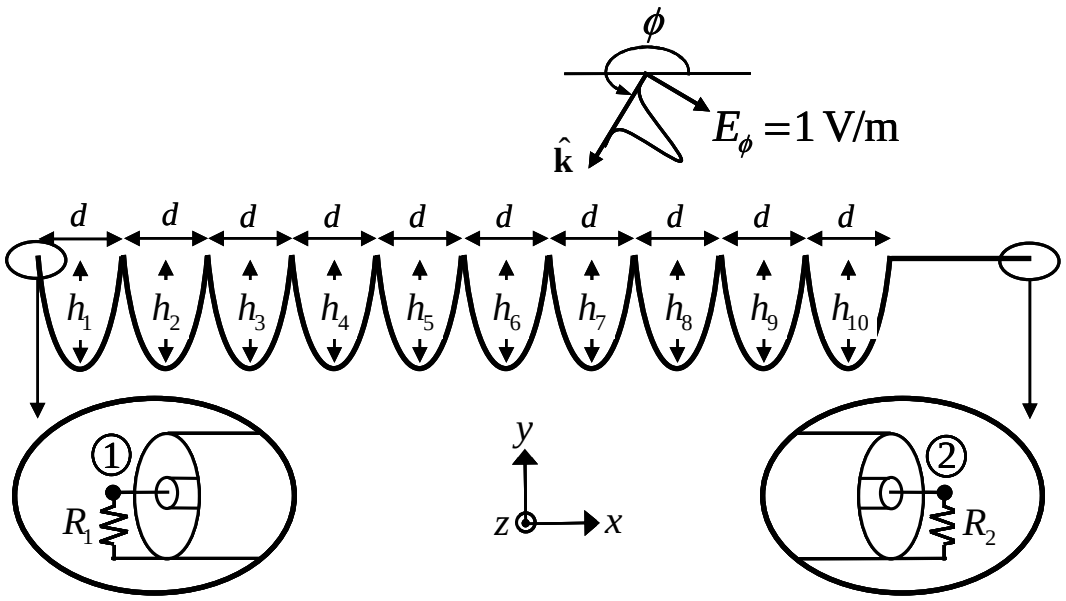

Figure 2–6 Geometry description of the RG-58 coaxial cable suspended at eleven nodes and the plane wave excitation.

Next, results obtained using S-3 integration rule and the MC method are compared in Table 2–6. In Table 2–6, $V_1(\mathbf{x})$ is the coupled voltage at node 1 at $f = 0.9$ GHz, and $E^{\mathrm{S,3}}[.]/\mathrm{std}^{\mathrm{S,3}}[.]$ and $E^{\mathrm{MC}}[.]/\mathrm{std}^{\mathrm{MC}}[.]$ are the averages/standard deviations computed by the S-3 and Monte Carlo methods, respectively. The relative differences between $\mathrm{std}^{\mathrm{S,3}}\left[\mathrm{Re}\{V_1(\mathbf{x})\}\right]$ and $\mathrm{std}^{\mathrm{MC}}\left[\mathrm{Re}\{V_1(\mathbf{x})\}\right]$, and $\mathrm{std}^{\mathrm{S,3}}\left[\mathrm{Im}\{V_1(\mathbf{x})\}\right]$ and $\mathrm{std}^{\mathrm{MC}}\left[\mathrm{Im}\{V_1(\mathbf{x})\}\right]$ are 1.43% and 4.09%, respectively. The relative differences between $E^{\mathrm{S,3}}\left[\mathrm{Re}\{V_1(\mathbf{x})\}\right]$ and $E^{\mathrm{MC}}\left[\mathrm{Re}\{V_1(\mathbf{x})\}\right]$, and $E^{\mathrm{S,3}}\left[\mathrm{Im}\{V_1(\mathbf{x})\}\right]$ and $E^{\mathrm{MC}}\left[\mathrm{Im}\{V_1(\mathbf{x})\}\right]$ are large for the simple reason that these quantities are (likely) approximations to zero.

superscript (k)	$E^{\mathrm{k}}\left[\mathrm{Re}\{V_1(\mathbf{x})\}\right]$ $(\mathrm{m}V)$	$E^{\mathrm{k}}\left[\mathrm{Im}\{V_1(\mathbf{x})\}\right]$ $(\mathrm{m}V)$	$\mathrm{std}^{\mathrm{k}}\left[\mathrm{Re}\{V_1(\mathbf{x})\}\right]$ $(\mathrm{m}V)$	$\mathrm{std}^{\mathrm{k}}\left[\mathrm{Im}\{V_1(\mathbf{x})\}\right]$ $(\mathrm{m}V)$
k = MC	0.00591	0.00217	0.03086	0.03444
k = S,3	0.00684	0.00529	0.03131	0.03303

Table 2–6 Averages and standard deviations of the $V_1(\mathbf{x})$ computed by the S-3 integration rule and the MC method.

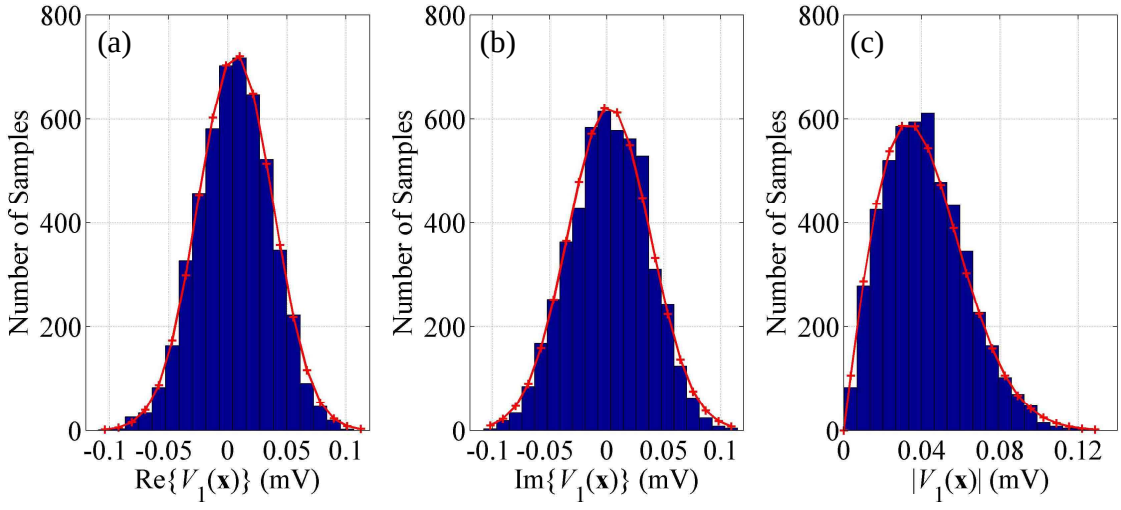

Figure 2–7 The pdfs of (a) the real and (b) the imaginary parts and (c) absolute value of $V_1(\mathbf{x})$ (obtained using the MC method).

The averages of the real and imaginary parts of $V_1(\mathbf{x})$ are expected to vanish because of phase cancellations that occur when the number of and/or variation in the parameters quantifying the uncertainties are large [65, 66]. Under these conditions, the pdfs of the real and imaginary parts of $V_1(\mathbf{x})$ and its absolute value are expected to behave as normal and Rayleigh pdfs, respectively [65, 66]. These facts are verified by the histograms obtained using the MC method [Figure 2–7 (a)-(c)]. For this example, the S-3 integration rule and the MC method required 26 and 5000 deterministic EMI/EMC simulations, respectively.

2.3.2 Computer Cards in a Shielded Box

Next, the Stroud-based SC method is used to statistically characterize coupled voltages at terminals of an RG-58 coaxial cable connecting two computer cards located inside shielding enclosures that are subject to excitation by a plane wave [Figure 2–8]. The shielding enclosures are identical; both contain a mother board and two daughter cards. The daughter card closest to the back of the box (1^{st} card) and the other one (2^{nd} card) are connected to the mother board with eight pins and one pin, respectively (see [60] for a more detailed description the cards and the pins). An RG-58 coaxial cable of length 70 cm but otherwise identical to the one used in Subsection 2.3.1.1 connects to the pins feeding the 2^{nd} cards. Two resistors, which might potentially model the resistance of cable connectors, are also connected to feed pins. The structure is illuminated by a plane wave propagating in $\hat{\mathbf{k}} = -\hat{\mathbf{x}}\sin(\theta) - \hat{\mathbf{z}}\cos(\theta)$ direction with $E_\theta = 1$ V/m.

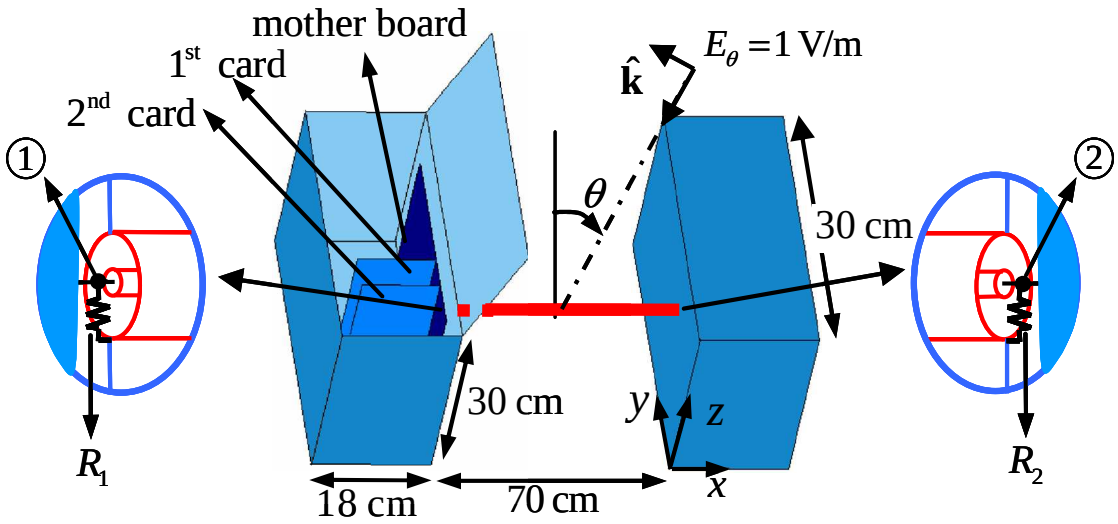

Figure 2–8 Geometry description of the computer cards, RG-58 cable connecting them, and the shielding enclosures and the plane-wave excitation

Three parameters characterize the uncertainty ($N_{\text{dof}} = 3$): the values of the terminating resistors R_1 and R_2, and the plane wave's angle of arrival θ; all are assumed beta distributed with $c^i = d^i = 1,\ i = 1,\ldots,3$, in the ranges $[48,52]\ \Omega$, $[48,52]\ \Omega$, and $[110,115]^\circ$, respectively. The S-3 and the TP integration rules are used to compute averages and standard deviations of the voltage $V_1(\mathbf{x})$ coupled onto node 1 at $f = 0.9\ \text{GHz}$; the TP rule uses a 5-point Gauss-Jacobi quadrature rule. The results are compared in Table 2–7, where $E^{\text{S,3}}[.]/\text{std}^{\text{S,3}}[.]$, and $E^{\text{TP}}[.]/\text{std}^{\text{TP}}[.]$ represent the averages/standard deviations computed by the S-3 and the TP integration rules, respectively. The averages and standard deviations computed by both integration rules match up to sixth and fourth digits, respectively. For this example, the S-3 and the TP integration rules required 6 and 125 deterministic EMI/EMC simulations, respectively.

superscript (k)	$E^{\text{k}}\left[\text{Re}\{V_1(\mathbf{x})\}\right]$ $(\text{m}V)$	$E^{\text{k}}\left[\text{Im}\{V_1(\mathbf{x})\}\right]$ $(\text{m}V)$	$\text{std}^{\text{k}}\left[\text{Re}\{V_1(\mathbf{x})\}\right]$ $(\text{m}V)$	$\text{std}^{\text{k}}\left[\text{Im}\{V_1(\mathbf{x})\}\right]$ $(\text{m}V)$
$\text{k} = \text{TP}$	0.14671	0.23200	0.01679	0.01683
$\text{k} = \text{S,3}$	0.14671	0.23200	0.01033	0.01028

Table 2–7 Averages and standard deviations of $V_1(\mathbf{x})$ computed by the S-3 and the TP integration rules.

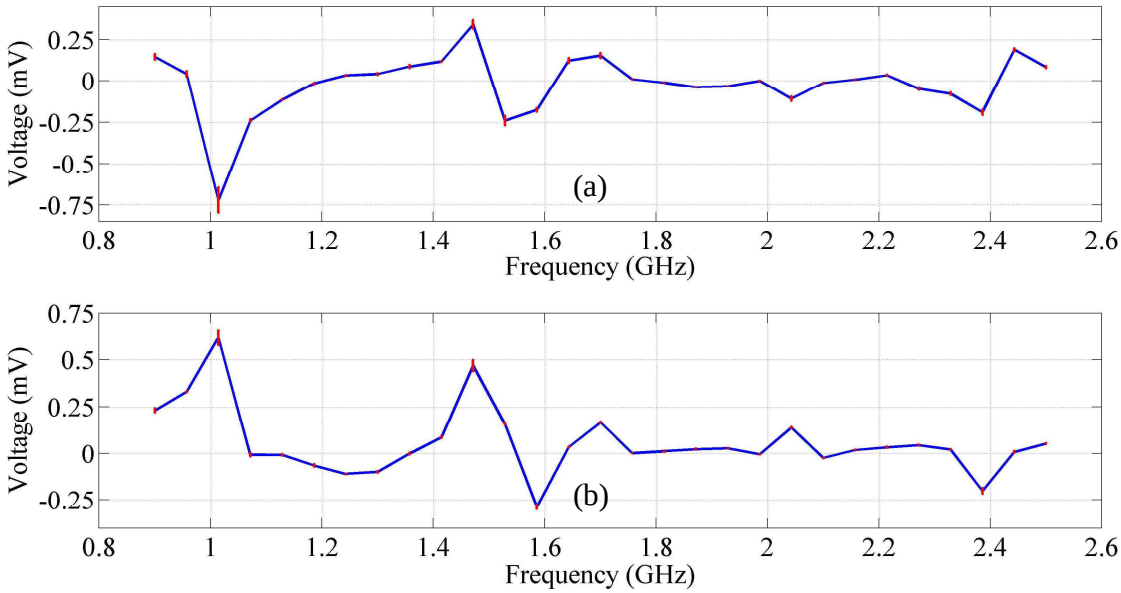

Figure 2–9 Error-bar plots for the average of (a) the real and (b) the imaginary parts of $V_1(\mathbf{x})$ at 29 frequencies equally located between $f = 0.9\,\text{GHz}$ and $f = 2.5\,\text{GHz}$ (computed by the S-3 integration rule)

For the sake of completeness, Figure 2–9 (a) and (b) show $\text{Re}\left\{E^{\text{S,3}}\left[V_1(\mathbf{x})\right]\right\}$ and $\text{Im}\left\{E^{\text{S,3}}\left[V_1(\mathbf{x})\right]\right\}$ vs. frequency with error bars obtained from $\text{Re}\left\{\text{std}^{\text{S,3}}\left[V_1(\mathbf{x})\right]\right\}$ and $\text{Im}\left\{\text{std}^{\text{S,3}}\left[V_1(\mathbf{x})\right]\right\}$, respectively. As expected, the standard deviation of the coupled voltage increases near the resonant frequencies of the system.

2.3.3 RG-58 Coaxial Cables in Loaded Cockpit

Finally, the Stroud-based SC method is used to statistically characterize voltages coupled onto the terminals of RG-58 coaxial cables situated inside the bay of an airplane cockpit under plane wave excitation [Figure 2–10 (a)]. The cockpit is loaded with three shielding enclosures interconnected by RG-58 coaxial cables, as well as nine additional floating RG-58 coaxial cables and two seats [Figure 2–10 (a)]. Aside from their length, all RG-58 coaxial cables are identical to those of Subsection 2.3.1.1. The cables are

located in a partially shielded compartment under the cockpit floor in three layers [Figure 2–10 (b)]. Cables C_2, C_3, and C_6 are 1.375 m long, cables C_1, C_4, C_5, and C_7 are 1 m long, and cables C_8 and C_9 are 0.575 m long. Cables C_1, C_6, and C_8 are terminated using resistors with values R_1 and R_2, R_3 and R_4, and R_5 and R_6, respectively; $R_i = 50\ \Omega$, $i = 1,...,6$. The surfaces of the seats are modeled as resistive surfaces with 377-Ω surface impedance. The structure is illuminated by a plane wave propagating in the $\hat{\mathbf{k}} = -\hat{\mathbf{x}}\cos(\theta) - \hat{\mathbf{y}}\sin(\theta)$ direction with $E_\theta = 1000$ V/m. Nine parameters characterize the uncertainty ($N_{\text{dof}} = 9$): the y coordinates of cables C_1, C_4, C_5, C_7, C_8, and C_9 [Figure 2–10 (b)], the y coordinates of the seat base plane, and the plane wave's angle of arrival θ. All nine random variables are beta distributed with $c^i = d^i = 0$, $i = 1,...,9$, in the range $\left[a^i, b^i\right]$; a^i and b^i are given in Table 2–8.

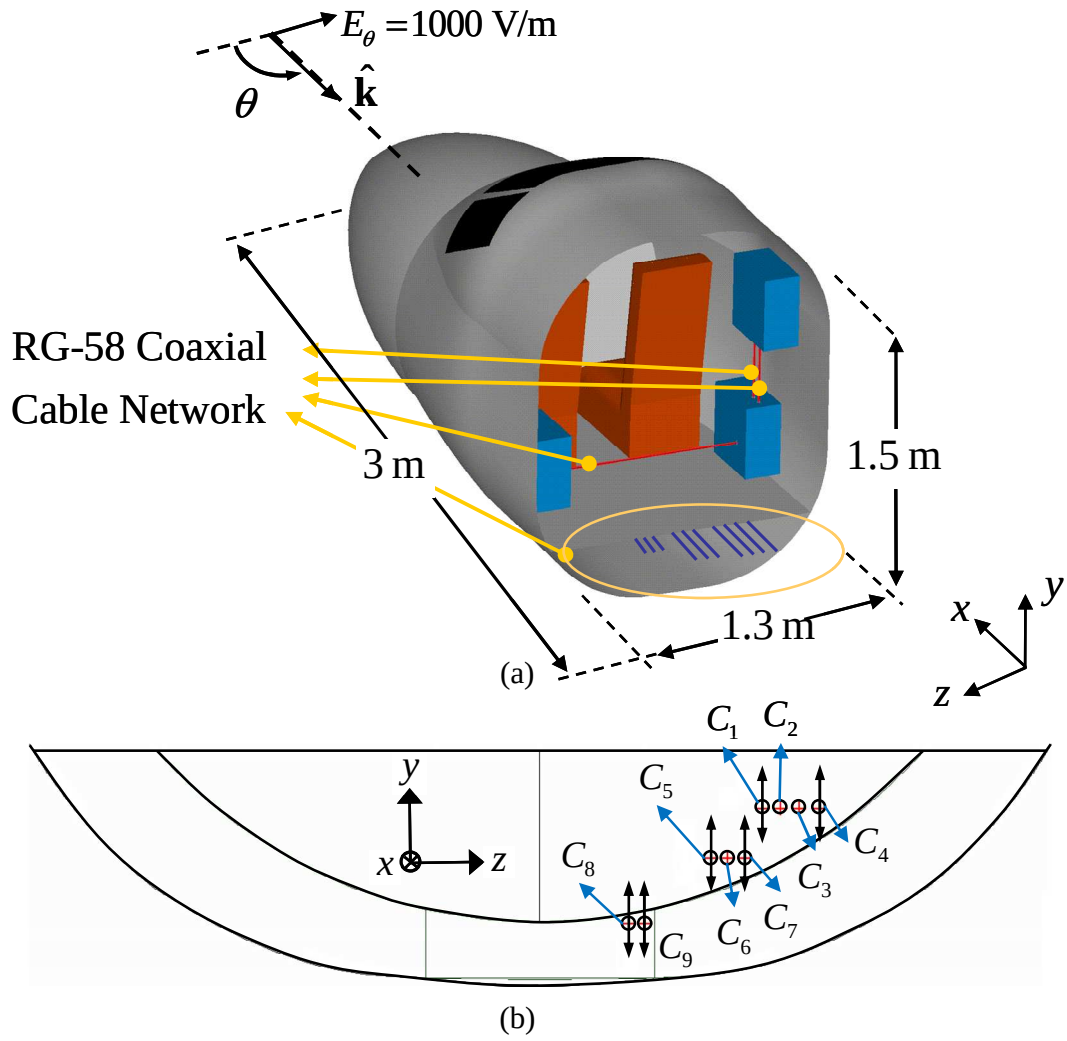

Figure 2–10 (a) Geometry description of the cockpit, shielding boxes, RG-58 coaxial cables, and the seats and the plane-wave excitation. (b) View from back of the cockpit: RG-58 coaxial cables (+) are located in the partially shielded compartment under the cockpit floor; black lines represent allowed vertical movement.

The S-3 integration rule is used to compute $E^{S,3}\left[\left|V_i(\mathbf{x})\right|\right]$ and $\text{std}^{S,3}\left[\left|V_i(\mathbf{x})\right|\right]$, $i=1,...,6$, the average and standard deviation of the absolute value of the coupled voltages on resistors R_i, $i=1,...,6$, at $f=0.9$ GHz [Table 2–9]. For this problem, only the S-3 integration rule, which required 18 deterministic simulations, was used because the time required for a single deterministic simulation was around 2-3 hours on 32

processors, and a TP integration rule with 2 points in each dimension and the MC method with a couple of digits accuracy would require $2^9 = 512$ and at least a few thousands simulations, respectively.

	a^i	b^i
$i=1$, y coordinate of the location of cable C_1 (m)	–0.46875	–0.40625
$i=2$, y coordinate of the location of cable C_4 (m)	–0.46875	–0.40625
$i=3$, y coordinate of the location of cable C_5 (m)	–0.53125	–0.46875
$i=4$, y coordinate of the location of cable C_7 (m)	–0.53125	–0.46875
$i=5$, y coordinate of the location of cable C_8 (m)	–0.59375	–0.53125
$i=6$, y coordinate of the location of cable C_9 (m)	–0.59375	–0.53125
$i=7$, y coordinate of the location of the first seat (m)	–0.342	–0.084
$i=8$, y coordinate of the location of the second seat (m)	–0.342	–0.084
$i=9$, arrival of excitation, $\theta\,(^\circ)$	185	235

Table 2–8 a^i and b^i, $i=1,...,9$, for all nine random variables (the plane-wave coupling scenario involving the RG-58 coaxial cable network located in a cockpit)

i	$E^{\mathrm{S},3}\left[\lvert V_i(\mathbf{x})\rvert\right]$ (V)	$\mathrm{std}^{\mathrm{S},3}\left[\lvert V_i(\mathbf{x})\rvert\right]$ (V)
1	0.01581	0.02828
2	0.01150	0.02535
3	0.22904	0.31644
4	0.23250	0.31522
5	0.32650	0.14404
6	0.03390	0.14523

Table 2–9 Averages and standard deviations of the absolute value of coupled voltages on the RG-58 coaxial cables situated in the bay of an airplane cockpit

CHAPTER 3
MULTI-ELEMENT PROBABILISTIC COLLOCATION METHOD

3.1 Introduction

Spectral methods are well-known for the solution of differential and integral equations as well as for the extraction of statistics of observables in large-scale simulations. The initial work using spectral methods for uncertainty quantification of engineering systems was proposed in early 1990s [7]. This work leveraged the Wiener's polynomial chaos [67] to extract statistics of observables due to the normally distributed random variables. In Wiener's work, the Hermite polynomials are selected as orthogonal bases, which are proven to be optimal for normally distributed random variables [68]. That said, these bases yield inaccurate statistics of observables when the random variables are distributed with non-Gaussian pdfs. To this end, the polynomial chaos was generalized for non-Gaussian pdfs [6] and henceforth termed as generalized polynomial chaos (gPC). According to gPC theory, the type of non-Gaussian pdf dictates the type of orthogonal polynomials used to extract statistics of observables. The last decade witnessed substantial research activities on the applications of gPC methods to many practical engineering problems [10].

To generate surrogate models of observables and extract their statistics, the gPC methods use the entire-domain orthogonal polynomials while the SC methods described in previous chapter leverage multivariate Lagrange interpolation functions. For that reason, the coefficients of SC expansion are solely the values of observables on collocation points while the coefficients of the gPC expansion are determined via either Galerkin [6-9] or collocation [10-12] methods. As the gPC Galerkin methods are *slightly* more accurate than their collocation counterparts [10], they call for the solution of large systems of coupled equations in gPC expansion coefficients, as well as rather intrusive modifications to deterministic solvers [11]. See [12, 13] for applications of gPC Galerkin methods in EMC/EMI analysis. gPC collocation methods are computationally more efficient as they compute gPC expansion coefficients via multi-dimensional integration; moreover, their implementation is non-intrusive as they can use available deterministic simulators to compute observables at collocation points. See [17, 75, 76] for applications of gPC collocation methods in EMC/EMI analysis.

Attractive as they may be, classical gPC methods seldom can be applied directly to statistical EMC/EMI analysis as they become inefficient and inaccurate for observables that vary non-smoothly in the random variables, as do voltages in resonant circuits subject to minor perturbations in the values of lumped elements, or fields in overmoded or quasi-resonant cavities. This deficiency stems from the fact that accurate representations of such observables only can be achieved using very high-order polynomials. Recently, several adaptive methods have been proposed to address this limitation. The multi-element gPC (ME-gPC) and probabilistic collocation (ME-PC) methods are *h*-adaptive refinement schemes for use in conjunction with gPC Galerkin and

collocation methods, respectively [31-33]. ME-gPC and ME-PC methods achieve their efficiency and accuracy by recursively and adaptively dividing the random domain into subdomains guided by the decay rates of the observables' local variances and by constructing separate local and low-order gPC expansions for each subdomain. Initial versions of these methods assumed uniformly distributed random variables [29], but recent adaptations allow for arbitrary distributions [30, 31].

This chapter elucidates a computational framework that builds upon the adaptive ME-PC method in [31] for statistically characterizing EMC/EMI observables that potentially vary rapidly/nonsmoothly across the random domain. The framework generates surrogate models of the observables by approximating them in terms of Legendre-chaos expansions. Observable values at collocation points identified by the adaptive ME-PC scheme are computed using the deterministic FFT-accelerated hybrid integral-equation simulator described in Section 2.2.4. Upon generation of the surrogate model, the MC method is used to compute the statistical moments, pdfs/cdfs of the observables, fully accounting for the pdfs of the random variables. The applicability of the scheme is demonstrated via its application to the statistical characterization of voltages in various transmission line networks and microwave amplifiers, and magnetic fields induced on car tire pressure sensors.

3.2 The Formulation

The proposed computational framework in this chapter leverages the ME-PC method of [31] to obtain statistical information (average, standard deviation, pdf, cdf, etc.) of $V(\mathbf{x})$ which potentially vary rapidly/non-smoothly. The details and a rigorous

error analysis of the method can be found in [31-33]. The ME-PC method is used to generate an easy-to-evaluate albeit approximate surrogate model of $V(\mathbf{x})$. To this end, it recursively and adaptively divides the random domain D into subdomains based on the decay rates of $V(\mathbf{x})$'s local variances, and constructs separate local and low-order gPC approximations for $V(\mathbf{x})$ on each subdomain. Upon convergence of the surrogate model, it is probed via MC method accounting for the distributions $w^i(\cdot)$ to generate statistical information pertaining to $V(\mathbf{x})$.

In what follows, the well-known gPC collocation method is described first. A recursive and adaptive strategy for constructing local and low-order polynomial approximations to $V(\mathbf{x})$ is explained next. Finally, the hybridization of the ME-PC method with Dirichlet kernel for EMC/EMI applications is expounded.

3.2.1 gPC Collocation Method

A p^{th}- order gPC expansion is used to approximate $V(\mathbf{x})$ in terms of N_{dof}-variate orthogonal Legendre polynomial basis functions, $\mathbf{P}_m(\mathbf{x})$, $m=0,\ldots,N_p$, as

$$V(\mathbf{x}) \simeq \sum_{m=0}^{N_p} v_m \mathbf{P}_m(\mathbf{x}). \tag{3.1}$$

Here $N_p = (N_{\text{dof}}+p)!/(N_{\text{dof}}!\,p!)-1$, the total number of terms in the expansion is N_p+1, and v_m is dubbed the m^{th} gPC expansion coefficient. In (3.1), $\mathbf{P}_m(\mathbf{x})$ is constructed as the tensor product of 1D Legendre polynomials $P^i_{d^i_m}(x^i)$, $i=1,\ldots,N_{\text{dof}}$, as

$$\mathbf{P}_m\left(\mathbf{x}\right)=\prod_{i=1}^{N_{\text{dof}}}P^i_{d^i_m}\left(x^i\right), \tag{3.2}$$

(Note: the superscript i on P denotes the 1D domain over which P is active, not a power or index of a modified Legendre polynomial). Here d^i_m is an element of a multi-index $d_m=d^1_m d^2_m ... d^{N_{\text{dof}}}_m$ satisfying $\sum_{i=1}^{N_{\text{dof}}} d^i_m \le p$; in (3.1) all possible multi-indices are considered. The above construct perhaps is best described via an example. Assume $N_{\text{dof}}=2$, $p=2$, and $N_p=5$; the Legendre polynomial basis functions, $\mathbf{P}_m\left(\mathbf{x}\right)$, $m=0,\ldots,5$, along with their multi-indices are

$$\begin{aligned}
\mathbf{P}_0\left(\mathbf{x}\right)&=P^1_0\left(x^1\right)P^2_0\left(x^2\right),\ d_0=00\\
\mathbf{P}_1\left(\mathbf{x}\right)&=P^1_1\left(x^1\right)P^2_0\left(x^2\right),\ d_1=10\\
\mathbf{P}_2\left(\mathbf{x}\right)&=P^1_0\left(x^1\right)P^2_1\left(x^2\right),\ d_2=01\\
\mathbf{P}_3\left(\mathbf{x}\right)&=P^1_2\left(x^1\right)P^2_0\left(x^2\right),\ d_3=20\\
\mathbf{P}_4\left(\mathbf{x}\right)&=P^1_1\left(x^1\right)P^2_1\left(x^2\right),\ d_4=11\\
\mathbf{P}_5\left(\mathbf{x}\right)&=P^1_0\left(x^1\right)P^2_2\left(x^2\right),\ d_5=02
\end{aligned}. \tag{3.3}$$

The 1D Legendre polynomials $P^i_n\left(x\right)$, $n=0,...,p$, $i=1,\ldots,N_{\text{dof}}$, satisfy the normalization/orthogonality conditions, i.e.

$$\int_{D^i} P^i_m\left(x^i\right)P^i_n\left(x^i\right)dx^i=\delta_{mn},\ \ i=1,...,N_{\text{dof}}, \tag{3.4}$$

where δ_{mn} represents the Kronecker delta function. As a result, the $\mathbf{P}_m\left(\mathbf{x}\right)$, $m=0,\ldots,N_p$, satisfy

$$\int_D \mathbf{P}_m\left(\mathbf{x}\right)\mathbf{P}_n\left(\mathbf{x}\right)d\mathbf{x}=\delta_{mn}. \tag{3.5}$$

The collocation-based gPC method generates the expansion coefficients v_m, $m = 0,\ldots, N_p$, by exploiting (3.5), i.e.

$$v_m = \int_D V(\mathbf{x})\mathbf{P}_m(\mathbf{x})\,d\mathbf{x}, \quad m = 0,...,N_p. \tag{3.6}$$

The N_{dof} - dimensional integral in (3.6) is computed via numerical quadrature using TP, SG, or ST-2/ST-3 integration rules explained in Section 2.2.3.1-2.2.3.3. Once the gPC expansion coefficients are obtained by (3.6), the mean and standard deviation of $V(\mathbf{x})$ over D can be computed. By substituting (3.1) in (2.2), we have

$$E\left[V(\mathbf{x})\right] \cong \sum_{m=0}^{N_p} \int_D v_m \mathbf{P}_m(\mathbf{x})\,d\mathbf{x} \tag{3.7}$$

with the assumption that $W(\mathbf{x})$ is uniform distribution. Note that the zeroth order term of Legendre polynomials is always 1, i.e. $P_0^i(x^i) = 1$ and hence $\mathbf{P}_0(\mathbf{x}) = 1$. Introducing $\mathbf{P}_0(\mathbf{x})$ in (3.7) yields

$$E\left[V(\mathbf{x})\right] \cong \sum_{m=0}^{N_p} v_m \int_D \mathbf{P}_0(\mathbf{x})\mathbf{P}_m(\mathbf{x})\,d\mathbf{x}. \tag{3.8}$$

Using the orthogonality relation in (3.5), one can obtain the mean of $V(\mathbf{x})$ over D as

$$E\left[V(\mathbf{x})\right] \cong v_0. \tag{3.9}$$

In a similar way, by substituting (3.1) in (2.3), i.e.,

$$\text{std}\left[V(\mathbf{x})\right] \cong \sqrt{\int_D \left(\sum_{m=0}^{N_p} v_m \mathbf{P}_m(\mathbf{x}) - v_0\right)^2 d\mathbf{x}}, \tag{3.10}$$

considering $\mathbf{P}_0(\mathbf{x})=1$, and using the orthogonality relation in (3.5), the analytic expression for the standard deviation of $V(\mathbf{x})$ over D can be obtained as

$$\mathrm{std}\left[V(\mathbf{x})\right] \cong \sqrt{\sum_{m=1}^{N_p} v_m^2} \ . \tag{3.11}$$

The gPC theory suggests that the type of pdf of the random variables dictates the type of polynomials used for expanding the observable [6]. Strictly speaking, Legendre polynomials only lead to optimal/exponential convergence of the expansion when the random variables are uniformly distributed. When they are normally distributed, for example, Hermite polynomials should be used instead; for the correspondence between distributions and orthogonal polynomials, see Table 3–1 [6].

pdf of $\mathbf{x}$, $W(\mathbf{x})$	Orthogonal Polynomial
Normal	Hermite
Uniform	Legendre
Beta	Jacobi
Gamma	Laguerre

Table 3–1 The correspondence between $W(\mathbf{x})$ and the orthogonal polynomials in gPC theory.

Selection of proper orthogonal polynomials for the chaos expansion in (3.1) yields optimal/exponential convergence of the expansion. This can be proved by a simple example. Suppose $N_{\mathrm{dof}}=1$ and $V\left(x^1\right)=1-x^1$, $x^1:[a^1,b^1]=[0,1]$. The pdf of x^1 is assumed to be uniform distribution and the pdf of $V\left(x^1\right)$ is estimated using surrogate models generated by Legendre chaos and Hermite chaos [Figure 3–1]. To compute coefficients of Hermite-chaos, the integration points dictated by Gauss-Hermite quadrature rule are mapped to the range $[a^1,b^1]$ using the transformation

$x^1 = a^1 + \left(b^1 - a^1\right)\left(0.5 + 0.5\text{erf}\left(z^1/\sqrt{2}\right)\right)$, where z^1 is normally distributed random variable [69].

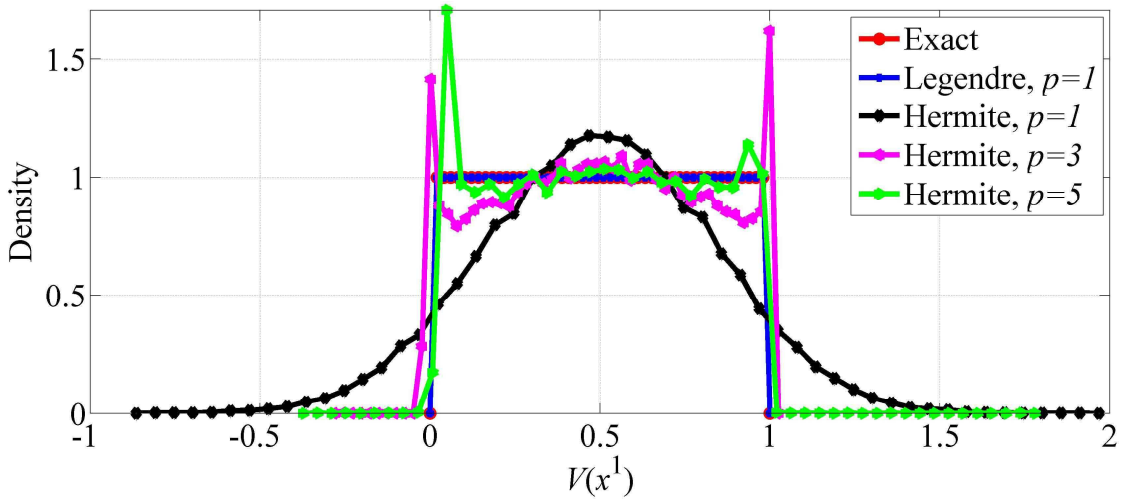

Figure 3–1 Exact pdf of $V\left(x^1\right)$ is compared with the pdfs generated via $V\left(x^1\right)$'s surrogate models obtained using Legendre chaos with $p=1$ and Hermite chaos with $p=1$, $p=2$, and $p=5$.

It's clear from Figure 3–1 that the pdf obtained by the surrogate model generated using Legendre chaos with $p=1$ is exactly the same as the pdf generated using exact $V\left(x^1\right)$ values. This is due to the fact that the Legendre polynomials provide optimal convergence for uniformly distributed random variables. On the other hand, even the pdf obtained by the surrogate model generated using Hermite chaos with $p=5$ is not as accurate as the pdf obtained by Legendre chaos.

Here, we use Legendre polynomials irrespective of the distribution of the random variables. Doing so decouples the construction of the surrogate model from the pdf of the random variables and permits the user to study the effect of the type of pdf on the statistics of the observable (albeit at a slightly higher computational cost than when using polynomials tailored to the pdf of the random variable). Also, when combined with the

adaptive multi-element scheme described below, the treatment of (local) gPC expansion on each element becomes mathematically tedious if the $w^i(\cdot)$ are not uniform [29]. This is due to the fact that non-uniform $w^i(\cdot)$, when restricted to a subdomain of D, become non-canonical.

3.2.2 The ME-PC Method

When $V(\mathbf{x})$ is a rapidly varying function of $\mathbf{x}$, (i) a very high-order gPC expansion may be required to ensure accuracy of the surrogate model and (ii) a large number of collocation points is needed to accurately compute the gPC expansion coefficients. As a result, the above gPC expansion becomes expensive to compute and evaluate; moreover, it may be inaccurate. In severe cases, when $V(\mathbf{x})$ is discontinuous, the gPC collocation method may not even converge due to the Gibbs phenomenon [32].

The fundamental idea behind the adaptive refinement procedure described below is to recursively divide the random domain D into non-overlapping subdomains and to approximate $V(\mathbf{x})$ using a local gPC expansion in each subdomain. The gPC coefficients, which are computed separately for each subdomain using the gPC collocation method described above, are then used to estimate $V(\mathbf{x})$'s statistical moments, pdf, and cdf.

Let $\tilde{D} = \prod_{i=1}^{N_{\text{dof}}} \tilde{D}^i$ with $\tilde{D}^i = \left[\tilde{a}^i, \tilde{b}^i\right]$ denote a random subdomain considered for adaptive refinement; the procedure starts with $\tilde{D} = D$. In what follows, a tilde on a symbol indicates that it represents a quantity pertinent to subdomain $\tilde{D}$. $V(\mathbf{x})$ for $\mathbf{x}$ in $\tilde{D}$ is approximated by a p^{th} - order gPC expansion (as in(3.1)) using $N_p + 1$ local gPC

coefficients, $\tilde{v}_m$, $m=0,\ldots,N_p$, and local basis functions, $\tilde{\mathbf{P}}_m(\mathbf{x})$, $m=0,\ldots,N_p$. The local gPC coefficients, $\tilde{v}_m$, $m=0,\ldots,N_p$, are obtained by evaluating an N_{dof}-variate integral over $\tilde{D}$ (as in(3.6)).

To determine if the local approximation of $V(\mathbf{x})$ is "accurate" and if subdomain $\tilde{D}$ should be split, the local variance of $V(\mathbf{x})$ is estimated using the coefficients of the p^{th}- order local gPC expansion as (note that variance is the square of standard deviation)

$$\text{var}_p\left[V(\mathbf{x})\right]=\sum_{m=1}^{N_p}\tilde{v}_m^2\,. \tag{3.12}$$

The coefficients of the p^{th}- order local gPC expansion can be used similarly to compute $\text{var}_{p-1}\left[V(\mathbf{x})\right]$. Next, the decay rate of the relative error between the p^{th}- and $(p-1)^{\text{th}}$- order local gPC expansions is computed as [31]

$$\gamma=\left(\text{var}_p\left[V(\mathbf{x})\right]-\text{var}_{p-1}\left[V(\mathbf{x})\right]\right)\Big/\text{var}_p\left[V(\mathbf{x})\right]. \tag{3.13}$$

The subdomain $\tilde{D}$ is selected for refinement if

$$(\gamma)^{\tau_1}J\geq\beta\,, \tag{3.14}$$

where β and τ_1 are the desired tolerance and a user-defined constant ($0<\tau_1<1$), respectively; J measures the size of $\tilde{D}$ relative to D, i.e. $J=\prod_{i=1}^{N_{\text{dof}}}(\tilde{b}^i-\tilde{a}^i)/(b^i-a^i)$. Note that, β acts not only as an accuracy threshold but also as a limit for the size of the smallest subdomain.

The efficiency of the adaptive scheme is increased by refining domain $\tilde{D}$ only along dimension(s) in which $V(\mathbf{x})$ varies rapidly. The "sensitivity" of each dimension in $\tilde{D}$ is defined as

$$\alpha^i = \tilde{v}^i \Big/ \left(\mathrm{var}_p \left[V(\mathbf{x}) \right] - \mathrm{var}_{p-1} \left[V(\mathbf{x}) \right] \right). \tag{3.15}$$

Here, $\tilde{v}^i$ stands for the p^{th} - order gPC coefficient that applies to the i^{th} dimension alone. In the example above, v_3 ($d_3 = 20$) and v_5 ($d_5 = 02$) are the applicable 2^{nd} - order gPC coefficients for the 1^{st} and 2^{nd} dimensions, respectively. Refinement of $\tilde{D}$ is performed along dimensions for which

$$\alpha^i \geq \tau_2 \cdot \left(\max_{i=1,\ldots,N_{\text{dof}}} \alpha^i \right) \tag{3.16}$$

by splitting the subdomain along those dimensions into two. Here, τ_2 again is a user-defined constant ($0 < \tau_2 < 1$).

The adaptive and recursive application of this procedure generates N_d non-overlapping subdomains $\tilde{D}_j = \prod_{i=1}^{N_{\text{dof}}} \tilde{D}_j^i$, $j = 1, \ldots, N_d$, with $\tilde{D}_j^i = \left[\tilde{a}_j^i, \tilde{b}_j^i \right]$ which do not require refinement, i.e. on which the p^{th} - order local gPC expansion is an "accurate" representation of observable $V(\mathbf{x})$ in $\tilde{D}_j$, $j = 1, \ldots, N_d$. The coefficients of the p^{th} - order local gPC expansion constructed in $\tilde{D}_j$, $\tilde{v}_{m,j}$, $m = 0, \ldots, N_p$, $j = 1, \ldots, N_d$, are stored during the adaptive refinement process to permit rapid evaluation of the surrogate model approximation to $V(\mathbf{x})$ and estimate statistical quantities applicable to $V(\mathbf{x})$.

By the law of total probability and the expression in (3.9), the global average, i.e., the average of $V(\mathbf{x})$ over D, can be approximated using

$$E\left[V(\mathbf{x})\right] \cong \sum_{j=1}^{N_d} \tilde{v}_{0,j} J_j \,, \tag{3.17}$$

where $J_j = \prod_{i=1}^{N_{\text{dof}}} (\tilde{b}_j^i - \tilde{a}_j^i) \big/ (b^i - a^i)$, and $\tilde{v}_{0,j}$ denotes the 0^{th} coefficient of the p^{th}-order local gPC expansion constructed in $\tilde{D}_j$. In a similar way, the global variance, i.e., the variance of $V(\mathbf{x})$ over D, can be derived by noting that

$$\text{var}\left[V(\mathbf{x})\right] \cong \sum_{j=1}^{N_d} J_j \int_{\tilde{D}_j} \left(V_j(\mathbf{x}) - E\left[V(\mathbf{x})\right]\right)^2 d\mathbf{x}\,, \tag{3.18}$$

where $V_j(\mathbf{x})$ denotes $V(\mathbf{x})$ in $\tilde{D}_j$. Expanding $V_j(\mathbf{x})$ in terms of local gPC expansion constructed in $\tilde{D}_j$ yields

$$\text{var}\left[V(\mathbf{x})\right] \cong \sum_{j=1}^{N_d} J_j \int_{\tilde{D}_j} \left(\sum_{m=1}^{N_p} \tilde{v}_{m,j} \tilde{\mathbf{P}}_{m,j}(\mathbf{x}) + \left(\tilde{v}_{0,j} \tilde{\mathbf{P}}_{0,j}(\mathbf{x}) - E\left[V(\mathbf{x})\right] \tilde{\mathbf{P}}_{0,j}(\mathbf{x}) \right) \right)^2 d\mathbf{x}\,. \tag{3.19}$$

Here $\tilde{\mathbf{P}}_{m,j}$ is the m^{th} local basis functions of local gPC expansion constructed in $\tilde{D}_j$ and $\tilde{\mathbf{P}}_{0,j}(\mathbf{x}) = 1$. By expanding the integrand and using the orthogonality relation in (3.5), one can obtain the final expression of global variance as

$$\text{var}\left[V(\mathbf{x})\right] \cong \sum_{j=1}^{N_d} J_j \left[\text{var}_p\left[V_j(\mathbf{x})\right] + \left(\tilde{v}_{0,j} - E\left[V(\mathbf{x})\right]\right)^2 \right], \tag{3.20}$$

where $\text{var}_p\left[V_j(\mathbf{x})\right]$ is the local variance of $V_j(\mathbf{x})$ estimated using the coefficients of the p^{th} - order local gPC expansion.

3.2.3 Fine-Tuning of the ME-PC Method for EMC/EMI Applications

In many EMC/EMI scenarios, the observable might be a periodic function in one (or several) of the (uniformly distributed) random variables/parameters (see Section 3.3.3 for an example). Along those dimensions, a Dirichlet kernel should be used to represent the periodically varying part of the observable instead of a gPC expansion. Assume that the observable $V(\mathbf{x})$ in subdomain $\tilde{D}$ is periodic in $x^{N_{\text{dof}}}$ with period 2π. Then, it can be expressed as a weighted sum of the Dirichlet kernels as

$$V(\mathbf{x}) = \sum_{n=-N}^{N} V\left(\left[x^1,...,x^{N_{\text{dof}}-1}, n\Delta x^{N_{\text{dof}}}\right]\right) DI_N\left(x^{N_{\text{dof}}} - n\Delta x^{N_{\text{dof}}}\right), \tag{3.21}$$

where the number of samples used in the $N_{\text{dof}}^{\text{th}}$ dimension is $2N+1$, $\Delta x^{N_{\text{dof}}} = 2\pi/(2N+1)$ is the spacing between these samples, and $DI_N(x)$ is the Dirichlet kernel [70], i.e.

$$DI_N(x) = \frac{\sin\left[(2N+1)x/2\right]}{(2N+1)\sin(x/2)}. \tag{3.22}$$

In (3.21), each of $V(\mathbf{x})$'s cuts, $V\left(\left[x^1,...,x^{N_{\text{dof}}-1}, n\Delta x^{N_{\text{dof}}}\right]\right)$, is approximated using the p^{th}-order local gPC expansion as

$$V\left(\left[x^1,...,x^{N_{\text{dof}}-1}, n\Delta x^{N_{\text{dof}}}\right]\right) \cong \sum_{m=0}^{N_p} \tilde{v}_m \tilde{\mathbf{P}}_m\left(x^1,...,x^{N_{\text{dof}}-1}\right)\Big|_n. \tag{3.23}$$

Inserting (3.23) into (3.21), an approximation to $V(\mathbf{x})$ is obtained:

$$V(\mathbf{x}) \cong \sum_{n=-N}^{N} \left[\sum_{m=0}^{N_p} \tilde{v}_m \tilde{\mathbf{P}}_m\left(x^1,...,x^{N_{\text{dof}}-1}\right)\right]_n DI_N\left(x^{N_{\text{dof}}} - n\Delta x^{N_{\text{dof}}}\right). \tag{3.24}$$

The expansion coefficients in (3.23) are obtained separately for all cuts as explained above. The refinement parameters γ and α^i, $i=1,\ldots,N_{\text{dof}}-1$, are also obtained for all cuts. If *one* of γ computed for all cuts satisfies the refinement criterion [see (3.14)], the subdomain $\tilde{D}$ is selected for the refinement. Likewise, a refinement is performed along the i^{th} dimension, if *one* of α^i, $i=1,\ldots,N_{\text{dof}}-1$, computed for all cuts satisfies the dimensional refinement criterion [see (3.16)]. The adaptive refinement process produces N_d subdomains (per cut) $\tilde{D}_j$, $j=1,\ldots,N_d$, which do not require adaptive refinement. The coefficients of p^{th}- order gPC expansions constructed in such domains, $\tilde{D}_j$, $j=1,\ldots,N_d$, are stored during the adaptive refinement process to obtain the surrogate model of $V(\mathbf{x})$ and global statistical moments.

Use of (3.24) in the adaptive refinement scheme increases the accuracy of the surrogate model of $V(\mathbf{x})$ and the efficiency of the adaptive ME-PC method used for constructing it. The former is attributed to the fact that a highly accurate Dirichlet kernel expansion in (3.21) is used to replace the orthogonal polynomial approximation along the $N_{\text{dof}}^{\text{th}}$ dimension. The latter is attributed to two facts: (i) the gPC expansion in (3.24) has one dimension less than the one used in the ME-PC method, and (ii) the periodic and possibly highly oscillatory variation along the $N_{\text{dof}}^{\text{th}}$ dimension does not have to be accounted for by the adaptive ME-PC scheme.

The utilization of the Dirichlet kernel in the gPC expansion does not require any modifications on the MC scheme carried out following the adaptive refinement process (Section 3.2.2). However, the expressions derived to obtain the statistical moments when

$w^i(\cdot)$, $i=1,\ldots,N_{\text{dof}}$, represent uniform distributions, should be modified. The new expression for the average of the observable $V(\mathbf{x})$ over D is

$$E\left[V(\mathbf{x})\right] \cong \frac{1}{2N+1}\sum_{j=1}^{N_d} J_j \sum_{n=-N}^{N} \tilde{v}_{0,j}\Big|_n . \tag{3.25}$$

Here, $\tilde{v}_{0,j}\Big|_n$ denotes the 0^{th} coefficient of the p^{th}- order local gPC expansion used to approximate $V_j\left(\left[x^1,...,x^{N_{\text{dof}}-1}, n\Delta x^{N_{\text{dof}}}\right]\right)$ in $\tilde{D}_j$. Similarly, the expression for the variance of the observable $V(\mathbf{x})$ over D becomes

$$\text{var}\left[V(\mathbf{x})\right] \cong \frac{1}{2N+1}\sum_{j=1}^{N_d} J_j \sum_{n=-N}^{N}\sum_{m=1}^{N_p} \tilde{v}_{m,j}^2\Big|_n + \left(\tilde{v}_{0,j}\Big|_n - E\left[V(\mathbf{x})\right]\right)^2 . \tag{3.26}$$

It should be noted that J_j in (3.25) and (3.26) is not the same as that in (3.17) and (3.20); here $J_j = \prod_{i=1}^{N_{\text{dof}}-1}(\tilde{b}_j^i - \tilde{a}_j^i)\big/(b^i - a^i)$. Detailed derivations of (3.25) and (3.26) are provided in Appendix A and Appendix B, respectively.

3.3 Application to the EMC/EMI Problems

This section illustrates the application of the adaptive ME-PC method to the statistical characterization of EMC/EMI phenomena on various realistic structures. Specifically, averages, standard deviations, and pdfs/cdfs of voltage and fields on several transmission line structures, a microwave amplifier, and a tire pressure monitoring system obtained using the proposed adaptive ME-PC technique are compared to those obtained using the nonadaptive gPC collocation method, and brute-force MC technique. Unless specified otherwise, the adaptive ME-PC method uses a Gauss-Legendre SG

integration rule with $l = 2$ (see the definition of l for SG integration method in Section 2.2.3.2), which can accurately integrate polynomials of degree five or less (for $N_{\text{dof}} \geq 3$), local gPC expansions with $p = 2$, and adaptive refinement constants τ_1 and τ_2 of 0.5. Unless noted otherwise, observables' averages and standard deviations (i.e. square roots of variances) estimated by adaptive ME-PC method are computed using (3.17) and (3.20) , while those estimated by nonadaptive gPC collocation technique are evaluated using (3.9) and (3.11). Observables' pdfs/cdfs are estimated by applying MC to surrogate models obtained using the ME-PC method and nonadaptive gPC collocation technique, or by directly evaluating $V(\mathbf{x})$ using analytical transfer functions or the deterministic simulator described in Section 2.2.4; such MC runs and the data they produce will be labeled as "brute force".

3.3.1 Transmission Lines Terminated by RLC Circuits

3.3.1.1 A Lossless Transmission Line

The adaptive ME-PC method is used to compute the statistical moments of the voltage on a lossless transmission line terminated by an RLC circuit [Figure 3–2]. The transmission line's characteristic impedance and length are $50\,\Omega$ and $0.4\,\text{m}$, respectively. The wave speed on the transmission line is 1.99×10^8 m/s. The value of the resistance in the RLC circuit is $2\,\Omega$. The transmission line is excited by a sinusoidal voltage source with frequency 486.28 MHz. Two parameters characterize the uncertainty in the problem ($N_{\text{dof}} = 2$): the inductance and the capacitance values, L and C (i.e., $\mathbf{x} = [L, C]$), which are assumed uniformly distributed in the ranges $\left[a^i, b^i\right]$, $i = 1, 2$;

$[5,15]$ nH and $[10,20]$ pF, respectively. The observables are the real and the imaginary parts of the voltage across the capacitor, $V_C^{\mathrm{Re}}(\mathbf{x})$ and $V_C^{\mathrm{Im}}(\mathbf{x})$; exact observable values are easily computed using the analytical transfer function of the circuit for a given $\mathbf{x}$.

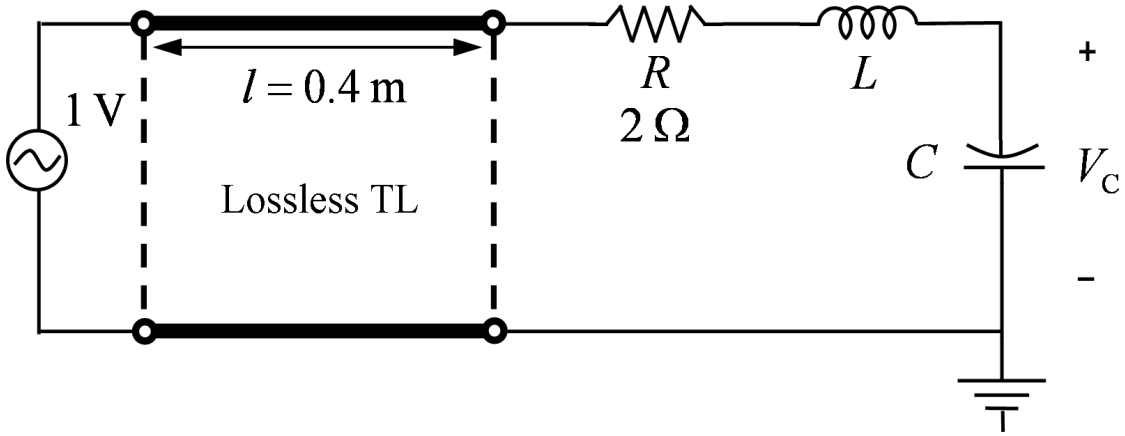

Figure 3–2 Geometry description of a lossless transmission line terminated by an RLC circuit

The average and standard deviation of $V_C^{\mathrm{Re}}(\mathbf{x})$ and $V_C^{\mathrm{Im}}(\mathbf{x})$ are computed using various methods. Table 3–2 presents the observable averages and standard deviations $E^{\mathrm{k}}[.]$ and $\mathrm{std}^{\mathrm{k}}[.]$ for $\mathrm{k}=\{\mathrm{BF, ST, TP}\}$, obtained by applying brute-force MC (BF) to the analytical transfer function, and by using nonadaptive gPC collocation methods with ST and TP integration rules; the latter uses 125 Gauss-Legendre points in each dimension. Also shown are $E^{\mathrm{k}}[.]$ and $\mathrm{std}^{\mathrm{k}}[.]$ for $\mathrm{k}=\{\mathrm{A\text{-}10^{-1}, A\text{-}10^{-2}, A\text{-}10^{-3}, A\text{-}10^{-4}}\}$ computed by the adaptive ME-PC method, which uses the TP integration method (with five Gauss-Legendre points in each dimension) to compute the expansion coefficients with $\beta=\{10^{-1},10^{-2},10^{-3},10^{-4}\}$.

superscript (k)	$E^{\mathrm{k}}\left[V_{\mathrm{C}}^{\mathrm{Re}}(\mathbf{x})\right]$ (V)	$E^{\mathrm{k}}\left[V_{\mathrm{C}}^{\mathrm{Im}}(\mathbf{x})\right]$ (V)	$\mathrm{std}^{\mathrm{k}}\left[V_{\mathrm{C}}^{\mathrm{Re}}(\mathbf{x})\right]$ (V)	$\mathrm{std}^{\mathrm{k}}\left[V_{\mathrm{C}}^{\mathrm{Im}}(\mathbf{x})\right]$ (V)

k = TP	0.1174	-2.1756	3.4290	3.1371
k = ST	0.0233	-0.7000	2.6835	0.4504
k = BF	0.1160	-2.1728	3.4268	3.1336
k = A-10^{-1}	0.1174	-2.1757	3.2629	3.1389
k = A-10^{-2}	0.1174	-2.1756	3.4218	3.1371
k = A-10^{-3}	0.1174	-2.1756	3.4289	3.1371
k = A-10^{-4}	0.1174	-2.1756	3.4290	3.1371

Table 3–2 Comparison of $E\left[V_{\mathrm{C}}^{\mathrm{Re}}(\mathbf{x})\right]/\mathrm{std}\left[V_{\mathrm{C}}^{\mathrm{Re}}(\mathbf{x})\right]$ and $E\left[V_{\mathrm{C}}^{\mathrm{Im}}(\mathbf{x})\right]/\mathrm{std}\left[V_{\mathrm{C}}^{\mathrm{Im}}(\mathbf{x})\right]$ computed using brute force MC method, nonadaptive gPC collocation methods with ST and TP integration rules, and the adaptive ME-PC method.

Relative errors,

$$
\begin{aligned}
err^{E^{\mathrm{k}},\mathrm{Re/Im}} &= \frac{\left|E^{\mathrm{k}}\left[V_C^{\mathrm{Re/Im}}(\mathbf{x})\right]-E^{\mathrm{TP}}\left[V_C^{\mathrm{Re/Im}}(\mathbf{x})\right]\right|}{\left|E^{\mathrm{TP}}\left[V_C^{\mathrm{Re/Im}}(\mathbf{x})\right]\right|} \\
err^{\mathrm{std}^{\mathrm{k}},\mathrm{Re/Im}} &= \frac{\left|\mathrm{std}^{\mathrm{k}}\left[V_C^{\mathrm{Re/Im}}(\mathbf{x})\right]-\mathrm{std}^{\mathrm{TP}}\left[V_C^{\mathrm{Re/Im}}(\mathbf{x})\right]\right|}{\left|\mathrm{std}^{\mathrm{TP}}\left[V_C^{\mathrm{Re/Im}}(\mathbf{x})\right]\right|}, \qquad (3.27) \\
&\mathrm{k}=\left\{\mathrm{BF},\mathrm{ST},\mathrm{TP},\mathrm{A\text{-}10^{-1}},\mathrm{A\text{-}10^{-2}},\mathrm{A\text{-}10^{-3}},\mathrm{A\text{-}10^{-4}}\right\}
\end{aligned}
$$

computed using $E^{\mathrm{TP}}[.]$ and $\mathrm{std}^{\mathrm{TP}}[.]$ as the reference, are presented in Table 3–3. Table 3–3 compares the number of deterministic simulations required by all four methods to compute the averages and standard deviations. Figure 3–3 (a)-(d) and Figure 3–4 (a)-(d) present $V_C^{\mathrm{Re,k}}(\mathbf{x})$ and $V_C^{\mathrm{Im,k}}(\mathbf{x})$, $\mathrm{k}=\left\{\mathrm{A\text{-}10^{-1}},\mathrm{A\text{-}10^{-2}},\mathrm{A\text{-}10^{-3}},\mathrm{A\text{-}10^{-4}}\right\}$, which are constructed by the adaptive ME-PC with $\beta=\left\{10^{-1},10^{-2},10^{-3},10^{-4}\right\}$, respectively. Finally, the two-dimensional random domains resulting from the adaptive refinements with $\beta=\left\{10^{-1},10^{-2},10^{-3},10^{-4}\right\}$ are shown in Figure 3–5 (a)-(d).

superscript (k)	$err^{\mathrm{E^k,Re}}$	$err^{\mathrm{E^k,Im}}$	$err^{\mathrm{std^k,Re}}$	$err^{\mathrm{std^k,Im}}$	Number of deterministic simulations
k = TP	-	-	-	-	15625
k = ST	8.0193×10^{-1}	6.7826×10^{-1}	2.1742×10^{-1}	8.5643×10^{-1}	4

k = BF	1.2383×10^{-2}	1.2597×10^{-3}	6.3747×10^{-4}	1.1077×10^{-3}	1000000
k = A-10^{-1}	6.9959×10^{-4}	8.3635×10^{-5}	4.8434×10^{-2}	5.7156×10^{-4}	275
k = A-10^{-2}	7.1992×10^{-6}	1.7218×10^{-8}	2.0861×10^{-3}	1.5607×10^{-7}	1225
k = A-10^{-3}	1.2440×10^{-12}	2.0041×10^{-12}	1.7976×10^{-5}	2.9572×10^{-11}	4725
k = A-10^{-4}	8.5138×10^{-15}	1.0000×10^{-16}	3.0848×10^{-8}	1.0000×10^{-16}	14575

Table 3–3 Comparison of the efficiency and accuracy of the brute force MC method, nonadaptive gPC collocation methods with ST and TP integration rules, and the adaptive ME-PC method in computing $E\left[V_{\mathrm{C}}^{\mathrm{Re}}(\mathbf{x})\right]/\mathrm{std}\left[V_{\mathrm{C}}^{\mathrm{Re}}(\mathbf{x})\right]$ and $E\left[V_{\mathrm{C}}^{\mathrm{Im}}(\mathbf{x})\right]/\mathrm{std}\left[V_{\mathrm{C}}^{\mathrm{Im}}(\mathbf{x})\right]$.

Several observations about the results are in order:

It is clear from the relative errors presented in Table 3–3 that $E^{\mathrm{A}\text{-}\beta}[.]$ and $\mathrm{std}^{\mathrm{A}\text{-}\beta}[.]$ converge to $E^{\mathrm{TP}}[.]$ and $\mathrm{std}^{\mathrm{TP}}[.]$, respectively, as β decreases. From an engineering perspective, $E^{\mathrm{k}}[.]$ and $\mathrm{std}^{\mathrm{k}}[.]$, $\mathrm{k}=\left\{\mathrm{TP},\mathrm{A}\text{-}10^{-1},\mathrm{A}\text{-}10^{-2},\mathrm{A}\text{-}10^{-3},\mathrm{A}\text{-}10^{-4}\right\}$ are practically identical for this problem. However, significant differences in $V_C^{\mathrm{Re,k}}(\mathbf{x})$ and $V_C^{\mathrm{Im,k}}(\mathbf{x})$, $\mathrm{k}=\left\{\mathrm{A}\text{-}10^{-1},\mathrm{A}\text{-}10^{-2},\mathrm{A}\text{-}10^{-3},\mathrm{A}\text{-}10^{-4}\right\}$ are observed as shown in Figure 3–3 (a)-(d) and Figure 3–4 (a)-(d). This can be explained by the "smoothing" effect of the integrals present in the expressions for the observable average and standard deviations.

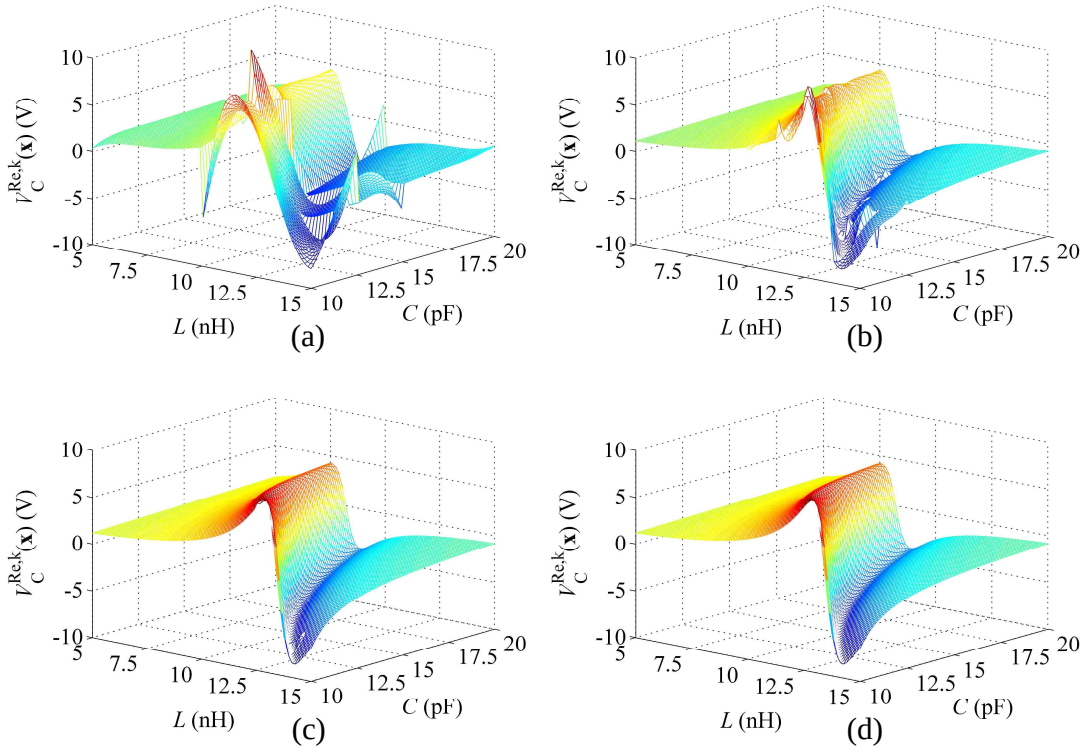

Figure 3–3 $V_C^{\mathrm{Re,k}}(\mathbf{x})$ for (a) $\mathrm{k} = \mathrm{A}\text{-}10^{-1}$, (b) $\mathrm{k} = \mathrm{A}\text{-}10^{-2}$, (c) $\mathrm{k} = \mathrm{A}\text{-}10^{-3}$, and (d) $\mathrm{k} = \mathrm{A}\text{-}10^{-4}$.

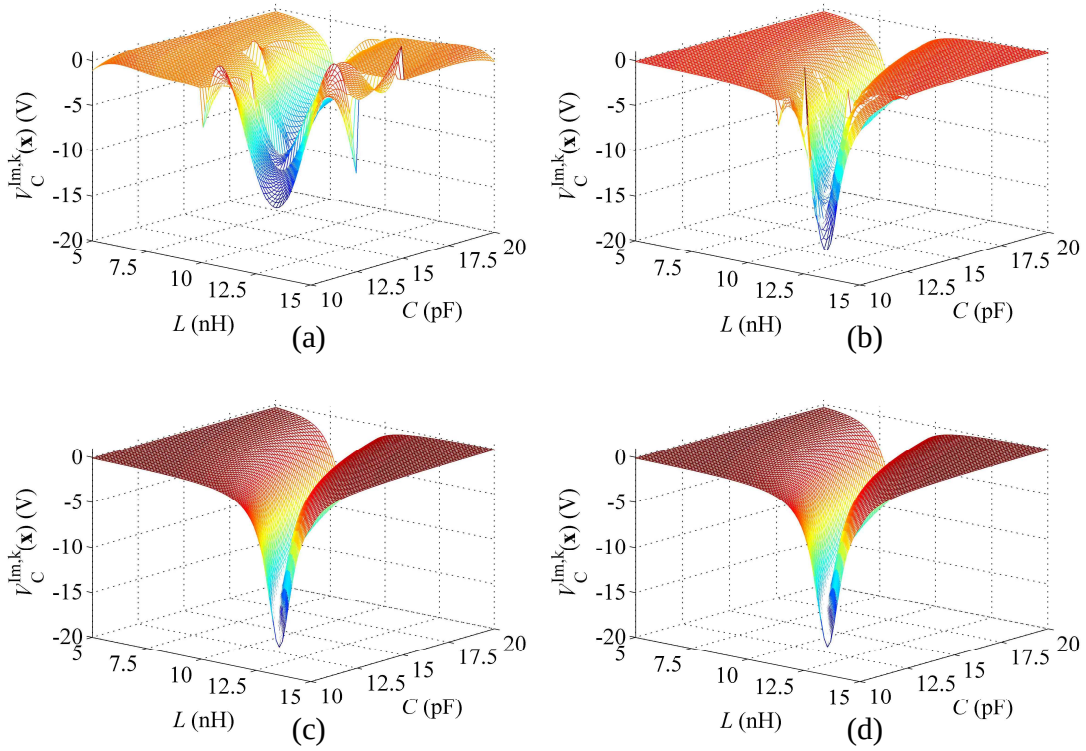

Figure 3–4 $V_C^{\mathrm{Im,k}}(\mathbf{x})$ for (a) k = A-10^{-1}, (b) k = A-10^{-2}, (c) k = A-10^{-3}, and (d) k = A-10^{-4}.

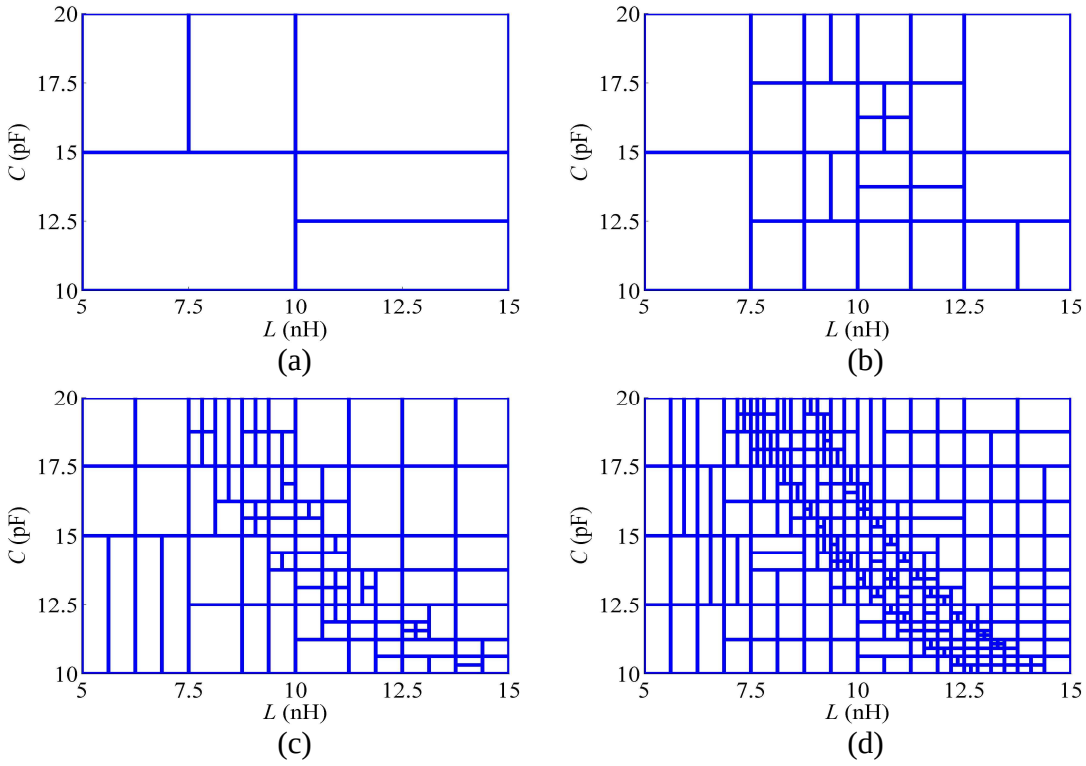

Figure 3–5 Adaptively refined random domains used in the construction of $V_C^{\mathrm{Re,k}}(\mathbf{x})$ and $V_C^{\mathrm{Im,k}}(\mathbf{x})$ for (a) k = A-10^{-1}, (b) k = A-10^{-2}, (c) k = A-10^{-3}, and (d) k = A-10^{-4}.

As β decreases, the adaptive ME-PC method carries out more recursive refinements to meet the required accuracy as shown in Figure 3–5 (a)-(d). Also, it is clear from these figures that for values of L and C that approach resonance conditions (where $V_C^{\mathrm{Re}}(\mathbf{x})$ and $V_C^{\mathrm{Im}}(\mathbf{x})$ vary very rapidly), the scheme automatically produces smaller subdomains to increase the accuracy of the gPC expansion for a given β.

3.3.1.2 Two Lossless Transmission Lines Connected with an Attenuator

The adaptive ME-PC method is used to compute the statistical moments and extract the pdfs of voltages on two lossless transmission lines. The first transmission line

is terminated by a 3 dB attenuator circuit; the second line is connected to an attenuator on one end and terminated by an RLC circuit on the other [Figure 3–6]. The transmission lines' characteristic impedance is $50\,\Omega$ and their wave speed is 1.99×10^{8} m/s. The first transmission line is excited by a sinusoidal voltage source with frequency 573 MHz.

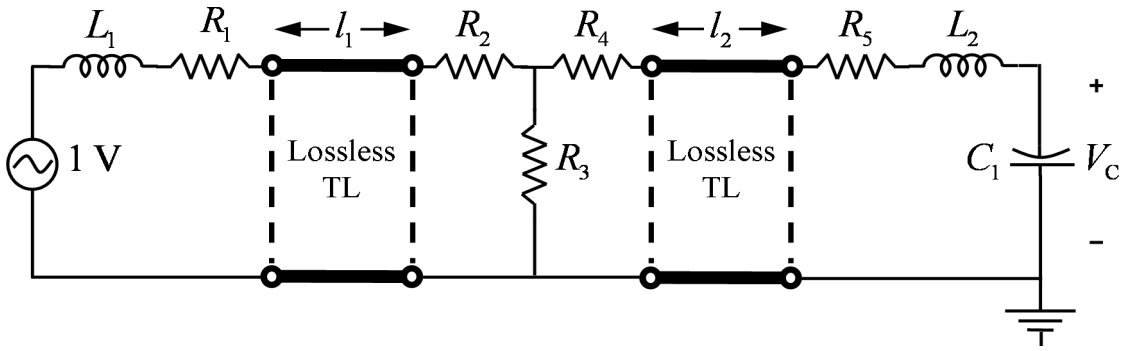

Figure 3–6 Geometry description of two losses transmission lines connected by a 3 dB attenuator; the second transmission line is terminated by an RLC circuit at the other end

Ten parameters characterize the uncertainty in the problem ($N_{\text{dof}}=10$): the inductance values L_1 and L_2, the resistance values R_1, R_2, R_3, R_4, and R_5, the lengths of the transmission lines l_1 and l_2, and the capacitance value C_1 (i.e., $\mathbf{x}=[L_1,L_2,R_1,R_2,R_3,R_4,R_5,l_1,l_2,C_1]$). All ten variables are assumed uniformly distributed in ranges $[a^i,b^i]$, $i=1,\ldots,10$; a^i and b^i are given in Table 3–4.

	a^i	b^i
$i=1$, L_1 (nH)	2.7	3.3
$i=2$, L_2 (nH)	2.7	3.3
$i=3$, R_1 (Ω)	0.17	0.23
$i=4$, R_2 (Ω)	7.2675	9.8325
$i=5$, R_3 (Ω)	120.632	163.208
$i=6$, R_4 (Ω)	7.2675	9.8325
$i=7$, R_5 (Ω)	0.17	0.23
$i=8$, l_1 (m)	0.245	0.255

$i=9$, l_2 (m)	0.245	0.255
$i=10$, C_1 (nF)	185	235

Table 3–4 Values of a^i and b^i, $i=1,\ldots,10$.

The observables are the real and the imaginary parts of the voltage across the capacitor, and its magnitude, $V_C^{\mathrm{Re}}(\mathbf{x})$ and $V_C^{\mathrm{Im}}(\mathbf{x})$, and $V_C^{\mathrm{Abs}}(\mathbf{x})$. Table 3–5 presents these observables' averages and standard deviations $E^{\mathrm{k}}[.]$ and $\mathrm{std}^{\mathrm{k}}[.]$ for $\mathrm{k}=\{\mathrm{BF},\ \mathrm{ST},\ \mathrm{TP}\}$, that are computed by brute-force MC (BF) applied to the analytical transfer function, and by using nonadaptive gPC collocation methods with ST and TP integration rules; the latter uses two Gauss-Legendre points in each dimension. The quantities $E^{\mathrm{k}}[.]$ and $\mathrm{std}^{\mathrm{k}}[.]$ are also computed using $\mathrm{k}=\{\mathrm{A\text{-}10^{-1}},\mathrm{A\text{-}10^{-2}}\}$, that is using the adaptive ME-PC method with $\beta=\{10^{-1},10^{-2}\}$.

superscript (k)	$\mathrm{E}^{\mathrm{k}}\left[V_{\mathrm{C}}^{\mathrm{Re}}(\mathbf{x})\right]$ (mV)	$\mathrm{E}^{\mathrm{k}}\left[V_{\mathrm{C}}^{\mathrm{Im}}(\mathbf{x})\right]$ (mV)	$\mathrm{std}^{\mathrm{k}}\left[V_{\mathrm{C}}^{\mathrm{Re}}(\mathbf{x})\right]$ (mV)	$\mathrm{std}^{\mathrm{k}}\left[V_{\mathrm{C}}^{\mathrm{Im}}(\mathbf{x})\right]$ (mV)
k = BF	-0.6455	26.5211	5.3068	2.8377
k = ST	-0.6866	26.4802	5.4775	2.5916
k = TP	-0.6913	26.5094	5.3223	2.7877
k = A-10^{-1}	-0.6930	26.5215	5.2730	2.8463
k = A-10^{-2}	-0.6928	26.5215	5.2728	2.8470

Table 3–5 Comparison of $E\left[V_{\mathrm{C}}^{\mathrm{Re}}(\mathbf{x})\right]/\mathrm{std}\left[V_{\mathrm{C}}^{\mathrm{Re}}(\mathbf{x})\right]$ and $E\left[V_{\mathrm{C}}^{\mathrm{Im}}(\mathbf{x})\right]/\mathrm{std}\left[V_{\mathrm{C}}^{\mathrm{Im}}(\mathbf{x})\right]$ computed using brute force MC method, nonadaptive gPC collocation methods with ST and TP integration rules, and the adaptive ME-PC method.

Relative errors,

$$err^{E^{\mathrm{k}},\mathrm{Re/Im}} = \frac{\left| E^{\mathrm{k}}\left[V_C^{\mathrm{Re/Im}}(\mathbf{x})\right] - E^{\text{A-}10^{-2}}\left[V_C^{\mathrm{Re/Im}}(\mathbf{x})\right]\right|}{\left|E^{\text{A-}10^{-2}}\left[V_C^{\mathrm{Re/Im}}(\mathbf{x})\right]\right|},$$

$$err^{\mathrm{std}^{\mathrm{k}},\mathrm{Re/Im}} = \frac{\left|\mathrm{std}^{\mathrm{k}}\left[V_C^{\mathrm{Re/Im}}(\mathbf{x})\right] - \mathrm{std}^{\text{A-}10^{-2}}\left[V_C^{\mathrm{Re/Im}}(\mathbf{x})\right]\right|}{\left|\mathrm{std}^{\text{A-}10^{-2}}\left[V_C^{\mathrm{Re/Im}}(\mathbf{x})\right]\right|}, \quad (3.28)$$

$$\mathrm{k} = \left\{\mathrm{BF},\mathrm{ST},\mathrm{TP},\text{A-}10^{-1},\text{A-}10^{-2}\right\}$$

computed using $E^{\text{A-}10^{-2}}[.]$ and $\mathrm{std}^{\text{A-}10^{-2}}[.]$ as the reference, are presented in Table 3–6. Additionally, pdfs of $V_C^{\mathrm{Re}}(\mathbf{x})$, $V_C^{\mathrm{Im}}(\mathbf{x})$, and $V_C^{\mathrm{Abs}}(\mathbf{x})$ are estimated via a 25000 - point MC simulation performed using $V_C^{\mathrm{Re,k}}(\mathbf{x})$, $V_C^{\mathrm{Im,k}}(\mathbf{x})$, $V_C^{\mathrm{Abs,k}}(\mathbf{x})$, $\mathrm{k} = \left\{\mathrm{BF},\mathrm{TP},\text{A-}10^{-1},\text{A-}10^{-2}\right\}$ [Figure 3–7 – Figure 3–9]. $V_C^{\mathrm{Re,k}}(\mathbf{x})$, $V_C^{\mathrm{Im,k}}(\mathbf{x})$, $V_C^{\mathrm{Abs,k}}(\mathbf{x})$, $\mathrm{k} = \left\{\mathrm{BF},\mathrm{TP}\right\}$, are computed by brute-force MC applied to the analytical transfer function, and by using nonadaptive gPC surrogate models obtained using TP integration rule (with two Gauss-Legendre points in each dimension). In addition, $V_C^{\mathrm{Re,k}}(\mathbf{x})$, $V_C^{\mathrm{Im,k}}(\mathbf{x})$, $V_C^{\mathrm{Abs,k}}(\mathbf{x})$, $\mathrm{k} = \left\{\text{A-}10^{-1},\text{A-}10^{-2}\right\}$, are obtained from surrogate models constructed using the adaptive ME-PC method with $\beta = \left\{10^{-1},10^{-2}\right\}$.

superscript (k)	$err^{\mathrm{E^k,Re}}$	$err^{\mathrm{E^k,Im}}$	$err^{\mathrm{std^k,Re}}$	$err^{\mathrm{std^k,Im}}$	Number of deterministic simulations
k = BF	6.8317×10^{-2}	1.7375×10^{-5}	6.4376×10^{-3}	3.2476×10^{-3}	25000
k = ST	9.0521×10^{-3}	1.5584×10^{-3}	3.8820×10^{-2}	8.9688×10^{-2}	20
k = TP	2.1580×10^{-3}	4.5821×10^{-4}	9.3863×10^{-3}	2.0810×10^{-2}	1024
k = A-10^{-1}	2.3369×10^{-4}	1.5969×10^{-6}	3.0823×10^{-5}	2.4429×10^{-4}	1305
k = A-10^{-2}	-	-	-	-	9657

Table 3–6 Comparison of the efficiency and accuracy of the brute force MC method, nonadaptive gPC collocation methods with ST and TP integration rules, and the adaptive ME-PC method in computing $E\left[V_{\mathrm{C}}^{\mathrm{Re}}(\mathbf{x})\right]/\mathrm{std}\left[V_{\mathrm{C}}^{\mathrm{Re}}(\mathbf{x})\right]$ and $E\left[V_{\mathrm{C}}^{\mathrm{Im}}(\mathbf{x})\right]/\mathrm{std}\left[V_{\mathrm{C}}^{\mathrm{Im}}(\mathbf{x})\right]$.

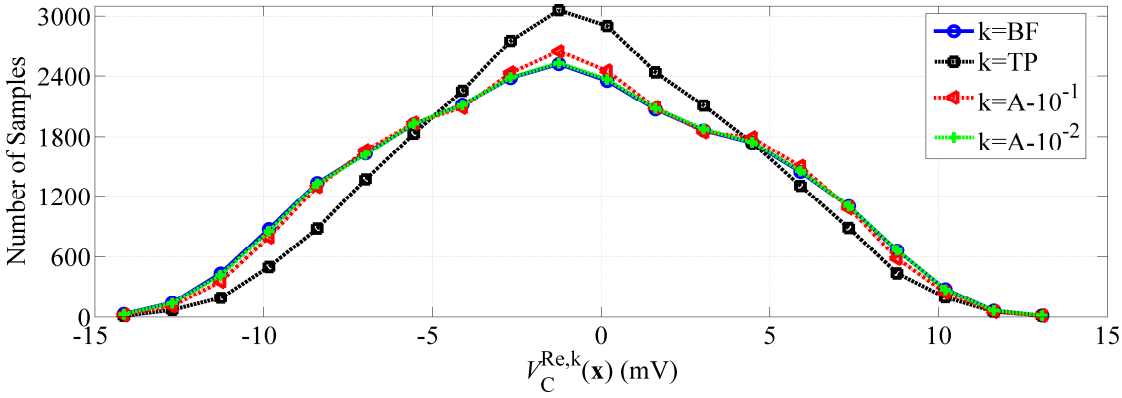

Figure 3–7 The pdfs obtained via $V_C^{Re,k}(\mathbf{x})$, $k=\{BF,TP,A\text{-}10^{-1},A\text{-}10^{-2}\}$.

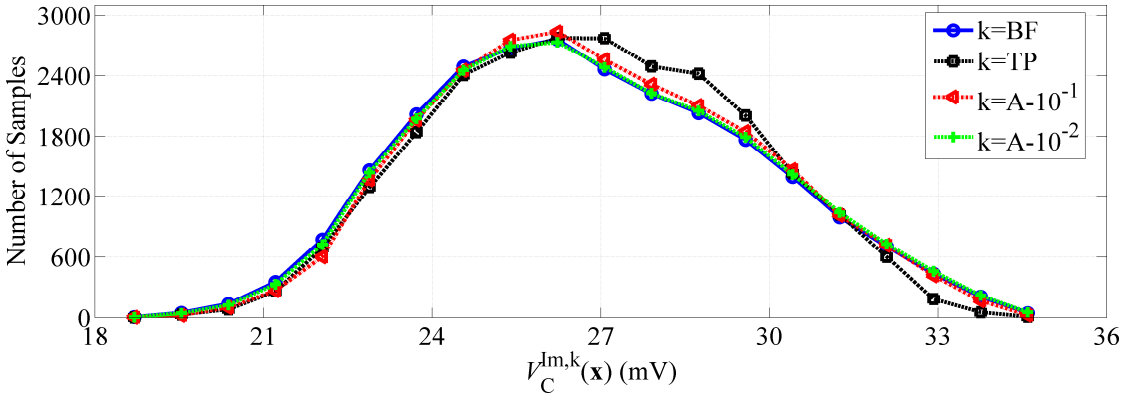

Figure 3–8 The pdfs obtained via $V_C^{Im,k}(\mathbf{x})$, $k=\{BF,TP,A\text{-}10^{-1},A\text{-}10^{-2}\}$.

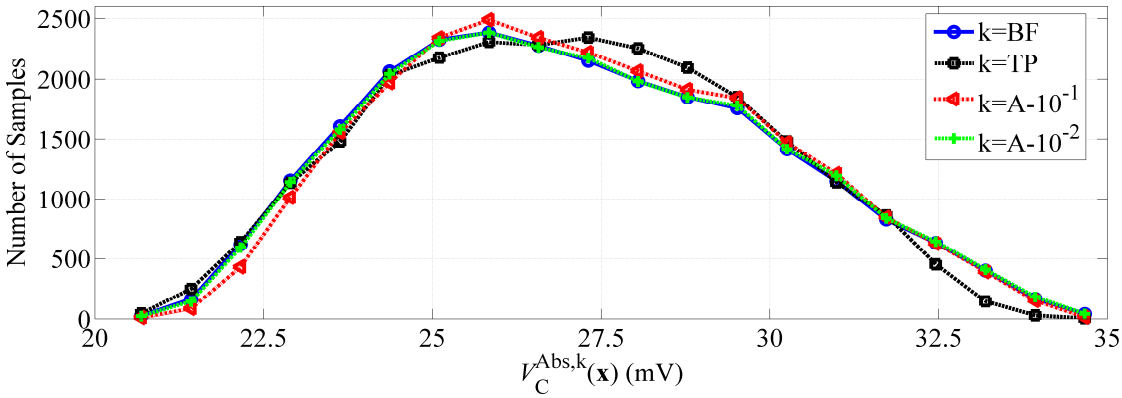

Figure 3–9 The pdfs obtained via $V_C^{Abs,k}(\mathbf{x})$, $k=\{BF,TP,A\text{-}10^{-1},A\text{-}10^{-2}\}$.

Several observations about the results are in order:

It is clear from the averages, standard deviations, and relative errors presented in Table 3–5 and Table 3–6 that the adaptive ME-PC method is slightly more accurate than the nonadaptive gPC collocation method using a TP integration rule. The real advantage of the adaptive ME-PC method however is demonstrated by Figure 3–7 – Figure 3–9: The pdfs obtained via $V_C^{\mathrm{Re,k}}(\mathbf{x})$, $V_C^{\mathrm{Im,k}}(\mathbf{x})$, and $V_C^{\mathrm{Abs,k}}(\mathbf{x})$, $\mathrm{k}=\{\text{A-}10^{-1},\text{A-}10^{-2}\}$, show clear convergence to the pdfs obtained via $V_C^{\mathrm{Re,k}}(\mathbf{x})$, $V_C^{\mathrm{Im,k}}(\mathbf{x})$, and $V_C^{\mathrm{Abs,k}}(\mathbf{x})$, $\mathrm{k}=\{\mathrm{BF}\}$, i.e. exact analytical transfer function values, and they are much more accurate than the pdfs obtained via $V_C^{\mathrm{Re,k}}(\mathbf{x})$, $V_C^{\mathrm{Im,k}}(\mathbf{x})$, and $V_C^{\mathrm{Abs,k}}(\mathbf{x})$, $\mathrm{k}=\{\mathrm{TP}\}$.

Table 3–6 demonstrates the efficiency of the adaptive ME-PC method by comparing the number of deterministic simulations required by all the methods to compute the averages and the standard deviations, and by nonadaptive gPC collocation method with TP integration ($\mathrm{k}=\{\mathrm{TP}\}$) and the adaptive ME-PC method ($\mathrm{k}=\{\text{A-}10^{-1},\text{A-}10^{-2}\}$) to construct $V_C^{\mathrm{Re,k}}(\mathbf{x})$, $V_C^{\mathrm{Im,k}}(\mathbf{x})$, and $V_C^{\mathrm{Abs,k}}(\mathbf{x})$. It should be noted here that the results of a more accurate nonadaptive gPC collocation method with TP integration are not included here since using three and four point (more accurate) Gauss-Legendre rule in each dimension would require a total of 59049 and 1048576 deterministic simulations, respectively.

3.3.2 Microwave Amplifier

Next, the adaptive ME-PC method is used to compute the statistical moments and extract the pdfs of the voltage coupled to the output port of a microwave amplifier. Matching microstrip stubs are located on a $0.7874\,\mathrm{mm}$ thick dielectric substrate with

relative permittivity $\varepsilon_r = 2.33$; the substrate is backed by a perfect electrically conducting ground plane of size $17.526\,\text{mm} \times 16.256\,\text{mm}$ [62]. The stubs are connected by a GaAs MESFET amplifier [Figure 3–10]; the small signal circuit model of the amplifier, which is extracted from its large-signal model under bias conditions $V_{g's'} = -0.81\,\text{V}$ and $V_{d's'} = 6.4\,\text{V}$, is shown in Figure 3–11. Two different EMI scenarios are considered: the amplifier is (i) unshielded and (ii) located in a shielding box [Figure 3–12]. In both scenarios, the structure is excited by a θ-polarized plane wave propagating in the $\hat{\mathbf{k}} = \hat{\mathbf{x}}\sin\theta + \hat{\mathbf{z}}\cos\theta$ direction. The amplitude of the excitation's electric field is $1\,\text{V/m}$ and the frequency is $6\,\text{GHz}$. Seven variables ($N_{\text{dof}} = 7$) parameterize the uncertainty in the problem: the values of parasitic inductors at the gate, drain, and source (L_g, L_d, and L_s), the values of parasitic resistors at the gate, drain and source, (R_g, R_d, and R_s), and the angle of arrival of the plane wave (θ) (i.e., $\mathbf{x} = \left[L_g, L_d, L_s, R_g, R_d, R_s, \theta \right]$).

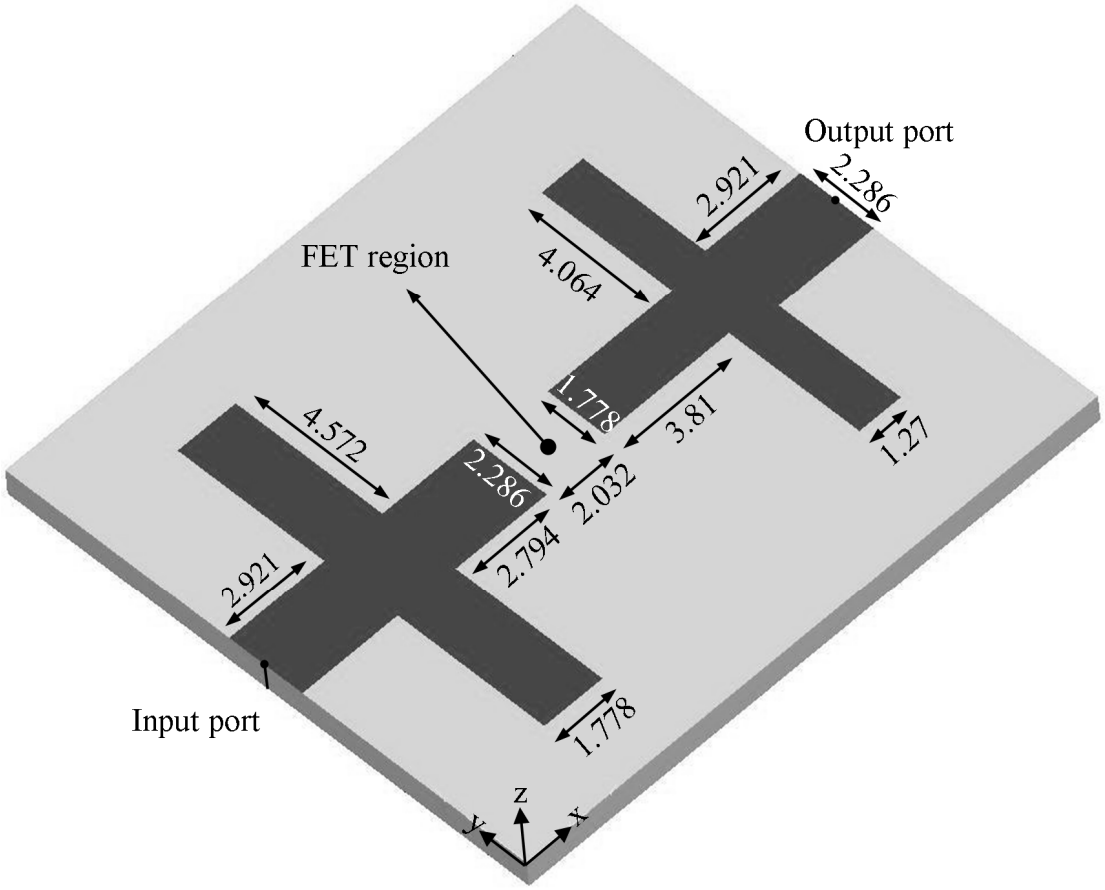

Figure 3–10 Geometry description of the microwave amplifier (all dimensions are in mm).

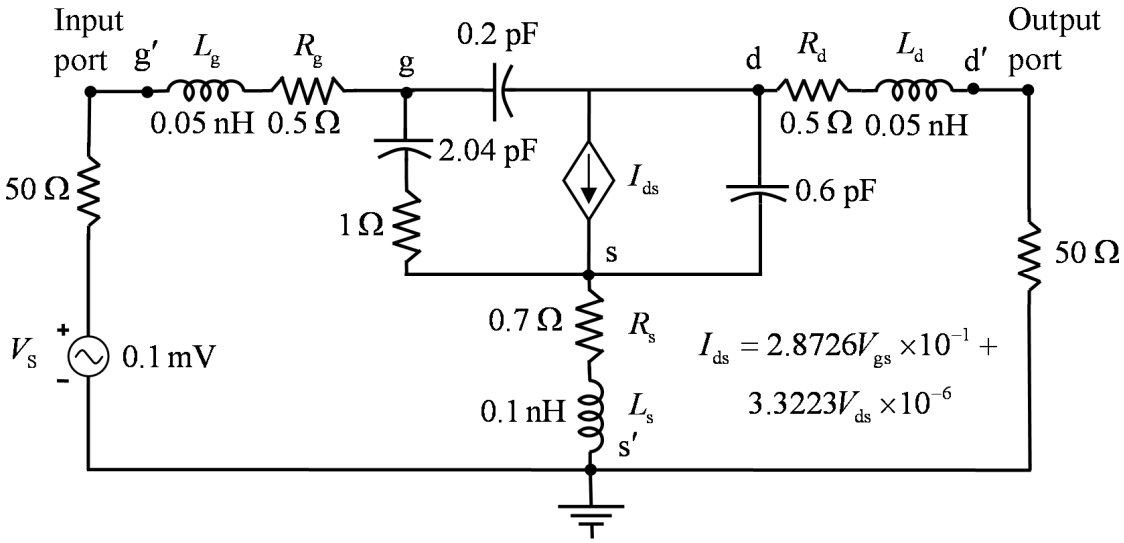

Figure 3–11 Small-signal circuit model of the MESFET amplifier.

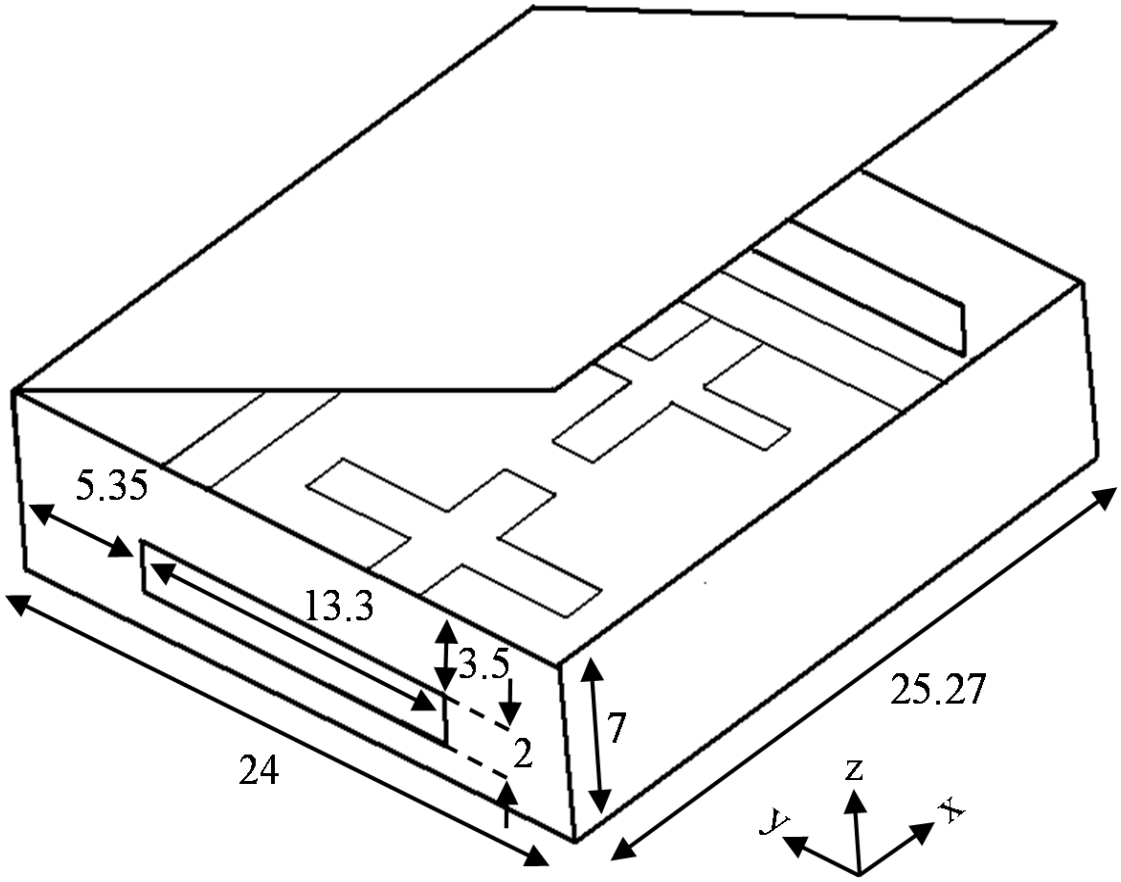

Figure 3–12 Geometry description of the shielding enclosure (all dimensions are in mm) (ceiling lifted up for illustration).

The random variables L_g, L_d, L_s, R_g, R_d, R_s, and θ are assumed normally distributed with means and standard deviations (μ^i, σ^i), $(i = 1,\ldots,7)$: $(0.05, 0.001)$ nH, $(0.05, 0.001)$ nH, $(0.1, 0.002)$ nH , $(0.5, 0.015)$ Ω, $(0.5, 0.015)$ Ω, $(0.7, 0.021)$ Ω, and $(127.5, 4.5)°$, respectively. The observable is the magnitude of the voltage coupled to the output port of the microwave amplifier, $V_{\mathrm{O}}^{\mathrm{Abs}}(\mathbf{x})$.

The pdf of $V_{\mathrm{O}}^{\mathrm{Abs}}(\mathbf{x})$ is estimated via a $25\,000$-point MC simulation performed using $V_{\mathrm{O}}^{\mathrm{Abs,k}}(\mathbf{x})$, $\mathrm{k} = \{\mathrm{BF,TP,A\text{-}10^{-1},A\text{-}10^{-2}}\}$. $V_{\mathrm{O}}^{\mathrm{Abs}}(\mathbf{x})$, $\mathrm{k} = \{\mathrm{BF,TP}\}$, are computed by

brute-force MC and by nonadaptive gPC surrogate model obtained using TP integration rule (with three Gauss-Legendre points in each dimension). Moreover, $V_{\mathrm{O}}^{\mathrm{Abs}}(\mathbf{x})$, $\mathrm{k}=\left\{\text{A-}10^{-1},\text{A-}10^{-2}\right\}$, are obtained from surrogate models constructed using the adaptive ME-PC method with $\beta=\left\{10^{-1},10^{-2}\right\}$. In Figure 3–13, the pdfs obtained via $V_{\mathrm{O}}^{\mathrm{Abs,A\text{-}10^{-2}}}(\mathbf{x})$ for the unshielded and shielded amplifiers, are compared. As expected, the pdf obtained via $V_{\mathrm{O}}^{\mathrm{Abs,A\text{-}10^{-2}}}(\mathbf{x})$ for the unshielded microwave amplifier is concentrated around higher values of the observable.

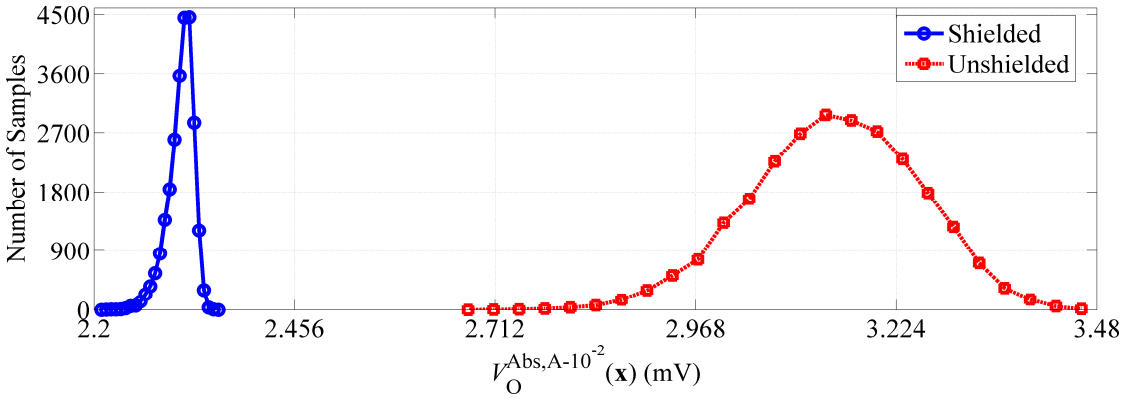

Figure 3–13 The pdfs obtained via $V_{\mathrm{O}}^{\mathrm{Abs,A\text{-}10^{-2}}}(\mathbf{x})$ for the shielded and unshielded amplifiers.

To demonstrate the accuracy of the estimated pdfs, the L-2 norm of the relative error between $V_{\mathrm{O}}^{\mathrm{Abs,BF}}(\mathbf{x})$ and $V_{\mathrm{O}}^{\mathrm{Abs,k}}(\mathbf{x})$ is computed using

$$err^{\mathrm{k}}=\sqrt{\sum_{i=1}^{25\,000}\left[V_{\mathrm{O}}^{\mathrm{Abs,k}}(\mathbf{x}_i)-V_{\mathrm{O}}^{\mathrm{Abs,BF}}(\mathbf{x}_i)\right]^2\Big/\sum_{i=1}^{25\,000}V_{\mathrm{O}}^{\mathrm{Abs,BF}}(\mathbf{x}_i)^2},\ \mathrm{k}=\left\{\mathrm{TP},\text{A-}10^{-1},\text{A-}10^{-2}\right\},\quad(3.29)$$

where $\mathbf{x}_i$ is the evaluation point dictated by the brute-force MC method.

	Shielded		Unshielded	
superscript (k)	err^{k}	Number of deterministic	err^{k}	Number of deterministic

		simulations		simulations
k = TP	4.7551×10^{-3}	2187	3.8382×10^{-3}	2187
k = A-10^{-1}	8.8366×10^{-4}	423	8.7892×10^{-4}	705
k = A-10^{-2}	9.6464×10^{-5}	1833	1.9046×10^{-4}	1833

Table 3–7 L-2 norm of relative error between $V_{\mathrm{O}}^{\mathrm{Abs,BF}}(\mathbf{x})$ and $V_{\mathrm{O}}^{\mathrm{Abs,k}}(\mathbf{x})$ and the number of deterministic simulations needed for constructing $V_{\mathrm{O}}^{\mathrm{Abs,k}}(\mathbf{x})$.

Table 3–7 presents err^{k}, $\mathrm{k}=\left\{\mathrm{TP},\mathrm{A\text{-}10^{-1}},\mathrm{A\text{-}10^{-2}}\right\}$, and the number of deterministic simulations required to construct $V_{\mathrm{O}}^{\mathrm{Abs,k}}(\mathbf{x})$, $\mathrm{k}=\left\{\mathrm{TP},\mathrm{A\text{-}10^{-1}},\mathrm{A\text{-}10^{-2}}\right\}$. It is clear from Table 3–7 that $V_{\mathrm{O}}^{\mathrm{Abs,k}}(\mathbf{x})$, $\mathrm{k}=\left\{\mathrm{A\text{-}10^{-1}},\mathrm{A\text{-}10^{-2}}\right\}$, are more accurate than $V_{\mathrm{O}}^{\mathrm{Abs,TP}}(\mathbf{x})$ even though their construction required far fewer deterministic simulations.

3.3.3 Tire Pressure Monitoring Sensor

Finally, the adaptive ME-PC method is used to statistically characterize the magnetic field induced on a sensor transponder due to an initiator coil antenna. The sensor transponder and the initiator coil are parts of a tire pressure monitoring (TPM) system [71]. The TPM system regularly monitors the air pressure of the tires and warns the driver when a tire is under-inflated. The most widely used TPM system uses a battery-operated small sensor transponder mounted on the car's tire rim behind the valve stem. The sensor transponder transmits the tire pressure and the temperature information to the central TPM receiver via a wireless link; a low-frequency coil antenna is often used to initiate the data transmission from the sensor transponder [71]. In the simulations, the initiator coil is modeled as a magnetic dipole with moment $0.073\ \mathrm{A\text{-}m^2}$ at frequency $125\ \mathrm{kHz}$; it is located within the car's fender, just above the tire [Figure 3–14]. The TPM sensor is located behind the valve stem. The ground is modeled as a lossy sheet with

conductivity 10^{-2} S/m as described in [72]. The tire is assumed not to have any effect on the wireless link between the initiator coil and the sensor transponder [73]; hence it is not included in the simulation. Two different scenarios are considered.

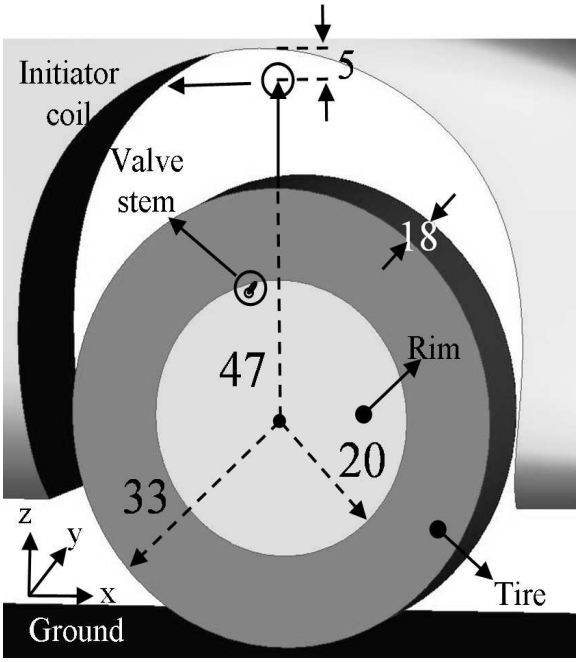

Figure 3–14 Description of the TPM sensor-initiator coil configuration (TPM sensor is placed behind the valve stem) (all dimensions are in cm).

3.3.3.1 Single Car

The TPM sensor-initiator coil configuration described above and shown in Figure 3–14 is located within the fender on the front passenger side of the car [Figure 3–15]. In this scenario, two parameters characterize the uncertainty ($N_{\text{dof}} = 2$): the rim's rotation and steering angles θ and ϕ (i.e., $\mathbf{x} = [\theta, \phi]$). The random variables θ and ϕ are assumed to be uniformly distributed in the ranges $[a^i, b^i]$, $i = 1, 2$; $[0, 360]^\circ$ and $[-45, 45]^\circ$, respectively. The observable is the magnitude of the magnetic field induced at the location of the TPM sensor, $H_1^{\text{Abs}}(\mathbf{x})$. The surrogate model of observable,

$H_1^{\text{Abs,k}}(\mathbf{x})$, is created using the adaptive ME-PC method with $\beta = 10^{-2}$, $\text{k} = \{\text{A-}10^{-2}\}$. Figure 3–16 presents $H_1^{\text{Abs,A-}10^{-2}}(\mathbf{x})$; furthermore, the cdfs obtained via $H_1^{\text{Abs,A-}10^{-2}}(\mathbf{x})$ and $H_1^{\text{Abs,A-}10^{-2}}\left(\mathbf{x}\big|_{\phi=0^\circ}\right)$ are compared in Fig. 4(d). During the construction of $H_1^{\text{Abs,A-}10^{-2}}(\mathbf{x})$, it is assumed that the dependence of $H_1^{\text{Abs}}(\mathbf{x})$ on θ is periodic. The Dirichlet kernel is used to increase the efficiency of the adaptive ME-PC method as described in Section 3.2.3; the Dirichlet kernel-accelerated adaptive ME-PC method required only 7 deterministic simulations.

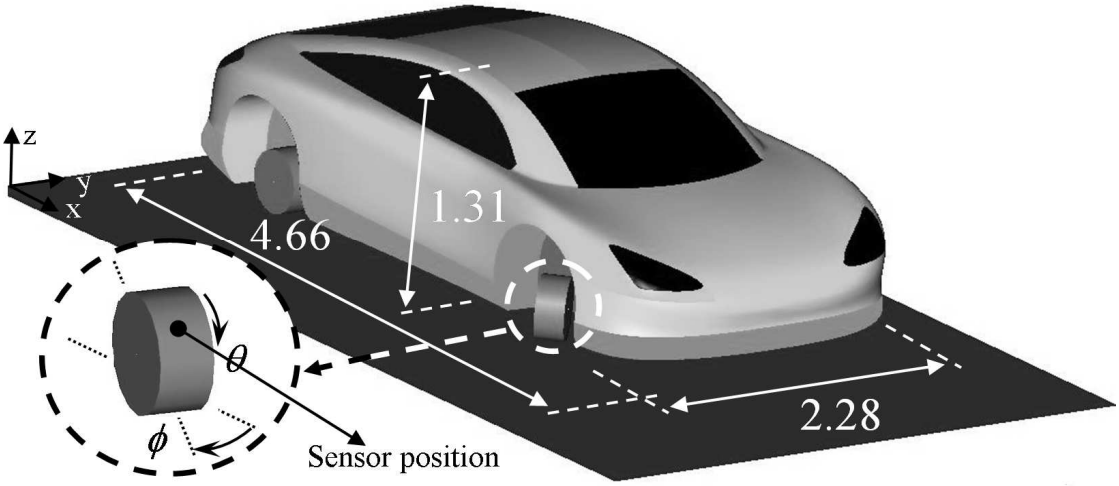

Figure 3–15 Geometry description of the car (all dimensions are in m) and the description of the random variables.

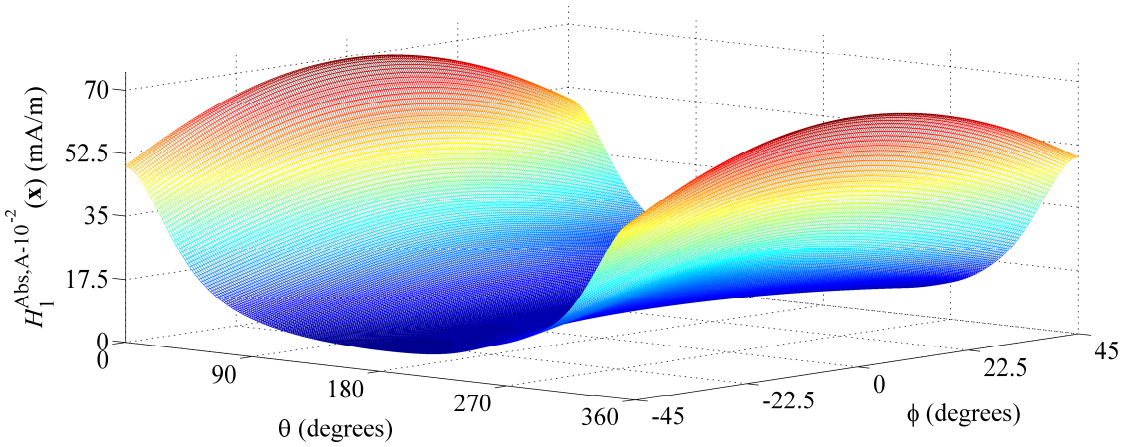

Figure 3–16 $H_1^{\text{Abs,A-10}^{-2}}(\mathbf{x})$ constructed using the Dirichlet kernel-accelerated adaptive ME-PC method with $\beta = 10^{-2}$.

To verify the accuracy of the proposed approach, the L-2 norm of the relative error between $H_1^{\text{Abs,A-10}^{-2}}(\mathbf{x})$ and $H_1^{\text{Abs}}(\mathbf{x})$ is computed using

$$err = \sqrt{\sum_{i=1}^{100}\left[H_1^{\text{Abs,A-10}^{-2}}(\mathbf{x}_i) - H_1^{\text{Abs}}(\mathbf{x}_i)\right]^2 \Big/ \sum_{i=1}^{100} H_1^{\text{Abs}}(\mathbf{x}_i)^2}, \tag{3.30}$$

where $\mathbf{x}_i$ is a randomly chosen evaluation point, and found to be $err = 2.7484\times10^{-3}$.

Several observations about the results are in order:

It is clear from Figure 3–16 that on a given θ cut, $H_1^{\text{Abs,A-10}^{-2}}(\mathbf{x})$ decreases while the rim is steered away from its normal position ($\phi = 0°$).

Figure 3–17 demonstrates that although the maximum values of $H_1^{\text{Abs,A-10}^{-2}}(\mathbf{x})$ and $H_1^{\text{Abs,A-10}^{-2}}\left(\mathbf{x}\big|_{\phi=0°}\right)$ are nearly identical, the minimum value of $H_1^{\text{Abs,A-10}^{-2}}(\mathbf{x})$ is 3 mA/m less than the minimum value of $H_1^{\text{Abs,A-10}^{-2}}\left(\mathbf{x}\big|_{\phi=0°}\right)$.

It should be noted here that the cdfs obtained via $H_1^{\text{Abs,A-10}^{-2}}(\mathbf{x})$ and $H_1^{\text{Abs,A-10}^{-2}}\left(\mathbf{x}\big|_{\phi=0^\circ}\right)$ are estimated using a 10000 - point MC simulation. Computation of the cdfs would not be possible without the surrogate model constructed using the Dirichlet kernel enhanced adaptive ME-PC method, due to long CPU times required by the deterministic EM simulator.

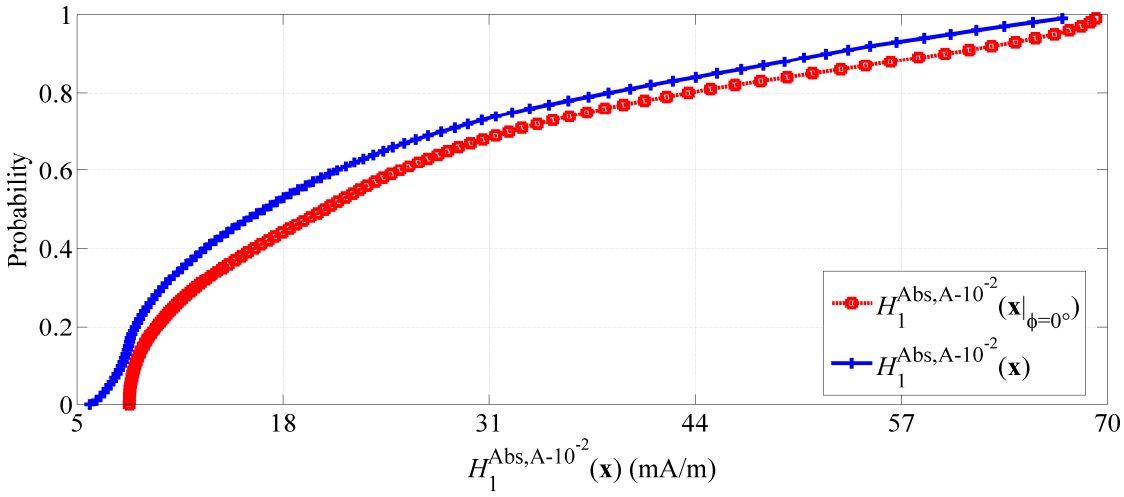

Figure 3–17 The cdfs obtained via $H_1^{\text{Abs,A-10}^{-2}}(\mathbf{x})$ and $H_1^{\text{Abs,A-10}^{-2}}\left(\mathbf{x}\big|_{\phi=0^\circ}\right)$.

3.3.3.2 Two Cars

In this scenario, two cars, both identical to the one used in the previous scenario, are positioned adjacent to each other [Figure 3–18]. The cars' front passenger side fenders are parallel to each other along x - and z - directions while the spacing between the fenders is $0.5\,\text{m}$ along the y - direction. Initiator coils are placed within fenders on the front passenger side of both cars. The TPM sensor is mounted on the rim on the first car's front passenger side.

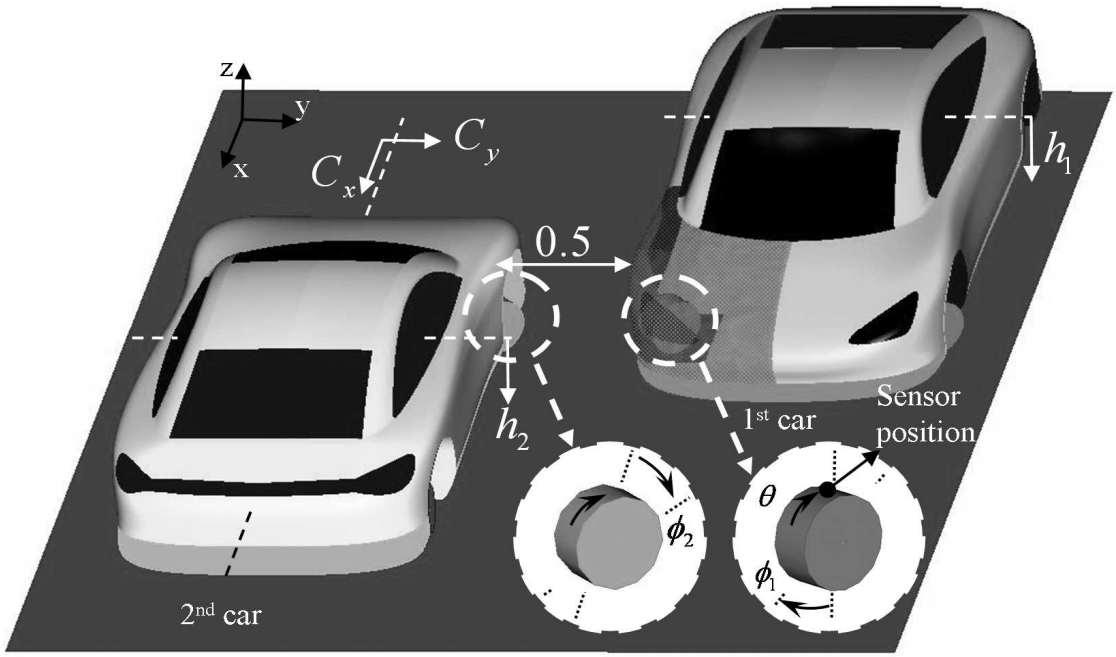

Figure 3–18 Geometry description of the cars (all dimensions are in m) and the description of the random variables.

The uncertainties in this configuration are characterized by seven random variables ($N_{\text{dof}} = 7$): the first car's rim rotation and steering angles θ and ϕ_1, the second car's rim steering angle ϕ_2, the shift in the second car's location along the x- direction C_x, the shift in the second car's location along y- direction C_y, the shift in the first car's location along the z- direction h_1, and the shift in the second car's location along z- direction h_2 (i.e., $\mathbf{x} = \left[\theta, \phi_1, \phi_2, C_x, C_y, h_1, h_2\right]$). The random variables θ, ϕ_1, ϕ_2, C_x, C_y, h_1, and h_2 are assumed to be uniformly distributed in the ranges $\left[a^i, b^i\right]$, $i = 1, \ldots, 7$; $[0, 360]^\circ$, $[-45, 45]^\circ$, $[-45, 45]^\circ$, $[-0.2, 0.2]\,\text{m}$, $[0, 0.4]\,\text{m}$, $[-2.5, 2.5]\,\text{cm}$, and $[-2.5, 2.5]\,\text{cm}$, respectively. The observable is the magnitude of the magnetic field induced at the location of the TPM sensor on the first car, $H_2^{\text{Abs}}(\mathbf{x})$. The surrogate model

of observable, $H_2^{\text{Abs,k}}(\mathbf{x})$, is constructed using the adaptive ME-PC method with $\beta = 10^{-2}$, $\text{k} = \{\text{A-}10^{-2}\}$. Figure 3–19 compares the cdfs obtained via $H_1^{\text{Abs,A-}10^{-2}}(\mathbf{x})$ and $H_2^{\text{Abs,A-}10^{-2}}(\mathbf{x})$. Just like $H_1^{\text{Abs,A-}10^{-2}}(\mathbf{x})$, $H_2^{\text{Abs,A-}10^{-2}}(\mathbf{x})$ is also constructed using the Dirichlet kernel-accelerated adaptive ME-PC method; the hybrid method required only 545 deterministic simulations to construct $H_2^{\text{Abs,A-}10^{-2}}(\mathbf{x})$.

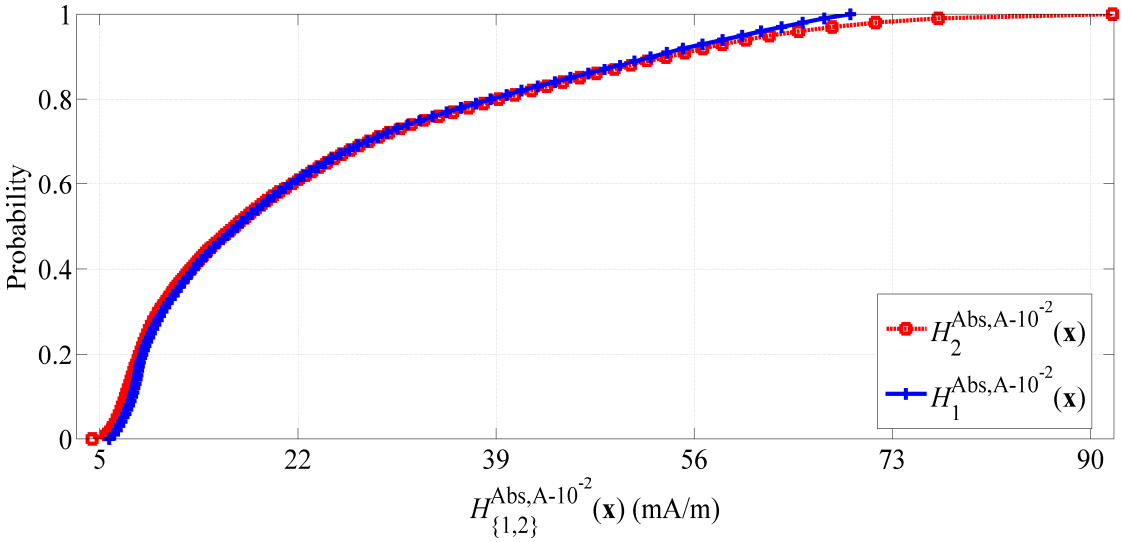

Figure 3–19 The cdfs obtained via $H_1^{\text{Abs,A-}10^{-2}}(\mathbf{x})$ and $H_2^{\text{Abs,A-}10^{-2}}(\mathbf{x})$.

Several observations about the results presented above are in order:

Figure 3–19 demonstrates that the maximum value of $H_2^{\text{Abs,A-}10^{-2}}(\mathbf{x})$ is 22 mA/m more than the maximum value of $H_1^{\text{Abs,A-}10^{-2}}(\mathbf{x})$ while the minimum values of $H_1^{\text{Abs,A-}10^{-2}}(\mathbf{x})$ and $H_2^{\text{Abs,A-}10^{-2}}(\mathbf{x})$ are nearly identical. In addition, the probability of $H_2^{\text{Abs,A-}10^{-2}}(\mathbf{x})$ being less than or equal to 69 mA/m (which is the maximum value of $H_1^{\text{Abs,A-}10^{-2}}(\mathbf{x})$) is 0.975.

Like the previous example, the cdf obtained via $H_2^{\text{Abs,A-}10^{-2}}(\mathbf{x})$ is estimated using a 10000- point MC simulation. Just like in the previous example, computation of the cdf would not be possible without the surrogate model constructed using the Dirichlet kernel enhanced adaptive ME-PC method.

CHAPTER 4
STATISTICAL CHARACTERIZATION OF TM WAVE PROPAGATION IN MINE ENVIRONMENTS

4.1 Introduction

Underground mines require reliable and effective communication and tracking systems during routine operations and emergency events. The MINER Act of 2006 [74] requires mine operators to implement wireless communication systems capable of surviving disasters and supporting two-way post-event communication and tracking functions. The design of such systems benefits from simulation frameworks capable of statistically characterizing wave propagation in mine tunnels and galleries occupied by miners, equipment, trolleys, and rails, and possibly obstructed by debris from a cave-in. Ideally, these frameworks should provide statistics of key observables (e.g., the pdf of the electric (E) field at a receiver, or any other quantity deemed important in the design of a wireless communication network), given uncertainty in the mine geometry, configuration, and excitation. Examples of such uncertainties include the material properties and surface roughnesses of the (lossy) rock, earth, and mine ore that surround the mine tunnels and galleries; the shape, material composition, and positions of the mining equipment, trolleys, and rails; and the positions and orientations of transmitting and receiving antennas.

Present simulation techniques for analyzing wave propagation in mines mostly rely on modal analysis [75], ray-tracing methods [76], or cascaded-impedance schemes [77]. These techniques neither account for the presence of miners and their equipment nor yield statistics of pertinent observables. In practice, the statistical characterization of wave propagation in mine environments is often carried out via measurement campaigns in non-active and empty mine tunnels [78]. However, there is a growing interest in characterization of wave propagation in active and non-empty mine tunnels [79, 80]. In [79], the effect of human body on the wave propagation in mine galleries is experimentally quantified for multiple input multiple output ultra-wideband communication systems. In [80], the researchers show their interest in quantifying the influence of locations of miners, mine carts, and antennas on to the wave propagation characteristics that should be accurately determined before installing wireless communication links in mine tunnels.

In this chapter, a simulation framework leveraging the ME-PC method described in Section 3.2.2 is used for statistically characterizing transverse magnetic (TM) wave propagation in active and non-empty mine tunnels. The ME-PC scheme employs a novel domain decomposition (DD) integral equation based deterministic simulator to (i) compute observables for various mine configurations represented by selected collocation points in the random domain and (ii) subsequently construct compact multivariate polynomial surrogate models that accurately approximate the observables, yet are computationally cheap to evaluate. Finally, the surrogate models are used in lieu of the computationally expensive deterministic simulator to extract pertinent statistics via the MC method. While in principle any deterministic simulator could be used to construct the

observables' surrogate models, DD strategy is especially useful for characterizing observables in mine environments that oftentimes span hundreds or even thousands of wavelengths. The DD method divides tunnels and galleries into subdomains and characterizes each of them independently prior to obtaining a global inter-domain solution by assembling subdomain solutions. The DD approach significantly expedites the computation of the observables for each mine configuration selected by the ME-PC scheme as it only requires re-characterization of the propagation properties of mine sections subject to uncertainty in configuration or composition. The details of DD integral equation based deterministic simulator could be found in [81]; only the application of the proposed simulation framework to the TM wave propagation in mine tunnels is illustrated here.

4.2 Application to the Wave Propagation in Mine Environments

This section illustrates the application of proposed framework to the statistical characterization of TM wave propagation in various mine tunnel configurations. In all examples considered here, the transmitters are unit sources operating at 900 MHz, the relative permittivity of the tunnel walls is $5-j$, and the rough tunnel walls are generated using the code given in [82] by setting the correlation length to $0.25\,\mathrm{m}$ and root mean square height to $0.1\,\mathrm{m}$. The observables are the magnitudes of the E-field's *z*-component, $\left|E_z(\mathbf{x})\right|$, computed at various receiver points, using two-dimensional DD-based deterministic simulator pertinent to the propagation of vertically polarized fields. The error in surrogate model is computed using

$$err^{\mathrm{k}} = \sqrt{\sum_{i=1}^{160}\left(\left|E_z(\mathbf{x}_i)\right| - \left|E_z^{\mathrm{k}}(\mathbf{x}_i)\right|\right)^2 \Big/ \sum_{i=1}^{160}\left|E_z(\mathbf{x}_i)\right|^2}, \tag{4.1}$$

where $\left|E_z^{\mathrm{k}}(\mathbf{x})\right|$ is the surrogate model generated using the ME-PC method with $\beta = \mathrm{k}$ and $\tau_1 = \tau_2 = 0.5$ and $\mathbf{x}_i$ is the randomly chosen evaluation point. The approximation to the pdf of $\left|E_z(\mathbf{x})\right|$ is generated by running a 1,000,000 point MC on $\left|E_z^{\mathrm{k}}(\mathbf{x})\right|$.

4.2.1 L-Shape Mine Tunnel

For the first example, an L-shape mine tunnel configuration [Figure 4–1] is considered. The mine tunnel geometry is divided into 14 physical subdomains [Figure 4–1], Ω_i, $i = 1,\ldots,14$. The transmitter is positioned at $(0,0)$ m in Ω_1. Each of Ω_2 and Ω_6 houses two perfectly electric conducting (PEC) carts while each one of Ω_i, $i \in \{4,8,11,13\}$, houses one PEC cart; all carts are modeled as $1.5\,\mathrm{m} \times 1\,\mathrm{m}$ rectangles. The center positions of the two carts in Ω_2, the one cart in Ω_4, and the first cart in Ω_6 are represented by (cx_j, cy_j) $j = 1,\ldots,4$, respectively. Each domain also houses two pillars modeled by cylinders with $0.15\,\mathrm{m}$ radius. Additionally, to model a (possible) partial collapse, a half cylinder with radius r_c is introduced in Ω_3; the half cylinder is centered at $(34.7,-2)$ m. Two different scenarios are considered.

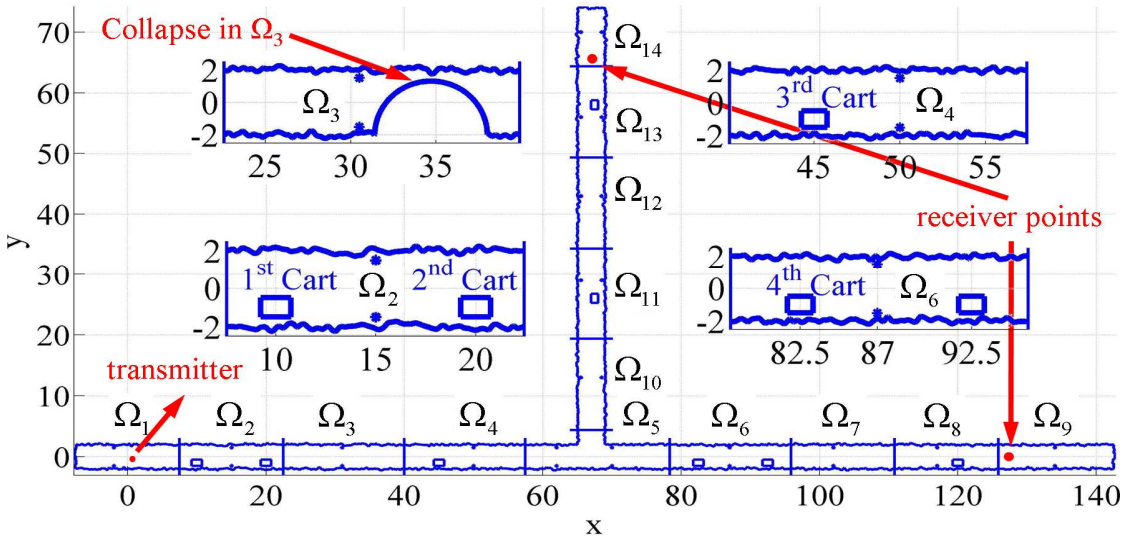

Figure 4–1 Layout of an L-shape tunnel.

4.2.1.1 PEC Carts

In the first scenario, cx_j and cy_j, $j=1,\ldots,4$, are random variables uniformly distributed in $[10,10.075]$ m, $[20,20.075]$ m, $[45,45.075]$ m, $[82.5,82.575]$ m, $[-1,-1.075]$ m, $[-1,-1.075]$ m, $[-1,-1.075]$ m, and $[-1,-1.075]$ m, respectively, while r_c is set to 0 m ($\mathbf{x}=[cx_1,\ldots,cx_4,cy_1,\ldots,cy_4]$, $N_{\text{dof}}=8$). The observables, $|E_z(\mathbf{x})|$, are computed at receivers located at $(127,0)$ m (in Ω_9) and $(66.5,67)$ m (in Ω_{14}). The surrogate models $|E_z^{\text{k}}(\mathbf{x})|$, $\text{k}=\{5\times10^{-2},10^{-2}\}$, are constructed via the ME-PC method with $\beta=\{5\times10^{-2},10^{-2}\}$; the ME-PC method uses the Gauss-Legendre quadrature based SG integration method (with $l=2$) to compute the coefficients of local gPC expansions with $p=2$ (see the definition of l for SG integration method in Section 2.2.3.2). To obtain $|E_z^{\text{k}}(\mathbf{x})|$, $\text{k}=\{5\times10^{-2},10^{-2}\}$, the proposed method required $\{3363,12567\}$ deterministic simulations. At each deterministic simulation, the TM wave propagation in

only subdomains Ω_2, Ω_4, and Ω_6 is re-characterized since the positions of carts in these domains are the only random variables. The maxima of err^{k}, $\mathrm{k}=\{5\times10^{-2},10^{-2}\}$, are computed as $\{1.0153,0.6718\}\times10^{-2}$. The pdfs of $|E_z(\mathbf{x})|$ (approximated by those of $|E_z^{\mathrm{k}}(\mathbf{x})|$) computed at receivers in Ω_9 and Ω_{14} match with Weibull and gamma distributions, respectively [Figure 4–2 (a)-(b)].

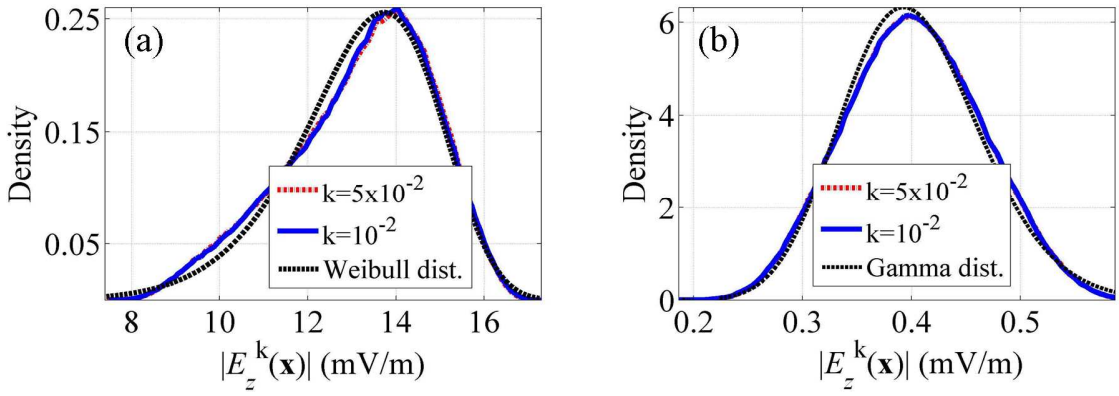

Figure 4–2 Empirical pdfs of $|E_z^{\mathrm{k}}(\mathbf{x})|$, $\mathrm{k}=\{5\times10^{-2},10^{-2}\}$, at receiver points (a) in Ω_9 and (b) in Ω_{14} and their best fitting distributions (8D Case).

4.2.1.2 Partial Collapse

In the second scenario, r_c is a random variable uniformly distributed in $[0.2,3.7]\mathrm{m}$, cx_j and cy_j, $j=1,\ldots,4$, are set to their mean values ($\mathbf{x}=[r_c]$, $N_{\mathrm{dof}}=1$). The observables, $|E_z(\mathbf{x})|$, are computed on grids of receiver points in Ω_4 and Ω_{10} with 0.075 m spacing along each dimension. The surrogate models $|E_z^{\mathrm{k}}(\mathbf{x})|$, $\mathrm{k}=\{10^{-1},10^{-2}\}$, are constructed via the ME-PC method with $\beta=\{10^{-1},10^{-2}\}$; The ME-PC method uses 12-point Gauss-Legendre quadrature rule to obtain the coefficients of local gPC expansions with $p=11$. To obtain $|E_z^{\mathrm{k}}(\mathbf{x})|$, $\mathrm{k}=\{10^{-1},10^{-2}\}$, the proposed method

required $\{156, 420\}$ deterministic simulations. For each deterministic simulation, only Ω_3 is re-characterized since r_c is the only random variable. The maxima of err^{k}, $\mathrm{k} = \{10^{-1}, 10^{-2}\}$, are computed as $\{7.3063, 1.6122\} \times 10^{-2}$. The pdfs of $|E_z(\mathbf{x})|$ (approximated by those of $|E_z^{\mathrm{k}}(\mathbf{x})|$) at the receiver grid points in Ω_4 and Ω_{10} have very long tails [Figure 4–3 (a)-(b)] and are not easily approximated by any classical distribution; this can be explained by the fact that the half cylinder interrupts the TM wave propagation significantly when $r_c > 3.4$ m. To illustrate the change in $|E_z(\mathbf{x})|$ due to r_c, $|E_z(\mathbf{x})|$ at receiver grid points in Ω_4, Ω_5, Ω_6, and Ω_{10} (with 0.075 m spacing along each dimension) are plotted for mine configurations with $r_c = 2$ m, $r_c = 2.55$ m, $r_c = 3$ m, and $r_c = 3.55$ m [Figure 4–4 (a)-(d)].

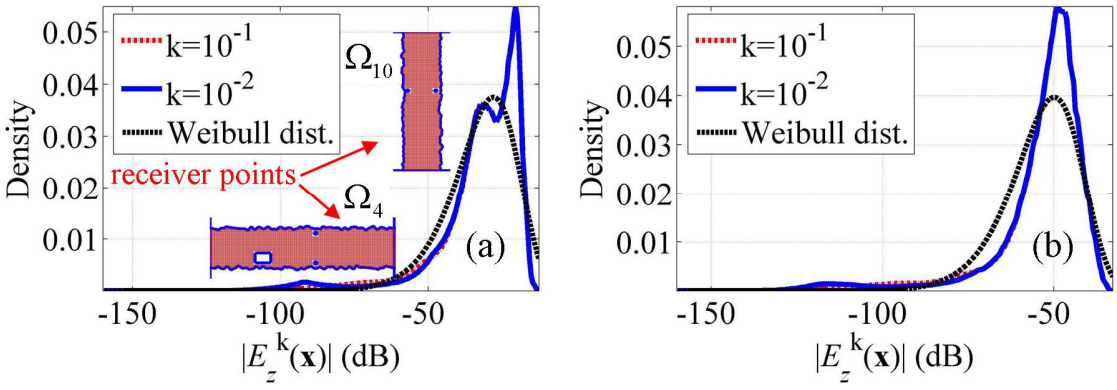

Figure 4–3 Empirical pdfs of $|E_z^{\mathrm{k}}(\mathbf{x})|$, $\mathrm{k} = \{10^{-1}, 10^{-2}\}$, on grids of receiver points selected (d) in Ω_4 and (e) in Ω_{10} (in dB scale) and their best fitting Weibull distributions (1D Case).

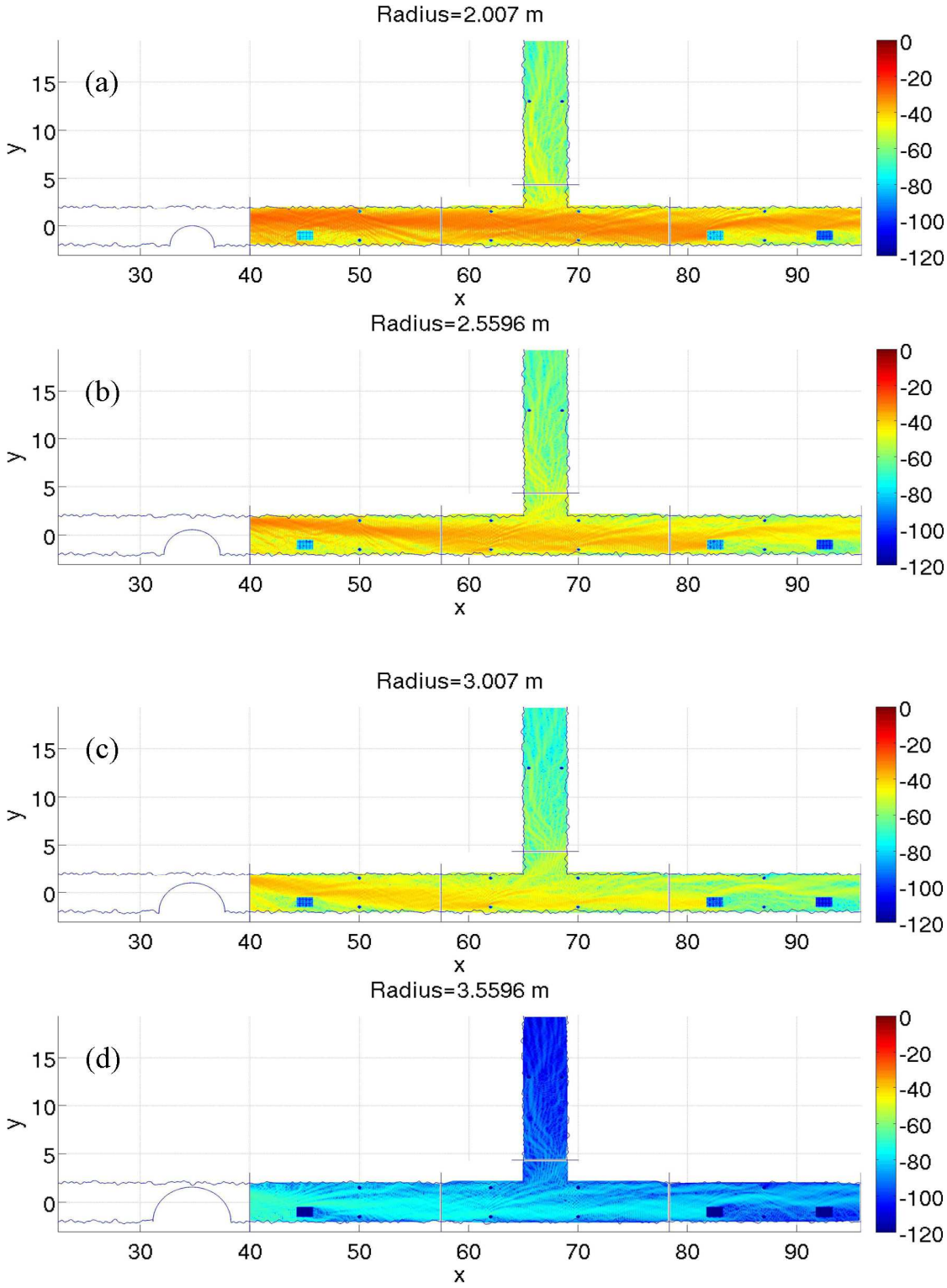
Radius=2.007 m
(a)
Radius=2.5596 m
(b)
Radius=3.007 m
(c)
Radius=3.5596 m
(d)
y
x
0
-20
-40
-60
-80
-100
-120
15
10
5
0
30
40
50
60
70
80
90

Figure 4–4 Plots of $|E_z(\mathbf{x})|$ on grids of receiver points selected in Ω_4, Ω_5, Ω_6, and Ω_{10} (in dB scale) when (a) $r_c = 2.0$ m, (b) $r_c = 2.5$ m, (c) $r_c = 3.0$ m, and (d) $r_c = 3.5$ m (1D Case).

4.2.2 Realistic Mine Tunnel

For the second example, a more realistic mine tunnel configuration [Figure 4–5] is considered. The mine tunnel geometry is divided into 28 physical subdomains, Ω_i, $i = 1, \ldots, 28$. The *x* and *y* coordinates of the transmitter's position, which is located in Ω_1, r_x and r_y, are random variables uniformly distributed in $[1.925, 2.075]$ m and $[1.925, 2.075]$ m, respectively ($\mathbf{x} = [r_x, r_y]$, $N_{\text{dof}} = 2$). The observables, $|E_z(\mathbf{x})|$, are computed on grids of receiver points in Ω_9, Ω_{10}, Ω_{11}, and Ω_{12} with 0.075 m spacing along each dimension.

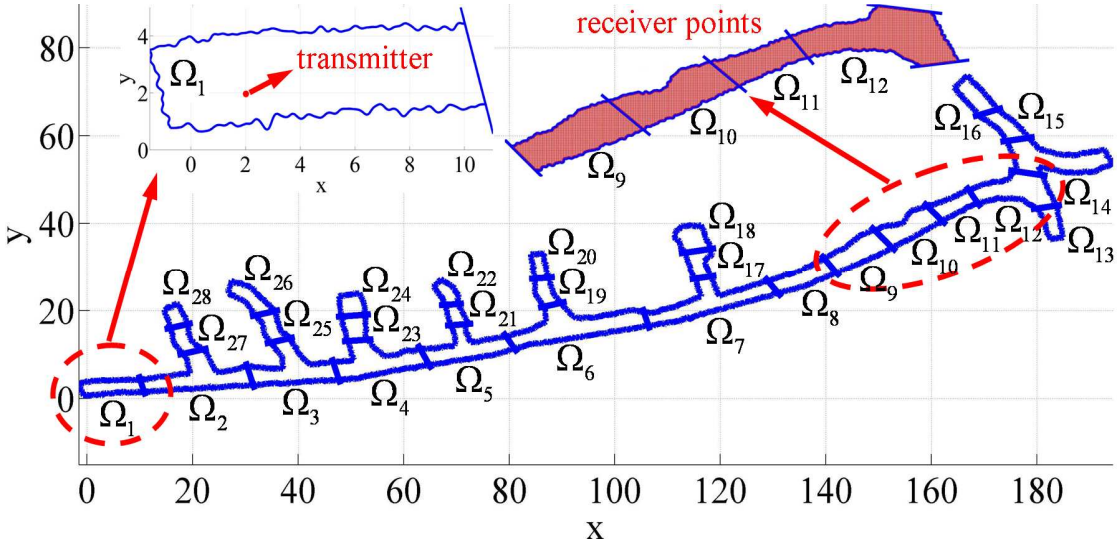

Figure 4–5 Layout of a realistic mine tunnel.

Means and standard deviations of $|E_z(\mathbf{x})|$ at receiver grid points [Figure 4–6 (a)-(b)] are computed by (3.17) and (3.20) using the ME-PC method with $\beta = 10^{-2}$; the ME-PC method uses the TP integration method with five Gauss-Legendre points in each

dimension to compute the coefficients of local gPC expansions with $p=4$. The surrogate models $\left|E_z^{\mathrm{k}}(\mathbf{x})\right|$, $\mathrm{k}=\left\{10^{-1},10^{-2}\right\}$, are constructed via the ME-PC method with $\beta=\left\{10^{-1},10^{-2}\right\}$, which required $\{125,1025\}$ deterministic simulations. Each deterministic simulation only re-characterizes TM wave propagation in subdomain Ω_1 since r_x and r_y are the only random variables. The maxima of err^{k}, $\mathrm{k}=\left\{10^{-1},10^{-2}\right\}$, are computed as $\{5.3734,0.5272\}\times10^{-2}$. The pdfs of $\left|E_z(\mathbf{x})\right|$ (approximated by those of $\left|E_z^{\mathrm{k}}(\mathbf{x})\right|$) computed at receiver point grids in Ω_9, Ω_{10}, Ω_{11}, and Ω_{12} match log-normal distributions [Figure 4–7 (a)-(d)].

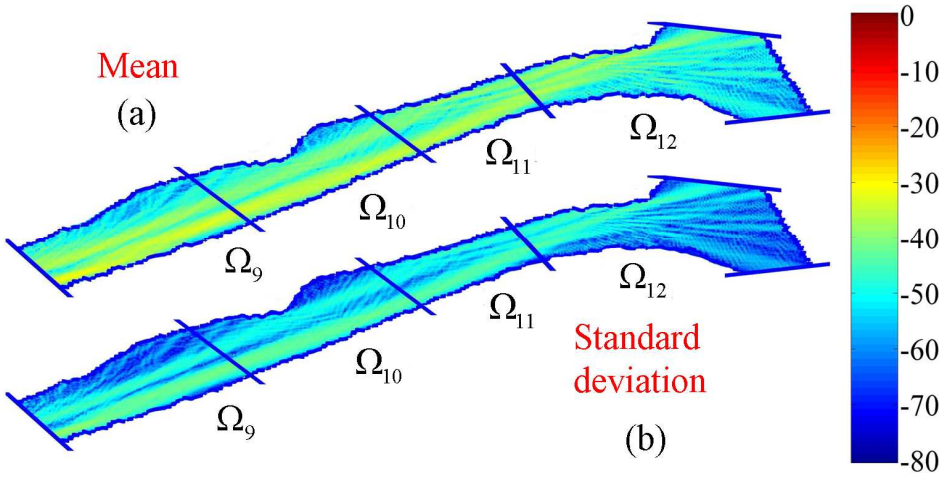

Figure 4–6 (a) Mean and (b) standard deviation of $\left|E_z^{\mathrm{k}}(\mathbf{x})\right|$, $\mathrm{k}=\left\{10^{-2}\right\}$, on grids of receiver points selected in Ω_9, Ω_{10}, Ω_{11}, and Ω_{12} (in dB scale).

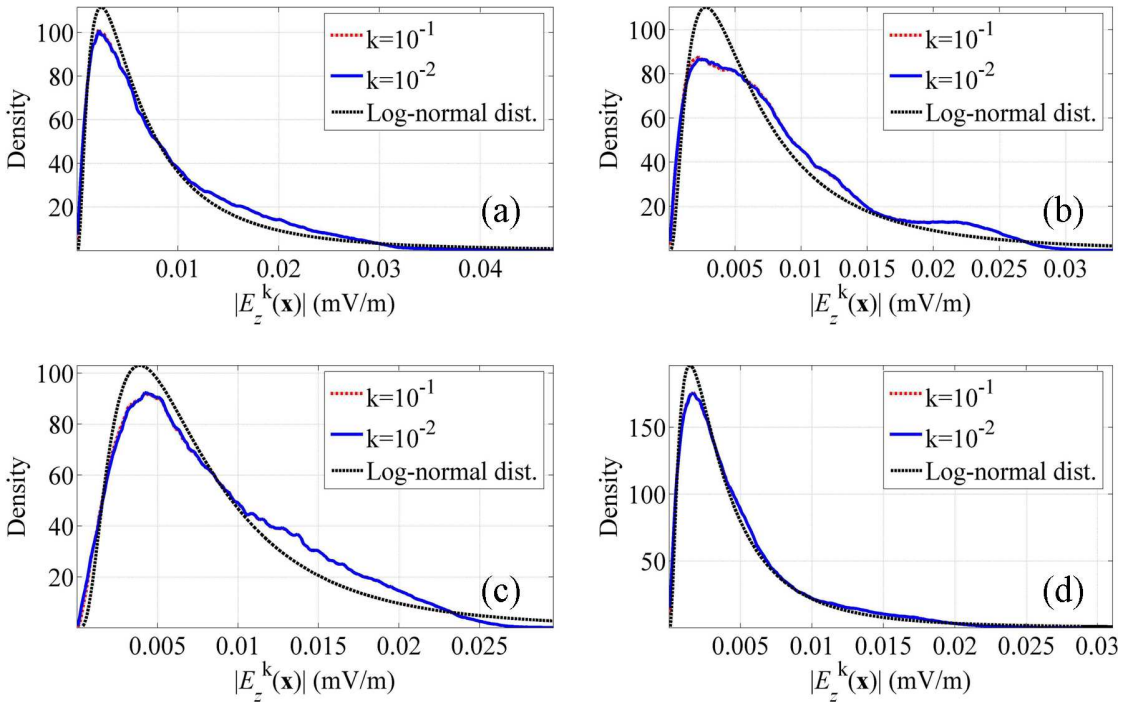

Figure 4–7 Empirical pdfs of $\left|E_z^{\mathrm{k}}(\mathbf{x})\right|$, $\mathrm{k}=\{10^{-1},10^{-2}\}$, computed on grids of receiver points selected in (a) Ω_9, (b) Ω_{10}, (c) Ω_{11}, and (e) Ω_{12} and their best fitting log-normal distributions.

CHAPTER 5
STATISTICAL CHARACTERIZATION OF EM WAVE PROPAGATION IN MINE ENVIRONMENTS

5.1 Introduction

In Chapter 4, the application of the ME-PC method to the statistical characterization of TM wave propagation in mine environments was presented. For many tunnel cross sections and wall constitutive parameters, the TM waves that propagate through tunnels dominate all other modes launched from the source [83]; if and when this happens, the statistical characterization of the wave propagation phenomena can proceed via the two-dimensional DD-based deterministic EM simulator. Unfortunately, for many tunnel cross sections and/or wall constitutive parameters, the TM modes do not dominate the overall field. Oftentimes, fields in rectangular/circular mine tunnels are dominated by *x*- or *y*- polarized hybrid modes [83-85] thereby rendering useless any simple two-dimensional EM simulator.

Existing three-dimensional simulation techniques for characterizing EM wave propagation in mine tunnels employ (multi-) modal decompositions [83-86], ray-tracing techniques [76], and full wave methods. Modal approaches and ray-tracing techniques cannot accurately account for the presence of miners and their equipments, as well as wall roughness (especially when it is comparable to the wavelength). Full-wave methods

do not suffer from such restrictions but require prohibitively large computational resources. At present, none of these methods provide the statistics of observables.

In this chapter, a simulation framework combining the ME-PC method with a novel three-dimensional full-wave EM simulator for statistically characterizing EM wave propagation in active and non-empty mine tunnels is presented. Specifically, the ME-PC method uses a three-dimensional full-wave EM simulator to (i) compute observables for various mine configurations represented by selected collocation points in the random domain and (ii) subsequently construct compact multivariate polynomial surrogate models that accurately approximate the observables, yet are computationally cheap to evaluate. Finally, the surrogate models are used in lieu of the computationally expensive three-dimensional full-wave EM simulator to extract pertinent statistics via the MC method. The three-dimensional full-wave EM simulator derives from a parallel surface integral equation (SIE) solver accelerated by both fast multipole and fast Fourier transform methods (FMM-FFT) [87-89] and can characterize the EM wave propagation in mine tunnels that are hundreds of wavelengths long. To the best of our knowledge, the three-dimensional EM solver proposed here is the first-ever full-wave solver capable of analyzing large-scale and realistically loaded mine environments. It follows that the proposed simulation framework that combines the ME-PC method with an FMM-FFT accelerated SIE solver represents the first-ever tool for rigorous statistical characterization of EM wave propagation in mine tunnel configurations with arbitrary cross-sections and loads.

In what follows, the FMM-FFT accelerated SIE-based three-dimensional full-wave solver is described first. Next, the three-dimensional full-wave solver is validated,

and the application of the proposed simulation framework to the statistical characterization of EM wave propagation in mine tunnels is demonstrated.

5.2 Three-Dimensional Full-Wave Solver

The SIE based three-dimensional full-wave solvers are widely used to characterize the EM wave scattering from dielectric and metallic surfaces. As the EM wave propagates in mine tunnels by scattering from dielectric surfaces on mine walls and PEC surfaces on mining equipments such as mine carts, SIE based three-dimensional full-wave solvers appear to be most appealing for efficient and rigorous characterization of EM wave propagation in mine environments compared to volume integral equation based full-wave solvers. For such characterization, the full-wave solver uses Poggio-Miller-Chang-Harrrington-Wu-Tsai (PMCHWT) formulation [90, 91] to account for the scattering from dielectric surfaces on mine walls and uses electric field integral equation (EFIE) formulation [92, 93] to account for the scattering from PEC surfaces on mine carts. However, direct implementation of such PMCHWT and EFIE based full-wave solver requires prohibitively large computational resources. For that reason, PMCHWT and EFIE based full-wave solver is implemented with FMM-FFT acceleration scheme.

In what follows, first the PMCHWT and EFIE formulations are reviewed. The numerical solution of SIEs is detailed next. After the FMM used to accelerate the SIE based full-wave solver is expounded, the FMM-FFT strategy is explained.

5.2.1 PMCHWT-EFIE Formulations

Consider a homogenous penetrable object with surface S and unit normal $\hat{\mathbf{n}} = \hat{\mathbf{n}}_1 = -\hat{\mathbf{n}}_2$ residing in an unbounded background medium [Figure 5–1 (a)]. The constitutive parameters of the background medium and the object are denoted by $\{\varepsilon_a, \mu_a\}$, $a = 1, 2$, respectively. Impressed sources $\{\mathbf{J}_a^i, \mathbf{M}_a^i\}$, $a = 1, 2$ reside external and internal to S. Radiating in unbounded media with constitutive parameters $\{\varepsilon_a, \mu_a\}$, $a = 1, 2$, these sources generate incident fields denoted by $\{\mathbf{E}_a^i, \mathbf{H}_a^i\}$. We wish to find total and scattered electric and magnetic fields $\{\mathbf{E}_a, \mathbf{H}_a\}$ and $\{\mathbf{E}_a^s, \mathbf{H}_a^s\}$, $a = 1, 2$ on both sides of surface S. To this end, the problem is reformulated in terms of the equivalent exterior and interior problems in Figure 5–1 (b)-(c).

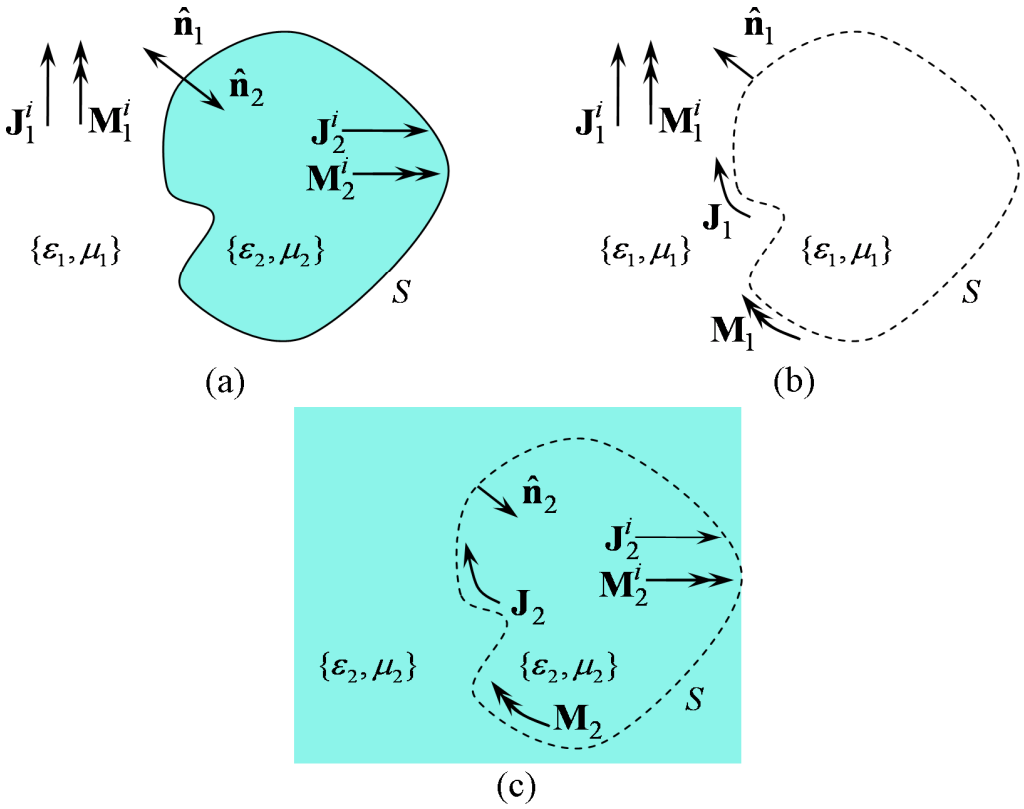

Figure 5–1 Generic geometry for PMCHWT formulation. (a) Original problem. (b) Equivalent exterior problem. (c) Equivalent interior problem.

In the equivalent exterior problem [Figure 5–1 (b)], total electric and magnetic fields $\{\mathbf{E}_1, \mathbf{H}_1\}$ can be expressed in terms of incident fields $\{\mathbf{E}_1^i, \mathbf{H}_1^i\}$ due to external sources $\{\mathbf{J}_1^i, \mathbf{M}_1^i\}$ and scattered fields $\{\mathbf{E}_1^s, \mathbf{H}_1^s\}$ due to the currents induced on S $\{\mathbf{J}_1, \mathbf{M}_1\}$, i.e.

$$\mathbf{E}_1(\mathbf{r}) = \mathbf{E}_1^i(\mathbf{r}) + \mathbf{E}_1^s(\mathbf{r}), \tag{5.1}$$

$$\mathbf{H}_1(\mathbf{r}) = \mathbf{H}_1^i(\mathbf{r}) + \mathbf{H}_1^s(\mathbf{r}), \tag{5.2}$$

where $\mathbf{r}$ denotes the coordinates of an observation point selected in the background medium and the fields inside the object are assumed to be zero. Similarly, in the equivalent interior problem [Figure 5–1 (c)], interior sources $\{\mathbf{J}_2^i, \mathbf{M}_2^i\}$ and the currents induced on S $\{\mathbf{J}_2, \mathbf{M}_2\}$ generate the total fields as

$$\mathbf{E}_2(\mathbf{r}) = \mathbf{E}_2^i(\mathbf{r}) + \mathbf{E}_2^s(\mathbf{r}), \tag{5.3}$$

$$\mathbf{H}_2(\mathbf{r}) = \mathbf{H}_2^i(\mathbf{r}) + \mathbf{H}_2^s(\mathbf{r}), \tag{5.4}$$

where $\mathbf{r}$ denotes the coordinates of an observation point selected inside the object. Continuity of tangential fields on surface S dictates

$$\hat{\mathbf{n}} \times \mathbf{E}_1(\mathbf{r}) = \hat{\mathbf{n}} \times \mathbf{E}_2(\mathbf{r}), \tag{5.5}$$

$$\hat{\mathbf{n}} \times \mathbf{H}_1(\mathbf{r}) = \hat{\mathbf{n}} \times \mathbf{H}_2(\mathbf{r}), \tag{5.6}$$

where $\mathbf{r}$ denotes the coordinates of an observation point selected on surface S. Substituting (5.1) and (5.3) into (5.5) and (5.2), and (5.4) into (5.6), and arranging terms yields

$$\hat{\mathbf{n}}\times\left(\mathbf{E}_1^s(\mathbf{r})-\mathbf{E}_2^s(\mathbf{r})\right)=\hat{\mathbf{n}}\times\left(\mathbf{E}_2^i(\mathbf{r})-\mathbf{E}_1^i(\mathbf{r})\right), \tag{5.7}$$

$$\hat{\mathbf{n}}\times\left(\mathbf{H}_1^s(\mathbf{r})-\mathbf{H}_2^s(\mathbf{r})\right)=\hat{\mathbf{n}}\times\left(\mathbf{H}_2^i(\mathbf{r})-\mathbf{H}_1^i(\mathbf{r})\right). \tag{5.8}$$

The scattered electric and magnetic fields $\left\{\mathbf{E}_a^s,\mathbf{H}_a^s\right\}$, $a=1,2$, can be expressed in terms the currents induced on S, $\left\{\mathbf{J}_a,\mathbf{M}_a\right\}$, $a=1,2$, as [91]

$$\mathbf{E}_a^s=\Im_a\left[\mathbf{J}_a\right]-\Re_a\left[\mathbf{M}_a\right], \tag{5.9}$$

$$\mathbf{H}_a^s=\Re_a\left[\mathbf{J}_a\right]+\Im_a\left[\mathbf{M}_a\right]/\eta_a^2, \tag{5.10}$$

where $\eta_a=\sqrt{\mu_a/\varepsilon_a}$. The integral operators $\Im_a[\cdot]$ and $\Re_a[\cdot]$ are defined as

$$\Im_a\left[\mathbf{X}\right]=-j\omega\mu_a\int_S\mathbf{X}(\mathbf{r}')G_a(\mathbf{r},\mathbf{r}')\,d\mathbf{r}'-\frac{1}{j\omega\varepsilon_a}\int_S\nabla\nabla'\cdot\mathbf{X}(\mathbf{r}')G_a(\mathbf{r},\mathbf{r}')\,d\mathbf{r}', \tag{5.11}$$

$$\Re_a\left[\mathbf{X}\right]=\nabla\times\int_S\mathbf{X}(\mathbf{r}')G_a(\mathbf{r},\mathbf{r}')\,d\mathbf{r}', \tag{5.12}$$

where $G_a(\mathbf{r},\mathbf{r}')=e^{-jk_a|\mathbf{r}-\mathbf{r}'|}/\left(4\pi|\mathbf{r}-\mathbf{r}'|\right)$ is the Green's function pertinent to the medium $a=1,2$, $\mathbf{X}=\left\{\mathbf{J}_a,\mathbf{M}_a\right\}$, and $k_a=\omega\sqrt{\mu_a\varepsilon_a}$. Substituting (5.9) and (5.10) in (5.7) and (5.8) and considering $\mathbf{J}=\mathbf{J}_1=-\mathbf{J}_2$ and $\mathbf{M}=\mathbf{M}_1=-\mathbf{M}_2$ yields

$$\hat{\mathbf{n}}\times\left(\Im_1\left[\mathbf{J}\right]+\Im_2\left[\mathbf{J}\right]-\left(\Re_1\left[\mathbf{M}\right]+\Re_2\left[\mathbf{M}\right]\right)\right)=\hat{\mathbf{n}}\times\left(\mathbf{E}_2^i(\mathbf{r})-\mathbf{E}_1^i(\mathbf{r})\right), \tag{5.13}$$

$$\hat{\mathbf{n}}\times\left(\Re_1\left[\mathbf{J}\right]+\Re_2\left[\mathbf{J}\right]+\left(\Im_1\left[\mathbf{M}\right]/\eta_1^2+\Im_2\left[\mathbf{M}\right]/\eta_2^2\right)\right)=\hat{\mathbf{n}}\times\left(\mathbf{H}_2^i(\mathbf{r})-\mathbf{H}_1^i(\mathbf{r})\right). \tag{5.14}$$

Eqns. (5.13) and (5.14) are well-known PMCHWT equations and can be solved simultaneously for $\left\{\mathbf{J},\mathbf{M}\right\}$ [91]. Now consider the object is non-penetrable (i.e. PEC

object). In this case, fields inside the object $\mathbf{E}_2^i(\mathbf{r})$ and $\mathbf{H}_2^i(\mathbf{r})$ are zero. Due to the boundary conditions on a PEC object, i.e. $\hat{\mathbf{n}}\times\mathbf{E}_1(\mathbf{r})=0$, Eqn. (5.13) reduces to the well-known EFIE, i.e.

$$\hat{\mathbf{n}}\times\Im_1[\mathbf{J}]=-\hat{\mathbf{n}}\times\mathbf{E}_1^i(\mathbf{r}). \tag{5.15}$$

To allow the PMCHWT solver for the characterization of EM propagation in realistically loaded mine environments, consider that there exist no external source in the background medium, i.e. $\mathbf{E}_1^i(\mathbf{r})=0$ and $\mathbf{H}_1^i(\mathbf{r})=0$, and that the electric currents induced on a PEC object with unit normal of $\hat{\mathbf{n}}_p$ residing inside the mine tunnel are represented by $\mathbf{J}_p$. By assuming that $\hat{\mathbf{n}}=\hat{\mathbf{n}}_p$ for PEC object and $\hat{\mathbf{n}}=\hat{\mathbf{n}}_1$ for mine walls, one can incorporate $\mathbf{J}_p$ into (5.13) and (5.14) as [94]

$$\hat{\mathbf{n}}\times\left(\Im_1[\mathbf{J}]+\Im_2[\mathbf{J}]-\left(\Re_1[\mathbf{M}]+\Re_2[\mathbf{M}]\right)+\Im_2\left[\mathbf{J}_p\right]\right)=\hat{\mathbf{n}}\times\mathbf{E}_2^i(\mathbf{r}), \tag{5.16}$$

$$\hat{\mathbf{n}}\times\left(\Re_1[\mathbf{J}]+\Re_2[\mathbf{J}]+\left(\Im_1[\mathbf{M}]/\eta_1^2+\Im_2[\mathbf{M}]/\eta_2^2\right)+\Re_2\left[\mathbf{J}_p\right]\right)=\hat{\mathbf{n}}\times\mathbf{H}_2^i(\mathbf{r}), \tag{5.17}$$

$$\hat{\mathbf{n}}\times\left(\Im_2[\mathbf{J}]-\Re_2[\mathbf{M}]+\Im_2\left[\mathbf{J}_p\right]\right)=\hat{\mathbf{n}}\times\mathbf{E}_{2,p}^i(\mathbf{r}). \tag{5.18}$$

Here $\left\{\mathbf{E}_2^i,\mathbf{H}_2^i\right\}$ represent the fields incident upon dielectric surface constituting mine walls while $\mathbf{E}_{2,p}^i$ denotes the electric field incident upon the PEC surface constituting mine carts inside mine tunnel. Eqns (5.16)-(5.18) are termed the "PMCHWT-EFIE" equations and can be solved simultaneously for $\left\{\mathbf{J},\mathbf{M},\mathbf{J}_p\right\}$ [94, 95].

5.2.2 Numerical Solution of SIEs

To solve the PMCHWT formulation in (5.13) and (5.14), the unknown electric and magnetic currents $\{\mathbf{J},\mathbf{M}\}$ are approximated in terms of linear combinations of Rao-Wilton-Glisson (RWG) basis functions [93] $\mathbf{f}_n$, $n=1,\ldots,N$, as

$$\mathbf{J}(\mathbf{r}') \cong \sum_{n=1}^{N} I_n^J \mathbf{f}_n(\mathbf{r}'), \tag{5.19}$$

$$\mathbf{M}(\mathbf{r}') \cong \sum_{n=1}^{N} I_n^M \mathbf{f}_n(\mathbf{r}'), \tag{5.20}$$

where I_n^J and I_n^M denote the unknown electric and magnetic current coefficients, respectively. Substituting (5.19) and (5.20) into (5.13) and (5.14) and testing with the same set of basis functions $\mathbf{f}_m$, $m=1,\ldots,N$, (i.e. Galerkin testing) yields a $2N\times 2N$ linear system of equations that can be expressed in the matrix form as [91]

$$\bar{\mathbf{Z}}\cdot\mathbf{I}=\mathbf{V}. \tag{5.21}$$

The MoM impedance matrix $\bar{\mathbf{Z}}$ consists of four $N\times N$ submatrices as

$$\bar{\mathbf{Z}}=\begin{bmatrix}\bar{\mathbf{Z}}^{EJ} & \bar{\mathbf{Z}}^{EM}\\ \bar{\mathbf{Z}}^{HJ} & \bar{\mathbf{Z}}^{HM}\end{bmatrix}_{2N\times 2N}. \tag{5.22}$$

These submatrices can be expressed as

$$\bar{\mathbf{Z}}_{mn}^{EJ}=\left\langle \mathbf{f}_m,(\mathfrak{I}_1+\mathfrak{I}_2)\mathbf{f}_n\right\rangle, \tag{5.23}$$

$$\bar{\mathbf{Z}}_{mn}^{EM}=\left\langle \mathbf{f}_m,-(\mathfrak{R}_1+\mathfrak{R}_2)\mathbf{f}_n\right\rangle, \tag{5.24}$$

$$\bar{\mathbf{Z}}_{mn}^{HJ}=\left\langle \mathbf{f}_m,(\mathfrak{R}_1+\mathfrak{R}_2)\mathbf{f}_n\right\rangle=-\bar{\mathbf{Z}}_{mn}^{EM}, \tag{5.25}$$

$$\overline{\mathbf{Z}}_{mn}^{HM} = \left\langle \mathbf{f}_m, \left(\Im_1 / \eta_1^2 + \Im_2 / \eta_2^2 \right) \mathbf{f}_n \right\rangle, \tag{5.26}$$

by dropping $\hat{\mathbf{n}}\times$ operators in the equations leading to them; this is allowed since the RWG functions are already defined tangential to surface S. Here, the inner product operator $\langle \cdot \rangle$ is defined as

$$\left\langle \mathbf{a}(\mathbf{r}'), \mathbf{b}(\mathbf{r}') \right\rangle = \int_S \mathbf{a}(\mathbf{r}') \mathbf{b}(\mathbf{r}') \, d\mathbf{r}'. \tag{5.27}$$

The vectors representing the unknown current coefficients and excitation are

$$\mathbf{I} = \begin{bmatrix} \mathbf{I}^J \\ \mathbf{I}^M \end{bmatrix}_{2N\times 1}, \tag{5.28}$$

$$\mathbf{V} = \begin{bmatrix} \mathbf{V}^E \\ \mathbf{V}^H \end{bmatrix}_{2N\times 1}, \tag{5.29}$$

where the excitation vector elements are computed by considering $\mathbf{E}_1^i(\mathbf{r}) = 0$ and $\mathbf{H}_1^i(\mathbf{r}) = 0$ as

$$\mathbf{V}_m^E = \left\langle \mathbf{f}_m, \mathbf{E}_2^i(\mathbf{r}) \right\rangle, \tag{5.30}$$

$$\mathbf{V}_m^H = \left\langle \mathbf{f}_m, \mathbf{H}_2^i(\mathbf{r}) \right\rangle. \tag{5.31}$$

The entries of the unknown current coefficient vector, excitation vector, and four submatrices can be written explicitly as follows: for $n = 1, \ldots, N$, $m = 1, \ldots, N$, $a = 1, 2$,

$$\mathbf{I}_n^J = I_n^J, \ \mathbf{I}_n^M = I_n^M, \tag{5.32}$$

$$\mathbf{V}_m^E = \int_{S_m} \mathbf{f}_m(\mathbf{r}) \mathbf{E}_2^i(\mathbf{r}) \, d\mathbf{r}, \tag{5.33}$$

$$\mathbf{V}_m^H = \int_{S_m} \mathbf{f}_m(\mathbf{r}) \mathbf{H}_2^i(\mathbf{r}) d\mathbf{r}, \tag{5.34}$$

$$\begin{aligned} \overline{\mathbf{Z}}_{mn,a}^{EJ} = & -j\omega\mu_a \int_{S_m} \mathbf{f}_m(\mathbf{r}) \int_{S_n} \mathbf{f}_n(\mathbf{r}') G_a(\mathbf{r},\mathbf{r}') d\mathbf{r}' d\mathbf{r} \\ & -\frac{1}{j\omega\varepsilon_a} \int_{S_m} \nabla\cdot\mathbf{f}_m(\mathbf{r}) \int_{S_n} \nabla'\cdot\mathbf{f}_n(\mathbf{r}') G_a(\mathbf{r},\mathbf{r}') d\mathbf{r}' d\mathbf{r} \end{aligned}, \tag{5.35}$$

$$\overline{\mathbf{Z}}_{mn,a}^{EM} = \int_{S_m} \mathbf{f}_m(\mathbf{r}) \nabla\times \int_{S_n} \mathbf{f}_n(\mathbf{r}') G_a(\mathbf{r},\mathbf{r}') d\mathbf{r}' d\mathbf{r}, \tag{5.36}$$

where S_n and S_m represent the triangles defined by source and testing RWG basis. The entries of $\overline{\mathbf{Z}}_{mn,a}^{HM}$ and $\overline{\mathbf{Z}}_{mn,a}^{HJ}$ can be obtained from (5.35) and (5.36), respectively.

To solve the PMCHWT-EFIE formulation in (5.16)-(5.18), the unknown electric and magnetic currents on dielectric surface $\{\mathbf{J},\mathbf{M}\}$ are approximated in terms of RWG basis functions as in (5.19) and (5.20). Similarly, the unknown electric current on the PEC surfaces $\mathbf{J}_p$ is expanded in terms of the same basis functions $\mathbf{f}_n$, $n=1,\ldots,N_p$, as [94]

$$\mathbf{J}_p(\mathbf{r}') \cong \sum_{n=1}^{N_p} I_n^{J_p} \mathbf{f}_n(\mathbf{r}'); \tag{5.37}$$

$I_n^{J_p}$ is referred to as the unknown electric current coefficients on the PEC surface. Substituting (5.19), (5.20), and (5.37) into (5.16)-(5.18) and applying the Galerkin testing procedure yields a $(2N+N_p)\times(2N+N_p)$ linear system of equations as [94]

$$\begin{bmatrix} \overline{\mathbf{Z}}^{EJ} & \overline{\mathbf{Z}}^{EM} & \overline{\mathbf{Z}}^{EJ_p} \\ \overline{\mathbf{Z}}^{HJ} & \overline{\mathbf{Z}}^{HM} & \overline{\mathbf{Z}}^{HJ_p} \\ \overline{\mathbf{Z}}^{E_pJ} & \overline{\mathbf{Z}}^{E_pM} & \overline{\mathbf{Z}}^{E_pJ_p} \end{bmatrix} \cdot \begin{bmatrix} \mathbf{I}^J \\ \mathbf{I}^M \\ \mathbf{I}^{J_p} \end{bmatrix} = \begin{bmatrix} \mathbf{V}^E \\ \mathbf{V}^H \\ \mathbf{V}^{E_p} \end{bmatrix}, \tag{5.38}$$

where the entries of unknown current coefficient vector, the excitation vector, and the submatrices in MoM impedance matrix are:

$$\mathbf{I}^{J_p} = I_n^{J_p}, \quad n = 1, \ldots, N_p, \tag{5.39}$$

$$\mathbf{V}_m^{E_p} = \int_{S_m} \mathbf{f}_m(\mathbf{r}) \mathbf{E}_{2,p}^{i}(\mathbf{r}) d\mathbf{r}, \quad m = 1, \ldots, N_p, \tag{5.40}$$

$$\begin{aligned} \bar{\mathbf{Z}}_{mn}^{EJ_p} = & -j\omega\mu_2 \int_{S_m} \mathbf{f}_m(\mathbf{r}) \int_{S_n} \mathbf{f}_n(\mathbf{r}') G_2(\mathbf{r}, \mathbf{r}') d\mathbf{r}' d\mathbf{r} \\ & -\frac{1}{j\omega\varepsilon_2} \int_{S_m} \nabla \cdot \mathbf{f}_m(\mathbf{r}) \int_{S_n} \nabla' \cdot \mathbf{f}_n(\mathbf{r}') G_2(\mathbf{r}, \mathbf{r}') d\mathbf{r}' d\mathbf{r}, \\ & m = 1, \ldots, N, \ n = 1, \ldots, N_p, \end{aligned} \tag{5.41}$$

$$\bar{\mathbf{Z}}_{mn}^{HJ_p} = \int_{S_m} \mathbf{f}_m(\mathbf{r}) \nabla \times \int_{S_n} \mathbf{f}_n(\mathbf{r}') G_2(\mathbf{r}, \mathbf{r}') d\mathbf{r}' d\mathbf{r}, \ m = 1, \ldots, N, \ n = 1, \ldots, N_p, \tag{5.42}$$

$$\begin{aligned} \bar{\mathbf{Z}}_{mn}^{E_pJ_p} = & -j\omega\mu_2 \int_{S_m} \mathbf{f}_m(\mathbf{r}) \int_{S_n} \mathbf{f}_n(\mathbf{r}') G_2(\mathbf{r}, \mathbf{r}') d\mathbf{r}' d\mathbf{r} \\ & -\frac{1}{j\omega\varepsilon_2} \int_{S_m} \nabla \cdot \mathbf{f}_m(\mathbf{r}) \int_{S_n} \nabla' \cdot \mathbf{f}_n(\mathbf{r}') G_2(\mathbf{r}, \mathbf{r}') d\mathbf{r}' d\mathbf{r}, \ . \\ & m = 1, \ldots, N_p, \ n = 1, \ldots, N_p. \end{aligned} \tag{5.43}$$

Note that the entries of $\{\mathbf{I}^J, \mathbf{I}^M\}$ and $\{\mathbf{V}^E, \mathbf{V}^H\}$ in (5.38) are the same as those in (5.32)-(5.34). The entries of submatrices $\bar{\mathbf{Z}}^{EJ}$, $\bar{\mathbf{Z}}^{EM}$, $\bar{\mathbf{Z}}^{HJ}$, and $\bar{\mathbf{Z}}^{HM}$ can be directly computed from (5.35) and (5.36). And the entries of $\bar{\mathbf{Z}}_{mn}^{E_pJ}$ and $\bar{\mathbf{Z}}^{E_pM}$ can be obtained from (5.41) and (5.42) by using $m = 1, \ldots, N_p$ and $n = 1, \ldots, N$ instead of $m = 1, \ldots, N$ and $n = 1, \ldots, N_p$.

5.2.3 The FMM Formulation

The linear system of equations in (5.21) can be solved either by direct or iterative solvers. Direct solvers (e.g. Gauss elimination method or lower-upper decompositions) have memory requirements and computational complexity of $O\left(N^3\right)$. They are fast and desirable when N is small. However, these methods require prohibitively large computational resources for the problems with moderate and large number of unknowns. For this reason, the linear system of equations generated by the conventional MoM is often solved by iteratively (e.g. using the transpose-free quasi-minimal residual or conjugate gradient method). Iterative solvers find the current coefficients by iteratively testing trial solutions; testing these solutions calls for one or more matrix-vector multiplications (i.e. $\bar{\mathbf{Z}} \cdot \mathbf{I}$) in each iteration. Hence, they require $O\left(N_{\text{iter}} N^2\right)$ operations and $O\left(N^2\right)$ memory, where N_{iter} is the number of iterations required for convergence; typically $N_{\text{iter}} \ll N$. Unfortunately the $O\left(N^2\right)$ complexity of the iterative solution scheme is still not acceptable for the problems with (very) large numbers of unknowns. To alleviate this computational burden, the FMM was developed to accelerate the matrix-vector multiplications required by iterative solvers [96, 97]. The single-level implementation of this method reduces the memory requirements to $O\left(N^{1.5}\right)$ and the number of operations to $O\left(N_{\text{iter}} N^{1.5}\right)$ [97] while its multi-level implementation requires $O\left(N \log N\right)$ memory and $O\left(N_{\text{iter}} N \log N\right)$ operations [98].

The FMM accomplishes the reduction in memory and computational complexity of matrix-vector multiplication by first splitting (5.21) into two parts as

$$\left(\bar{\mathbf{Z}}^{\text{near}} + \bar{\mathbf{Z}}^{\text{far}}\right) \cdot \mathbf{I} = \mathbf{V}, \tag{5.44}$$

where $\bar{\mathbf{Z}}^{\text{near}}$ represents the near-field interactions between nearby basis and testing functions while $\bar{\mathbf{Z}}^{\text{far}}$ models interactions between well-separated basis and testing functions. While the $\bar{\mathbf{Z}}^{\text{near}} \cdot \mathbf{I}$ part of matrix-vector multiplication is computed by conventional MoM method, the $\bar{\mathbf{Z}}^{\text{far}} \cdot \mathbf{I}$ part of the multiplication is performed by the FMM. The FMM puts source and testing basis functions $\left\{\mathbf{f}_n\left(\mathbf{r}'\right), \mathbf{f}_m\left(\mathbf{r}\right)\right\}$ into groups and efficiently computes the result of $\bar{\mathbf{Z}}^{\text{far}} \cdot \mathbf{I}$ for well-separated basis functions via multipole/plane wave expansions applicable to each group.

Consider that the source and testing basis functions reside inside well-separated spheres [Figure 5–2]. The source and testing spheres are centered at $\mathbf{r}_S$ and $\mathbf{r}_T$ while the source and testing points are located at $\mathbf{r}'$ and $\mathbf{r}$. With this knowledge, the Green's function can be written as [97]

$$G_a\left(\mathbf{r}, \mathbf{r}'\right) = \frac{e^{-jk_a|\mathbf{r}-\mathbf{r}'|}}{4\pi|\mathbf{r}-\mathbf{r}'|} = \frac{e^{-jk_a|\mathbf{D}+\mathbf{d}|}}{4\pi|\mathbf{D}+\mathbf{d}|}, \tag{5.45}$$

where $\mathbf{D} = \mathbf{r}_T - \mathbf{r}_S$, and $\mathbf{d} = \mathbf{r} - \mathbf{r}_T + \mathbf{r}_S - \mathbf{r}'$. The FMM relies on an expansion of the Green's function via Gegenbauer's addition theorem [97, 99] as

$$G_a\left(\mathbf{r}, \mathbf{r}'\right) = \frac{e^{-jk_a|\mathbf{D}+\mathbf{d}|}}{4\pi|\mathbf{D}+\mathbf{d}|} = \frac{-jk_a}{4\pi} \sum_{l=0}^{\infty} (-1)^l (2l+1)\, j_l\left(k_a d\right) h_l^2\left(k_a D\right) P_l\left(\hat{\mathbf{d}} \cdot \hat{\mathbf{D}}\right), \tag{5.46}$$

where $\mathbf{D} = D\hat{\mathbf{D}}$, $\mathbf{d} = d\hat{\mathbf{d}}$, $j_l(\cdot)$ denotes the spherical Bessel function of the first kind, $h_l^2(\cdot)$ is the spherical Hankel function of the second kind, and $P_l(\cdot)$ denotes the Legendre polynomial of order l. The expansion in (5.46) is valid provided that $d < D$.

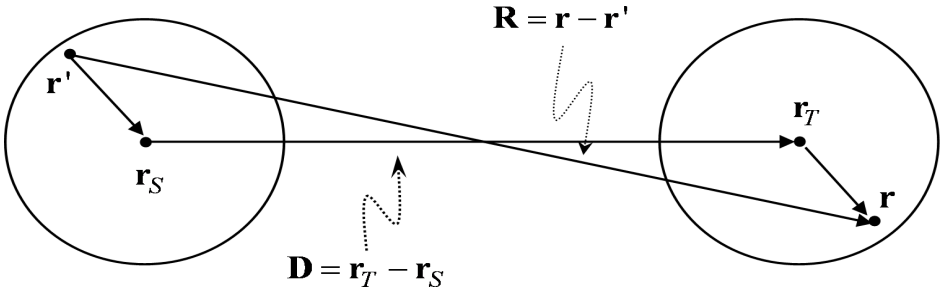

Figure 5–2 The vector quantities illustrating the relationship between source and testing basis functions.

The elementary identity in [100] (p.410) that involves to converting the product of $j_l(\cdot)$ with $P_l(\cdot)$ into a surface integral of propagating waves over a unit sphere Ω, i.e.,

$$j_l(k_a d) P_l\left(\hat{\mathbf{d}} \cdot \hat{\mathbf{D}}\right) = \frac{(-j)^{-l}}{4\pi} \iint_{\Omega} e^{-jk_a \hat{\mathbf{k}}_a \cdot \mathbf{d}} P_l\left(\hat{\mathbf{k}}_a \cdot \hat{\mathbf{D}}\right) d^2 \hat{\mathbf{k}}_a , \tag{5.47}$$

can be substituted in (5.46) to yield

$$\frac{e^{-jk_a|\mathbf{D}+\mathbf{d}|}}{4\pi|\mathbf{D}+\mathbf{d}|} = \frac{-jk_a}{(4\pi)^2} \iint_{\Omega} d^2 \hat{\mathbf{k}}_a e^{-jk_a \hat{\mathbf{k}}_a \cdot \mathbf{d}} \sum_{l=0}^{\infty} (-j)^l (2l+1) h_l^2(k_a D) P_l\left(\hat{\mathbf{k}}_a \cdot \hat{\mathbf{D}}\right). \tag{5.48}$$

Here $\hat{\mathbf{k}}_a = \mathbf{k}_a / k_a$ denotes a unit vector pointing along the direction of a propagating plane wave. Truncating the infinite series in (5.48) to degree L and rearranging terms yields

$$G_a(\mathbf{r}, \mathbf{r}') = \frac{e^{-jk_a|\mathbf{r}-\mathbf{r}'|}}{4\pi|\mathbf{r}-\mathbf{r}'|} \approx \frac{-jk_a}{(4\pi)^2} \iint_{\Omega} d^2 \hat{\mathbf{k}}_a e^{-j\mathbf{k}_a \cdot (\mathbf{r}-\mathbf{r}_T)} T_L(\mathbf{k}_a, \mathbf{D}) e^{j\mathbf{k}_a \cdot (\mathbf{r}'-\mathbf{r}_S)} , \tag{5.49}$$

where $T_L(\mathbf{k}_a, \mathbf{D})$ denotes the translation operator defined as

$$T_L(\mathbf{k}_a, \mathbf{D}) = \sum_{l=0}^{L} (-j)^l (2l+1) h_l^2(k_a D) P_l\left(\hat{\mathbf{k}}_a \cdot \hat{\mathbf{D}}\right). \tag{5.50}$$

Note that the translation operator $T_L(\mathbf{k}_a, \mathbf{D})$ is a function of $\mathbf{k}_a$ and $\mathbf{D}$, and independent of the positions of source point $\mathbf{r}'$ and testing point $\mathbf{r}$. This allows computing the interactions between n source points inside the source sphere and a testing point in the testing sphere using only one translation operator, i.e.

$$\sum_n \frac{e^{-jk_a|\mathbf{r}-\mathbf{r}_n'|}}{4\pi|\mathbf{r}-\mathbf{r}_n'|} \approx \frac{-jk_a}{(4\pi)^2} \iint_\Omega d^2\hat{\mathbf{k}}_a e^{-j\mathbf{k}_a\cdot(\mathbf{r}-\mathbf{r}_T)} T_L(\mathbf{k}_a, \mathbf{D}) \sum_n e^{j\mathbf{k}_a\cdot(\mathbf{r}_n'-\mathbf{r}_S)}, \tag{5.51}$$

and greatly decreases the computational complexity of a matrix-vector multiplication. For each point in the source sphere, the *outgoing wave expansion* first is characterized by the factor $e^{j\mathbf{k}_a\cdot(\mathbf{r}'-\mathbf{r}_S)}$. Next outgoing wave expansions for all sources in the source sphere are coherently *aggregated* to obtain the outgoing wave expansion of source sphere. This expansion is next transmitted to the testing sphere by the translation operator $T_L(\mathbf{k}_a, \mathbf{D})$. The transmitted expansion is then multiplied by the *incoming wave expansion* of a testing point, characterized by the factor $e^{-j\mathbf{k}_a\cdot(\mathbf{r}-\mathbf{r}_T)}$, and integrated over the unit sphere Ω (*disaggregation*). Note that the transmitted expansion to the testing sphere can also be used to obtain the cumulative effect of n source points to many testing points in the testing sphere. To utilize the aggregation-translation-disaggregation strategy in the $\overline{\mathbf{Z}}^{\text{far}} \cdot \mathbf{I}$ part of matrix-vector multiplication, the FMM first sorts all basis functions in boxes enclosed by spheres and pre-computes outgoing and incoming wave expansions of all basis functions as well as the translation operators linking all possible source-testing sphere pairs. During the matrix-vector multiplication stage, it multiplies the outgoing wave expansions of all basis functions with the current coefficients provided by the iterative solver, performs aggregation-translation-disaggregation steps, and finds the

contributions to $\mathbf{V}$ from $\bar{\mathbf{Z}}^{\text{far}} \cdot \mathbf{I}$. Before describing the deployment of the FMM in our PMCWHT-EFIE formulation, a couple of important issues for the implementation of FMM are addressed.

The first important issue in the implementation of FMM is the selection of the optimal quadrature rule for evaluating the surface integral in (5.49). To do that, the exponential term in the integrand can be expanded as [99]

$$e^{-jk_a d(\mathbf{k}_a \cdot \mathbf{d})} = \sum_{l=0}^{\infty} (-j)^l (2l+1)\, j_l(k_a d)\, P_l\left(\hat{\mathbf{k}}_a \cdot \hat{\mathbf{d}}\right). \tag{5.52}$$

Substituting (5.52) into (5.49) yields

$$G_a(\mathbf{r},\mathbf{r}') \approx \frac{-jk_a}{(4\pi)^2} \sum_{l'=0}^{\infty} \sum_{l=0}^{L} (-j)^{l+l'} (2l+1)(2l'+1) h_l^2(k_a D) \\ j_{l'}(k_a d) \iint_{\Omega} d^2\hat{\mathbf{k}}_a P_l\left(\hat{\mathbf{k}}_a \cdot \hat{\mathbf{D}}\right) P_{l'}\left(\hat{\mathbf{k}}_a \cdot \hat{\mathbf{d}}\right), \tag{5.53}$$

where the integrand is the product of two Legendre functions. By using the addition theorem for Legendre functions, the integrand can be expressed in terms of spherical harmonics functions. Assume that the infinite series with index l' is also truncated at L. Then the exact integration scheme for evaluating the integral of spherical harmonics of order L can be obtained by selecting $(L+1)$-point Gauss-Legendre quadrature rule in the θ-direction and $(2L+1)$-point uniform Simpson's rule in the ϕ-direction. Consequently, $(L+1)(2L+1)$ points are needed to evaluate the surface integral over the unit sphere Ω in (5.49) [101].

The second important issue in the implementation of the FMM is the selection of the optimal truncation number L (or the number of multipoles) for the translation

operator. The selection of L depends on the maximum of the diameters of spheres and the wavenumber and can be done using the semi-empirical formula proposed by Rokhlin [97]

$$L = k_a d + 10\log\left(k_a d + \pi\right), \tag{5.54}$$

where d denotes the maximum of diameters of spheres. Chew and Song revised this formula later and suggested [101]

$$L = k_a d + 1.8\beta^{2/3}\left(k_a d\right)^{1/3}, \tag{5.55}$$

where $\beta = \log_{10}\left(1/\varepsilon\right)$ and ε is the desired accuracy. It has been reported in [101] that the difference between the estimated L via (5.55) and the true L is varying in between -1 through 2 for $1 < kd < 500$ and $10^{-1} < \varepsilon < 10^{-10}$. However, this formula might fail to provide the optimum L when the spacing between source and testing spheres is small. To fix this deficiency, an algorithmic approach to determine the optimum L for varying sphere diameters and spacings was proposed in [102].

The FMM approximation in (5.49) can be used in the PMCWHT formulation as [101]

$$\begin{aligned}\left\langle \mathbf{f}_m, \Im_a \mathbf{f}_n \right\rangle = \frac{-k_a^2 \eta_a}{16\pi^2} \int_{\Omega} d^2\hat{\mathbf{k}}_a \int_{S_m} d\mathbf{r} e^{-j\mathbf{k}_a\cdot\left(\mathbf{r}-\mathbf{r}_T\right)} \mathbf{f}_m\left(\mathbf{r}\right) \\ T_L\left(\mathbf{k}_a, \mathbf{D}\right)\left(\bar{\mathbf{I}} - \hat{\mathbf{k}}_a\hat{\mathbf{k}}_a\right) \int_{S_n} d\mathbf{r}' e^{j\mathbf{k}_a\cdot\left(\mathbf{r}'-\mathbf{r}_S\right)} \mathbf{f}_n\left(\mathbf{r}'\right)\end{aligned}, \tag{5.56}$$

$$\begin{aligned}\left\langle \mathbf{f}_m, \Re_a \mathbf{f}_n \right\rangle = \frac{k_a^2}{16\pi^2} \int_{\Omega} d^2\hat{\mathbf{k}}_a \int_{S_m} d\mathbf{r} e^{-j\mathbf{k}_a\cdot\left(\mathbf{r}-\mathbf{r}_T\right)} \left(\mathbf{f}_m\left(\mathbf{r}\right) \times \hat{\mathbf{k}}_a\right) \\ T_L\left(\mathbf{k}_a, \mathbf{D}\right) \int_{S_n} d\mathbf{r}' e^{j\mathbf{k}_a\cdot\left(\mathbf{r}'-\mathbf{r}_S\right)} \mathbf{f}_n\left(\mathbf{r}'\right)\end{aligned}. \tag{5.57}$$

Since $\left(\bar{\mathbf{I}}-\hat{\mathbf{k}}_a\hat{\mathbf{k}}_a\right)=\hat{\boldsymbol{\theta}}\hat{\boldsymbol{\theta}}+\hat{\boldsymbol{\varphi}}\hat{\boldsymbol{\varphi}}$ and $\left(\bar{\mathbf{I}}-\hat{\mathbf{k}}_a\hat{\mathbf{k}}_a\right)\mathbf{V}=V_\theta\hat{\boldsymbol{\theta}}+V_\phi\hat{\boldsymbol{\varphi}}$, only θ and ϕ components of outgoing and incoming wave expansions sampled at quadrature points are stored. These equations are directly used in the PMCHWT-EFIE formulation in (5.41)-(5.43) as well.

Implementation of the FMM can be better explained by an example. Suppose that a meshed structure is decomposed into boxes [Figure 5–3]. Each interior edge shared by two triangles forms a basis function and each box contains a group of basis functions. Boxes have edges with the length of δ and are indexed (u,v,w) that characterize distances between the origin and the box centers. Distances between box centers and local origin along *x*, *y*, and *z* directions (i.e. $\left(d_x,d_y,d_z\right)$) are obtained by $\left(d_x,d_y,d_z\right)=\left((u-1)\delta+0.5\delta,(v-1)\delta+0.5\delta,(w-1)\delta+0.5\delta\right)$. Assume that there exist U, V, and W boxes along the *x*, *y*, and *z* directions, respectively, and $B_{u,v,w}$ denotes a box with indices (u,v,w), $u=1,\ldots,U$, $v=1,\ldots,V$, $w=1,\ldots,W$.

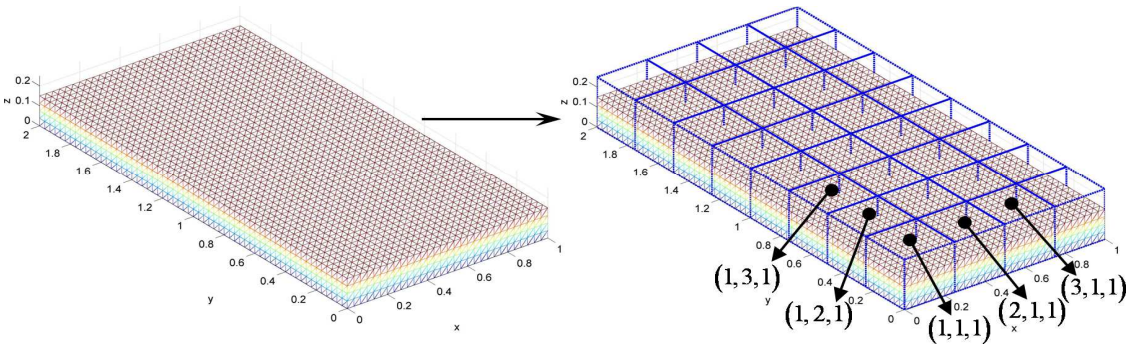

Figure 5–3 Decomposition of a structure into boxes and numbering of boxes.

Each box knows the ids of basis functions that reside in that box and the ids of boxes that sit in its near- and far-field; the lists of these ids are denoted $I^{NF}_{u,v,w}$ and $I^{FF}_{u,v,w}$. For instance, the example in Figure 5–3 shows that boxes $B_{1,2,1}$ and $B_{2,1,1}$ are in the near-field

of $B_{1,1,1}$ and the ids of those boxes are stored in $I_{1,1,1}^{NF}$. Similarly the boxes $B_{1,3,1}$ and $B_{3,1,1}$ are in far-field of $B_{1,1,1}$ if one box spacing is assumed for far-field assignment. The ids of those boxes are stored in $I_{1,1,1}^{FF}$. The matrix-vector multiplication of elements representing interactions between basis and testing functions in near-field boxes are performed with the conventional MoM method. To compute matrix-vector multiplication of elements represented by far-field boxes, first, the aggregation step is performed by computing the outgoing wave expansion of a source box as

$$\tilde{\mathbf{F}}_{u,v,w}\left(\hat{\mathbf{k}}_a\right)=\sum_{n\in B_{u,v,w}}\int_{S_n}d\mathbf{r}'e^{j\mathbf{k}_a\cdot\left(\mathbf{r}'-\mathbf{r}_S\right)}\left(\bar{\mathbf{I}}-\hat{\mathbf{k}}_a\hat{\mathbf{k}}_a\right)\cdot\mathbf{f}_n\left(\mathbf{r}'\right)I_n^J\,, \tag{5.58}$$

where $\mathbf{r}_S$ is the center of source box $B_{u,v,w}$ and n is the id of basis function that resides in $B_{u,v,w}$. Next, the translation step is performed by multiplying the outgoing wave expansion of the source box with the translation operator computed for a source-testing boxes pair, i.e.,

$$\tilde{\mathbf{G}}_{u',v',w'}\left(\hat{\mathbf{k}}_a\right)=\sum_{B_{u',v',w'}\in I_{u,v,w}^{FF}}T_L\left(\mathbf{k}_a,\mathbf{D}\right)\tilde{\mathbf{F}}_{u,v,w}\left(\hat{\mathbf{k}}_a\right). \tag{5.59}$$

Here the indices of the testing box are represented by $\left(u',v',w'\right)$, the indices of $B_{u',v',w'}$ should be in the list of $I_{u,v,w}^{FF}$, and $\mathbf{D}=\mathbf{r}_T-\mathbf{r}_S$ where $\mathbf{r}_T$ is the center of testing box $B_{u',v',w'}$. To perform the disaggregation step, the translated wave expansion is multiplied with the incoming wave expansion of basis function with id m that resides in $B_{u,v,w}$, i.e.

$$\bar{\mathbf{Z}}_{mn}^{\text{far}}\cdot\mathbf{I}_n\Big|_{\substack{m\in B_{u',v',w'}\\ n\in B_{u,v,w}}}=\sum_{m\in B_{u',v',w'}}\int_{\Omega}d^2\hat{\mathbf{k}}_a\int_{S_m}d\mathbf{r}e^{-j\mathbf{k}_a\cdot\left(\mathbf{r}-\mathbf{r}_T\right)}\mathbf{f}_m\left(\mathbf{r}\right)\tilde{\mathbf{G}}_{u',v',w'}\left(\hat{\mathbf{k}}_a\right). \tag{5.60}$$

The procedure outlined here is single-level implementation of FMM. Although the overall complexity of this implementation is $O\left(N^{3/2}\right)$, it can be reduced to $O\left(N^{4/3}\log^{2/3}N\right)$ [88] by employing the FMM-FFT strategy explained next.

5.2.4 The FMM-FFT Strategy

The FMM approximation is accelerated by a sequence of FFT operations by exploiting the Teoplitz property of translation operator [87-89]. It can be seen from the example in Figure 5–3 that the centers of boxes coincide with the points on a regular 3D lattice. Assume that the centers of source and testing boxes are denoted by $\mathbf{r}_{u,v,w}$ and $\mathbf{r}_{u',v',w'}$. Then the translation operator $T_L\left(\mathbf{k}_a,\mathbf{D}\right)$ can be written explicitly as $T_L\left(\mathbf{k}_a,\left|\mathbf{r}_{u',v',w'}-\mathbf{r}_{u,v,w}\right|\right)$. For each direction $\mathbf{k}_a$, the translation operators for all possible source-testing box combinations can be written in matrix form as

$$\overline{T}_L\left(\mathbf{k}_a\right)=\begin{bmatrix}\ddots & \vdots & \\ \cdots & T_L\left(\mathbf{k}_a,\left|\mathbf{r}_{u',v',w'}-\mathbf{r}_{u,v,w}\right|\right) & \cdots \\ \iddots & \vdots & \ddots\end{bmatrix}_{\substack{(2U+1)\times\\(2V+1)\times\\(2W+1)}}, \tag{5.61}$$

where $u'=-U+1,\ldots,U$, $v'=-V+1,\ldots,V$, and $w'=-W+1,\ldots,W$ while $(u,v,w)=(1,1,1)$. It's worthwhile to note that the three-dimensional $\overline{T}_L\left(\mathbf{k}_a\right)$ matrix is (block-block) Toeplitz and the multiplication of this matrix with a matrix that has the outgoing wave expansion values of all source boxes for each direction $\mathbf{k}_a$ can be seen as a three-dimensional circular convolution [87]:

$$\tilde{\mathbf{G}}_{u',v',w'}\left(\hat{\mathbf{k}}_a\right)=\sum_{u,v,w}T_L\left(\mathbf{k}_a,\left|\mathbf{r}_{u',v',w'}-\mathbf{r}_{u,v,w}\right|\right)\tilde{\mathbf{F}}_{u,v,w}\left(\hat{\mathbf{k}}_a\right)=\overline{T}_L\left(\mathbf{k}_a\right)*\overline{\mathbf{F}}\left(\hat{\mathbf{k}}_a\right). \tag{5.62}$$

Here

$$\bar{\mathbf{F}}\left(\hat{\mathbf{k}}_a\right)=\begin{bmatrix} \ddots & \vdots & \\ \cdots & \tilde{\mathbf{F}}_{u,v,w}\left(\hat{\mathbf{k}}_a\right) & \cdots \\ & \vdots & \ddots \end{bmatrix}_{U\times V\times W} \tag{5.63}$$

and $u=1,\ldots,U$, $v=1,\ldots,V$, $w=-W+1,\ldots,W$. This convolution process is accelerated by FFT and inverse FFT (IFFT) operations as

$$\tilde{\mathbf{G}}_{u',v',w'}\left(\hat{\mathbf{k}}_a\right)=IFFT\left\{FFT\left\{\bar{T}_L\left(\mathbf{k}_a\right)\right\}FFT\left\{\bar{\mathbf{F}}\left(\hat{\mathbf{k}}_a\right)\right\}\right\}, \tag{5.64}$$

after increasing the dimensions of the $\bar{\mathbf{F}}\left(\hat{\mathbf{k}}_a\right)$ matrix to $\left(2U-1\right)\times\left(2V-1\right)\times\left(2W-1\right)$ and padding zero to the additional space in matrix. In practice, the factor $FFT\left\{\bar{T}_L\left(\mathbf{k}_a\right)\right\}$ is computed prior to the matrix-vector multiplication stage of the FMM. Also the factor $FFT\left\{\bar{\mathbf{F}}\left(\hat{\mathbf{k}}_a\right)\right\}$ is computed in the matrix-vector multiplication stage of the FMM since the current coefficients are updated by the iterative solver in each iteration.

5.3 Numerical Results

This section illustrates the validation of the three-dimensional full wave solver and the application of the proposed framework to the statistical characterization of EM wave propagation in realistically loaded mine tunnel configurations.

5.3.1 The Validation of Three-Dimensional Full-Wave Solver

To validate the three-dimensional full-wave solver, two different straight rectangular mine tunnel configurations are considered. In both configurations, the

constitutive parameters of mine walls are chosen as $\varepsilon_r = 3$, $\mu_r = 1$, and $\sigma = 0.001\,\text{S/m}$, the cross-sections of both tunnels are $1.85\text{m} \times 2.24\text{m}$ (width×height), and dipoles with unit moments are used as transmitters.

5.3.1.1 325m Long Tunnel

In the first example, EM wave propagation in a 325m long straight rectangular mine tunnel is characterized [Figure 5–4]. A *z*-directed dipole operating at $455\,\text{MHz}$ is positioned at $(0.9, 50, 1)\,\text{m}$. The mine walls are discretized using $N = 11,641,728$ RWG basis functions; the average RWG edge size is $3.9\,\text{cm}$. To validate the accuracy of the full-wave solver, the magnitudes of the E-field's *z*-component, $|E_z|$, are computed at points on a line between $(0.9, 51, 1)\,\text{m}$ and $(0.9, 325, 1)\,\text{m}$; the points on the line are selected with $10\,\text{cm}$ spacing. The $|E_z|$ values obtained by the full-wave solver are compared with those obtained by approximate multi-modal decomposition method in [86] [Figure 5–5].

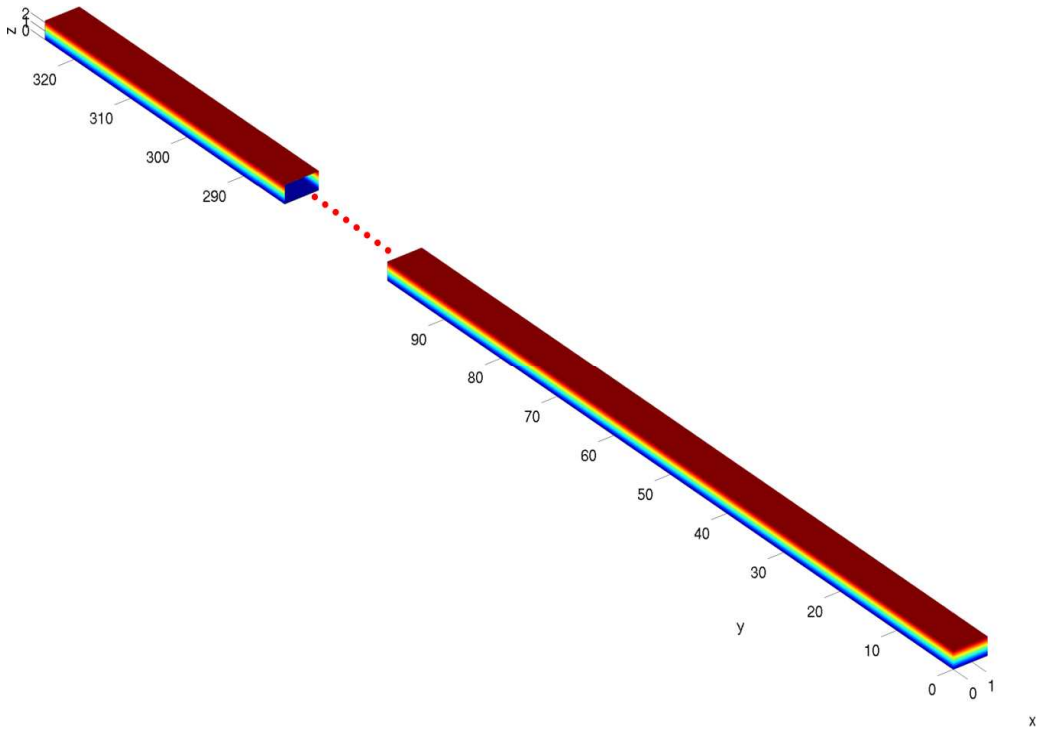

Figure 5–4 The geometry of 325m long mine tunnel with the cross-section of $1.85\text{m}\times 2.24\text{m}$.

The $|E_z|$ values obtained by multi-modal decomposition are vertically displaced 50dB away from the $|E_z|$ values obtained by full-wave solver for easier visual comparison. It is apparent from Figure 5–5 that the results are in good agreement. As the multi-modal decomposition method only computes *z*- polarized hybrid modes and ignores the other modes launched from the source, its prediction of the $|E_z|$ values in the near-field of the dipole is questionable. Moreover, since the multi-modal decomposition formulation neglects the effects of the walls at both ends of mine tunnel, it cannot capture the standing wave phenomena that occurs near the wall at $y = 325\text{ m}$.

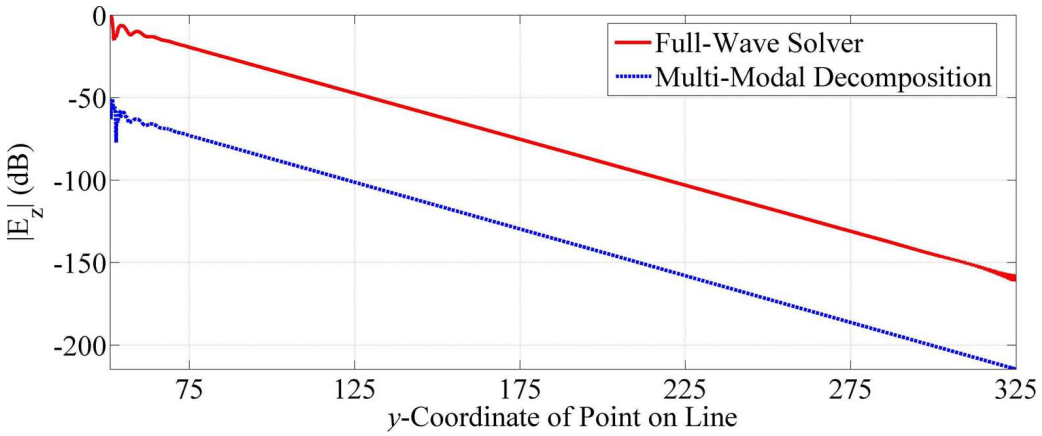

Figure 5–5 The $|E_z|$ values obtained by full-wave solver and multi-modal decomposition for 325 m long tunnel (the latter is displaced 50 dB downward).

5.3.1.2 250m Long Tunnel

In the second example, EM wave propagation in a 250m long straight rectangular mine tunnel is characterized [Figure 5–6]. An *x*-directed dipole operating at $915\,\text{MHz}$ is positioned at $(0.9, 50, 1)\,\text{m}$. The mine walls are discretized using $N = 30,874,992$ RWG basis functions; the average RWG edge size is $2.4\,\text{cm}$. The magnitudes of the E-field's *x*-component, $|E_x|$, are computed at points with 10cm spacing on a line between $(0.9, 51, 1)\,\text{m}$ and $(0.9, 250, 1)\,\text{m}$. The $|E_x|$ values obtained by the full-wave solver are compared with those obtained by multi-modal decomposition [86] [Figure 5–7]. The results obtained by multi-modal decomposition are displaced 50dB downward for easier visual comparison. Again, the results are seen to be in good agreement.

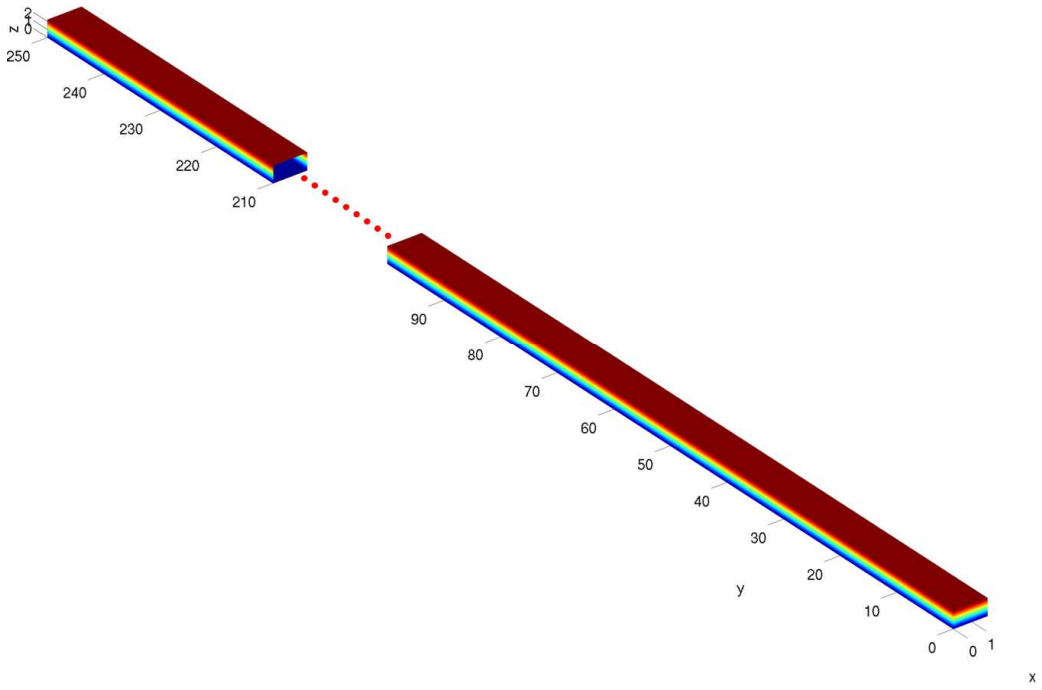

Figure 5–6 The geometry of 250m long mine tunnel with the cross-section of $1.85\text{m}\times 2.24\text{m}$.

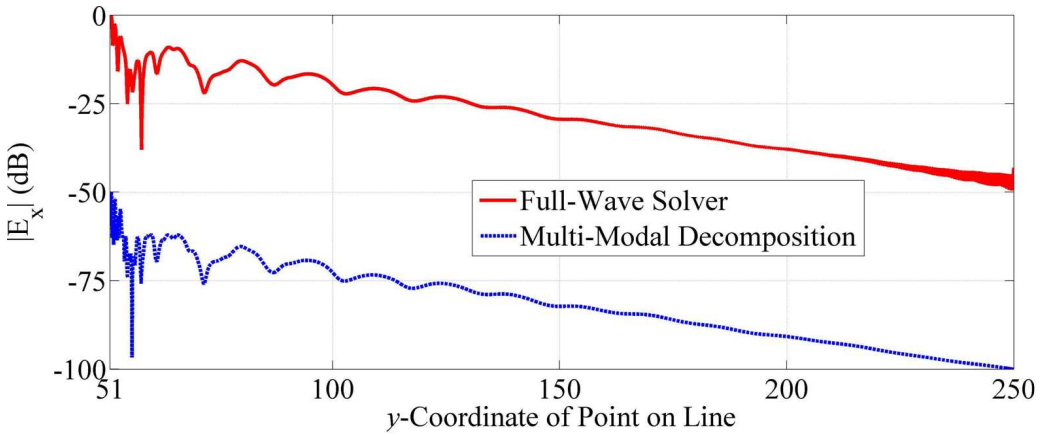

Figure 5–7 The $|E_x|$ values obtained by full-wave solver and multi-modal decomposition for 250 m long tunnel (the latter is displaced 50 dB downward).

5.3.2 The Application to the Statistical Characterization of EM Wave Propagation

In the example considered here, the transmitter is a *z*-directed dipole operating at 455 MHz and positioned at (r_x, r_y, r_z) , the constitutive parameters of the mine walls are $\varepsilon_r = 3$, $\mu_r = 1$, and $\sigma = 0.001\,\text{S/m}$, and the dimensions of the mine tunnel are $1.85\text{m} \times 2.24\text{m} \times 30\text{m}$ (width×height×length) [Figure 5–8]. PEC mine carts are modeled by truncated inverted pyramids with the base and top cross-sections of $0.5\text{m} \times 0.6\text{m}$ and $0.8\text{m} \times 0.6\text{m}$, respectively; the heights of the truncated inverted pyramids are 0.6m [Figure 5–8]. The wheels of the mine carts are formed by circular plates with the radii of $0.1\,\text{m}$. The center positions of the carts are represented by (cx_j, cy_j, cz_j) $j = 1, \ldots, 4$. The observables are the magnitudes of the E-field's *z*-component, $\left|E_z(\mathbf{x})\right|$, computed at various receiver points using three-dimensional full-wave EM simulator. The error in surrogate model is computed using

$$err^{\text{k}} = \sqrt{\sum_{i=1}^{160} \left(\left|E_z(\mathbf{x}_i)\right| - \left|E_z^{\text{k}}(\mathbf{x}_i)\right| \right)^2 \Big/ \sum_{i=1}^{160} \left|E_z(\mathbf{x}_i)\right|^2}, \tag{5.65}$$

where $\left|E_z^{\text{k}}(\mathbf{x})\right|$ is the surrogate model generated using the ME-PC method with $\beta = \text{k}$ and $\tau_1 = \tau_2 = 0.5$ and $\mathbf{x}_i$ is the randomly chosen evaluation point. The approximation to the pdf of $\left|E_z(\mathbf{x})\right|$ is generated by running a 1,000,000 point MC run on $\left|E_z^{\text{k}}(\mathbf{x})\right|$.

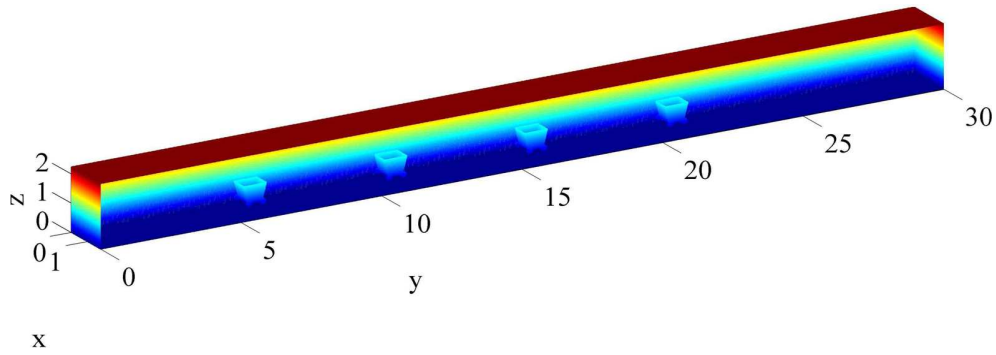

Figure 5–8 The geometry of a straight rectangular mine tunnel loaded with mine carts.

5.3.2.1 Dipole

In the first scenario, r_x, r_y, and r_z are random variables uniformly distributed in $[0.625,1.125]$ m, $[0.82,1.42]$ m, and $[1.0,1.6]$ m ($\mathbf{x}=[r_x,r_y,r_z]$, $N_{\text{dof}}=3$). The centers of mine carts (cx_j,cy_j,cz_j), $j=1,\ldots,4$, are positioned at $(0.65,6+(j-1)\times 5,0.55)$ m, $j=1,\ldots,4$. To illustrate the nature of the EM wave propagation in this mine tunnel configuration, the densities of electric and magnetic currents induced on dielectric mine walls and PEC cart surfaces are plotted in Figure 5–9 when the dipole is fixed at $(0.925,1,1.12)$ m. The observables, $|E_z(\mathbf{x})|$, are computed at receivers located on grid points selected in a cube with side length of 0.6 m and centered at $(0.925,25.0,1.12)$ m; the spacing between grid points along *x*-, *y*-, and *z*- directions is 0.06 m and total number of grid points in cube is 1331.

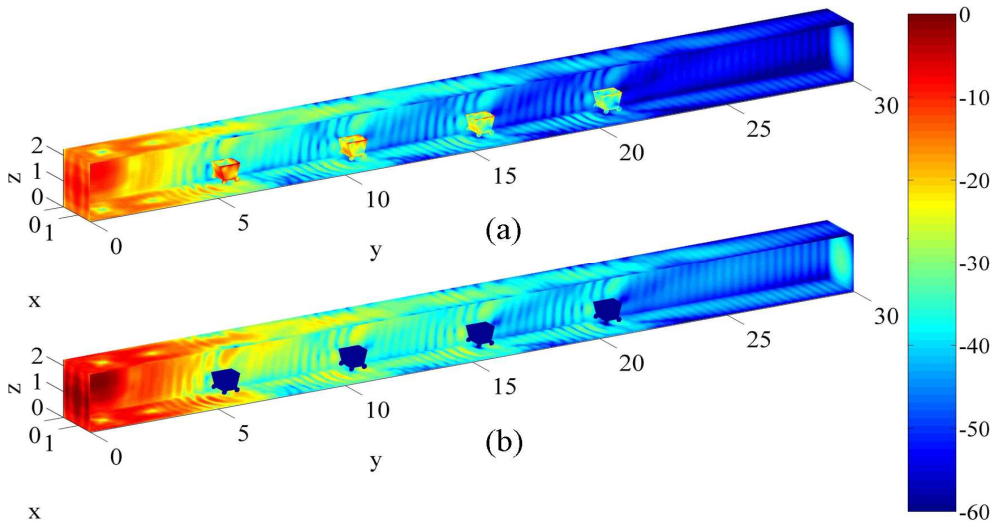

Figure 5–9 The densities of (a) electric and (b) magnetic currents induced on mine tunnel walls and mine carts when the dipole is positioned at $(0.925,1,1.12)$ m .

The surrogate models $\left|E_z^{\mathrm{k}}(\mathbf{x})\right|$, $\mathrm{k}=\{10^{-1}\}$, are constructed via the ME-PC method with $\beta=\{10^{-1}\}$; the ME-PC method uses the TP integration method with five Gauss-Legendre points in each dimension to compute the coefficients of local gPC expansions with $p=4$. To obtain $\left|E_z^{\mathrm{k}}(\mathbf{x})\right|$, $\mathrm{k}=\{10^{-1}\}$, the proposed method required $\{375\}$ deterministic simulations. The maximum of err^{k}, $\mathrm{k}=\{10^{-1}\}$, is computed as $\{6.4387\}\times10^{-3}$. The pdf of $\left|E_z(\mathbf{x})\right|$ (approximated by that of $\left|E_z^{\mathrm{k}}(\mathbf{x})\right|$) computed at receivers match with Nakagami distribution [Figure 4–2].

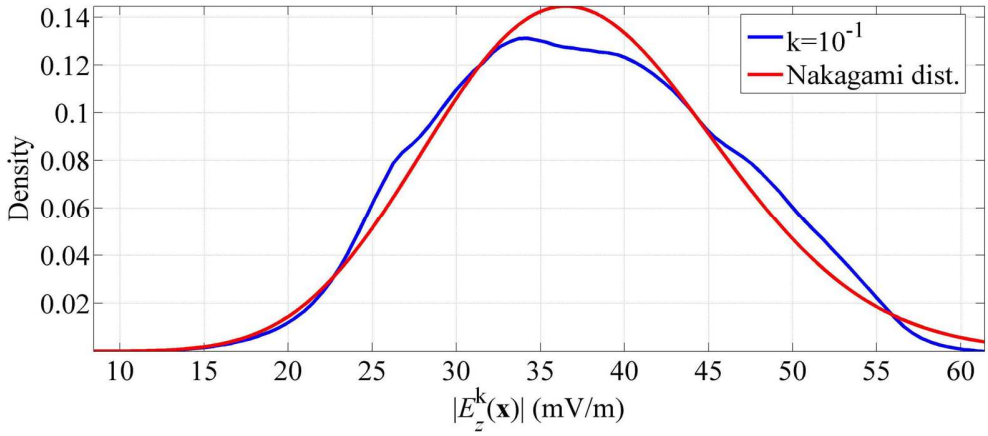

Figure 5–10 Empirical pdf of $\left|E_z^{\mathrm{k}}(\mathbf{x})\right|$, $\mathrm{k}=\{10^{-1}\}$, at receiver points and its best fitting distribution (3D Case).

5.3.2.2 PEC Carts

In the second scenario, cy_j, $j=1,\ldots,4$, are random variables uniformly distributed in $[5.7,6.3]$ m, $[10.7,11.3]$ m, $[15.7,16.3]$ m, and $[20.7,21.3]$ m, respectively, while cx_j and cz_j are set to their nominal values and the transmitter is positioned at $(0.925,1,1.12)$ m ($\mathbf{x}=[cy_1,\ldots,cy_4]$, $N_{\mathrm{dof}}=4$). The observables, $\left|E_z(\mathbf{x})\right|$, are computed at receivers located on grid points selected in a cube specifications of which are given in Section 5.3.2.1. The surrogate models $\left|E_z^{\mathrm{k}}(\mathbf{x})\right|$, $\mathrm{k}=\{10^{-1}\}$, are constructed via the ME-PC method with $\beta=\{10^{-1}\}$; the ME-PC method uses the Gauss-Legendre quadrature based SG integration method (with $l=2$) to compute the coefficients of local gPC expansions with $p=2$. To obtain $\left|E_z^{\mathrm{k}}(\mathbf{x})\right|$, $\mathrm{k}=\{10^{-1}\}$, the proposed method required $\{969\}$ deterministic simulations. The maximum of err^{k}, $\mathrm{k}=\{10^{-1}\}$, is computed as $\{5.0691\}\times10^{-2}$. The pdf of $\left|E_z(\mathbf{x})\right|$ (approximated by that of $\left|E_z^{\mathrm{k}}(\mathbf{x})\right|$) computed at receivers match with Weibull distribution [Figure 5–11].

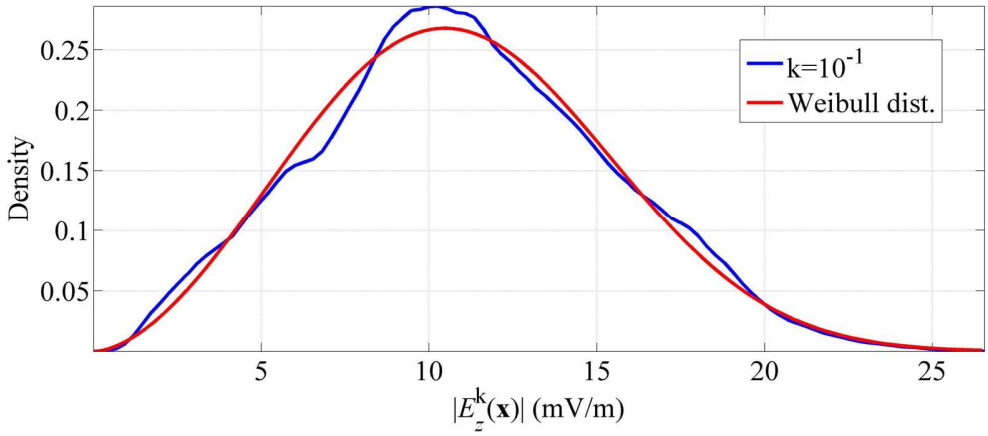

Figure 5–11 Empirical pdf of $\left|E_z^{\mathrm{k}}(\mathbf{x})\right|$, $\mathrm{k}=\{10^{-1}\}$, at receiver points and its best fitting distribution (4D Case).

CHAPTER 6
HIGH DIMENSIONAL MODEL REPRESENTATION TECHNIQUE

6.1 Introduction

The ME-PC method introduced in Section 3.2.2 is highly efficient and accurate for surrogate model generation of EM observables that vary rapidly and/or are discontinuous functions of random variables. However, its applicability is limited to the moderate-dimensional random domains as the number of subdomains resulting from adaptive refinement and the number of collocation points in each subdomain become excessively large while N_{dof} increases. The former is attributed to the fact that the number of subdomains scales with $2^{N_{\text{dof}}}$ when the adaptive refinement is performed along all dimensions. The latter is attributed to the fact that even the SG construction yields tens of thousands of collocation points for the evaluation of local gPC expansion in each subdomain when $N_{\text{dof}} \geq 10$.

The abovementioned difficulties in constructing the surrogate models in high-dimensions are not unique to the methods for UQ and have also been encountered in methods used to model the input-output relationships of physical systems. This issue has motivated the researchers to develop a reduced-order representation of input-output relationship so called high-dimensional model representation (HDMR) expansion. The

HDMR expansion, also called as ANOVA (analysis of variance) decomposition in statistics, was first introduced by Fisher [36] and has been applied in many contexts other than surrogate model generation [39, 110, 111]. Later on, it was re-introduced in [35] to obtain surrogate models of input-output relationships in chemical systems and applied to the finance to compute multivariate integrals [43] and ultimately to the UQ via ME-PC method [39] and adaptive sparse grid collocation method [40].

This chapter elucidates an HDMR extension to the ME-PC method that permits the accurate and efficient construction of surrogate models for EM observables in high-dimensions. The HDMR expansion expresses the observable as finite sums of "component functions" that represent independent and combined contributions of random variables to the observable [35]; The HDMR expansion is built iteratively by including only the "most significant" component functions to minimize the computational cost of building the surrogate model [42, 46]. The component functions that feature in the HDMR expansion are approximated via the ME-PC method. HDMR-generated surrogate models enable the efficient and accurate stochastic characterization of electronic systems subject to many more manufacturing uncertainties that can not be addressed using the ME-PC method. The technique derives its efficiency from the fact that only low-order correlations between random variables that contribute significantly to an observable are incorporated in the expansion; the method automatically excludes less significant high-order contributions from the surrogate model, thereby dramatically reducing the computational cost associated with its generation and evaluation. To the best of our knowledge, the method proposed here is the first systematic approach to the statistical characterization of EM observables in high-dimensional random domains using the

HDMR method. It's also unique among UQ methods since it significantly differs from the work in [39], which combines the ME-PC method with non-iteratively constructed HDMR expansions. In addition, the proposed method is finely-tuned for stochastic EM analysis via its hybridization with a vector-fitting algorithm. The applicability of the proposed method is demonstrated via its application to the statistical characterization of voltages in various transmission line networks and a cascaded multiconductor transmission line network.

6.2 The Formulation

This section details the iterative HDMR method for characterizing observables in high dimensional random domains. The HDMR expansion is described first. Then, the integration of the HDMR expansion with the ME-PC method is expounded. An iterative scheme to construct the HDMR expansion by including only the most significant component functions is explained next. Finally, the hybridization of HDMR technique with the vector fitting algorithm for efficient and accurate stochastic EM analysis is described.

6.2.1 The HDMR Technique

The HDMR expansion enables to approximate $V(\mathbf{x})$ in terms of component functions as [35, 40]

$$V(\mathbf{x}) = \sum_{\mathbf{u}\subseteq\Omega} V_{\mathbf{u}}(\mathbf{x}^{\mathbf{u}}), \tag{6.1}$$

where $\Omega = \{1, \ldots, N_{\text{dof}}\}$ is the general set of random variable indices, $\mathbf{u}$ is a subset of Ω, i.e. $\mathbf{u} \subseteq \Omega$, and $|\mathbf{u}|$ denotes the cardinality of subset $\mathbf{u}$. $\mathbf{x}^{\mathbf{u}}$ is a $|\mathbf{u}|$-dimensional random vector and $V_{\mathbf{u}}(\mathbf{x}^{\mathbf{u}})$ represents the component functions defined over D. For example, for $\mathbf{u} = \varnothing$, $V_{\mathbf{u}}(\mathbf{x}^{\mathbf{u}}) = V_{\varnothing}(x^{\varnothing}) = V_0$ is the zeroth-order component function which is constant over D; for $\mathbf{u} = \{1\}$, $V_{\mathbf{u}}(\mathbf{x}^{\mathbf{u}}) = V_1(x^1)$ is the first-order component function that represents the individual contribution of x^1 to $V(\mathbf{x})$; for $\mathbf{u} = \{1,2\}$, $V_{\mathbf{u}}(\mathbf{x}^{\mathbf{u}}) = V_{12}(x^1, x^2)$ is the second-order component function that describes the interactive contribution of x^1 and x^2 to $V(\mathbf{x})$; and for $\mathbf{u} = \{1,2,4\}$, $V_{\mathbf{u}}(\mathbf{x}^{\mathbf{u}}) = V_{124}(x^1, x^2, x^4)$ is the third-order component function that reveals the combined contribution of x^1, x^2, and x^4 to $V(\mathbf{x})$. The HDMR construction in (6.1) can be better described by an example. Assume that $N_{\text{dof}} = 3$ and $\Omega = \{1,2,3\}$. All possible subsets of Ω, $\mathbf{u}$, and all component functions $V_{\mathbf{u}}(\mathbf{x}^{\mathbf{u}})$ corresponding to these possible subsets are given in Table 6–1.

Subset, $\mathbf{u}$	Component function, $V_{\mathbf{u}}(\mathbf{x}^{\mathbf{u}})$	Cardinality of $\mathbf{u}$, $\lvert\mathbf{u}\rvert$
$\varnothing$	V_0	0
{1}	$V_1(x^1)$	1
{2}	$V_2(x^2)$	1
{3}	$V_3(x^3)$	1
{1,2}	$V_{12}(x^1, x^2)$	2
{1,3}	$V_{13}(x^1, x^3)$	2
{2,3}	$V_{23}(x^2, x^3)$	2
{1,2,3}	$V_{123}(x^1, x^2, x^3)$	3

Table 6–1 The correspondence between subsets of $\Omega = \{1,2,3\}$ and the component functions used to build HDMR expansion and the cardinalities of subsets.

For this example case, one can construct the HDMR expansion in (6.1) using the component functions given in Table 6–1 as

$$V(\mathbf{x}) = V_0 + V_1\left(x^1\right) + V_2\left(x^2\right) + V_3\left(x^3\right) + V_{12}\left(x^1, x^2\right) + V_{13}\left(x^1, x^3\right) + V_{23}\left(x^2, x^3\right) + V_{123}\left(x^1, x^2, x^3\right). \quad (6.2)$$

The advantage of such construction can be illustrated by selecting an observable that consists of a constant term and monomials such as $V(\mathbf{x}) = 1 + \left(x^1\right)^2 + \left(x^2\right)^2 + \left(x^3\right)^2$, (Note: the indices (or superscripts) of random variables are written inside parentheses while their powers are intentionally left outside to avoid confusion). The component functions V_0, $V_1\left(x^1\right)$, $V_2\left(x^2\right)$, and $V_3\left(x^3\right)$ in (6.2) are needed to approximate $V(\mathbf{x})$ while the remaining component functions in (6.2) are redundant. In many physical systems, like in this example observable, the low-order component functions significantly contribute to the observables; this fact renders the HDMR expansions highly suitable for surrogate model generation of $V(\mathbf{x})$ in high-dimensional random domains using the low-order component functions (i.e. surrogate models constructed in lower-dimensional random domains).

Depending on the way of obtaining component functions, two different types of HDMR techniques are proposed in literature: ANOVA-HDMR and CUT-HDMR. ANOVA-HDMR utilizes analysis of variance (ANOVA) decomposition used in statistics, which measures the contribution of each component function's variance to the global variance of observable [37]. To obtain component functions, such technique requires the numerical evaluation of N_{dof}-dimensional integral which is prohibitively expensive as

discussed at the beginning of Section 4.1. On the other hand, CUT-HDMR technique [35] obtains the component functions using the observable values on lines, planes, and hyperplanes passing through a reference point in random domain. To this end, the CUT-HDMR technique is much more efficient than ANOVA-HDMR technique and is the focus of this study. Both methods with the emphasis on CUT-HDMR method are reviewed next.

6.2.1.1 ANOVA-HDMR

In ANOVA-HDMR, the component functions are approximated as [37, 44, 103]

$$V_{\mathbf{u}}\left(\mathbf{x}^{\mathbf{u}}\right)=\int_{D^{\Omega\setminus\mathbf{u}}} V\left(\mathbf{x}\right)d\mathbf{x}^{\Omega\setminus\mathbf{u}}-\sum_{\mathbf{v}\subset\mathbf{u}} V_{\mathbf{v}}\left(\mathbf{x}^{\mathbf{v}}\right). \tag{6.3}$$

Here $\mathbf{x}^{\Omega\setminus\mathbf{u}}$ represents the vector of random variables whose indices are different than the indices belonging to subset $\mathbf{u}$. Note that the integration domain $D^{\Omega\setminus\mathbf{u}}$ is the random domain where the random vector $\mathbf{x}^{\Omega\setminus\mathbf{u}}$ lies and $\mathbf{v}$ is a subset of $\mathbf{u}$. For the example given above, the component functions obtained via ANOVA-HDMR are given as follows:

$$
\begin{aligned}
|\mathbf{u}| = 0, \quad & V_0 = \int_D V(\mathbf{x})\, d\mathbf{x}, \\
|\mathbf{u}| = 1, \quad & V_1(x^1) = \int_{D^2}\int_{D^3} V(\mathbf{x})\, dx^2 dx^3 - V_0, \\
& V_2(x^2) = \int_{D^1}\int_{D^3} V(\mathbf{x})\, dx^1 dx^3 - V_0, \\
& V_3(x^3) = \int_{D^1}\int_{D^2} V(\mathbf{x})\, dx^1 dx^2 - V_0, \\
|\mathbf{u}| = 2, \quad & V_{12}(x^1, x^2) = \int_{D^3} V(\mathbf{x})\, dx^3 - V_0 - V_1(x^1) - V_2(x^2), \\
& V_{13}(x^1, x^3) = \int_{D^2} V(\mathbf{x})\, dx^2 - V_0 - V_1(x^1) - V_3(x^3), \\
& V_{23}(x^2, x^3) = \int_{D^1} V(\mathbf{x})\, dx^1 - V_0 - V_2(x^2) - V_3(x^3), \\
|\mathbf{u}| = 3, \quad & V_{123}(x^1, x^2, x^3) = V(\mathbf{x}) - V_{12}(x^1, x^2) - V_{13}(x^1, x^3) - V_{23}(x^2, x^3) \\
& \qquad - V_1(x^1) - V_2(x^2) - V_3(x^3) - V_0.
\end{aligned}
\tag{6.4}
$$

Summing the recursively constructed component functions by ANOVA-HDMR yields a finite and exact expansion of $V(\mathbf{x})$. Nevertheless, the construction of each component function is computationally costly as each component function has V_0 term, computation of which calls for numerical evaluation of N_{dof}-dimensional integral. In practice, the V_0 term is computed via N_{MC}- point MC method [104]. Then the first-order component functions are computed by selecting m distinct values of x^i, $i = 1, \ldots, N_{\text{dof}}$, along each dimension, for each random point selected during computation of V_0. Note that while the value of x^i changes, the values of other random variables are set to their corresponding values of random point. By doing so, mN_{MC} deterministic simulations are needed to compute each first-order component function. The second-order component functions are computed in a similar fashion: both x^i and x^j, $i, j = 1, \ldots, N_{\text{dof}}$, $i \neq j$, take m distinct values on a Cartesian grid formed by their products while the remaining random variables

are set to their corresponding values of random point. At this case, $m^2 N_{\mathrm{MC}}$ deterministic simulations are needed to obtain each second order component functions [104]. To this end, the application of ANOVA-HDMR to the surrogate model generation in high-dimensional random domains is not efficient for large-scale EM problems.

6.2.1.2 CUT-HDMR

In CUT-HDMR, the component functions are expressed in terms of observable values on cuts passing through a reference point $\bar{\mathbf{x}}$ [35, 38], i.e.

$$V_{\mathbf{u}}\left(\mathbf{x}^{\mathbf{u}}\right) = V\left(\mathbf{x}^{\mathbf{u}}\right)\Big|_{\mathbf{x}=\bar{\mathbf{x}}\setminus\mathbf{x}^{\mathbf{u}}} - \sum_{\mathbf{v}\subset\mathbf{u}} V_{\mathbf{v}}\left(\mathbf{x}^{\mathbf{v}}\right), \tag{6.5}$$

where $\mathbf{x} = \bar{\mathbf{x}} \setminus \mathbf{x}^{\mathbf{u}}$ indicates that the random variables whose indices other than the indices belonging to subset $\mathbf{u}$ are set to the corresponding values of reference point. The reference point in this study is select as the mass center of D, i.e., $\bar{\mathbf{x}} = \left[\bar{x}^1, \ldots, \bar{x}^{N_{\mathrm{dof}}}\right] = \left[(a^1 + b^1)/2, \ldots, (a^{N_{\mathrm{dof}}} + b^{N_{\mathrm{dof}}})/2\right]$. It may be selected as the centroid of SG integration rule [105], as a random point at which the observable value is closest to the global mean [106], or as a random point determined due to the weights of dimensions [107]. For the example given above, the component functions obtained via CUT-HDMR are given as follows:

$$
\begin{aligned}
&|\mathbf{u}|=0, \quad V_0 = V\left(\bar{\mathbf{x}}\right), \\
&|\mathbf{u}|=1, \quad V_1\left(x^1\right) = V\left(x^1, \bar{x}^2, \bar{x}^3\right) - V_0, \\
&\qquad\quad V_2\left(x^2\right) = V\left(\bar{x}^1, x^2, \bar{x}^3\right) - V_0, \\
&\qquad\quad V_3\left(x^3\right) = V\left(\bar{x}^1, \bar{x}^2, x^3\right) - V_0, \\
&|\mathbf{u}|=2, \quad V_{12}\left(x^1, x^2\right) = V\left(x^1, x^2, \bar{x}^3\right) - V_0 - V_1\left(x^1\right) - V_2\left(x^2\right), \\
&\qquad\quad V_{13}\left(x^1, x^3\right) = V\left(x^1, \bar{x}^2, x^3\right) - V_0 - V_1\left(x^1\right) - V_3\left(x^3\right), \\
&\qquad\quad V_{23}\left(x^2, x^3\right) = V\left(\bar{x}^1, x^2, x^3\right) - V_0 - V_2\left(x^2\right) - V_3\left(x^3\right), \\
&|\mathbf{u}|=3, \quad V_{123}\left(x^1, x^2, x^3\right) = V\left(x^1, x^2, x^3\right) - V_{12}\left(x^1, x^2\right) - V_{13}\left(x^1, x^3\right) - V_{23}\left(x^2, x^3\right) \\
&\qquad\qquad\qquad - V_1\left(x^1\right) - V_2\left(x^2\right) - V_3\left(x^3\right) - V_0.
\end{aligned}
\quad . \quad (6.6)
$$

To recursively obtain the component functions, the observable value on reference point $\bar{\mathbf{x}}$ (for $|\mathbf{u}|=0$) is computed and the observable values on lines (for $|\mathbf{u}|=1$), planes (for $|\mathbf{u}|=2$), and hyperplanes (for $|\mathbf{u}|\geq 3$) passing through $\bar{\mathbf{x}}$ are interpolated using the ME-PC method described in Section 3.2.2. Note that the computation of V_0 term only requires the computation of observable value on $\bar{\mathbf{x}}$ which is much cheaper than the evaluation of N_{dof}-dimensional integral in ANOVA-HDMR technique.

There is a striking resemblance between the HDMR expansion and multivariate Taylor expansion [40, 108], which can be written for the above given example as [109, 110]

$$
\begin{aligned}
V\left(\mathbf{x}\right) = V\left(\bar{\mathbf{x}}\right) &+ \sum_{i^1=1}^{N_{\text{dof}}} \sum_{j=1}^{\infty} \frac{1}{j!} \frac{\partial^j V}{\partial (x^{i^1})^j} \left(\bar{\mathbf{x}}\right) \left(x^{i^1} - \bar{x}^{i^1}\right)^j + \\
&\sum_{i^1<i^2}^{N_{\text{dof}}} \sum_{j=1}^{\infty} \sum_{k=1}^{\infty} \frac{1}{j!k!} \frac{\partial^{j+k} V}{\partial (x^{i^1})^j (x^{i^2})^k} \left(\bar{\mathbf{x}}\right) \left(x^{i^1} - \bar{x}^{i^1}\right)^j \left(x^{i^2} - \bar{x}^{i^2}\right)^k + \\
&\sum_{j=1}^{\infty} \sum_{k=1}^{\infty} \sum_{l=1}^{\infty} \frac{1}{j!k!l!} \frac{\partial^{j+k+l} V}{\partial (x^1)^j (x^2)^k (x^3)^l} \left(\bar{\mathbf{x}}\right) \left(x^1 - \bar{x}^1\right)^j \left(x^2 - \bar{x}^2\right)^k \left(x^3 - \bar{x}^3\right)^l
\end{aligned}
\quad . \quad (6.7)
$$

By expanding the summations with indices i^1 and i^2, the correspondence between each term of Taylor expansion and each component function of HDMR expansion can be revealed. The terms which are solely functions of x^{i^1}, $i^1 = 1,\ldots,3$, correspond to the first order component functions while those which contain x^{i^1} and x^{i^2}, $i^1, i^2 = 1,\ldots,3; i^1 < i^2$, are pertinent to the second order component functions. It's apparent from (6.6) and (6.7) that the HDMR expansion is finite and exact while the Taylor expansion is infinite and approximate. For this reason, it's expected that the HDMR expansion should provide more accurate approximations to the observables than the Taylor expansion [40, 108-110].

6.2.2 Integrating HDMR with ME-PCM

In CUT-HDMR context, the HDMR expansion can be explicitly written as [111]

$$V(\mathbf{x}) = \sum_{\mathbf{u}\subseteq\Omega} V_{\mathbf{u}}(\mathbf{x}^{\mathbf{u}}) = \sum_{\mathbf{u}\subseteq\Omega}\sum_{\mathbf{v}\subseteq\mathbf{u}} (-1)^{|\mathbf{u}|-|\mathbf{v}|} V(\mathbf{x}^{\mathbf{v}})\Big|_{\mathbf{x}=\bar{\mathbf{x}}\setminus\mathbf{x}^{\mathbf{v}}}, \tag{6.8}$$

(Note: See [111] for the proof). As illustrated above, the term $V(\mathbf{x}^{\mathbf{v}})\Big|_{\mathbf{x}=\bar{\mathbf{x}}\setminus\mathbf{x}^{\mathbf{v}}}$ in (6.8) represents the observable values on cuts formed along the random variables whose indices belong to subset $\mathbf{v}$ while the remaining random variables are set to the corresponding values of $\bar{\mathbf{x}}$. Let $\tilde{D}^{\mathbf{v}} = \prod_{i=1}^{|\mathbf{v}|} \tilde{D}^{\mathbf{v}^i}$ with $\tilde{D}^{\mathbf{v}^i} = \left[\tilde{a}^{\mathbf{v}^i}, \tilde{b}^{\mathbf{v}^i}\right]$ denote a cut (line, plane, or hyperplane) in random domain formed along dimensions with indices belonging to subset $\mathbf{v}$ and considered for the adaptive refinement by the ME-PC method, here $\mathbf{v}^i$ denotes i^{th} element of subset $\mathbf{v}$. In what follows, a $\mathbf{v}$ superscript on a symbol indicates

that it represents a quantity pertinent to cut $\tilde{D}^{\mathbf{v}}$. The term $V\left(\mathbf{x}^{\mathbf{v}}\right)\Big|_{\mathbf{x}=\bar{\mathbf{x}}\setminus\mathbf{x}^{\mathbf{v}}}$ in (6.8) can be approximated using the p^{th} - order local gPC expansion as

$$V\left(\mathbf{x}^{\mathbf{v}}\right)\Big|_{\mathbf{x}=\bar{\mathbf{x}}\setminus\mathbf{x}^{\mathbf{v}}} = \sum_{m=0}^{N_p} \tilde{v}_m^{\mathbf{v}}\, \tilde{\mathbf{P}}_m\left(\mathbf{x}^{\mathbf{v}}\right)\Big|_{\mathbf{x}=\bar{\mathbf{x}}\setminus\mathbf{x}^{\mathbf{v}}}, \tag{6.9}$$

where $\tilde{v}_m^{\mathbf{v}}$ and $\tilde{\mathbf{P}}_m\left(\mathbf{x}^{\mathbf{v}}\right)\Big|_{\mathbf{x}=\bar{\mathbf{x}}\setminus\mathbf{x}^{\mathbf{v}}}$, $m=0,\ldots,N_p$, denote the local gPC coefficients and $|\mathbf{v}|$-variate local orthogonal Legendre polynomial basis functions (defined over cut $\tilde{D}^{\mathbf{v}}$). Inserting (6.9) into (6.8), an approximation to each component functions $V_{\mathbf{u}}\left(\mathbf{x}^{\mathbf{u}}\right)$ and therefore $V\left(\mathbf{x}\right)$ is obtained:

$$V\left(\mathbf{x}\right) = \sum_{\mathbf{u}\subseteq\Omega} V_{\mathbf{u}}\left(\mathbf{x}^{\mathbf{u}}\right) = \sum_{\mathbf{u}\subseteq\Omega}\sum_{\mathbf{v}\subseteq\mathbf{u}} (-1)^{|\mathbf{u}|-|\mathbf{v}|} \sum_{m=0}^{N_p} \tilde{v}_m^{\mathbf{v}}\, \tilde{\mathbf{P}}_m\left(\mathbf{x}^{\mathbf{v}}\right)\Big|_{\mathbf{x}=\bar{\mathbf{x}}\setminus\mathbf{x}^{\mathbf{v}}}. \tag{6.10}$$

The local gPC coefficients, $\tilde{v}_m^{\mathbf{v}}$, $m=0,\ldots,N_p$, are obtained by evaluating a $|\mathbf{v}|$-variate integral over $\tilde{D}^{\mathbf{v}}$ (as in (3.6)). The expansion coefficients in (6.10) are obtained separately for all cuts defined along dimensions with indices belonging to $\mathbf{v}$. The refinement parameters $\gamma^{\mathbf{v}}$ and $\alpha^{\mathbf{v}^i}$, $i=1,\ldots,|\mathbf{v}|$, are also computed separately for all cuts. For each cut, If $\gamma^{\mathbf{v}}$ satisfies the refinement criterion [see (3.14)], the cut $\tilde{D}^{\mathbf{v}}$ is selected for the refinement. Likewise, a refinement is performed along the i^{th} dimension, if $\alpha^{\mathbf{v}^i}$, $i=1,\ldots,|\mathbf{v}|$, satisfies the dimensional refinement criterion [see (3.16)]. The adaptive refinement process produces $N_d^{\mathbf{v}}$ elements (for each cut) $\tilde{D}_j^{\mathbf{v}}$, $j=1,\ldots,N_d^{\mathbf{v}}$, which do not require adaptive refinement. The coefficients of p^{th} - order gPC expansions constructed

in such elements, $\tilde{D}_j^{\mathbf{v}}$, $j=1,\ldots,N_d^{\mathbf{v}}$, are stored during the adaptive refinement process to obtain the surrogate model of $V(\mathbf{x})$ and thereby its global statistical moments.

By the law of total probability and using (3.17), the average of each component function can be approximated as

$$E\left[V_{\mathbf{u}}\left(\mathbf{x}^{\mathbf{u}}\right)\right] \cong \sum_{\mathbf{v}\subseteq\mathbf{u}} (-1)^{|\mathbf{u}|-|\mathbf{v}|} \sum_{j=1}^{N_d^{\mathbf{v}}} \tilde{v}_{0,j}^{\mathbf{v}} J_j^{\mathbf{v}}, \tag{6.11}$$

where $\tilde{v}_{0,j}^{\mathbf{v}}$ denotes the 0^{th} coefficient of the p^{th}- order local gPC expansion constructed in $\tilde{D}_j^{\mathbf{v}}$, $J_j^{\mathbf{v}}$ measures the size of $\tilde{D}_j^{\mathbf{v}}$ relative to $\tilde{D}^{\mathbf{v}}$, i.e., $J_j^{\mathbf{v}} = \prod_{i=1}^{|\mathbf{v}|} (\tilde{b}_j^{\mathbf{v}^i} - \tilde{a}_j^{\mathbf{v}^i}) \big/ (b^{\mathbf{v}^i} - a^{\mathbf{v}^i})$. Using (6.11), the global average of $V(\mathbf{x})$ over D can be estimated as

$$E\left[V(\mathbf{x})\right] \cong \sum_{\mathbf{u}\subseteq\Omega} E\left[V_{\mathbf{u}}\left(\mathbf{x}^{\mathbf{u}}\right)\right]. \tag{6.12}$$

In a similar way, the variance of each component function can be approximated via

$$\operatorname{var}\left[V_{\mathbf{u}}\left(\mathbf{x}^{\mathbf{u}}\right)\right] \cong \sum_{\mathbf{v}\subseteq\mathbf{u}} (-1)^{|\mathbf{u}|-|\mathbf{v}|} \sum_{j=1}^{N_d^{\mathbf{v}}} J_j^{\mathbf{v}} \left[\sum_{m=1}^{N_p} \left(\tilde{v}_{m,j}^{\mathbf{v}}\right)^2 + \left(\tilde{v}_{0,j}^{\mathbf{v}} - E\left[V_{\mathbf{u}}\left(\mathbf{x}^{\mathbf{u}}\right)\right]\right)^2 \right], \tag{6.13}$$

where $\tilde{v}_{m,j}^{\mathbf{v}}$ denotes the m^{th} coefficient of the p^{th}- order local gPC expansion constructed in $\tilde{D}_j^{\mathbf{v}}$. Using (6.13), the global variance of $V(\mathbf{x})$ over D can be estimated as

$$\operatorname{var}\left[V(\mathbf{x})\right] \cong \sum_{\mathbf{u}\subseteq\Omega} \operatorname{var}\left[V_{\mathbf{u}}\left(\mathbf{x}^{\mathbf{u}}\right)\right]. \tag{6.14}$$

6.2.3 Iterative HDMR Method

As mentioned in Section 6.2.1, the efficiency of HDMR technique directly depends on the proper selection of the most important component functions and inclusion of those in HDMR expansion. This matter is crucial as the number of component functions scales with $\sum_{j=0}^{|\mathbf{u}|} N_{\text{dof}}!/(j!(N_{\text{dof}}-j)!)$ which increases rapidly with N_{dof}.As an example, given that $|\mathbf{u}|=3$ and $N_{\text{dof}}=100$, the number of component functions that feature in HDMR expansion is 166751. For that reason, the direct application of CUT-HDMR in realistic large-scale problems for large N_{dof} is not feasible. The high cost of CUT-HDMR method can be reduced substantially by integrating an iterative scheme to the method, which automatically selects random variables that significantly contribute to $V(\mathbf{x})$ and iteratively includes these variables' higher-order component functions in the CUT-HDMR expansion.

In theory, the iterative scheme hinges upon determining *effective dimensionality* of high-dimensional observables [40, 44]. The indices of random variables that significantly contribute to $V(\mathbf{x})$ are specified in an index set that has minimum possible number of elements; this number is denoted by N_{t} and so called *truncation dimension* [40, 44]. The HDMR expansion constructed with such index set should satisfy

$$\sum_{\mathbf{u}\subseteq\{1,\ldots,N_{\text{t}}\}} E\left[V_{\mathbf{u}}\left(\mathbf{x}^{\mathbf{u}}\right)\right] \Big/ E\left[V(\mathbf{x})\right] > \delta, \tag{6.15}$$

where $\delta \in (0,1]$. Furthermore, the minimum possible number which represents the maximum order of component functions in HDMR expansion is denoted by N_{s} and so

called *superposition dimension* [40, 44]. The HDMR expansion constructed to such order should satisfy

$$\sum_{|\mathbf{u}|\subseteq N_s} E\left[V_{\mathbf{u}}\left(\mathbf{x}^{\mathbf{u}}\right)\right] \Big/ E\left[V\left(\mathbf{x}\right)\right] > \delta . \tag{6.16}$$

The superposition dimension is also called the order of HDMR expansion. In some cases, two components of effective dimensionality, N_t and N_s, can be estimated a priori due to the physics of the problem. In such cases, the HDMR expansion can be constructed by starting from the higher-order component functions to the lower-order ones (as in [39]). Note that the lower order component functions can be interpolated from the highest order ones with no computational cost. However, in many practical scenarios, N_t and N_s can not be known a priori and should be determined in a part of an iterative scheme. The main idea in such iterative scheme is assigning a weight to each component function which measures the contribution of each component function to the observable. Using these weights, the iterative scheme constructs the HDMR expansion starting from the lower-order component functions to the higher-order ones.

The iterative scheme starts by computing the weights associated with the first-order component functions as [40, 44]

$$\zeta_{\mathbf{u}} = \left| E\left[V_{\mathbf{u}}\left(\mathbf{x}^{\mathbf{u}}\right)\right] \Big/ V_0 \right| ; \quad |\mathbf{u}| = 1 . \tag{6.17}$$

The weights $\zeta_{\mathbf{u}}$ are measures of the contributions of first-order component functions' means to the overall mean computed via constant zeroth-order component function. If $\zeta_{\mathbf{u}}$ is larger than a prescribed tolerance ε_1, then the component function is assumed to

contribute significantly to $V(\mathbf{x})$. The indices of random variables pertinent to these important component functions are stored in the general index set $\Omega = \{1, \ldots, N_t\}$. The second-order component functions involving these important random variables whose indices belong to Ω are marked as candidates for constructing the HDMR expansion at the second level; they are only added to the expansion if their weights are larger than ε_1. This scheme is repeated in an iterative manner for all levels. For example, assume that the indices of the important random variables are found to be $\{1,2,4\}$. Then, the second-order component functions with indices $\{1,2\}$, $\{1,4\}$, and $\{2,4\}$ are considered to be included in the HDMR expansion at the second level. At the end of second level, assume that *any* of second-order component functions with indices $\{1,2\}$, $\{1,4\}$, and $\{2,4\}$ is found to be insignificant. Then none of third order component functions is considered to be included in the HDMR expansion since *all* component functions whose indices are the subsets of the index set of a candidate third-order component function should be indentified as significant. On the other hand, assume that second-order component functions with indices $\{1,2\}$, $\{1,4\}$, and $\{2,4\}$ are *all* found to be significant. Then, the third order component function with index $\{1,2,4\}$ is considered to be included in the HDMR expansion at the third level. Note that at the higher levels, the weights of the component functions $V_{\mathbf{u}}\left(x^{\mathbf{u}}\right)$, $|\mathbf{u}| \geq 2$ are computed by [40]

$$\zeta_{\mathbf{u}} = \left| E\left[V_{\mathbf{u}}\left(\mathbf{x}^{\mathbf{u}}\right)\right] \right| \Big/ \left| \sum_{|\mathbf{v}|<|\mathbf{u}|-1} E\left[V_{\mathbf{v}}\left(\mathbf{x}^{\mathbf{v}}\right)\right] \right|; \quad |\mathbf{u}| \geq 2. \tag{6.18}$$

To provide an additional stopping criterion, the decay rate of relative difference between observable means computed at two consecutive levels is defined as [40]

$$\kappa = \left| \sum_{|\mathbf{v}|<|\mathbf{u}|} E\left[V_{\mathbf{v}}\left(\mathbf{x}^{\mathbf{v}}\right)\right] - \sum_{|\mathbf{v}|<|\mathbf{u}|-1} E\left[V_{\mathbf{v}}\left(\mathbf{x}^{\mathbf{v}}\right)\right] \right| \Big/ \left| \sum_{|\mathbf{v}|<|\mathbf{u}|-1} E\left[V_{\mathbf{v}}\left(\mathbf{x}^{\mathbf{v}}\right)\right] \right|. \quad (6.19)$$

If κ is smaller than a prescribed tolerance ε_2, hen the cut-HDMR expansion is assumed to have converged and $|\mathbf{u}|$ is assigned as N_s. Once the iterative construction is completed, the component functions identified as insignificant are also included in the expansion to increase the accuracy of surrogate model since they have already been computed for identification. It should be noted here that decreasing the tolerance ε_1 may result in increasing number of component functions in HDMR expansion. And decreasing the tolerance ε_2 may yield increasing number of iterations in iterative scheme. A couple of notes regarding to the iterative scheme is in order. The weights defined in (6.17) reveal the relative differences between the means computed by zeroth order component function and the first-order component functions, since each first-order component function is defined as $V_i\left(x^i\right) = V\left(\mathbf{x}\right)\big|_{\mathbf{x}=\bar{\mathbf{x}}\setminus x^i} - V_0$, $i = 1,\ldots,N_{\text{dof}}$. However, these weights may mislead the iterative scheme for some observables such as $V\left(\mathbf{x}\right) = 1 + \left(x^1 x^2\right)^2 + \left(x^3\right)^2$, $x^i \in [-1,1]$, $i = 1,\ldots,3$, for which the weights are computed as $\zeta_1 = 0$, $\zeta_2 = 0$, and $\zeta_3 = 2/3$. In such case, although only x^3 appears to be the significant random variable, the remaining random variables are equally important. This deficiency of the iterative scheme, reported in other studies as well [44], can be corrected by an effective screening technique [112] that introduces an additional computational cost to the HDMR construction. Nevertheless, the HDMRs constructed in numerical examples of this thesis never suffered from this deficiency. Furthermore, in case V_0 is equal to zero, the weights in (6.17) can simply be defined as $E\left[V_{\mathbf{u}}\left(\mathbf{x}^{\mathbf{u}}\right)\right]$.

6.2.4 Fine-Tuning of Iterative HDMR for EM Analysis

In many broadband EM scenarios, the observable is also a function of frequency in one of (uniformly distributed) random variables or parameters (see Section 7.2.2 for an example). Along this dimension, an expansion of partial fractions [113] can be used to represent the frequency variation of the observable. Assume that the observable $V(\mathbf{x})$ is a function of frequency in $x^{N_{\text{dof}}}$ within the range $[f_{beg}, f_{end}]$. Then, it can be expressed using the HDMR and partial fraction expansions as

$$V\left(\mathbf{x}, x^{N_{\text{dof}}}\right) \approx \sum_{m=1}^{N_{\text{pf}}} \sum_{\mathbf{u}\subseteq\Omega} V_{\mathbf{u}}\left(\mathbf{x}^{\mathbf{u}}\right) PF_m\left(x^{N_{\text{dof}}}\right), \tag{6.20}$$

where $\Omega = \{1, \ldots, N_{\text{dof}} - 1\}$ is the general set of random variable indices, the number of partial fractions used in the $N_{\text{dof}}^{\text{th}}$ dimension is N_{pf}, $PF_m\left(x^{N_{\text{dof}}}\right)$ denotes the partial fraction defined as

$$PF_m\left(x^{N_{\text{dof}}}\right) = \frac{c_m}{x^{N_{\text{dof}}} - a_m} + d\,, \tag{6.21}$$

where a_m and c_m are the poles and residues of partial sum and d is a constant. In (6.20), HDMR expansion is used to approximate observable along the dimensions whose indices belong to Ω while the partial fractions are employed in $N_{\text{dof}}^{\text{th}}$ dimension. Those two methods are interfaced by selecting N_{f} number of cuts along $N_{\text{dof}}^{\text{th}}$ dimension and approximating the observable values along those cuts via the iterative HDMR technique explained in Section 6.2.3. Let $\hat{V}\left(x_k^{N_{\text{dof}}}\right)$, $k = 1, \ldots, N_{\text{f}}$, represent the observable values approximated by iterative HDMR on each cut, where

$x_k^{N_{\text{dof}}} = f_{\text{beg}} + (k-1)(f_{\text{end}} - f_{\text{beg}})/(N_{\text{f}} - 1)$. The algorithm, so called vector fitting [113-115], estimates the optimum a_m, c_m, and d by first locating the poles and then determining the residues in an iterative manner. The main idea in vector fitting algorithm is defining a weighting function as

$$WF_m\left(x^{N_{\text{dof}}}\right) = \frac{\tilde{c}_m}{x^{N_{\text{dof}}} - a_m} + d\,, \tag{6.22}$$

and introducing a rational approximation to this weighting function as [113]

$$\sum_{m=1}^{N_{\text{pf}}} \frac{c_m}{x^{N_{\text{dof}}} - a_m} + d \approx \left(\left(\sum_{m=1}^{N_{\text{pf}}} \frac{\tilde{c}_m}{x^{N_{\text{dof}}} - a_m}\right) + 1\right) \hat{V}\left(x_k^{N_{\text{dof}}}\right). \tag{6.23}$$

Here, the unknowns, c_m, $\tilde{c}_m$, d, and a_m, can be obtained in an iterative manner. To solve (6.23) for unknowns, an overdetermined linear system of equations is introduced as

$$\mathbf{A}\mathbf{y} = b\,, \tag{6.24}$$

where $b = \left[\hat{V}\left(x_1^{N_{\text{dof}}}\right), \ldots, \hat{V}\left(x_{N_{\text{pf}}}^{N_{\text{dof}}}\right)\right]^T$, $\mathbf{y} = \left[c_1, \ldots, c_{N_{\text{pf}}}, d, \tilde{c}_1, \ldots, \tilde{c}_{N_{\text{pf}}}\right]^T$, and

$$\mathbf{A} = \begin{bmatrix} \dfrac{1}{x^{N_{\text{dof}}} - a_1} & \cdots & \dfrac{1}{x^{N_{\text{dof}}} - a_{N_{\text{pf}}}} & 1 & \dfrac{\hat{V}\left(x_1^{N_{\text{dof}}}\right)}{x^{N_{\text{dof}}} - a_1} & \cdots & \dfrac{\hat{V}\left(x_1^{N_{\text{dof}}}\right)}{x^{N_{\text{dof}}} - a_{N_{\text{pf}}}} \\ \vdots & & \vdots & & \vdots & & \vdots \\ \dfrac{1}{x^{N_{\text{dof}}} - a_1} & \cdots & \dfrac{1}{x^{N_{\text{dof}}} - a_{N_{\text{pf}}}} & 1 & \dfrac{\hat{V}\left(x_{N_{\text{f}}}^{N_{\text{dof}}}\right)}{x^{N_{\text{dof}}} - a_1} & \cdots & \dfrac{\hat{V}\left(x_{N_{\text{f}}}^{N_{\text{dof}}}\right)}{x^{N_{\text{dof}}} - a_{N_{\text{pf}}}} \end{bmatrix}. \tag{6.25}$$

The linear system of equations in (6.24) can be solved in a least squares sense through the QR decomposition after properly locating initial poles, $a_1, \ldots, a_{N_{\text{pf}}}$ (for the proper selection of initial poles, see the discussion in [113]). After obtaining $\mathbf{y}$ (i.e. residuals

and constant d) one can have the new poles, which will be used in next iteration, from the eigenvalues of the matrix Υ defined as

$$\Upsilon = \begin{bmatrix} a_1 & & & \\ & a_2 & & \\ & & \ddots & \\ & & & a_{N_{\mathrm{pf}}} \end{bmatrix} - \begin{bmatrix} 1 \\ 1 \\ \vdots \\ 1 \end{bmatrix} \begin{bmatrix} \tilde{c}_1 \\ \tilde{c}_2 \\ \vdots \\ \tilde{c}_{N_{\mathrm{pf}}} \end{bmatrix}^T . \tag{6.26}$$

The computations of (6.24) and (6.26) are repeated in each iteration with new poles and residues until the L-2 norm of difference between the new poles and starting poles is negligible. Once the iterations are completed, the observable variation along $N_{\mathrm{dof}}^{\mathrm{th}}$ dimension is approximated using the latest poles, residuals, and the constant d as

$$\hat{V}\left(x^{N_{\mathrm{dof}}}\right) = \sum_{m=1}^{N_{\mathrm{pf}}} \frac{c_m}{x^{N_{\mathrm{dof}}} - a_m} + d . \tag{6.27}$$

In this thesis, the vector fitting toolbox provided in [116] is directly used to obtain optimum poles and residues. Typically, N_{pf} is set to $\lfloor (N_{\mathrm{f}} - 1)/2 \rfloor$, and N_{f} is selected large enough to maintain the lowest possible least squares approximation error.

6.3 Application to the EMC/EMI Problems

This section illustrates the application of the iterative HDMR method to the statistical characterization of EMC/EMI phenomena on various realistic structures. Specifically, pdfs of voltages on several transmission line structures including a parallel wire network, a parallel interconnect network, and a cascaded multiconductor transmission line network using the proposed iterative HDMR technique are compared to

those obtained using the brute-force MC technique. In all examples considered here, the networks are excited by a sinusoidal voltage source with unit amplitude and the observables are the magnitudes of the voltages at the output terminals of networks, $\left|V_{\mathrm{O}}(\mathbf{x})\right|$. Unless specified otherwise, the iterative HDMR technique uses the adaptive ME-PC method with $\beta = 10^{-4}$, $\tau_1 = \tau_2 = 0.5$, TP integration rule (with three Gauss-Legendre points in each dimension), and local gPC expansions with $p = 2$. Observables' pdfs are estimated by applying $25\,000$ - point MC to surrogate models obtained using the iterative HDMR method or by directly evaluating $\left|V_{\mathrm{O}}(\mathbf{x})\right|$ using the deterministic simulator described in Section 2.2.4 that is executed by inputting the per-unit-length impedance and admittance matrices of networks calculated using the code in [117]; such MC runs and the data they produce will be labeled as "brute force". The error in surrogate model is computed using

$$err^{\mathrm{k}} = \sqrt{\sum_{i=1}^{25000} \left(\left|V_{\mathrm{O}}^{\mathrm{k}}(\mathbf{x}_i)\right| - \left|V_{\mathrm{O}}^{\mathrm{BF}}(\mathbf{x}_i)\right| \right)^2 \Big/ \sum_{i=1}^{25000} \left|V_{\mathrm{O}}^{\mathrm{BF}}(\mathbf{x}_i)\right|^2}, \tag{6.28}$$

where $\mathbf{x}_i$ is the evaluation point dictated by brute-force (BF) MC method, $\left|V_{\mathrm{O}}^{\mathrm{k}}(\mathbf{x})\right|$ is the surrogate model generated using the iterative HDMR method with $\varepsilon_1 = \mathrm{k}$ and $\varepsilon_2 = 10^{-16}$, and $\left|V_{\mathrm{O}}^{\mathrm{BF}}(\mathbf{x})\right|$ represents the observable computed by brute-force MC applied to the full-wave EM simulator or the deterministic simulator. Once the accurate surrogate models are generated for the examples below, the global sensitivity indices, so called Sobol indices, are computed by taking the ratio of each component function's variance to the global variance of $V(\mathbf{x})$, i.e.

$$S_{\mathbf{u}} = \mathrm{var}\left[V_{\mathbf{u}}\left(\mathbf{x}^{\mathbf{u}}\right)\right] \Big/ \mathrm{var}\left[V\left(\mathbf{x}\right)\right]. \tag{6.29}$$

These indices are then used to show contributions of random variables and their higher order correlations to the observables.

6.3.1 Parallel Wires

For the first example, a parallel wire transmission line network is considered [Figure 4–1]. The network consists of five lossless wires with length of $10\,\mathrm{m}$ and radius of $0.4\,\mathrm{mm}$ and is excited from the 1st wire by a sinusoidal voltage source with frequency of $10\,\mathrm{MHz}$. The wires are parallel to each other along *y*-direction above an infinitely long ground plane at $z=0$, centered at $\left(cx_i, 0, cz_i\right)$, $i=1,\ldots,5$, and terminated by resistors at the source side $R_{S,i}$, $i=1,\ldots,5$, and the load side $R_{L,i}$, $i=1,\ldots,5$. The observable, $\left|V_{\mathrm{O}}\left(\mathbf{x}\right)\right|$, is the output voltage across the load side resistor of 5th wire. Twenty parameters characterize the uncertainty in the problem ($N_{\mathrm{dof}}=20$): the center positions of wires along *x*-direction cx_i, $i=1,\ldots,5$, the center positions of wires along *z*-direction cz_i, $i=1,\ldots,5$, the values of resistances at the source side $R_{S,i}$, $i=1,\ldots,5$, and the values of resistances at the load side $R_{L,i}$, $i=1,\ldots,5$, (i.e., $\mathbf{x}=\left[cx_1,\ldots,cx_5,cz_1,\ldots,cz_5,R_{S,1},\ldots,R_{S,5},R_{L,1},\ldots,R_{L,5}\right]$). The random variables cx_i, $i=1,\ldots,5$, are normally distributed with means $\left(i-1\right)\times 3\,\mathrm{cm}$, $i=1,\ldots,5$, and standard deviation $0.33\,\mathrm{cm}$. The remaining random variables $cz_1,\ldots,cz_5$, and $R_{S,1},\ldots,R_{L,5}$ are normally distributed with means $3\,\mathrm{cm}$ and $50\,\Omega$ and standard deviations $0.33\,\mathrm{cm}$ and $3.3\,\Omega$, respectively.

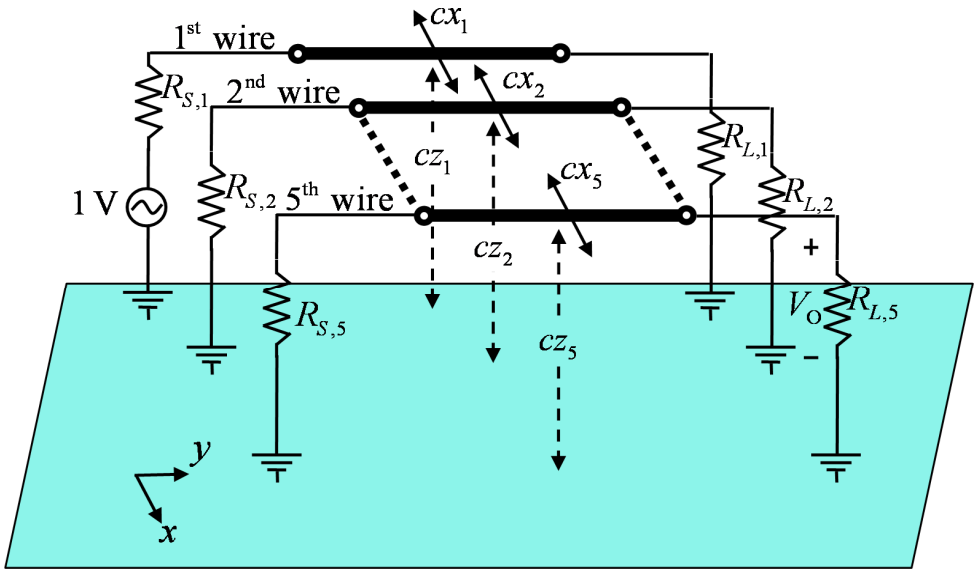

Figure 6–1 Geometry description of a parallel wire transmission line network.

The surrogate models $\left|V_{\mathrm{O}}^{\mathrm{k}}(\mathbf{x})\right|$, $\mathrm{k}=\left\{10^{-2},10^{-4},10^{-6}\right\}$, are constructed via the iterative HDMR method with $\varepsilon_1=\left\{10^{-2},10^{-4},10^{-6}\right\}$. To obtain $\left|V_{\mathrm{O}}^{\mathrm{k}}(\mathbf{x})\right|$, $\mathrm{k}=\left\{10^{-2},10^{-4},10^{-6}\right\}$, the iterative HDMR method required $\left\{61,988,7306\right\}$ deterministic simulations. The iterative HDMR technique automatically included the component functions up to first level for $\varepsilon_1=10^{-2}$ and up to third level for $\varepsilon_1=10^{-4}$ and $\varepsilon_1=10^{-6}$. err^{k}, $\mathrm{k}=\left\{10^{-2},10^{-4},10^{-6}\right\}$, are computed as $\left\{1.7587\times10^{-2},4.1245\times10^{-3},4.1218\times10^{-3}\right\}$. It's apparent from err^{k}, $\mathrm{k}=\left\{10^{-2},10^{-4},10^{-6}\right\}$, that relative error in surrogate model decreases and saturates as ε_1 decreases although more component functions are included in HDMR expansion. This is due to the fact that the errors in component functions approximated by the ME-PC method with $\beta=10^{-4}$ are at the orders of 10^{-3} and limits the decrease in surrogate model's relative error. The pdfs of $\left|V_{\mathrm{O}}(\mathbf{x})\right|$ are estimated using $\left|V_{\mathrm{O}}^{\mathrm{k}}(\mathbf{x})\right|$, $\mathrm{k}=\left\{\mathrm{BF},10^{-2},10^{-4},10^{-6}\right\}$ [Figure 6–2]. It is clear from Figure 6–2 that the pdfs obtained

via $\left|V_{\mathrm{O}}^{\mathrm{k}}(\mathbf{x})\right|$, $\mathrm{k}=\{10^{-4},10^{-6}\}$, match with the pdf obtained via $\left|V_{\mathrm{O}}^{\mathrm{k}}(\mathbf{x})\right|$, $\mathrm{k}=\{\mathrm{BF}\}$. This illustrates the accuracy of proposed scheme in pdf estimation.

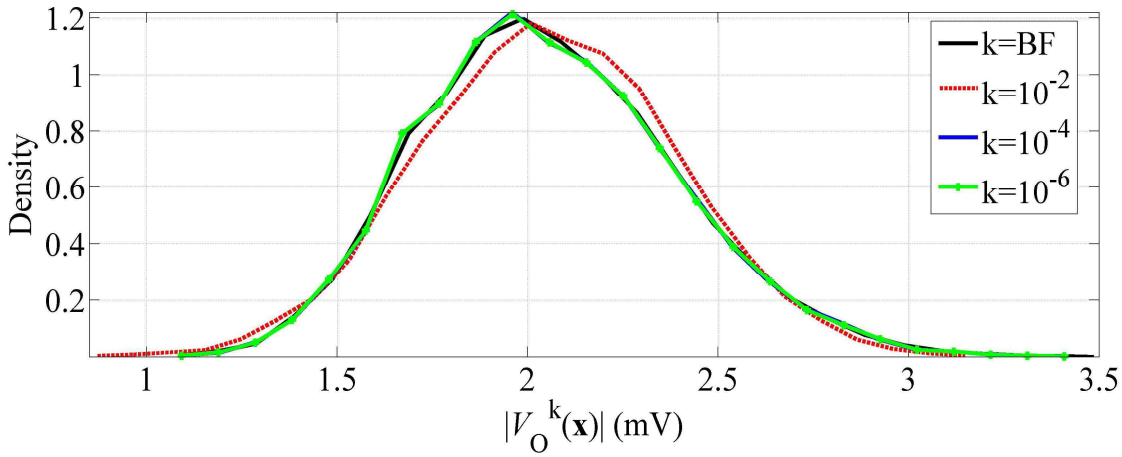

Figure 6–2 The pdfs obtained via $\left|V_{\mathrm{O}}^{\mathrm{k}}(\mathbf{x})\right|$, $\mathrm{k}=\{\mathrm{BF},10^{-2},10^{-4},10^{-6}\}$.

Moreover, the Sobol indices are computed using $\left|V_{\mathrm{O}}^{\mathrm{k}}(\mathbf{x})\right|$, $\mathrm{k}=\{10^{-6}\}$ and processed to illustrate the contribution of each component function's variance to global variance of $\left|V_{\mathrm{O}}(\mathbf{x})\right|$ [Figure 6–3]. Clearly, the variances of first order component functions pertinent to the cz_1 and cz_5 contribute significantly to the overall variance. The contributions from the first order component functions pertinent to cz_2, cz_3, cz_4, cx_1, cx_5, and $R_{L,5}$ are not negligible if the relative error of global variance is desired to be lower than 7 %.

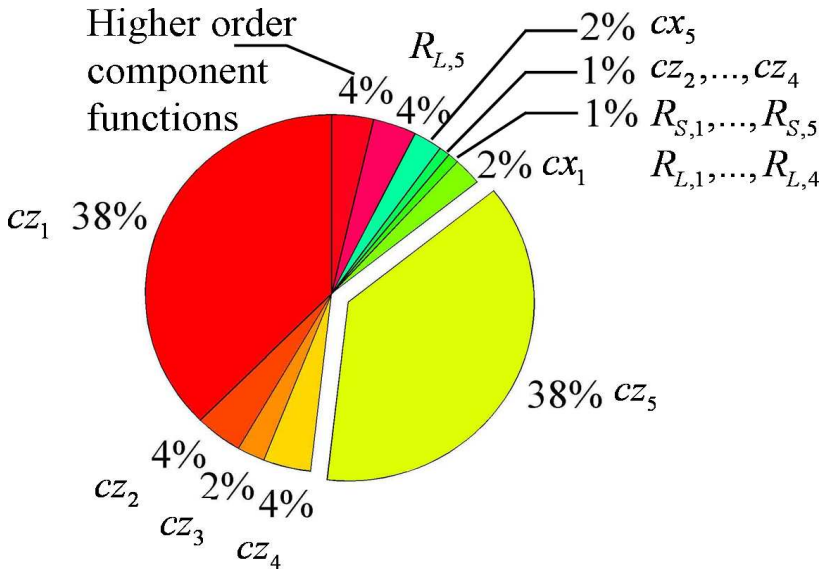

Figure 6–3 The contributions from the variances of first-order and higher-order component functions to the overall variance.

6.3.2 Parallel Microstrip Lines

In the second example, a parallel microstrip transmission line network is considered [Figure 6–4]. The network consists of infinitesimally thin ten conductors with length of $5\,\text{cm}$ that resides on a dielectric substrate with thickness of $103.33\,\mu\text{m}$ and relative permittivity of 3.55; the substrate is backed by a ground plane. The network is excited from the 1st conductor by a sinusoidal voltage source with frequency $2.4\,\text{GHz}$. The conductors with widths t_i, $i=1,\ldots,10$, are parallel to each other along *y*-direction, centered at $(cx_i, 0, 103.33)\,\mu\text{m}$, $i=1,\ldots,10$, and terminated by resistors at the source side $R_{S,i}$, $i=1,\ldots,10$, and the load side $R_{L,i}$, $i=1,\ldots,10$. The observable, $\left|V_{\text{O}}(\mathbf{x})\right|$, is the output voltage across the load side resistor of 5th conductor.

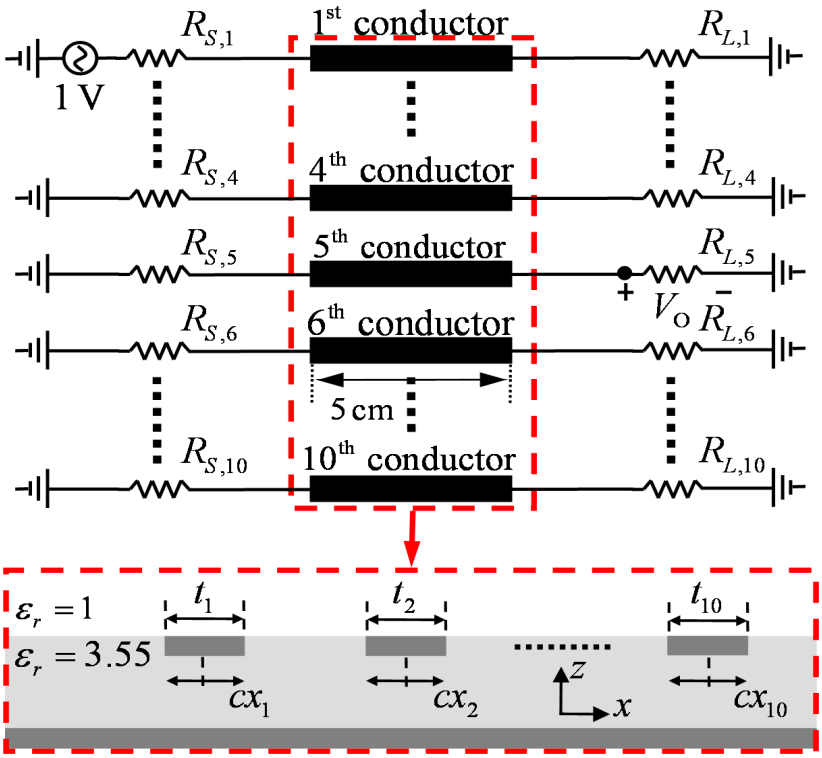

Figure 6–4 Geometry description of a parallel microstrip transmission line network.

Forty parameters characterize the uncertainty in the problem ($N_{\text{dof}} = 40$): ($N_{\text{dof}} = 40$): the center positions of conductors along x-direction cx_i, $i = 1,\ldots,10$, the widths of conductors t_i, $i = 1,\ldots,10$, the values of resistances at the source side $R_{S,i}$, $i = 1,\ldots,10$, and the values of resistances at the load side $R_{L,i}$, $i = 1,\ldots,10$, (i.e., $\mathbf{x} = \left[cx_1,\ldots,cx_{10},t_1,\ldots,t_{10},R_{S,1},\ldots,R_{S,10},R_{L,1},\ldots,R_{L,10}\right]$). The random variables cx_i, $i = 1,\ldots,10$, are normally distributed with means $(i-1)\times 461.8\,\mu\text{m}$, $i = 1,\ldots,10$, and standard deviation $3.3\,\mu\text{m}$ while the remaining ones $t_1,\ldots,t_{10}$ and $R_{S,1},\ldots,R_{L,10}$ are normally distributed with means $230.9\,\mu\text{m}$ and $50\,\Omega$ and standard deviations $3.3\,\mu\text{m}$ and $3.3\,\Omega$, respectively. The surrogate models $\left|V_{\text{O}}^{\text{k}}(\mathbf{x})\right|$, $\text{k} = \left\{10^{-2},10^{-4},10^{-6}\right\}$, are constructed via the iterative HDMR method with $\varepsilon_1 = \left\{10^{-2},10^{-4},10^{-6}\right\}$ which required

$\{121, 211, 4036\}$ deterministic simulations. The iterative HDMR technique automatically included the component functions up to first level for $\varepsilon_1 = 10^{-2}$ and up to second level for $\varepsilon_1 = 10^{-4}$ and $\varepsilon_1 = 10^{-6}$. err^{k}, $\mathrm{k} = \{10^{-2}, 10^{-4}, 10^{-6}\}$, are computed as $\{6.1636\times10^{-4}, 4.7396\times10^{-4}, 6.0120\times10^{-5}\}$. It's apparent from err^{k}, $\mathrm{k} = \{10^{-2}, 10^{-4}, 10^{-6}\}$, that the relative error in surrogate model decreases significantly when more component functions are included in HDMR expansion. The pdfs of $|V_{\mathrm{O}}(\mathbf{x})|$ are estimated using $|V_{\mathrm{O}}^{\mathrm{k}}(\mathbf{x})|$, $\mathrm{k} = \{\mathrm{BF}, 10^{-2}, 10^{-4}, 10^{-6}\}$ [Figure 6–5]. It is clear from Figure 6–5 that the pdf obtained via $|V_{\mathrm{O}}^{\mathrm{k}}(\mathbf{x})|$, $\mathrm{k} = \{10^{-6}\}$, is exactly the same with the pdf obtained via $|V_{\mathrm{O}}^{\mathrm{k}}(\mathbf{x})|$, $\mathrm{k} = \{\mathrm{BF}\}$ while the discrepancies between the pdf obtained via $|V_{\mathrm{O}}^{\mathrm{k}}(\mathbf{x})|$, $\mathrm{k} = \{\mathrm{BF}\}$ and the pdfs obtained via $|V_{\mathrm{O}}^{\mathrm{k}}(\mathbf{x})|$, $\mathrm{k} = \{10^{-2}, 10^{-4}\}$, are negligible.

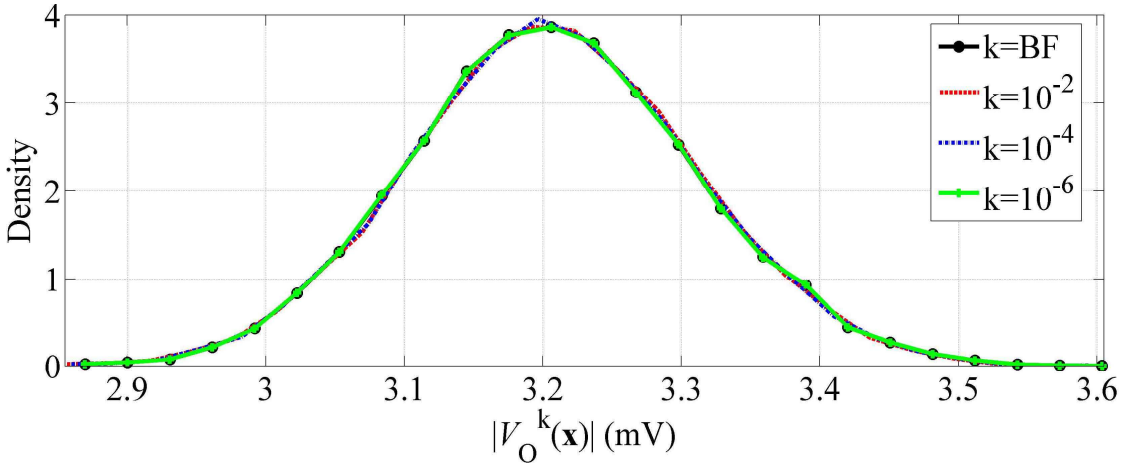

Figure 6–5 The pdfs obtained via $|V_{\mathrm{O}}^{\mathrm{k}}(\mathbf{x})|$, $\mathrm{k} = \{\mathrm{BF}, 10^{-2}, 10^{-4}, 10^{-6}\}$.

In addition, the Sobol indices are computed using $|V_{\mathrm{O}}^{\mathrm{k}}(\mathbf{x})|$, $\mathrm{k} = \{10^{-6}\}$, to illustrate the contribution of each component function's variance to global variance of $|V_{\mathrm{O}}(\mathbf{x})|$ [Figure

6–6]. Clearly, the variances of first order component functions pertinent to the t_1, t_5, $R_{S,1}$, and $R_{L,5}$ contribute significantly to the overall variance. The contributions from the component functions pertinent to the other random variables and their higher order correlations should also be accounted for if the global variance is wanted to be estimated with a relative error less than 5 %.

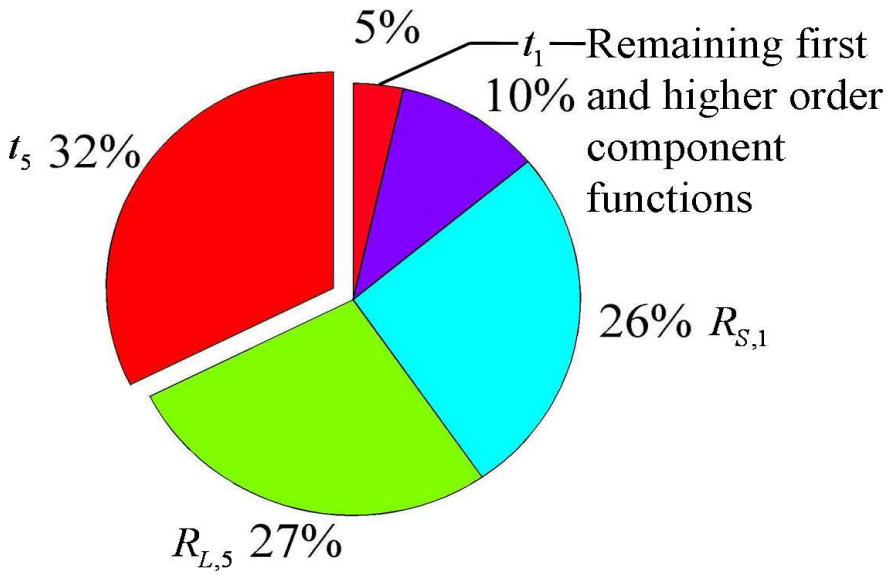

Figure 6–6 The contributions from the variances of first-order and higher-order component functions to the overall variance.

6.3.3 Cascaded Multiconductor Transmission Line Network

In the last example, a cascaded multiconductor transmission line network is considered [Figure 6–7 (a)]. The network is constructed by connecting 40 blocks, each of which consists of serially connected three-conductor transmission line networks [Figure 6–7 (a)-(b)].

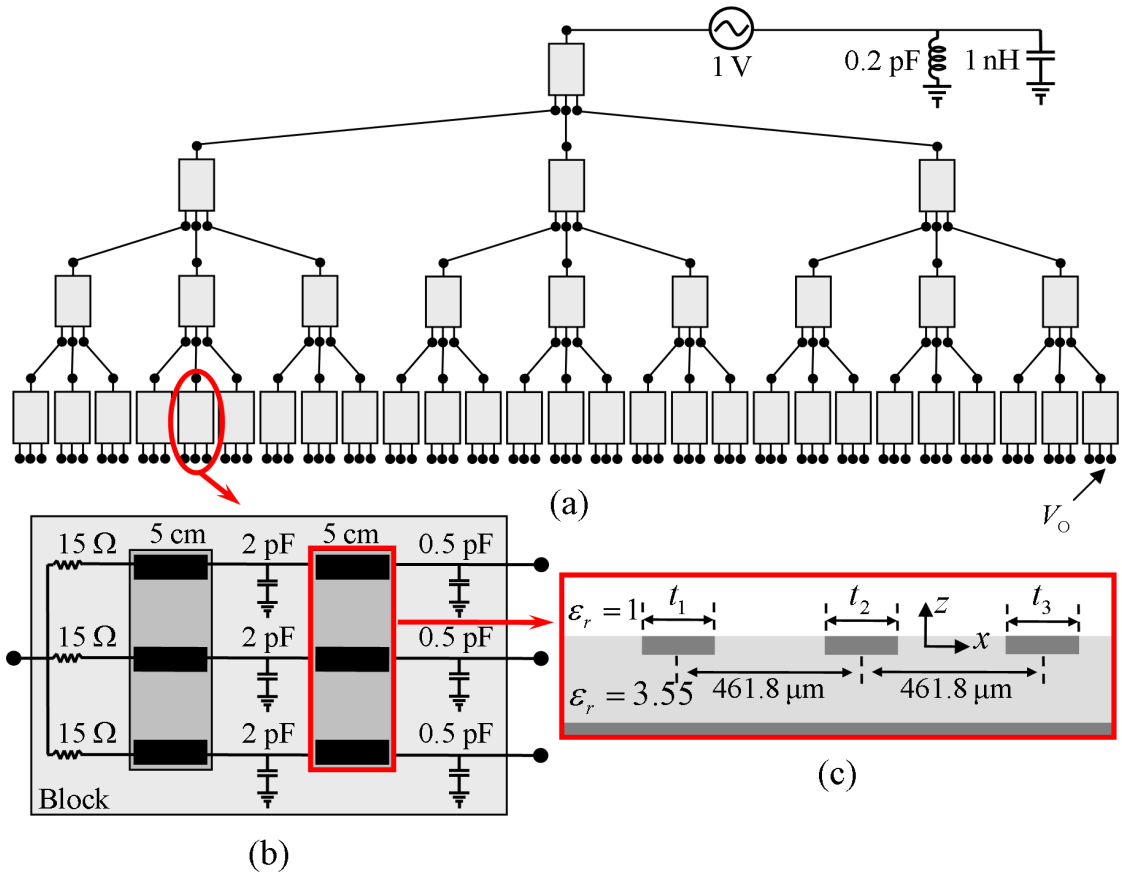

Figure 6–7 (a) Cascaded multiconductor transmission line network. (b) Building block of the cascaded network. (c) Configuration of the three-conductor transmission line.

Each of these conductors with length of 5 cm resides on a dielectric substrate with thickness of 103.33 μm and relative permittivity of 3.55; the substrate is backed by a ground plane and the spacing between conductors is 461.8 μm [Figure 6–7 (c)]. The network is excited by a sinusoidal voltage source with frequency 2.4 GHz. The observable, $|V_O(\mathbf{x})|$, is the amplitude of the voltage at the output terminal of the network [Figure 6–7 (a)]. 240 parameters characterize the uncertainty in the network ($N_{dof} = 240$). The widths of the all conductors, t_i, $i = 1, \ldots, 240$, are assumed to be normally distributed random variables with mean 230.9 μm and standard deviation

3.3 μm. The surrogate models $\left|V_{\mathrm{O}}^{\mathrm{k}}(\mathbf{x})\right|$, $\mathrm{k}=\left\{10^{-2},10^{-4}\right\}$ are constructed via the iterative HDMR method with $\varepsilon_1=\left\{10^{-2},10^{-4}\right\}$ which required $\{721,856\}$ deterministic simulations. The iterative HDMR technique automatically included the component functions up to first level for $\varepsilon_1=10^{-2}$ and up to second level for $\varepsilon_1=10^{-4}$. err^{k}, $\mathrm{k}=\left\{10^{-2},10^{-4}\right\}$, are computed as $\left\{1.3384\times10^{-4},1.1474\times10^{-4}\right\}$. The pdfs of $\left|V_{\mathrm{O}}(\mathbf{x})\right|$ are estimated using $\left|V_{\mathrm{O}}^{\mathrm{k}}(\mathbf{x})\right|$, $\mathrm{k}=\left\{10^{-2},10^{-4}\right\}$ [Figure 6–8]. It is clear from Figure 6–8 that the pdfs obtained via $\left|V_{\mathrm{O}}^{\mathrm{k}}(\mathbf{x})\right|$, $\mathrm{k}=\left\{10^{-2},10^{-4}\right\}$, are in perfect agreement with the pdf obtained via $\left|V_{\mathrm{O}}^{\mathrm{k}}(\mathbf{x})\right|$, $\mathrm{k}=\{\mathrm{BF}\}$.

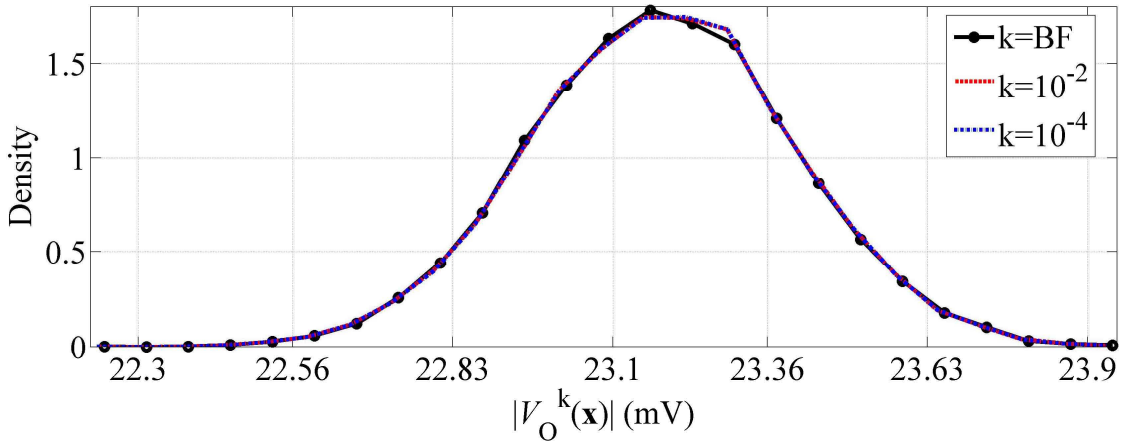

Figure 6–8 The pdfs obtained via $\left|V_{\mathrm{O}}^{\mathrm{k}}(\mathbf{x})\right|$, $\mathrm{k}=\left\{\mathrm{BF},10^{-2},10^{-4}\right\}$.

CHAPTER 7
EFFICIENT GA-BASED EM OPTIMIZATION USING HDMR-GENERATED SURROGATE MODELS

7.1 Introduction

Since the early 1990s, genetic algorithms (GAs) have been successfully applied to the design of a wide range of EM devices, from frequency selective surfaces and microwave absorbers to microwave filters, waveguides, and antennas [118-123]. The appeal of GAs stems from their capacity to straightforwardly treat mixed discrete-continuous design domains and multiple objectives, as well as their ability to uncover strong local or even global objective function optima. Many other nature-inspired optimization techniques enjoy similar benefits. Unfortunately, GAs often require the evaluation of objective functions for a large number of design candidates while canvassing multimodal design domains to find optimal designs. This limits their applicability to the design of electrically large EM systems, for which the evaluation of each objective function requires the execution of a CPU-intensive full-wave EM simulator. Therefore, the GA-based optimization of electrically-large EM systems often relies on (semi-) analytical [124], perturbation-based [125], or surrogate modeling [126] methods to accelerate the evaluation of pertinent observables or objective functions. Unfortunately, semi-analytical and perturbation-based techniques are limited in scope.

Therefore, GA-based optimization methods assisted by surrogate models are becoming standard practice in the design of such EM systems [126-131].

In [126], artificial neural networks was trained to construct surrogate models of active input impedances of stacked patch antennas. These surrogate models were then used by GA to find optimal spacings between stack patch antennas in a linear array for lowest possible active voltage standing wave ratios (VSWRs) and side lobe levels (SLLs) over a frequency band and a scan angle range. Specifically, GA used such surrogate models, constructed in low dimensional design domains, in lieu of evaluating the active VSWRs and SLLs via computationally expensive EM simulator. As well as neural networks method, the kriging method was also used to generate surrogate models for designs of various EM devices including a microwave filter and a textile antenna [127]. Specifically, the kriging generated surrogate models were only employed in the regions of strong optima to increase the efficiency of GA-based optimization. Moreover, space mapping techniques have extensively been used in the design of EM structures [128-131]. In such techniques, two types of simulation models (with their corresponding design domains) are required: a computationally expensive fine simulation model and a computationally cheap coarse simulation model. Typically, when the fine simulation model is a microwave structure, its corresponding coarse simulation model is a circuit equivalent of the structure. The surrogate model is constructed between the inputs of coarse design domain and the inputs of fine design domain. The technique finds the optimal design by performing optimization in the coarse design domain and mapping it to the fine design domain using the surrogate model.

In this chapter, a simulation framework leveraging the iterative HDMR technique described in Section 6.2.3 is used to construct accurate surrogate models for observables or objective functions pertinent to the optimization and design of EM devices. The HDMR technique builds accurate surrogate models of rapidly varying observables or their pertinent objective functions in high-dimensions that can not be constructed using conventional neural networks and kriging methods [132]. Once accurate surrogate models have been built by iterative HDMR technique, the proposed framework runs a classical GA to search the multidimensional design domain for optimal designs. Although the notation used in this chapter is the same as that is used in other chapters, some terms differ from the ones introduced before. In what follows, the terms such as *design* variable, vector, and domain that correspond to *random* variable, vector, and domain are used to follow the jargon used for optimization problems.

7.2 Application to the EM Optimization Problems

In this section, the accuracy and efficiency of the simulation framework is demonstrated through its application to the placement of uniformly excited sources in a linear array, selection of locations of stacked patch microstrip antennas in a linear array, and the placement of antennas on a naval ship. Unless otherwise stated, in all numerical examples below, HDMR expansions are built up to level 2, all first order component functions and several second order component functions that are manually selected due to the physics of numerical examples are included in HDMR expansions. The HDMR technique uses the adaptive ME-PC method with $\beta = 10^{-2}$, $\tau_1 = \tau_2 = 0.5$, TP integration

rule (with five Gauss-Legendre points in each dimension), and local gPC expansions with $p = 4$. The error in surrogate model is computed using

$$err = \sqrt{\sum_{i=1}^{100} \left(\left| V(\mathbf{x}_i) \right| - \left| \tilde{V}(\mathbf{x}_i) \right| \right)^2 \Big/ \sum_{i=1}^{100} \left| V(\mathbf{x}_i) \right|^2}, \tag{7.1}$$

where $\mathbf{x}_i$ is the randomly selected evaluation point, $\tilde{V}(\mathbf{x})$ is the surrogate model of observable generated using the iterative HDMR method with $\varepsilon_1 = 10^{-16}$ and $\varepsilon_2 = 10^{-16}$. Once the accurate surrogate models are generated for the examples below, the classical GA is run for 500 generations with the crossover probability of 0.8 and the population size of 20000.

7.2.1 Linear Array of Sources Points

In the first example, the proposed method is applied to the design of a linear array of uniformly excited source points. The linear array consists of 48 source points that are positioned along *z*-axis and symmetric about the array center [Figure 7–1]. The design variables are the positions of source points at the right hand side of array center, cz_i, $i = 1, \ldots, 24$, ($\mathbf{x} = [cz_1, \ldots, cz_{24}]$, $N_{\text{dof}} = 24$); that can vary in the ranges $\left[a^i, b^i \right] = \left[0.125 + (i-1)0.25, 0.5 + (i-1) \right] \lambda$, $i = 1, \ldots, 24$,where λ is the wavelength. The observables are the SLL and the radiation pattern values at 1001 equally spaced θ points, $E_\theta((i-1)\Delta\theta)$, $\Delta\theta = 90°/1000$, $i = 1, \ldots, 1001$, that can be computed by

$$E_\theta(\theta) = 2\sin\theta \left| \sum_{n=1}^{24} \cos\left(\frac{2\pi}{\lambda} cz_n \cos\theta \right) \right|, \tag{7.2}$$

where $\sin\theta$ represents the radiation pattern of each source point. The design goal is to achieve minimum possible SLL; here it's selected as 30 dB, i.e. $\text{SLL} < -30\,\text{dB}$. The design constraint is that the spacing between adjacent source points should be between $0.25\,\lambda$ and $1\,\lambda$.

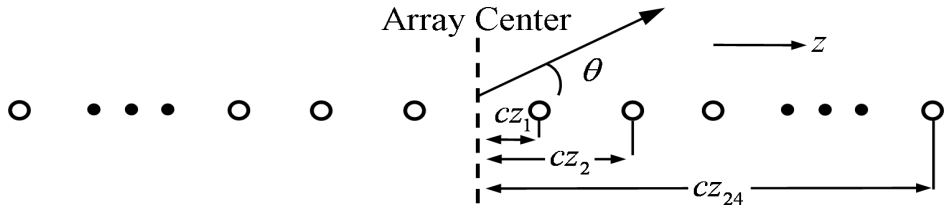

Figure 7–1 Geometry of a linear array that consists of 48 source points.

The surrogate models of SLL and its pertinent radiation pattern values are generated using the HDMR technique that uses the adaptive ME-PC method with TP integration rule (with 20 Gauss-Legendre points in each dimension), and local gPC expansions with $p = 19$. The technique builds the HDMR expansion by including only all first order component functions since the radiation pattern given in (7.2) is the sum of univariate functions. The proposed method required 2120 analytic function calls to generate surrogate models with maximum error of 1.8751×10^{-3}. Once the surrogate models are generated, a classical GA is run for the optimum design point which is found to be $\mathbf{x} = [\ 0.2231,\ 0.5045,\ 0.9158,\ 1.2481,\ 1.5467,\ 1.9671,\ 2.2815,\ 2.6540,\ 3.0417,\ 3.4462,\ 3.9529,\ 4.2101,\ 4.6417,\ 5.0215,\ 5.6011,\ 6.0316,\ 6.5681,\ 7.1238,\ 7.6524,\ 8.3037,\ 9.0997,\ 10.0138,\ 11.0138,\ 12.0138\ ]\lambda$. Same design point is found by running a direct GA that uses the exact function values instead of approximate values probed from surrogate models. Figure 7–2 compares the radiation patterns of the linear arrays synthesized using the direct GA relying on exact function values and the GA

assisted by HDMR generated surrogate models; the radiation patterns are in perfect agreement as the maximum error in surrogate models are at the orders of 10^{-3}. At the optimum design point, the SLL is computed as -28.5dB, which is 0.2 dB lower than that reported in [133]. Synthesizing this large array using a direct GA that relies on function calls instead of surrogate models would not be possible when each function call corresponds to CPU intensive EM simulation.

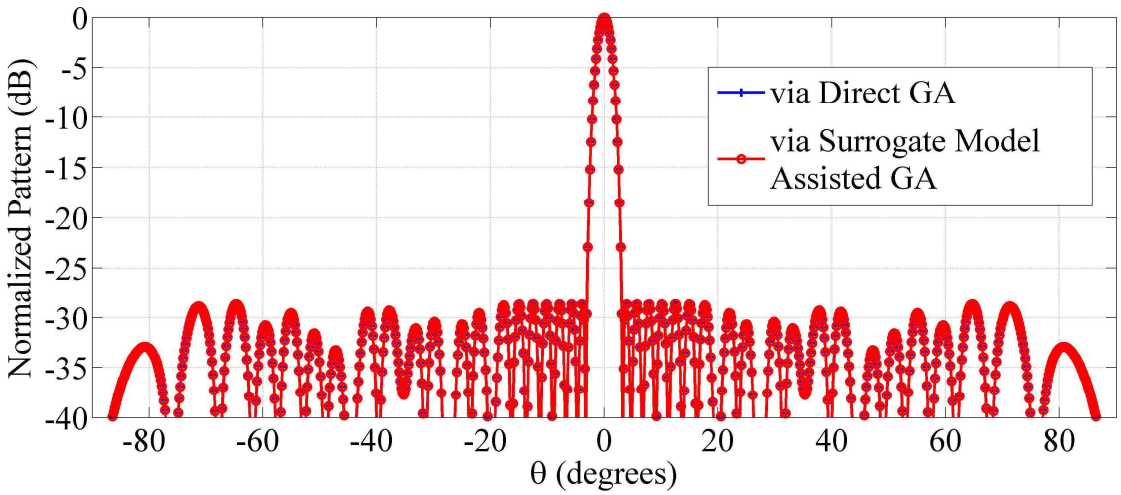

Figure 7–2 Radiation pattern of synthesized linear array.

7.2.2 Linear Array of Stacked Patch Antennas

In the second example, the proposed method is applied to the design of a linear array of stacked patch antennas [Figure 4–5 (a)-(b)]. The stacked patch antenna composes of 8 mm thick upper/lower substrates with relative dielectric constants of 2.40/3.27 and loss tangents of 0.0012/0.0020, respectively [126]. The antenna is fed by a probe and operates in a frequency band from 1.14 GHz to 1.26 GHz. The linear array consists of ten antenna elements parallel to each other along *x*- and *z*- axes [Figure 4–5 (c)]. The design variables are the center positions of antenna elements along *y*-axis, cy_1, cy_2, cy_3, cy_4, cy_5, cy_6, cy_7, cy_8, cy_9, and cy_{10}, ($\mathbf{x} = [cy_1, \ldots, cy_{10}]$, $N_{\text{dof}} = 10$); that can vary in ranges

$[-50,50]$ mm, $[150,250]$ mm, $[350,450]$ mm, $[550,650]$ mm, $[750,850]$ mm, $[950,1050]$ mm, $[1150,1250]$ mm, $[1350,1450]$ mm, $[1550,1650]$ mm, and $[1750,1850]$ mm, respectively. The observables are active VSWR_i^k, SLL^k, $i=1,\ldots,10$, $k=1,\ldots,N_\text{f}$, where $N_\text{f}=21$ is the number of equally-spaced frequency samples selected over the frequency band, and the radiation pattern values at 91 equally spaced θ points, $E_\phi^k\left((j-1)\Delta\theta\right)$, $\Delta\theta=90°/90$, $j=1,\ldots,91$, $k=1,\ldots,N_\text{f}$. The observables are computed using the full-wave EM simulator of Zeland IE3D, which assumes infinite ground plane and dielectric substrates. The design goals are to achieve $\text{SLL}^k \le$ -15 dB and active $\text{VSWR}_i^k \le 2$, $i=1,\ldots,10$, $k=1,\ldots,21$.

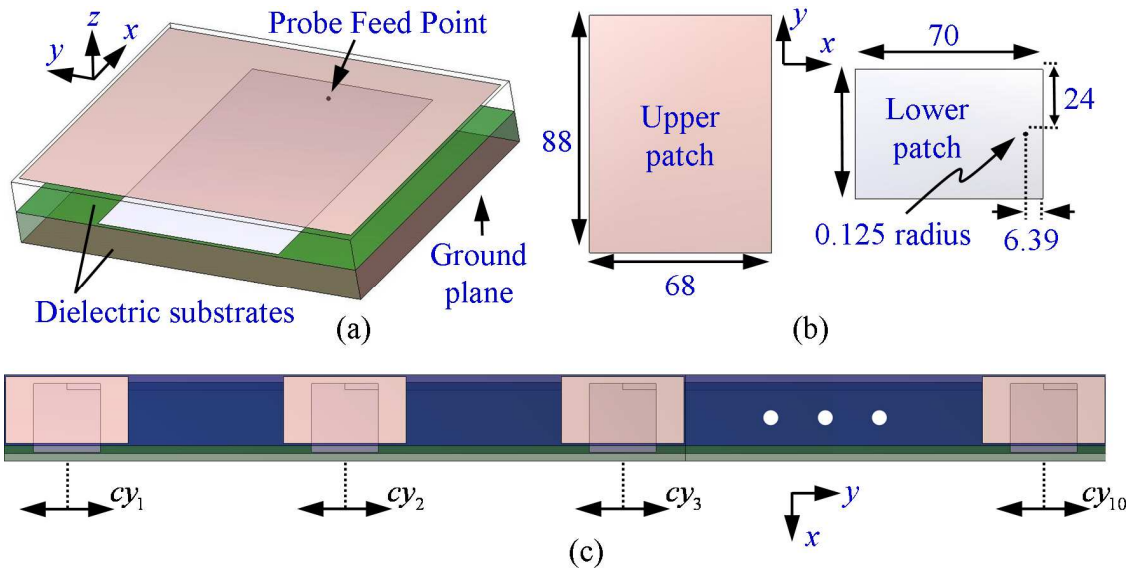

Figure 7–3 (a) Stacked patch antenna geometry. (b) Dimensions of patches (in mm). (c) Linear array of ten stacked patch antennas.

The surrogate models of active VSWR_i^k, SLL^k, $i=1,\ldots,10$, $k=1,\ldots,21$, and their pertinent radiation pattern values are generated using the vector fitting enhanced HDMR technique described in Section 6.2.4; the HDMR technique builds HDMR

expansions by including all first order component functions and the second order component functions with indices $\{m, m+1\}$, $m = 1,\ldots,9$, and $\{n, n+2\}$, $n = 1,\ldots,8$. The proposed method required 3625 deterministic simulations to generate surrogate models of $\left\{\text{active VSWR}_i^k, \text{SLL}^k\right\}$, $i = 1,\ldots,10$, $k = 1,\ldots,21$, with maximum errors of $\left\{3.4513\times10^{-2}, 7.1596\times10^{-3}\right\}$. Once the surrogate models are generated, a classical GA is run to find the optimum design in D. Optimum design point is found to be $\mathbf{x} = [$ 11.30, 193.35, 447.02, 631.53, 832.38, 992.60, 1187.69, 1372.35, 1642.70, 1822.64 $]$ mm. Active VSWRs and SLLs of the GA-synthesized array are compared with those of a uniformly spaced array with inter-element spacing of 200 mm [Figure 7–4 (a)-(k)]. Moreover, the radiation pattern of GA-synthesized array is plotted at five different frequencies [Figure 7–5]. Apparently, the proposed method finds a design that meets the specified design goals. Synthesizing this large array using a GA by relying on full-wave EM simulations would be impractical compared to the proposed method.

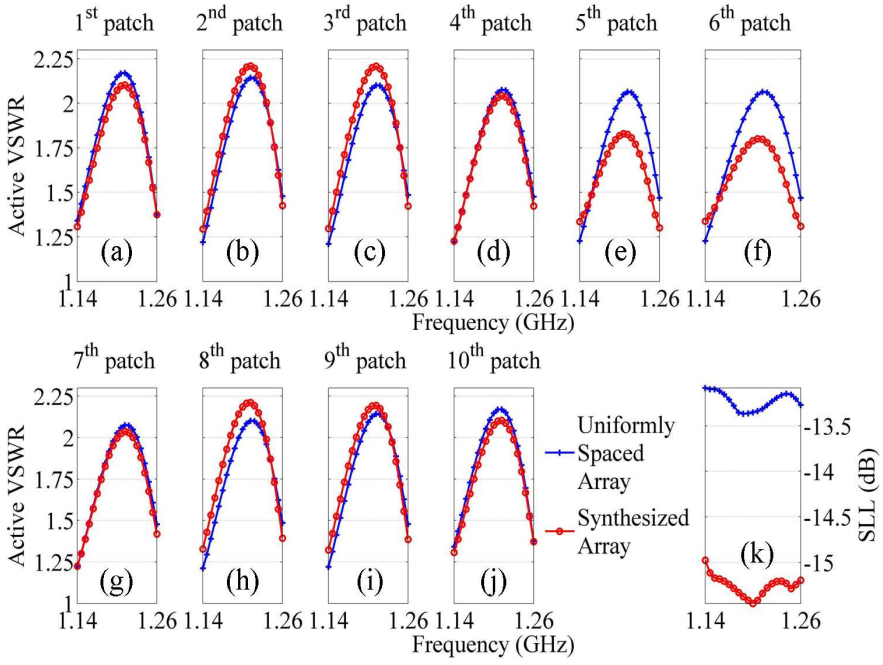

Figure 7–4 Comparison of (a)-(j) active VSWRs and (k) SLLs of synthesized array with those of uniformly spaced array over the frequency band.

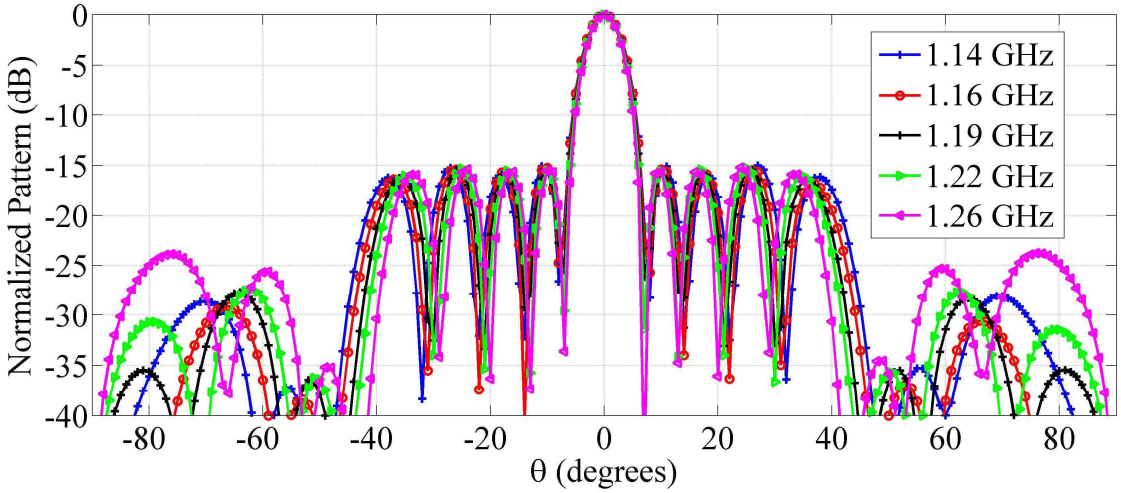

Figure 7–5 Radiation pattern of synthesized array at five different frequencies.

7.2.3 Monopoles on a Naval Ship

In the last example, the proposed method is applied to the placement of monopole antennas on a naval ship. The monopole antennas with length of $8\,\text{m}$ and radius of $2\,\text{cm}$ are excited from their bottoms by a sinusoidal voltage source with frequency of $30\,\text{MHz}$. The antennas are positioned on rectangular platforms at $z = 7.92\,\text{m}$ and $z = -9.16\,\text{m}$ [Figure 7–6]. The design variables are the center positions of bottoms of monopoles on rectangular platforms, cx_1, cy_1, cx_2, and cy_2, ($\mathbf{x} = [cx_1, cy_1, cx_2, cy_2]$, $N_{\text{dof}} = 4$); that can vary in ranges $[85,95]\,\text{m}$, $[-5,5]\,\text{m}$, $[51,59]\,\text{m}$, and $[-1.5,1.5]\,\text{m}$, respectively. The observable is the coupling between monopole antennas, $|S_{12}|$ (in dB scale), that are computed using the deterministic simulator described in Section 2.2.4. The design goal is to achieve minimum possible coupling; here it's selected as 50 dB, i.e. $|S_{12}| \leq -50\,\text{dB}$.

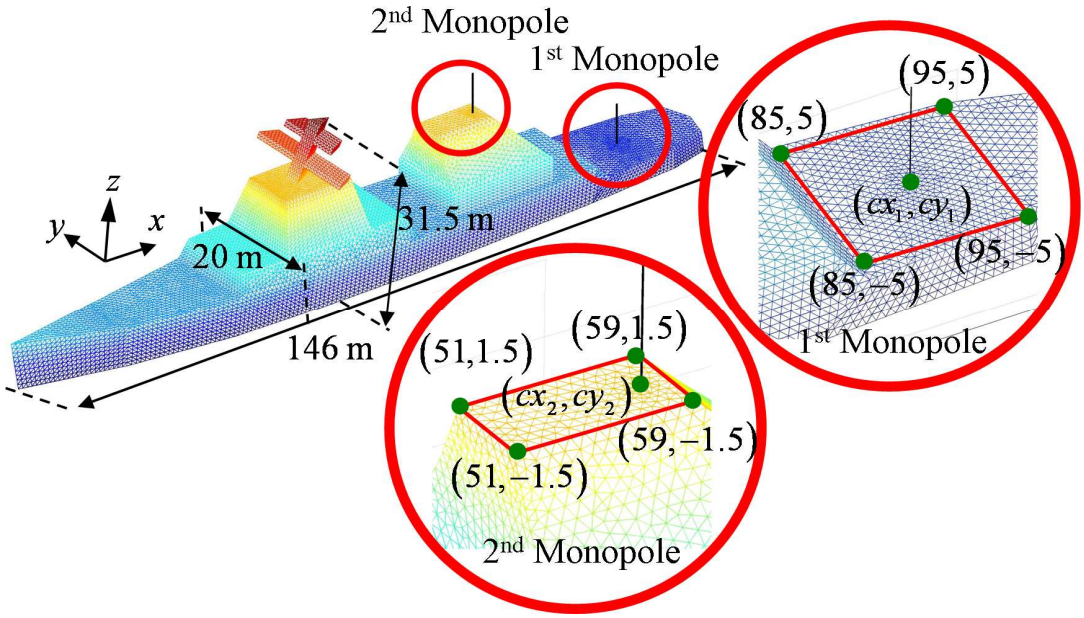

Figure 7–6 Geometry description of the naval ship and the platforms on which the monopoles are placed.

The surrogate model of $|S_{12}|$ is generated using the HDMR technique that builds HDMR expansion by including all first and second order component functions. The proposed method required 1500 deterministic simulations to generate surrogate model of $|S_{12}|$ with the error of 1.2743×10^{-2}. Once the surrogate models are generated, a classical GA is run to find the optimum design in D. Optimum design point is found to be $\mathbf{x}=[95, 2.89, 51, -1.5]$ m. At this design point, $|S_{12}|$ is computed as -48.8572 dB. For the sake of completeness, the radiation patterns of monopoles at optimum design point are illustrated in Figure 7–7.

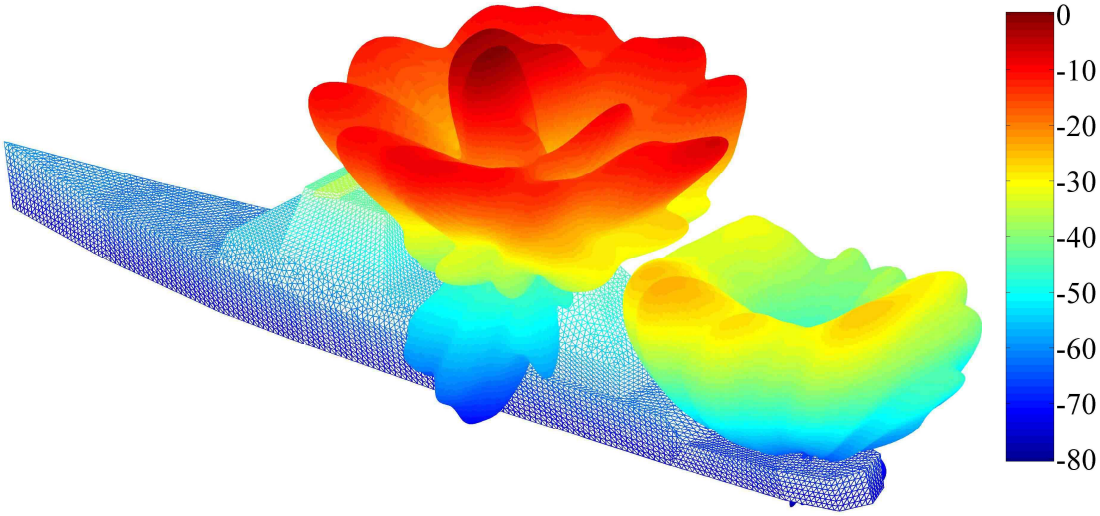

Figure 7–7 Radiation patterns of monopoles positioned at design point.

CHAPTER 8
CONCLUSIONS

8.1 Conclusions

In this thesis, efficient collocation methods with their applications to the EM analysis were presented. First, a Stroud-based SC method was introduced for statistically characterizing EMC/EMI phenomena on electrically large and complex platforms. Its accuracy and efficiency were demonstrated through its application to the several real-world stochastic EMC/EMI scenarios. Second, an adaptive ME-PC method suitable for observables that potentially vary rapidly/nonsmoothly across the random domain was presented. The accuracy and efficiency of the ME-PC method were enhanced by its hybridization with Dirichlet kernel and demonstrated through its applications to the statistical characterization of EMC/EMI observables on electrically large and complex platforms and statistical characterization of TM and EM wave propagation through mine tunnels. In addition, a novel three-dimensional full-wave solver was proposed to be used in conjunction with the ME-PC method for statistically characterizing EM wave propagation in mine tunnels. Finally, a computational framework combining iterative HDMR technique with the ME-PC method was proposed. The proposed computational framework is finely tuned to broadband EM applications by its hybridization with the expansion of partial fractions. The accuracy and efficiency of the proposed computational

framework were illustrated via its applications to the several real-world EMC/EMI scenarios and surrogate model based EM optimization problems.

8.2 Ongoing Work

The iterative HDMR technique is currently being applied to the statistical characterization of EM fields induced by transcranial magnetic stimulation (TMS) devices. TMS devices are used for studying brain functions and treating neurological disorders. Their functionality can not be ensured without carefully accounting for the uncertainties in TMS setup including the conductivities and sizes of brain tissues and the position of TMS device over the head. Preliminary results of this project show that the iterative HDMR method accurately and efficiently obtain the surrogate models of EM fields induced in a three sphere head model and in a real brain and thereby their statistics.

8.3 Contributions

The following journal papers and conference papers/abstracts related to the work presented in this thesis are either published, submitted, or currently being prepared.

8.3.1 Journal Papers

[1] H. Bağcı, A. C. Yücel, J. S. Hesthaven, and E. Michielssen, "A fast Stroud-based collocation method for statistically characterizing EMI/EMC phenomena on complex platforms," *IEEE Trans. Electromagn. Comp.*, vol. 51, no. 2, pp. 301-311, May 2009

[2] A. C. Yücel, H. Bağcı, and E. Michielssen, "An adaptive multi-element probabilistic collocation method for statistical EMC/EMI characterization," *IEEE Trans. Electromagn. Comp.*, (Accepted for publication)

[3] A. C. Yücel, O. Bakır, H. Bağcı, and E. Michielssen, "Statistical characterization of wave propagation in mine environments," (in preparation, will be submitted to *IEEE Antennas Wireless Propag. Lett*.)

[4] A. C. Yücel, H. Bağcı, and E. Michielssen, "Stochastic EMC/EMI analysis via iterative high dimensional model representation technique," (in preparation, will be submitted to *IEEE Trans. Electromagn. Comp*.)

[5] A. C. Yücel and E. Michielssen, "Fast GA-based electromagnetic optimization using HDMR-generated surrogate models," (in preparation, will be submitted to *IEEE Trans. Antennas Propag.*)

[6] A. C. Yücel, Y. Liu, H. Bağcı, and E. Michielssen, "A fast-multipole domain decomposition integral equation solver for characterizing electromagnetic wave propagation in mine environments," (in preparation, will be submitted to *IEEE Trans. Antennas Propag.*)

[7] L. Gomez, A. C. Yücel, L. Hernandez-Garcia, and E. Michielssen, "Uncertainty quantification in transcranial magnetic stimulation," (in preparation, will be submitted to *Brain Stimulation*)

[8] Y. Liu, A. C. Yücel, V. Lomakin, and E. Michielssen, "A scalable parallel implementation of the plane wave time domain algorithm on graphics processing unit-augmented clusters," (in preparation, will be submitted to *IEEE Antennas Wireless Propag. Lett*.)

8.3.2 Conference Papers and Abstracts

[1] A. C. Yücel, Y. Liu, H. Bağcı, and E. Michielssen, "A fast-multipole domain decomposition integral equation solver for characterizing electromagnetic wave propagation in mine environments," will be presented at *CNC-USNC/URSI National Radio Sci. Meet.*, 2013

[2] L. Gomez, A. C. Yücel, L. Hernandez-Garcia, and E. Michielssen, "Uncertainty quantification in Transcranial Magnetic Stimulation," will be presented at *CNC-USNC/URSI National Radio Sci. Meet.*, 2013

[3] A. C. Yücel and E. Michielssen, "Efficient GA-based electromagnetic optimization using HDMR-generated surrogate models," in Proc. *IEEE Int. Symp. Antennas Propagat.*, 2012

[4] O. Bakır, A. C. Yücel, H. Bağcı, and E. Michielssen, "Statistical characterization of wave propagation in mine environments," in Proc. *IEEE Int. Symp. Antennas Propagat.*, 2012

[5] Y. Liu, A. C. Yücel, V. Lomakin, and E. Michielssen, "A scalable parallel implementation of the plane wave time domain algorithm on graphics processing unit-augmented clusters," in Proc. *CNC-USNC/URSI National Radio Sci. Meet.*, 2012

[6] A. C. Yücel and E. Michielssen, "Efficient collocation methods for surrogate model-assisted GA-based electromagnetic optimization," in Proc. of *CIMPA-MCSE*, Jeddah, KSA, January 5-12, 2012

[7] H. Bağcı, A. C. Yücel, and E. Michielssen, "Efficient collocation methods for stochastic characterization of EMC/EMI phenomena on electrically large platforms," in Proc. of *CIMPA-MCSE*, Jeddah, KSA, January 5-12, 2012

[8] A. C. Yücel, H. Bağcı, and E. Michielssen, "Efficient stochastic EMC/EMI analysis using HDMR-generated surrogate models," in Proc. *URSI XXX General Assembly*, Istanbul, Turkey 2011

[9] A. C. Yücel and E. Michielssen, "GA-based electromagnetic optimization using HDMR-generated surrogate models," in Proc. *CNC-USNC/URSI National Radio Sci. Meet.*, 2011

[10] A. C. Yücel, H. Bağcı, and E. Michielssen, "An h-adaptive stochastic collocation method for stochastic EMC/EMI analysis," in Proc. *IEEE Int. Symp. Antennas Propagat.*, 2010

[11] A. C. Yücel, H. Bağcı, and E. Michielssen, "Stochastic electromagnetic analysis via high dimensional model representation," in Proc. *CNC-USNC/URSI National Radio Sci. Meet.*, 2010

[12] O. Bakır, A. C. Yücel, H. Bağcı, and E. Michielssen, "Stochastic characterization of wave propagation in mine environments," in Proc. *CNC-USNC/URSI National Radio Sci. Meet.*, 2010

[13] A. C. Yücel, H. Bağcı, and E. Michielssen, "Fast probability density function estimation for statistical EMC/EMI characterization," in Proc. *CNC-USNC/URSI National Radio Sci. Meet.*, 2009

[14] H. Bağcı, C. Yavuz, A. C. Yücel, J. S. Hesthaven, and E. Michielssen, "A fast and parallel Stroud-based stochastic collocation method for statistical EMI/EMC analysis," in Proc. *IEEE Int. Symp. Electromagn. Compat.*, 2008

[15] A. C. Yücel, F. P. Andriulli, and E. Michielssen, "Parallel self-tuning MLFMA library," in Proc. *URSI XXIX General Assembly*, Chicago, IL, Aug. 2008

APPENDICES

APPENDIX A
DERIVATION OF EQUATION (3.25)

The expected value of an observable $V(\mathbf{x})$ over the random domain D can be expressed as

$$E\left[V(\mathbf{x})\right] = \int_D V(\mathbf{x})\, d\mathbf{x}\,. \tag{B.1}$$

Inserting (3.24) into (B.1) yields

$$E\left[V(\mathbf{x})\right] \cong \int_D \sum_{n=-N}^{N} \left[\sum_{m=0}^{N_p} \tilde{v}_m \tilde{\mathbf{P}}_m \left(x^1, ..., x^{N_{\text{dof}}-1} \right) \right]_n DI_N \left(x^{N_{\text{dof}}} - n\Delta x^{N_{\text{dof}}} \right) d\mathbf{x}\,. \tag{B.2}$$

Since the random variables are assumed to be mutually independent, (B.2) can be rewritten as

$$E\left[V(\mathbf{x})\right] \cong \sum_{n=-N}^{N} \int_{x^{N_{\text{dof}}}} DI_N \left(x^{N_{\text{dof}}} - n\Delta x^{N_{\text{dof}}} \right) dx^{N_{\text{dof}}} \left[\int_{x^1 \cdots x^{N_{\text{dof}}-1}} \sum_{m=0}^{N_p} \tilde{v}_m \tilde{\mathbf{P}}_m \left(x^1, ..., x^{N_{\text{dof}}-1} \right) dx^1 \cdots dx^{N_{\text{dof}}-1} \right]_n . \tag{B.3}$$

The expression in (B.3) can be split into two parts as

$$E\left[V(\mathbf{x})\right] = \sum_{n=-N}^{N} I\left(x^{N_{\text{dof}}} \right) \left[I\left(x^1, \ldots, x^{N_{dof}-1} \right) \right]_n . \tag{B.4}$$

The integral inside square bracket, $I\left(x^1,\ldots,x^{N_{\text{dof}}-1}\right)$, can be written by introducing $\tilde{\mathbf{P}}_0\left(x^1,...,x^{N_{\text{dof}}-1}\right)=1$ as

$$I\left(x^1,\ldots,x^{N_{dof}-1}\right)=\sum_{m=0}^{N_p}\tilde{v}_m\int_{x^1\cdots x^{N_{dof}-1}}\tilde{\mathbf{P}}_m\left(x^1,...,x^{N_{\text{dof}}-1}\right)\tilde{\mathbf{P}}_0\left(x^1,...,x^{N_{\text{dof}}-1}\right)dx^1\cdots dx^{N_{dof}-1}\ . \quad \text{(B.5)}$$

Using the normalization/orthogonality condition, (B.5) can be reduced to

$$I\left(x^1,\ldots,x^{N_{\text{dof}}-1}\right)=\tilde{v}_0\,. \quad \text{(B.6)}$$

Using (3.22), the remaining integral can be written explicitly as

$$I\left(x^{N_{\text{dof}}}\right)=\int_{x^{N_{\text{dof}}}}\frac{\sin\left[\left(2N+1\right)\left(x^{N_{\text{dof}}}-n\Delta x^{N_{\text{dof}}}\right)/2\right]}{\left(2N+1\right)\sin\left(\left(x^{N_{\text{dof}}}-n\Delta x^{N_{\text{dof}}}\right)/2\right)}dx^{N_{\text{dof}}}\ . \quad \text{(B.7)}$$

Using the Lemma 6.4 in [134], the integral of Dirichlet kernel, $I\left(x^{N_{\text{dof}}}\right)$, is obtained as

$$I\left(x^{N_{\text{dof}}}\right)=2\pi/\left(2N+1\right). \quad \text{(B.8)}$$

Since the assumed the distribution of $x^{N_{\text{dof}}}$ is uniform distribution, i.e. $w^i\left(x^{N_{\text{dof}}}\right)=1/2\pi$, the resulting expression for $E\left[V\left(\mathbf{x}\right)\right]$ is obtained as

$$E\left[V\left(\mathbf{x}\right)\right]=\frac{1}{2N+1}\sum_{n=-N}^{N}\tilde{v}_0\big|_n\,. \quad \text{(B.9)}$$

As the adaptive refinement scheme is employed on each cut along $N_{\text{dof}}^{\text{th}}$ dimension, (B.9) can be adopted to the ME-PC formulation by considering the law of total probability as

$$E\left[V(\mathbf{x})\right] = \frac{1}{2N+1}\sum_{n=-N}^{N}\sum_{j=1}^{N_d}\tilde{v}_{0,j}\Big|_n J_j = \frac{1}{2N+1}\sum_{j=1}^{N_d} J_j \sum_{n=-N}^{N}\tilde{v}_{0,j}\Big|_n \quad . \tag{B.10}$$

APPENDIX B
DERIVATION OF EQUATION (3.26)

The variance of an observable $V(\mathbf{x})$ over the random domain D can be expressed as

$$\mathrm{var}\left[V(\mathbf{x})\right] = E\left[\left(V(\mathbf{x})\right)^2\right] - \left(E\left[V(\mathbf{x})\right]\right)^2. \tag{C.1}$$

Using (3.21), the term $E\left[\left(V(\mathbf{x})\right)^2\right]$ can be written as

$$E\left[\left(V(\mathbf{x})\right)^2\right] \cong \int_D \left[\sum_{n=-N}^{N} V\left(\left[x^1,...,x^{N_{\mathrm{dof}}-1}, n\Delta x^{N_{\mathrm{dof}}}\right]\right) DI_N\left(x^{N_{\mathrm{dof}}} - n\Delta x^{N_{\mathrm{dof}}}\right)\right]^2 d\mathbf{x}. \tag{C.2}$$

Expanding the summation in (C.2) yields

$$E\left[\left(V(\mathbf{x})\right)^2\right] \cong \int_D \left[V_0\big|_{-N\Delta x^{N_{\mathrm{dof}}}} DI_N\left(x^{N_{\mathrm{dof}}} + N\Delta x^{N_{\mathrm{dof}}}\right) + \ldots + V_0\big|_{N\Delta x^{N_{\mathrm{dof}}}} DI_N\left(x^{N_{\mathrm{dof}}} - N\Delta x^{N_{\mathrm{dof}}}\right)\right]^2 d\mathbf{x}. \tag{C.3}$$

where $V_0\big|_{n\Delta x^{N_{\mathrm{dof}}}} = V\left(\left[x^1,...,x^{N_{\mathrm{dof}}-1}, n\Delta x^{N_{\mathrm{dof}}}\right]\right)$ is used temporarily for the sake of compactness. The square of integrand can be evaluated as

$$
\begin{aligned}
E\left[\left(V(\mathbf{x})\right)^2\right] \cong \int_D & \left(V_0\big|_{-N\Delta x^{N_{\text{dof}}}}\ DI_N\left(x^{N_{\text{dof}}}+N\Delta x^{N_{\text{dof}}}\right)\right)^2+\ldots+ \\
& \left(V_0\big|_{N\Delta x^{N_{\text{dof}}}}\ DI_N\left(x^{N_{\text{dof}}}-N\Delta x^{N_{\text{dof}}}\right)\right)^2+ \\
& \Big[2V_0\big|_{-N\Delta x^{N_{\text{dof}}}}\ V_0\big|_{(-N+1)\Delta x^{N_{\text{dof}}}}\ DI_N\left(x^{N_{\text{dof}}}+N\Delta x^{N_{\text{dof}}}\right) \\
& DI_N\left(x^{N_{\text{dof}}}+(N-1)\Delta x^{N_{\text{dof}}}\right)+\ldots+ \\
& 2V_0\big|_{(N-1)\Delta x^{N_{\text{dof}}}}\ V_0\big|_{N\Delta x^{N_{\text{dof}}}}\ DI_N\left(x^{N_{\text{dof}}}-(N-1)\Delta x^{N_{\text{dof}}}\right) \\
& DI_N\left(x^{N_{\text{dof}}}-N\Delta x^{N_{\text{dof}}}\right)\Big]d\mathbf{x}
\end{aligned}
\quad . \qquad \text{(C.4)}
$$

The sum of the terms in square bracket is zero since the integral of each term along $N_{\text{dof}}^{\text{th}}$ dimension is zero (for the proof see Appendix B.1). Therefore, expression in (C.4) is simplified as

$$
\begin{aligned}
E\left[\left(V(\mathbf{x})\right)^2\right] &\cong \int_D \left(V_0\big|_{-N\Delta x^{N_{\text{dof}}}}\ DI_N\left(x^{N_{\text{dof}}}+N\Delta x^{N_{\text{dof}}}\right)\right)^2+\ldots+ \\
&\quad \left(V_0\big|_{N\Delta x^{N_{\text{dof}}}}\ DI_N\left(x^{N_{\text{dof}}}-N\Delta x^{N_{\text{dof}}}\right)\right)^2 d\mathbf{x} \\
&\cong \int_D \sum_{n=-N}^{N}\left(V_0\big|_{-n\Delta x^{N_{\text{dof}}}}\ DI_N\left(x^{N_{\text{dof}}}-n\Delta x^{N_{\text{dof}}}\right)\right)^2 d\mathbf{x}
\end{aligned}
\quad . \qquad \text{(C.5)}
$$

By considering that $V_0\big|_{n\Delta x^{N_{\text{dof}}}} = V\left(\left[x^1,...,x^{N_{\text{dof}}-1},n\Delta x^{N_{\text{dof}}}\right]\right)$ and the random variables are mutually independent, (C.5) can be rewritten explicitly as

$$
\begin{aligned}
E\left[\left(V(\mathbf{x})\right)^2\right] \cong & \sum_{n=-N}^{N}\int_{x^{N_{\text{dof}}}} DI_N^2\left(x^{N_{\text{dof}}}-n\Delta x^{N_{\text{dof}}}\right)dx^{N_{\text{dof}}} \\
& \left[\int_{x^1\cdots x^{N_{\text{dof}}-1}}\left(\sum_{m=0}^{N_p}\tilde{v}_m\tilde{\mathbf{P}}_m\left(x^1,...,x^{N_{\text{dof}}-1}\right)\right)^2 dx^1\cdots dx^{N_{\text{dof}}-1}\right]_n
\end{aligned}
\quad . \qquad \text{(C.6)}
$$

The expression in (C.6) can be split into two parts as

$$
E\left[\left(V(\mathbf{x})\right)^2\right] \cong \sum_{n=-N}^{N} I\left(x^{N_{\text{dof}}}\right)\left[I\left(x^1,\ldots,x^{N_{dof}-1}\right)\right]_n . \qquad \text{(C.7)}
$$

Expanding the summation inside $I\left(x^1,\ldots,x^{N_{\text{dof}}-1}\right)$ yields

$$I\left(x^1,\ldots,x^{N_{dof}-1}\right)=\int_{x^1\cdots x^{N_{dof}-1}}\left(\tilde{v}_0\tilde{\mathbf{P}}_0\left(x^1,...,x^{N_{\text{dof}}-1}\right)+...+\tilde{v}_{N_p}\tilde{\mathbf{P}}_{N_p}\left(x^1,...,x^{N_{\text{dof}}-1}\right)\right)^2 dx^1\cdots dx^{N_{dof}-1} \quad \text{(C.8)}$$

The square of integrand in (C.8) can be evaluated as

$$\begin{aligned}I\left(x^1,\ldots,x^{N_{dof}-1}\right)=\int_{x^1\cdots x^{N_{dof}-1}}&\left(\tilde{v}_0\tilde{\mathbf{P}}_0\left(x^1,...,x^{N_{\text{dof}}-1}\right)\right)^2+...+\\&\left(\tilde{v}_{N_p}\tilde{\mathbf{P}}_{N_p}\left(x^1,...,x^{N_{\text{dof}}-1}\right)\right)^2+\\&\Big[\tilde{v}_0\tilde{\mathbf{P}}_0\left(x^1,...,x^{N_{\text{dof}}-1}\right)\tilde{v}_1\tilde{\mathbf{P}}_1\left(x^1,...,x^{N_{\text{dof}}-1}\right)+...+\\&\tilde{v}_{N_p-1}\tilde{\mathbf{P}}_{N_p-1}\left(x^1,...,x^{N_{\text{dof}}-1}\right)\tilde{v}_{N_p}\tilde{\mathbf{P}}_{N_p}\left(x^1,...,x^{N_{\text{dof}}-1}\right)\Big]\\&dx^1\cdots dx^{N_{dof}-1}\end{aligned} \quad \text{(C.9)}$$

Since the integral of each term in square bracket of (C.9) is zero due to the normalization/orthogonality relation, (C.9) can be simplified as

$$I\left(x^1,\ldots,x^{N_{dof}-1}\right)=\int_{x^1\cdots x^{N_{dof}-1}}\left(\tilde{v}_0\tilde{\mathbf{P}}_0\left(x^1,...,x^{N_{\text{dof}}-1}\right)\right)^2+...+\left(\tilde{v}_{N_p}\tilde{\mathbf{P}}_{N_p}\left(x^1,...,x^{N_{\text{dof}}-1}\right)\right)^2 dx^1\cdots dx^{N_{dof}-1} \quad \text{(C.10)}$$

The remaining integrals can be evaluated again using orthogonality relation and the resulting expression for $I\left(x^1,\ldots,x^{N_{\text{dof}}-1}\right)$ is obtained as

$$I\left(x^1,\ldots,x^{N_{dof}-1}\right)=\sum_{m=0}^{N_p}\tilde{v}_m^2 . \quad \text{(C.11)}$$

Using (3.22), the term $I\left(x^{N_{\text{dof}}}\right)$ in (C.7) can be written explicitly as

$$I\left(x^{N_{\text{dof}}}\right)=\int_{x^{N_{\text{dof}}}}\left(\frac{\sin\left[\left(2N+1\right)\left(x^{N_{\text{dof}}}-n\Delta x^{N_{\text{dof}}}\right)/2\right]}{\left(2N+1\right)\sin\left(\left(x^{N_{\text{dof}}}-n\Delta x^{N_{\text{dof}}}\right)/2\right)}\right)^2 dx^{N_{\text{dof}}}\,. \tag{C.12}$$

The integral of the square of Dirichlet kernel $I\left(x^{N_{\text{dof}}}\right)$ is obtained as (for the proof see Appendix B.2)

$$I\left(x^{N_{\text{dof}}}\right)=2\pi/\left(2N+1\right). \tag{C.13}$$

Since the assumed the distribution of $x^{N_{\text{dof}}}$ is uniform distribution, i.e. $w^i\left(x^{N_{\text{dof}}}\right)=1/2\pi$, the resulting expression for $I\left(x^{N_{\text{dof}}}\right)$ is obtained as

$$I\left(x^{N_{\text{dof}}}\right)=1/\left(2N+1\right). \tag{C.14}$$

Substituting (C.14) and (C.11) in (C.7) yields

$$\begin{aligned}E\left[\left(V\left(\mathbf{x}\right)\right)^2\right]&\cong\frac{1}{\left(2N+1\right)}\sum_{n=-N}^{N}\left[\sum_{m=0}^{N_p}\tilde{v}_m^2\right]_n\\&\cong\frac{1}{\left(2N+1\right)}\sum_{n=-N}^{N}\sum_{m=0}^{N_p}\tilde{v}_m^2\Big|_n\end{aligned}\,. \tag{C.15}$$

As the adaptive refinement scheme is employed on each cut along $N_{\text{dof}}^{\text{th}}$ dimension, (C.15) can be adopted to the ME-PC formulation by considering the law of total probability as

$$E\left[\left(V\left(\mathbf{x}\right)\right)^2\right]\cong\frac{1}{\left(2N+1\right)}\sum_{j=1}^{N_d}J_j\sum_{n=-N}^{N}\sum_{m=0}^{N_p}\tilde{v}_{m,j}^2\Big|_n\,. \tag{C.16}$$

Substituting (C.16) and (B.10) in (C.1) yields

$$\operatorname{var}\left[V(\mathbf{x})\right]=\frac{1}{(2N+1)}\sum_{j=1}^{N_d}J_j\sum_{n=-N}^{N}\sum_{m=0}^{N_p}\tilde{v}_{m,j}^2\Big|_n-\left(\frac{1}{2N+1}\sum_{j=1}^{N_d}J_j\sum_{n=-N}^{N}\tilde{v}_{0,j}\Big|_n\right)^2. \tag{C.17}$$

Here, 0^{th} coefficient of the p^{th}- order local gPC expansion in the first term can be written separately as

$$\operatorname{var}\left[V(\mathbf{x})\right]=\frac{1}{(2N+1)}\sum_{j=1}^{N_d}J_j\sum_{n=-N}^{N}\sum_{m=1}^{N_p}\tilde{v}_{m,j}^2\Big|_n+\left[\frac{1}{(2N+1)}\sum_{j=1}^{N_d}J_j\sum_{n=-N}^{N}\tilde{v}_{0,j}^2\Big|_n-\left(\frac{1}{2N+1}\sum_{j=1}^{N_d}J_j\sum_{n=-N}^{N}\tilde{v}_{0,j}\Big|_n\right)^2\right]. \tag{C.18}$$

The terms in square bracket in (C.18) yields the variance of $\tilde{v}_{0,j}\big|_n$, i.e.

$$E\left[\left(\tilde{v}_{0,j}\big|_n-E\left[\tilde{v}_{0,j}\big|_n\right]\right)^2\right]=E\left[\tilde{v}_{0,j}^2\big|_n\right]-\left(E\left[\tilde{v}_{0,j}\big|_n\right]\right)^2, \tag{C.19}$$

where $E[X]$, $X=\tilde{v}_{0,j}\big|_n,\tilde{v}_{0,j}^2\big|_n,\left(\tilde{v}_{0,j}\big|_n-E\left[\tilde{v}_{0,j}\big|_n\right]\right)^2$, is given as

$$E[X]=\frac{1}{(2N+1)}\sum_{j=1}^{N_d}J_j\sum_{n=-N}^{N}X\,. \tag{C.20}$$

Using (C.19) and (C.20), the expression in (C.18) can be updated as

$$\operatorname{var}\left[V(\mathbf{x})\right]=\frac{1}{(2N+1)}\sum_{j=1}^{N_d}J_j\sum_{n=-N}^{N}\sum_{m=1}^{N_p}\tilde{v}_{m,j}^2\Big|_n+\frac{1}{(2N+1)}\sum_{j=1}^{N_d}J_j\sum_{n=-N}^{N}\left(\tilde{v}_{0,j}\big|_n-E\left[\tilde{v}_{0,j}\big|_n\right]\right)^2. \tag{C.21}$$

When $X = \tilde{v}_{0,j}\big|_n$, the expression in (C.20) is the same as that in (B.10). So the final expression for the variance of an observable $V(\mathbf{x})$ over the random domain D can be obtained as

$$\mathrm{var}\left[V(\mathbf{x})\right] = \frac{1}{(2N+1)} \sum_{j=1}^{N_d} J_j \sum_{n=-N}^{N} \sum_{m=1}^{N_p} \tilde{v}_{m,j}^2\big|_n + \left(\tilde{v}_{0,j}\big|_n - E\left[V(\mathbf{x})\right]\right)^2 . \qquad \text{(C.22)}$$

B.1 Proof for Equation (C.5)

Assume $N = 1$, the integral of the first term in square bracket of (C.4) along $N_{\mathrm{dof}}^{\mathrm{th}}$ dimension can be written as

$$I = \int_0^{2\pi} DI_1\left(x^{N_{\mathrm{dof}}} + \Delta x^{N_{\mathrm{dof}}}\right) DI_1\left(x^{N_{\mathrm{dof}}}\right) dx^{N_{\mathrm{dof}}} . \qquad \text{(C.23)}$$

Due to the proof of Lemma 6.4 in [134], Dirichlet kernels in integrand can be written explicitly as

$$I = \int_0^{2\pi} \left(1 + 2\cos\left(x^{N_{\mathrm{dof}}} + \Delta x^{N_{\mathrm{dof}}}\right)\right)\left(1 + 2\cos\left(x^{N_{\mathrm{dof}}}\right)\right) dx^{N_{\mathrm{dof}}} . \qquad \text{(C.24)}$$

By noting $\Delta x^{N_{\mathrm{dof}}} = 2\pi/3$, the result of integral in (C.24) is found to be 0. Similarly, the results of the integrals of remaining terms in square bracket of (C.4) along $N_{\mathrm{dof}}^{\mathrm{th}}$ dimension are computed as 0. Although the proof here is given for $N = 1$, it is valid for any integer value of N.

B.2 Proof for Equation (C.13)

To evaluate the integral in (C.12), the Dirichlet kernel can be written in terms of cosine functions as [134]

$$\begin{aligned} DI_N\left(x^{N_{\text{dof}}}\right) &= \frac{\sin\left[\left(2N+1\right)x^{N_{\text{dof}}}/2\right]}{\left(2N+1\right)\sin\left(x^{N_{\text{dof}}}/2\right)} \\ &= \frac{1}{\left(2N+1\right)}\left[1+2\cos\left(x^{N_{\text{dof}}}\right)+\ldots+2\cos\left(Nx^{N_{\text{dof}}}\right)\right] \end{aligned} . \tag{C.25}$$

Inserting (C.25) into (C.12) yields

$$\begin{aligned} I\left(x^{N_{\text{dof}}}\right) = \frac{1}{\left(2N+1\right)^2}\int_{x^{N_{\text{dof}}}} &\left(1+2\cos\left(x^{N_{\text{dof}}}-n\Delta x^{N_{\text{dof}}}\right)+\ldots+\right. \\ &\left.2\cos\left(N\left(x^{N_{\text{dof}}}-n\Delta x^{N_{\text{dof}}}\right)\right)\right)^2 dx^{N_{\text{dof}}} \end{aligned} . \tag{C.26}$$

Considering the interval for $x^{N_{\text{dof}}}$ is $[0,2\pi]$, the result of the integral in (C.26) is 6π for $N=1$, 10π for $N=2$, and 14π for $N=3$. By induction, the result of integral in (C.26) is obtained as $2\pi\left(2N+1\right)$ for any integer value of N. To this end, the integral of the square of Dirichlet kernel $I\left(x^{N_{\text{dof}}}\right)$ is obtained as

$$I\left(x^{N_{\text{dof}}}\right) = 2\pi/\left(2N+1\right). \tag{C.27}$$

REFERENCES

[1] R. Holland and R. S. John, *Statistical electromagnetics*. Philadelphia,PA: Taylor & Francis, 1999.

[2] S. K. Goudos, E. E. Vafiadis, and J. N. Sahalos, "Monte Carlo simulation for the prediction of the emission level from multiple sources inside shielded enclosures," *IEEE Trans. Electromagn. Compat.*, vol. 44, pp. 291-308, 2002.

[3] J. Vaessen, O. Sy, M. van Beurden, A. Tijhuis, and B. Michielsen, "Monte-Carlo method applied to a stochastically varying wire above a PEC ground plane," in *Proc. EMC Europe Workshop*, Paris, France, 2007, pp. 1-5.

[4] G. Lucca, "Induced Noise in a Telephone Circuit: a Monte Carlo Approach," in *Proc. 20th Int. Zurich Symp. EMC*, Zurich, Switzerland, 2009, pp. 229-232.

[5] G. S. Fishman, *Monte Carlo: Concepts, algorithms, and applications*. Berlin, Germany: Springer-Verlag, 1995.

[6] D. Xiu and G. E. Karniadakis, "The Wiener-Askey polynomial chaos for stochastic differential equations," *SIAM J. Sci. Comput.*, vol. 24, pp. 619-644, 2002.

[7] R. G. Ghanem and P. D. Spanos, *Stochastic Finite Elements: A Spectral Approach*. New York: Dover, 1991.

[8] D. Xiu and G. E. Karniadakis, "Modeling uncertainty in flow simulations via generalized polynomial chaos," *J. Comput. Phys.*, vol. 187, pp. 137-167, 2003.

[9] D. Xiu, D. Lucor, C. H. Su, and G. E. Karniadakis, "Performance evaluation of generalized polynomial chaos," in *Proc. Int. Conf. Comput. Sci.*, Melbourne, Australia, 2003, pp. 346-354.

[10] D. Xiu, "Fast numerical methods for stochastic computations: A review," *Commun. Comput. Phys.*, vol. 5, pp. 242-272, 2009.

[11] D. Xiu, "Efficient collocational approach for parametric uncertainty analysis," *Commun. Comput. Phys.*, vol. 2, pp. 293-309, 2007.

[12] I. S. Stievano, P. Manfredi, and F. G. Canavero, "Stochastic analysis of multiconductor cables and interconnects," *IEEE Trans. Electromagn. Compat.*, vol. 53, pp. 501-507, 2011.

[13] R. S. Edwards, A. C. Marvin, and S. J. Porter, "Uncertainty analyses in the finite-difference time-domain method," *IEEE Trans. Electromagn. Compat.*, vol. 52, pp. 155-163, 2010.

[14] I. S. Stievano, P. Manfredi, and F. G. Canavero, "Parameters variability effects on multiconductor interconnects via Hermite polynomial chaos," *IEEE Trans. Compon., Packag., Manuf. Technol.*, vol. 1, pp. 1234-1239.

[15] A. C. Yucel, H. Bagci, and E. Michielssen, "Fast probability density function estimation for statistical EMC/EMI characterization," presented at the USNC/URSI Nat. Radio Sci. Meet., Charleston, SC, 2009.

[16] S. Jianxiang, W. Hanfeng, C. Ji, and F. Jun, "Analysis of via impedance variations with a polynomial chaos method," in *Proc. IEEE Int. Symp. on EMC*, 2011, pp. 899-904.

[17] O. Aiouaz, D. Lautru, M.-F. Wong, E. Conil, A. Gati, J. Wiart, and V. Hanna, "Uncertainty analysis of the specific absorption rate induced in a phantom using a stochastic spectral collocation method," *Ann. Telecommun.*, vol. 66, pp. 409-418, 2011.

[18] H. Bagci, A. C. Yucel, J. S. Hesthaven, and E. Michielssen, "A fast Stroud-based collocation method for statistically characterizing EMI/EMC phenomena on complex platforms," *IEEE Trans. Electromagn. Compat.*, vol. 51, pp. 301-311, 2009.

[19] H. Bagci, C. Yavuz, A. C. Yucel, J. S. Hesthaven, and E. Michielssen, "A fast and parallel stroud-based stochastic collocation method for statistical EMI/EMC analysis," in *Proc. IEEE Int. Symp. EMC*, Detroit, MI, 2008, pp. 1-5.

[20] C. Chauviere, J. S. Hesthaven, and C. L. Wilcox, "Efficient computation of RCS from scatterers of uncertain shapes," *IEEE Trans. Antennas Propagat.*, vol. 55, pp. 1437-1448, May 2007.

[21] C. Chauviere, J. S. Hesthaven, and L. Lurati, "Computational modeling of uncertainty in time-domain electromagnetics," *SIAM J. Sci. Comput.*, vol. 28, pp. 751-775, 2006.

[22] L. R. A. X. de Menezes, A. Ajayi, C. Christopoulos, P. Sewell, and G. A. Borges, "Efficient computation of stochastic electromagnetic problems using unscented transforms," *IET Sci. Meas. Technol.*, vol. 2, pp. 88-95, 2008.

[23] O. O. Sy, M. C. v. Beurden, B. L. Michielsen, and A. G. Tijhuis, "Variance and kurtosis-based characterization of resonances in stochastic transmission lines: local versus global random geometries," *Turk. J. Electr. Eng. Co.*, vol. 17, pp. 217-230, 2009.

[24] F. Diouf and F. Canavero, "Crosstalk statistics via collocation method," in *Proc. IEEE Int. Symp. EMC*, Austin, TX, 2009, pp. 92-97.

[25] A. Ajayi, P. Ingrey, P. Sewell, and C. Christopoulos, "Direct computation of statistical variations in electromagnetic problems," *IEEE Trans. Electromagn. Compat.*, vol. 50, pp. 325-332, 2008.

[26] A. Ajayi, "Direct computation of statistical variations in electromagnetic problems," PhD Thesis, The University of Nottingham, 2008.

[27] S. M. Smith and C. Furse, "A stochastic FDTD method for statistically varying biological tissues," in *Proc. IEEE AP-S. Int. Symp.*, 2011, pp. 2274-2277.

[28] O. O. Sy, "Computation of stochastic observables in electromagnetic interaction theory," PhD Thesis, Technische Universiteit Eindhoven, 2009.

[29] X. Wan and G. E. Karniadakis, "An adaptive multi-element generalized polynomial chaos method for stochastic differential equations," *J. Comput. Phys.,* vol. 209, pp. 617-642, 2005.

[30] X. Wan and G. E. Karniadakis, "Multi-element generalized polynomial chaos for arbitrary probability measures," *SIAM J. Sci. Comput.,* vol. 28, pp. 901-928, 2006.

[31] J. Foo, X. Wan, and G. E. Karniadakis, "The multi-element probabilistic collocation method (ME-PCM): Error analysis and applications," *J. Comput. Phys.,* vol. 227, pp. 9572-9595, 2008.

[32] X. Ma and N. Zabaras, "An adaptive hierarchical sparse grid collocation algorithm for the solution of stochastic differential equations," *J. Comput. Phys.,* vol. 228, pp. 3084-3113, 2009.

[33] N. Agarwal and N. R. Aluru, "A domain adaptive stochastic collocation approach for analysis of MEMS under uncertainties," *J. Comput. Phys.,* vol. 228, pp. 7662-7688, 2009.

[34] N. Agarwal and N. R. Aluru, "Weighted Smolyak algorithm for solution of stochastic differential equations on non-uniform probability measures," *Internat. J. Numer. Methods Engrg.,* vol. 85, pp. 1365-1389, 2011.

[35] H. Rabitz, Ö. F. Alis, J. Shorter, and K. Shim, "Efficient input-output model representations," *Comput. Phys. Commun.,* vol. 117, pp. 11-20, 1999.

[36] R. Fisher, *Statistical methods for research workers*. Edinburgh: Oliver and Boyd, 1925.

[37] I. M. Sobol, "Global sensitivity indices for nonlinear mathematical models and their Monte Carlo estimates," *Math. Comput. Sim.,* vol. 55, pp. 271-280, 2001.

[38] H. Rabitz and O. F. Alis, "General foundations of high-dimensional model representations," *J. Math. Chem.,* vol. 25, 1999.

[39] J. Foo and G. E. Karniadakis, "Multi-element probabilistic collocation method in high dimensions," *J. Comput. Phys.,* vol. 229, pp. 1536-1557, 2010.

[40] X. Ma and N. Zabaras, "An adaptive high-dimensional stochastic model representation technique for the solution of stochastic partial differential equations," *J. Comput. Phys.,* vol. 229, pp. 3884-3915, 2010.

[41] S. Rahman, "A dimensional decomposition method for stochastic fracture mechanics," *Eng. Frac. Mech.,* vol. 73, pp. 2093-2109, 2006.

[42] H. Xu and S. Rahman, "Decomposition methods for structural reliability analysis," *Probabilist. Eng. Mech.,* vol. 20, pp. 239-250, 2005.

[43] M. Griebel, "Sparse grids and related approximation schemes for high dimensional problems," in *Proc. of the Conf. on Foundations of Comput. Math.*, Santander, Spain, 2005.

[44] M. Griebel and M. Holtz, "Dimension-wise integration of high-dimensional functions with applications to finance," *J. Complexity*, vol. 26, pp. 455-489, 2010.

[45] D. Xiu, *Numerical methods for stochastic computations: A spectral method approach*: Princeton university press, 2010.

[46] M. A. Tatang, W. Pan, R. G. Prinn, and G. J. McRae, "An efficient method for parametric uncertainty analysis of numerical geophysical models," *J. Geophys. Res.*, vol. 102, pp. 21925-21932, 1997.

[47] L. Mathelin and M. Hussaini, "A stochastic collocation algorithm for uncertainty analysis," NASA Langley Research Center, Hampton, VA, Tech. Rep. NASA/CR-2003-212153, Feb. 2003.

[48] D. Xiu and J. S. Hesthaven, "High-order collocation methods for differential equations with random inputs," *SIAM J. Sci. Comput.*, vol. 27, pp. 1118-1139, 2005.

[49] G. D'Antona, A. Monti, F. Ponci, and L. Rocca, "Maximum entropy multivariate analysis of uncertain dynamical systems based on the Wiener-Askey polynomial chaos," *IEEE Trans. Instrum. Meas.*, vol. 56, pp. 689-695, 2007.

[50] R. E. Caflisch, "Monte Carlo and quasi-Monte Carlo methods," *Acta Numerica*, vol. 7, pp. 1-49, 1998.

[51] B. Paul, L. F. Bennett, and N. Harald, "Implementation and tests of low-discrepancy sequences," *ACM Trans. Model. Comput. Simul.*, vol. 2, pp. 195-213, 1992.

[52] I. Babuska, F. Nobile, and R. Tempone, "A stochastic collocation method for elliptic partial differential equations with random input data," *SIAM J. Numer. Anal.*, vol. 45, pp. 1005-1034, 2007.

[53] P. J. Davis and P. Rabinowitz, *Numerical Integration*. London, U.K.: Blaisdell, 1967.

[54] S. A. Smolyak, "Quadrature and interpolation formulas for tensor products of certain classes of functions," *Soviet Math. Dokl.*, vol. 4, pp. 240-243, 1963.

[55] A. H. Stroud, "Remarks on the disposition of points in numerical integration formulas " *Math. Comput.*, vol. 11, pp. 257-261, 1957.

[56] A. H. Stroud, "Numerical integration formulas of degree two," *Math. Comput.*, vol. 14, pp. 21-26, 1960.

[57] A. H. Stroud, *Approximate Calculation of Multiple Integrals*. Englewood Cliffs, NJ: Prentice-Hall, 1971.

[58] V. I. Krylov, *Approximate Calculation of Integrals*. New York: Macmillan, 1962.

[59] D. Xiu, "Numerical integration formulas of degree two," *Appl. Numer. Math.*, vol. 58, pp. 1515-1520, 2008.

[60] H. Bagci, A. E. Yilmaz, J. M. Jin, and E. Michielssen, "Fast and rigourous analysis of EMC/EMI phenomena on electrically large and complex cable-loaded structures," *IEEE Trans. Electromagn. Compat.*, vol. 49, pp. 361-381, 2007.

[61] H. Bagci, A. E. Yilmaz, and E. Michielssen, "An FFT-accelerated time-domain multiconductor transmission line simulator," *IEEE Trans. Electromagn. Compat.*, vol. 52, pp. 199-214, 2010.

[62] A. E. Yilmaz, J.-M. Jin, and E. Michielssen, "A parallel FFT accelerated transient field-circuit simulator," *IEEE Trans. Microw. Theory Tech.*, vol. 53, pp. 2851-2865, 2005.

[63] E. F. Vance, *Coupling to Shielded Cables*. New York: Wiley, 1978.

[64] W. E. Byerly, *Elements of the integral calculus, with a key to the solution of differential equations, and a short table of integrals*. New York: G.E. Stechert & Co., 1941.

[65] D. A. Hill, "Plane wave integral representation for fields in reverberation chambers," *IEEE Trans. Electromagn. Compat.*, vol. 40, pp. 209-217, Aug. 1998.

[66] D. A. Hill and J. M. Ladbury, "Spatial-correlation functions of fields and energy density in areverberation chamber," *IEEE Trans. Electromagn. Compat.*, vol. 44, pp. 95-101, Feb. 2002.

[67] N. Wiener, "The Homogeneous Chaos," *Amer. J. Math.*, vol. 60, pp. 897-936, 1938.

[68] R. H. Cameron and W. T. Martin, "The Orthogonal Development of Non-Linear Functionals in Series of Fourier-Hermite Functionals," *Ann. of Math.*, vol. 48, pp. 385-392, 1947.

[69] S. S. Isukapalli, "Uncertainty analysis of transport-transformation models," Ph.D. dissertation, Univ. New Jersey, New Brunswick, NJ, 1999.

[70] S. R. Dooley and A. K. Nandi, "Notes on the interpolation of discrete periodic signals using sinc function related approaches," *IEEE Trans. Signal Process.*, vol. 48, pp. 1201-1203, 2000.

[71] A. Saitou, Y. Takahashi, T. Ooba, K. Iwazumi, F. Higuchi, and K. Kobayashi, "Variation detection device, data communication apparatus, and method of detecting variation," U.S. Patent 7528708, May 5, 2009.

[72] W. C. Chew, M. S. Tong, and B. Hu, *Integral equation methods for electromagnetic and elastic waves*. San Rafael, CA: Morgan and Claypool, 2009.

[73] J. D. Brunett, "Efficient integral equation algorithms and their application to RFID installation," Ph.D. dissertation, Univ. Michigan, Ann Arbor, MI, 2008.

[74] *Mine Improvement and New Emergency Response Act of 2006 (MINER Act), Pub. L. No. 108-236 (S 2803)*, June 2006.

[75] Y. P. Zhang, G. X. Zheng, and J. H. Sheng, "Radio propagation at 900 MHz in underground coal mines," *IEEE Trans. Antennas Propag.*, vol. 49, pp. 757-762, 2001.

[76] Y. P. Zhang, "Novel model for propagation loss prediction in tunnels," *IEEE Trans. Veh. Technol.*, vol. 52, pp. 1308-1314, 2003.

[77] M. Ndoh, G. Y. Delisle, and R. Le, "A novel approach to propagation prediction in confined and diffracting rough surfaces," *Int. J. Numer. Model. El.*, vol. 16, pp. 535-555, 2003.

[78] S. Yarkan, S. Guzelgoz, H. Arslan, and R. R. Murphy, "Underground Mine Communications: A Survey," *IEEE Commun. Surveys Tuts.*, vol. 11, pp. 125-142, 2009.

[79] I. B. Mabrouk, L. Talbi, M. Nedil, and K. Hettak, "The effect of the human body on MIMO-UWB signal propagation in an underground mine gallery," *J. Electromagnet. Wave*, vol. 26, pp. 560-569, 2012.

[80] A. Chehri, P. Fortier, and P. M. Tardif, "Characterization of the ultra-wideband channel in confined environments with diffracting rough surfaces," *Wireless Pers. Commun*, vol. 62, pp. 859–877, 2012.

[81] A. C. Yucel, O. Bakir, H. Bagci, and E. Michielssen, "Statistical characterization of wave propagation in mine environments " *IEEE Antennas Wireless Propag. Lett.*, under review.

[82] L. Tsang, J. A. Kong, K.-H. Ding, and C. O. Ao, *Scattering of Electromagnetic Waves, Numerical Simulations* New York: John Wiley & Sons, Inc., 2001.

[83] D. G. Dudley, M. Lienard, S. F. Mahmoud, and P. Degauque, "Wireless propagation in tunnels," *IEEE Antennas Propag. Mag.*, vol. 49, pp. 11-26, 2007.

[84] A. Emslie, R. Lagace, and P. Strong, "Theory of the propagation of UHF radio waves in coal mine tunnels," *IEEE Trans. Antennas Propag.*, vol. 23, pp. 192-205, 1975.

[85] K. D. Laakmann and W. H. Steier, "Waveguides: characteristic modes of hollow rectangular dielectric waveguides," *Appl. Opt.*, vol. 15, pp. 1334-1340, 1976.

[86] Z. Sun and I. F. Akyildiz, "Channel modeling and analysis for wireless networks in underground mines and road tunnels," *IEEE Trans. Commun.*, vol. 58, pp. 1758-1768, 2010.

[87] R. L. Wagner, S. Jiming, and W. C. Chew, "Monte Carlo simulation of electromagnetic scattering from two-dimensional random rough surfaces," *IEEE Trans. Antennas Propag.*, vol. 45, pp. 235-245, 1997.

[88] C. Waltz, K. Sertel, M. A. Carr, B. C. Usner, and J. L. Volakis, "Massively parallel fast multipole method solutions of large electromagnetic scattering problems," *IEEE Trans. Antennas Propag.*, vol. 55, pp. 1810-1816, 2007.

[89] J. M. Taboada, L. Landesa, F. Obelleiro, J. L. Rodriguez, J. M. Bertolo, M. G. Araujo, J. C. Mourino, and A. Gomez, "High scalability FMM-FFT electromagnetic solver for supercomputer systems," *IEEE Antennas Propag. Mag.*, vol. 51, pp. 20-28, 2009.

[90] A. J. Poggio and E. K. Miller, "Integral equation solutions of three-dimensional scattering problems," in *Computer techniques for electromagnetics*, ed R. Mittra, New York: Pergamon, 1973.

[91] K. Umashankar, A. Taflove, and S. Rao, "Electromagnetic scattering by arbitrary shaped three-dimensional homogeneous lossy dielectric objects," *IEEE Trans. Antennas Propag.*, vol. 34, pp. 758-766, 1986.

[92] R. F. Harrington, *Field computation by moment methods*. Piscataway, NJ: IEEE Press, 1993.

[93] S. M. Rao, D. R. Wilton, and A. W. Glisson, "Electromagnetic scattering by surfaces of arbitrary shape," *IEEE Trans. Antennas Propagat.*, vol. 30, pp. 409-418, May 1982.

[94] S. M. Rao, C. C. Cha, R. L. Cravey, and D. L. Wilkes, "Electromagnetic scattering from arbitrary shaped conducting bodies coated with lossy materials of arbitrary thickness," *IEEE Trans. Antennas Propag.*, vol. 39, pp. 627-631, 1991.

[95] L. N. Medgyesi-Mitschang, J. M. Putnam, and M. B. Gedera, "Generalized method of moments for three-dimensional penetrable scatterers," *J. Opt. Soc. Am. A*, vol. 11, pp. 1383-1398, 1994.

[96] V. Rokhlin, "Diagonal forms of translational operators for the Helmholtz equation in three dimensions," *Appl. Comput. Harmon. Anal.*, vol. 1, pp. 82-93, Dec. 1993.

[97] R. Coifman, V. Rokhlin, and S. Wandzura, "The fast multipole method for the wave equation: a pedestrian prescription," *IEEE Antennas Propag. Mag.*, vol. 35, pp. 7-12, 1993.

[98] J. M. Song, C. C. Lu, and W. C. Chew, "Multilevel fast multipole algorithm for electromagnetic scattering by large complex objects," *IEEE Trans. Antennas Propag.*, vol. 45, pp. 1488-1493, 1997.

[99] M. Abramowitz and I. A. Stegun, *Handbook of mathematical functions*: Dover Publications, 1964.

[100] J. A. Stratton, *Electromagnetic Theory*, First ed. New York: McGraw Hill, 1941.

[101] W. C. Chew, J.-M. Jin, E. Michielssen, and J. M. Song(eds.), *Fast and Efficient Algorithms in Computational Electromagnetics*. Norwood,MA: Artech House, Inc., 2001.

[102] A. C. Yücel, F. P. Andriulli, and E. Michielssen, "Parallel self-tuning MLFMA library," in *Proc. URSI XXIX General Assembly*, Chicago, IL, 2008.

[103] M. Holtz, "Sparse grid quadrature in high dimensions with applications in finance and insurance," PhD Thesis, Institut für Numerische Simulation, Universität Bonn, 2008.

[104] G. Li, S.-W. Wang, and H. Rabitz, "Practical approaches to construct RS-HDMR component functions," *J. Phys. Chem. A*, vol. 106, pp. 8721-8733, 2002.

[105] Z. Gao and J. S. Hesthaven, "On ANOVA expansions and strategies for choosing the anchor point," *Appl. Math. and Comp.*, vol. 217, pp. 3274-3285, 2010.

[106] I. M. Sobol, "Theorems and examples on high dimensional model representation," *Reliab. Eng. Syst. Safe.*, vol. 79, pp. 187-193, 2003.

[107] Z. Zhang, M. Choi, and G. E. Karniadakis, "Anchor points matter in anova decomposition," in *Spectral and High Order Methods for Partial Differential Equations*. vol. 76, ed: Springer, 2011, pp. 347-355.

[108] X. Ma, "An efficient computational framework for uncertainty quantification in multiscale systems," PhD Thesis, Cornell university, Ithaca, NY, 2010.

[109] H. Xu and S. Rahman, "A generalized dimension-reduction method for multi-dimensional integration in stochastic mechanics," *Int. J. Numer. Meth. Engng.*, vol. 65, pp. 2292-2292, 2006.

[110] G. Li, C. Rosenthal, and H. Rabitz, "High dimensional model representations," *J. Phys. Chem. A.*, vol. 105, pp. 7765-7777, 2001.

[111] F. Y. Kuo, I. H. Sloan, G. W. Wasilkowski, and H. Wozniakowski, "On the decompositions of multivariate functions," Technical Report, University of New South Wales, 2008.

[112] M. Gunzburger and A. Labovsky, "An efficient and accurate numerical method for high-dimensional stochastic PDEs," *SIAM J. Sci. Comput.*, in press.

[113] B. Gustavsen and A. Semlyen, "Rational approximation of frequency domain responses by vector fitting," *IEEE Trans. Power Del.*, vol. 14, pp. 1052-1062, 1999.

[114] B. Gustavsen, "Improving the pole relocating properties of vector fitting," *IEEE Trans. Power Del.*, vol. 21, pp. 1587-1592, 2006.

[115] D. Deschrijver, M. Mrozowski, T. Dhaene, and D. D. Zutter, "Macromodeling of multiport systems using a fast implementation of the vector fitting method," *IEEE Microw. Wireless Compon. Lett.*, vol. 18, pp. 383-385, 2008.

[116] The vector fitting web site [Online]. Available: http://www.energy.sintef.no/Produkt/VECTFIT/index.asp.

[117] C. R. Paul, *Analysis of multiconductor transmission lines* 2nd ed. New York: Wiley-IEEE Press, 2007.

[118] S. E. Fisher, D. S. Weile, E. Michielssen, and W. Woody, "Pareto Genetic Algorithm Based Optimization of Log-Periodic Monopole Arrays Mounted On Realistic Platforms," *J. Electromagnet. Wave.*, vol. 13, pp. 571-598, 1999.

[119] D. S. Weile and E. Michielssen, "Genetic algorithm optimization applied to electromagnetics: a review," *IEEE Trans. Antennas Propagat.*, vol. 45, pp. 343-353, 1997.

[120] D. S. Weile and E. Michielssen, "Community genetic algorithm design of symmetric E-plane microwave filters," *Microw. Opt. Techn. Let.*, vol. 21, pp. 28-35, 1999.

[121] D. S. Weile and E. Michielssen, "Analysis of frequency selective surfaces using two-parameter generalized rational Krylov model-order reduction," *IEEE Trans. Antennas Propagat.*, vol. 49, pp. 1539-1549, 2001.

[122] D. S. Weile and E. Michielssen, "The control of adaptive antenna arrays with genetic algorithms using dominance and diploidy," *IEEE Trans. Antennas Propagat.*, vol. 49, pp. 1424-1433, 2001.

[123] D. S. Weile, E. Michielssen, and D. E. Goldberg, "Genetic algorithm design of Pareto optimal broadband microwave absorbers," *IEEE Trans. Electromagn. Compat.*, vol. 38, pp. 518-525, 1996.

[124] E. M. Koper, W. D. Wood, and S. W. Schneider, "Aircraft antenna coupling minimization using genetic algorithms and approximations," *IEEE Trans. Aerosp. Electron. Syst.*, vol. 40, pp. 742-751, 2004.

[125] A. Boag, E. Michielssen, and R. Mittra, "Design of electrically loaded wire antennas using genetic algorithms," *IEEE Trans. Antennas Propag.*, vol. 44, pp. 687-695, 1996.

[126] C. S. DeLuccia and D. H. Werner, "Nature-Based Design of Aperiodic Linear Arrays with Broadband Elements Using a Combination of Rapid Neural-Network Estimation Techniques and Genetic Algorithms," *IEEE Antennas Propagat. Mag.*, vol. 49, pp. 13-23, 2007.

[127] I. Couckuyt, F. Declercq, T. Dhaene, H. Rogier, and L. Knockaert, "Surrogate-based infill optimization applied to electromagnetic problems," *Int. J. RF Microw. C E*, vol. 20, pp. 492-501, 2010.

[128] J. W. Bandler, R. M. Biernacki, C. Shao Hua, P. A. Grobelny, and R. H. Hemmers, "Space mapping technique for electromagnetic optimization," *IEEE Trans. Microwave Theory Tech.*, vol. 42, pp. 2536-2544, 1994.

[129] J. W. Bandler, Q. S. Cheng, S. A. Dakroury, A. S. Mohamed, M. H. Bakr, K. Madsen, and J. Sondergaard, "Space mapping: the state of the art," *IEEE Trans. Microwave Theory Tech.*, vol. 52, pp. 337-361, 2004.

[130] S. Koziel and J. W. Bandler, "Space-Mapping Optimization With Adaptive Surrogate Model," *IEEE Trans. Microwave Theory Tech.*, vol. 55, pp. 541-547, 2007.

[131] S. Koziel, J. W. Bandler, and K. Madsen, "Space Mapping With Adaptive Response Correction for Microwave Design Optimization," *IEEE Trans. Microwave Theory Tech.*, vol. 57, pp. 478-486, 2009.

[132] A. A. Giunta, L. P. Swiler, S. L. Brown, M. S. Eldred, M. D. Richards, and E. C. Cyr, "The surfpack software library for surrogate modeling of sparse irregularly spaced multidimensional data," in *Proc. 11th AIAA/ISSMO Multidisciplinary Analysis and Optimization Conf.*, Portsmouth, VA, 2006.

[133] P. Kozakowski, M. Mrozowski, and W. Zieniutycz, "Synthesis of nonuniformly spaced arrays using genetic algorithm," in *12th Int. Conf. Microw. and Radar*, 1998, pp. 340-344.

[134] D. Bressoud, *A radical approach to real analysis*. Washington, DC: The Mathematical Association of America, 2006.